

THE REPLICATION OF MICRON SCALE PILLAR
ARRAYS FOR MEDICAL ULTRASOUND
APPLICATIONS

By

TIMOTHY JACK CLIPSHAM

A thesis submitted to The University of Birmingham
for the degree DOCTOR OF PHILOSOPHY

Department of Metallurgy and Materials
College of Engineering and Physical Sciences
The University of Birmingham
September 2009

UNIVERSITY OF
BIRMINGHAM

University of Birmingham Research Archive

e-theses repository

This unpublished thesis/dissertation is copyright of the author and/or third parties. The intellectual property rights of the author or third parties in respect of this work are as defined by The Copyright Designs and Patents Act 1988 or as modified by any successor legislation.

Any use made of information contained in this thesis/dissertation must be in accordance with that legislation and must be properly acknowledged. Further distribution or reproduction in any format is prohibited without the permission of the copyright holder.

Abstract

1-3 Piezocomposites show significant improvements over conventional, monolithic transducers. However, a 10 MHz piezocomposite would require a pillar array structure with an aspect ratio of > 9 and a feature size of $< 30 \mu\text{m}$; which makes fabrication difficult and increasing the operating frequency challenging. Several processes have been developed to improve on the industry standard, dice and fill, but they remain laboratory based. Viscous polymer (VP) embossing has been demonstrated as a route to smaller feature sizes and higher aspect ratios, but the process is limited by the availability of suitable moulds, which must be replicated to make the process cost effective.

This thesis reviews the micro replication and fabrication processes necessary to produce moulds for 1-3 piezocomposites, and characterises the replication process from hot embossing to a functioning 1-3 piezocomposite. It demonstrates that the Bosch process and electroforming can be combined to produce a master with a deeper array structure than has been previously demonstrated by these two processes. Piezocomposites have also been made which have pillar widths that are not possible by dice and fill, by filling hot embossed moulds that have aspect ratios of 14 and feature sizes of $30 \mu\text{m}$.

Dedication

To my wife, Victoria Lucy Clipsham, to whom I am
forever grateful for her love and support

Acknowledgments

The author would like to thank Prof T W Button for his help and advice during the project and Mr C Meggs for his assistance in building the control box for the hot embossing rig. The author is also grateful of the collaborative work carried out by Dr C Dunare, of the Scottish Microelectronics Centre, and the electroforming carried out by Xueyong Wei, of the Micro-engineering and Nano-technology Research Group at the University of Birmingham. Funding for this project was provided by the Engineering and Physical Sciences Research Council award reference no: EP/P50130X/1.

1 Introduction	1
2 Medical Ultrasound and Piezocomposites.....	4
2.1 High Frequency Medical Ultrasound	4
2.2 Piezocomposites	5
2.2.1 Acoustic Impedance	6
2.2.2 Electrical Impedance	7
2.2.3 Thickness Mode Electromechanical Coupling Constant.....	10
2.2.4 Piezocomposite Geometry and Resonances	11
2.2.5 Piezocomposite Summary	16
2.3 Piezocomposite Fabrication Routes.....	17
2.3.1 Dice and Fill	18
2.3.2 Ceramic Injection Moulding.....	19
2.3.3 Viscous Polymer Embossing as a Lost Mould Technique	20
2.3.4 Piezocomposite Fabrication Summary	23
2.4 Chapter References.....	24
3 Micro Replication and Fabrication.....	28
3.1 Micro Replication Processes for Polymer Moulds	28
3.1.1 Process Requirements.....	28
3.1.2 Micro Replication Process Outlines	31
3.1.3 Characteristics of Micro Replication Processes	33
3.1.4 Achievable Feature Sizes, Aspect Ratios and Materials	35
3.1.4.1 Micro Injection Moulding	36
3.1.4.2 Reaction Injection Moulding.....	38
3.1.4.3 Hot Embossed Structures	38
3.1.5 Geometry of the Replicated Structures.....	43
3.1.6 Selection of the Replication Process	45
3.1.7 Improving the Aspect Ratio & Feature Size of Hot Embossed Structures.....	46
3.1.8 1-3 Piezocomposites with Tapered Pillars	49
3.2 Micro Fabrication Techniques for the Master Tool.....	51
3.2.1 UV Lithography.....	52
3.2.2 LIGA.....	62

3.2.3 Laser Ablation	62
3.2.4 Micro Electro Discharge Machining (μ EDM).....	68
3.2.5 The Bosch Process.....	73
3.2.6 Electroforming.....	89
3.2.7 Selection of Master Tool Fabrication Technique	92
3.3 Chapter References.....	93
4 Project Aims, Objectives and Approach	101
5 Experimental and Analytical Procedures.....	106
5.1 Hot Embossing Rig Familiarisation	106
5.1.1 The Hot Embossing Process	107
5.1.2 Procedure for Investigating the Main Parameters	108
5.1.2.1 Isothermal vs. Non-isothermal Hot Embossing.....	109
5.1.3 Characterisation Methods	110
5.1.3.1 Percentage Mould Fill Method and Errors	110
5.1.3.2 De-embossing Force Method and Error	112
5.1.3.3 Severity of Defects Method.....	113
5.1.3.4 Curvature of the Substrate during De-embossing.....	114
5.2 Fabrication of Moulded Piezocomposites	115
5.2.1 Hot embossing Procedure.....	116
5.2.2 Mould Preparation Procedure.....	116
5.2.3 Twin Roll Milling.....	118
5.2.4 VP Embossing	118
5.2.5 Mould Dissolution	119
5.2.6 Burnout and Sintering.....	119
5.2.7 Backfilling	120
5.2.8 Lapping	120
5.2.9 Corona Poling	120
5.2.10 Electroding	121
5.3 Characterisation of Moulded Piezocomposites	123
5.3.1 Dimensions of the Master Tool, Mould and Dried Ceramic Pillars.....	123
5.3.2 Dimensions of the Sintered Bristle Block	125
5.3.3 Master Tool, Dried and Sintered Pillar Height.....	125

5.3.4 Mould Height.....	126
5.3.5 Comparisons between Process Stages	126
5.3.6 Determination of the Velocity of Sound in PZT	127
5.4 Chapter References.....	128
6 Master Tool and Piezocomposite Design	130
6.1 Considered Array Geometries	131
6.2 Dimensions of Pillar Arrays	132
6.3 Selection of Taper Range	133
6.4 Selection of Size Range.....	139
6.4.1 Minimum Feature Size	139
6.4.2 Aspect Ratio	143
6.4.3 Lapping Depth.....	146
6.5 Array Design and Summary	150
7 Master Tool Fabrication	154
7.1 Feasibility Study of Laser Ablation.....	154
7.1.1 Direct Fabrication of the Master Tool	154
7.1.2 Indirect Fabrication of the Master Tool.....	156
7.2 Feasibility Study of the Bosch Process	161
7.3 Master Tool Fabrication via the Bosch Process	165
7.4 Electroforming of Silicon Pre-forms	169
7.5 Master Tool Fabrication Summary.....	174
7.6 Chapter References.....	176
8 The Hot Embossing Rig	178
8.1 Design Considerations and Optimisation	178
8.1.1 Heated and Water Cooled Platens	179
8.1.1.1 Embossing Temperature and Pressure.....	179
8.1.1.2 Cooling Rate	183
8.1.1.3 Heating Rate and Temperature Control.....	186
8.1.1.4 Clamps and Mounting Stage	188
8.1.1.5 In Situ Testing	191
8.1.2 Control Box Specification and Design.....	192
8.1.2.1 Control Box Specification	193

8.1.2.2 Control Box Design	194
8.1.3 Design and Modification Summary	198
8.2 Hot Embossing Rig Familiarisation	200
8.2.1 Master Tool Used for Hot Embossing Rig Familiarisation	200
8.2.2 Embossing Temperature	202
8.2.2.1 Percentage Mould Fill	202
8.2.2.2 De-embossing Force	204
8.2.2.3 Common Defects	208
8.2.3 Embossing Load	215
8.2.3.1 Mould Fill	215
8.2.3.2 De-embossing Force	216
8.2.3.3 Common Defects	218
8.2.4 Dwell Time	220
8.2.4.1 Mould fill	220
8.2.4.2 De-embossing Force	223
8.2.4.3 Common Defects	225
8.2.5 De-embossing Temperature	228
8.2.5.1 De-embossing Force	228
8.2.5.2 Deformation to the Substrate during De-embossing	230
8.2.6 Summary of the Effect of Parameter Changes	233
8.3 Typical Cycle Times, Set-up Times and Equipment Costs	236
8.4 Chapter References	238
9 Fabrication and Characterisation of Moulded Piezocomposites	241
9.1 Master Tool	241
9.2 Hot Embossed Moulds	246
9.3 Dried Pillars after Mould Dissolution	254
9.4 Sintered Pillars	263
9.5 Piezocomposite Performance	270
9.6 Process Overview	276
9.7 Chapter References	282
10 Summary, Conclusions and Further Work	284
10.1 Summary	284

10.2 Conclusion.....	290
10.3 Further Work	292
11 Appendix	296
11.1 The Glass Transition Temperature of the PMMA.....	296
11.2 Particle Size Distribution.....	297
11.3 Expanded Technical Drawing of the Corona Poling Jig	298
11.4 Spreadsheet Screen Shot.....	299
11.5 Additional Details of the Hot Embossing Rig.....	301
11.5.1 Mounting Bars	301
11.5.2 Control Box Parts list	303
11.5.3 Control Box Layout.....	303

Table of Abbreviations

DRIE	Deep Reactive Ion Etching
ECC	Electromechanical Coupling Constant
ICP	Inductively Coupled Plasma
IQR	Interquartile Range
L/D	Die Land Length to Die Diameter Ratio
LED	Light Emitting Diode
LIGA	<i>(German Acronym)</i> X-ray Lithographie, Galvoformung und Abformtechnik, <i>(English Translation)</i> X-ray Lithography, electroforming and moulding
MIT	Massachusetts Institute of Technology
PC	Polycarbonate
PID	Proportional Integral Derivative
PMMA	Polymethyl methacrylate <i>...(Censored for commercial reasons)...</i>
PVDF	Polyvinylidene Difluoride
PZT	Lead Zirconate Titanate
Q1	First Quartile
Q3	Second Quartile
r.f.	Radio Frequency
Ra	Arithmetic Mean Roughness
RIM	Reaction Injection Moulding
RMS	Root Mean Squared
SEM	Scanning Electron Microscope
SMC	Scottish Microelectronics Centre
SSR	Solid State Relay <i>...(Censored for commercial reasons)...</i>
Tg	Glass Transition Temperature <i>...(Censored for commercial reasons)...</i>
UK-LMC	United Kingdom Laser Machining Centre
VP	Viscous Polymer
VPP	Viscous Polymer Processing
μEDM	Micro Electro Discharge Machining
μIM	Micro Injection Moulding

Chapter 1

Introduction

1 Introduction

In the field of medical ultrasound there is a push to image smaller and smaller structures within the body. This requires the transducer to operate at higher frequencies such that the component that creates the ultrasonic wave, the piezoelectric element, must be made smaller. One type of piezoelectric element that has seen significant research is the 1-3 piezocomposite which offers improved performance over monolithic materials. However, achieving a 10 MHz piezocomposite requires minimum features sizes of $< 30 \mu\text{m}$, and a 30 MHz piezocomposite requires a minimum feature size of $< 10 \mu\text{m}$. These requirements make fabricating these devices demanding because not only is the feature size small, but in some stages of the manufacturing process, aspect ratios as high as 9 or 16 are required.

The industry standard manufacturing route for 1-3 piezocomposites, 'dice and fill', struggles to make such small structures, and low production yields makes such a processes uneconomic. There are many techniques that have been explored to replace this method but many remain laboratory based. A promising technique is viscous polymer (VP) embossing, whereby ceramic dough is pressed into a polymer mould, dried, and then demoulded before sintering. Demoulding small feature sized, high aspect ratio ceramic structures is difficult, and must be achieved by mould dissolution. However, this means that the mould is destroyed every time a piezocomposite is made, and makes the process expensive. A solution to this is to use a micro replication technique to produce many moulds from a single master.

This thesis aims to develop a viable route for 1-3 piezocomposites that can be scaled up out of the laboratory but still be capable of producing piezocomposites into the $> 30 \text{ MHz}$ range,

such that the piezocomposites have smaller feature sizes, and higher aspect ratios than is possible by dice and fill. A review of the appropriate micro fabrication and micro replication processes is carried out, which pays particular attention to the design considerations of each stage from the fabrication of the master through to the final piezocomposite. From this review the Bosch process and electroforming were selected to produce a master for replication. A rig for micro replication has been designed, constructed and optimised for producing the piezocomposite moulds. These moulds were then embossed to characterise the VP and hot embossing processes, which produced very high aspect ratio, small feature sized moulds in the process.

Chapter 2

Medical Ultrasound and Piezocomposites

2 Medical Ultrasound and Piezocomposites

2.1 High Frequency Medical Ultrasound

Medical ultrasound is a common diagnostic technique that is, quick and easy to use, non-invasive, and does not expose the patient to any harmful radiation. It can be used in a range of frequencies, where conventional medical ultrasound typically operates at 3 to 10 MHz, but high frequency medical ultrasound operates at > 30 MHz and provides a microscopic resolution [1].

High frequency medical ultrasound has a low penetration depth and a high resolution which makes it particularly useful for imaging sub-surface structures such as in the eye and the skin [1]. Improving the resolution offers the opportunity to extend its use in dermatology and ophthalmology, as well as in small animal and intravascular imaging [1]. One such example for high frequency ultrasound is in the planning of excisional biopsy of cutaneous melanoma, whereby the tumour depth and the presence of tumour satellites can be identified before surgery [1].

The resolution of the image is related to the wavelength, such that the smaller the wavelength the smaller the structure that can be resolved. Equation 2.1 shows the link between the wavelength, λ , the frequency, f , and the velocity, c , of the ultrasonic wave used for imaging. The equation indicates that the push for an improved resolution leads to a push for a higher frequency ultrasound.

$$c = f\lambda \qquad \text{Equation 2.1}$$

2.2 Piezocomposites

An ultrasonic transducer is composed of a piezoelectric element, matching layers, backing layers, a lens, housing and cabling. The most important component in an ultrasonic transducer is the piezoelectric element, which converts electrical energy in to mechanical energy or visa versa [1, 2]. The piezoelectric element is made from a piezoelectric material that, upon the application of an electric field, produces a strain or visa versa. Typical piezoelectric materials used for the piezoelectric elements are the ceramic, lead zirconate titanate (PZT), the polymer, polyvinylidene diflouride (PVDF), or a composite material, known as a piezocomposite [2]. A piezocomposite is made from piezoelectric ceramic in an inactive polymer matrix and can come in a variety of configurations. One of the most widely studied types of piezocomposite is the 1-3 piezocomposite, which is shown in Figure 2.1 and consists of piezoelectric ceramic rods (typically PZT) upstanding in a polymer matrix. [3].

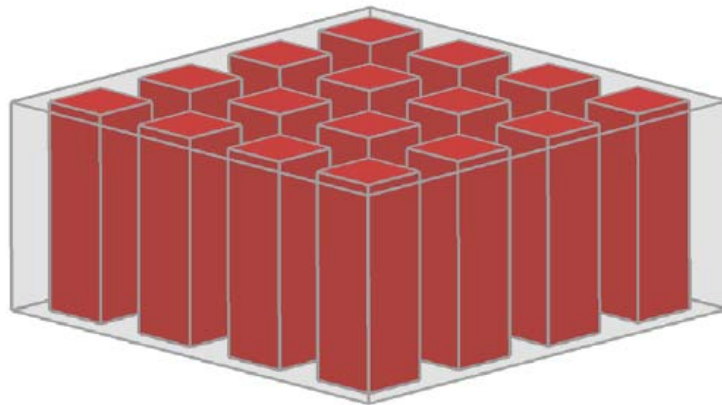


Figure 2.1. A 1-3 piezocomposites that consists of piezoelectric ceramic pillars surrounded by an inactive polymer matrix [3]

The properties of the piezoelectric materials affect the ability of the transducer to perform its function. To understand some of the properties required for a piezoelectric material we must first understand what the piezoelectric element is required to achieve.

The role of the piezoelectric element is to receive an electrical pulse from the driving electronics, convert the electrical energy into mechanical energy, and then transmit the acoustic wave across the interface into the body that is being imaged. The acoustic wave is then reflected by the internal structures of the body, and the piezoelectric element receives the weak acoustic signals emanating from them. The piezoelectric element must then efficiently convert the acoustic wave back into an electrical signal, before being interpreted into an image by a computer [4, 5]. The ability of the signal to cross the electrical and mechanical interfaces is dependent upon the matching of the electrical impedances of the circuit, and the matching of the acoustic impedances of the imaging medium. The signal strength is also reduced when the piezoelectric element converts the energy from one form to another, which is described by electromechanical coupling factor, k_t .

2.2.1 Acoustic Impedance

The acoustic impedance, Z , of a medium is the product of the density of the medium and the velocity of sound through it. The units of acoustic impedance are $\text{kg m}^{-2} \text{s}^{-1}$ or Rayl [6]. The acoustic impedance is analogous to the refractive index of light waves; such that the ratio of the refractive indexes controls how readily the wave will cross an interface between the two mediums [4]. Thus, when an acoustic wave tries to cross an interface, a proportion of the wave is reflected back and does not propagate into the second medium. This effect allows us to image the internal structures of the body, but can also cause large losses in the signal strength when the signal crosses from the transducer into the body. Therefore it is desirable to have a good match in the acoustic impedance of the piezoelectric element and the body [6].

The typical acoustic impedance of PZT is ~ 35 MRayl and for PVDF it is 3.4 MRayl. The acoustic impedance of soft tissue ranges from 1.3 to 1.7 MRayl and for hard tissue it ranges from 3.8 to 7.4 MRayl [6]. Therefore by comparing these values it can be seen that acoustic impedance of PVDF is particularly close to that of the human body, whilst for PZT the acoustic impedance matching is poor [7]. An advantage of piezocomposites is that they can be engineered to match the acoustic impedance of the body. The acoustic impedance varies linearly with the volume fraction of the piezoceramic and falls within a range of 3 for a low volume fraction to 35 MRayl for a high volume fraction. However these values are extremes and the most useful range is from 5 to 15 MRayl, which ensures that the impedance is close to that of the body, but without sacrificing the other properties of a piezocomposite [3].

2.2.2 Electrical Impedance

Electrical impedance, Z , is measured in ohms (Ω) and consists of a resistance component, X_R , and two reactance components, inductive reactance, X_L , and capacitive reactance, X_C . Resistance is caused by a resistor that opposes the *flow of current*, whilst the reactance is caused by inductors and capacitors that oppose the *change in current* and the *change in voltage* respectively. The impedance of an electrical component is simply the sum of the reactance and resistance expressed in complex form [8].

When an electrical component is operated using direct current the change in current and voltage only occurs when the device is switched on or off, such that only the resistance component needs to be considered. However, when a transducer is used for ultrasound applications it is operated using an alternating current, such that all three components should be considered. Conveniently though, piezoelectric elements are commonly made of an

insulator, with two electrodes on opposite faces and can therefore be approximated to a parallel plate capacitor [6]. Thus, both the resistance and inductive reactance components can be ignored, and it is only necessary to consider the capacitive reactance when calculating the electrical impedance. The capacitive reactance can be calculated from Equation 2.2 where f is the frequency of the voltage and C is the capacitance [8].

$$X_c = \frac{1}{(2\pi f C)} \quad \text{Equation 2.2}$$

Since transducers commonly exist as thin plates the capacitance can be found from the equation:

$$C = \frac{\epsilon_0 \epsilon_r A}{d} \quad \text{Equation 2.3}$$

where ϵ_0 is the relative permeability of free space, ϵ_r is the relative dielectric constant, A is the area of the plate, and d is the thickness of the plate.

Equation 2.2 and Equation 2.3 can be combined to define Equation 2.4. By realising that the relative permeability of free space is a constant, the area and thickness are controlled by the geometry of the piezoelectric element, and that the frequency is defined by the required resolution, it is possible to identify that the only material property that controls the electrical impedance is the relative dielectric constant, ϵ_r [4].

$$X_c = \frac{d}{2\pi f \epsilon_0 \epsilon_r A} \quad \text{Equation 2.4}$$

A high relative dielectric constant results in a low electrical impedance. The product of ϵ_0 and ϵ_r is the effective dielectric constant when the piezoelectric material is not clamped. For PVDF this is 9.7×10^{-11} F / m and for PZT5H it is 3010×10^{-11} F / m [2]. By substituting into Equation 2.4, with other standard values, the electrical impedance can be estimated and a comparison between PZT and PVDF can be easily made.

For both monolithic transducers it is assumed that $f = 30$ MHz, $A = 1$ mm² such that when considering a monolithic piezoelectric element made from PZT, where $\epsilon_0 \epsilon_r = 3010 \times 10^{-11}$ F/m and $d = 66$ μ m, X_c can be calculated to be:

$$X_c = 11.6 \Omega$$

Similarly, for a PVDF piezoelectric element with values of $\epsilon_0 \epsilon_r = 9.7 \times 10^{-11}$ F/m and $d = 35$ μ m, the reactive capacitance is, $X_c = 1915 \Omega$.

There are several orders of magnitude between these two values. The aim is to match the electrical impedance of the piezoelectric element to the electronic circuitry, so that a good transmission of the signal can be attained. The electrical impedance of standard circuitry is 50Ω and therefore neither material satisfies this criterion. However, other electronic components can be used to adjust the electrical impedance [9], and it is often desirable to have a higher dielectric constant because it is easier to move high currents at low voltages rather than the reverse [4].

As with the acoustic impedance, a 1-3 piezocomposite can be engineered with a controlled effective dielectric constant, enabling the impedance to the circuitry to be better matched. The effective dielectric constant varies linearly with the volume fraction of piezoceramic,

from the extreme of 10×10^{-11} F / m for low volume fractions to 1000×10^{-11} F / m for high volume fractions [4].

2.2.3 Thickness Mode Electromechanical Coupling Constant

The ability of a material to convert one form of energy into another is called the Electromechanical Coupling Constant (ECC) and is defined in Equation 2.5:

$$EEC = \frac{\text{Stored Mechanical Energy}}{\text{Total Stored Energy}} \quad \text{Equation 2.5}$$

This equation is a measure of the performance of the material to convert the electrical energy to mechanical energy [2].

Transducers are typically driven at the resonance frequency, which corresponds to the thickness of the piezoelectric element. The thickness mode ECC which is known as the k_t , describes the ECC in the thickness direction and is the ratio of the stored mechanical energy in the thickness direction, to the total stored energy. The thickness mode ECC is always less than the ECC [4, 5].

A high k_t is a particular advantage because less of the signal strength is lost when the energy is converted from electrical to mechanical, or vice versa. The k_t for PVDF is typically less than 30%, for PZT k_t is 40-50%, and in piezocomposites k_t is much higher at around 60-75% but this greatly depends on the volume fraction [4, 5].

The increase in k_t appears to be counterintuitive, since a proportion of the active material is removed. However, it can be understood by considering a piezoelectric pillar surrounded by soft polymer. For example, when an electric field is applied to the pillar it causes it to shorten and the sides begin to bulge at the expense of the polymer. However, when this is compared to a pillar surrounded by a stiff ceramic, or even a piezoceramic that also wishes to bulge, shortening the pillar becomes much more difficult [10]. The k_t of a piezocomposite is at its largest at a volume fraction of between 20 and 80 % ceramic. At high volume fractions there is insufficient polymer to deform preferentially, and the piezoceramic rods are constrained laterally. At small volume fractions the large amount of polymer is unable to be deformed by the ceramic rods, such that the k_t value becomes low again [5].

2.2.4 Piezocomposite Geometry and Resonances

A piezoelectric element typically has a planar or sheet geometry. This sheet is made from a single material in the case of monolithic PZT or PVDF, but in 1-3 piezocomposites it is made of pillars standing side by side in a polymer matrix. The thickness of the sheet is an important dimension because the resonance caused by the thickness of the piezoelectric element is typically used to increase the strength of the signal, and therefore defines the operating frequency [2].

The thickness resonance is caused by some of the acoustic wave being reflected back into the piezoelectric element when it is strained. If the reflected wave is exactly in phase with the next wave the amplitude is increased by constructive interference. Therefore the resonant thickness mode first occurs when half the wavelength is equal to the thickness of the

transducer [11]. The lowest operating frequency can therefore be calculated by substituting into $\lambda = 2t$ into Equation 2.1 and rearranging to give:

$$f_t = \frac{c}{2t} \quad \text{Equation 2.6}$$

where f_t is the thickness mode frequency, c is the velocity of sound in the piezoelectric element and t is the thickness of the piezoelectric element [11].

From Equation 2.6 it can be seen that for a good resolution image a small wavelength is required, and therefore a high operating frequency is needed. Thus, to insure that the operating frequency coincides with the thickness resonance, the piezoelectric element must be made thin. The typical thickness of a monolithic piezoelectric can be calculated by rearranging Equation 2.6:

$$t = \frac{c}{2f_t} \quad \text{Equation 2.7}$$

For PZT, $c = 3970 \text{ ms}^{-1}$ [2] such that the thickness of a PZT transducer operating at 30 MHz would be $66 \text{ }\mu\text{m}$, or for a PVDF transducer, where $c = 2070 \text{ ms}^{-1}$ [2], the thickness would be $t = 3.45 \times 10^{-6} = 35 \text{ }\mu\text{m}$.

In a piezocomposite the velocity of sound varies according to the volume fraction, such that the required thickness of a 30 MHz transducer is between the thicknesses of a PZT and PVDF piezoelectric element. These calculations demonstrate that a piezoelectric element must be

between 30 and 60 μm for high frequency ultrasound, and represents a significant challenge for their fabrication.

In piezocomposites the thickness is not the smallest dimension since they are composed of many pillars. These pillars, and their spacing, have corresponding resonances that affect the performance of the transducer. 1-3 Piezocomposites can have pillars in many sizes, shapes and distributions. The pillars are typically square or circular depending on the piezocomposite fabrication route used. The pillars are normally arranged uniformly, but they can also be arranged in a pattern or even randomly.

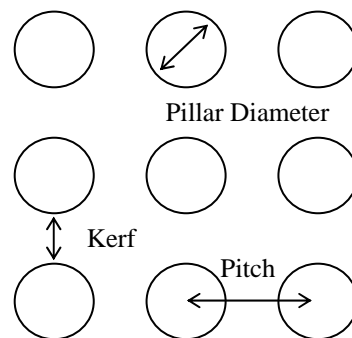


Figure 2.2 The dimensions that define a 1-3 piezocomposite using a square packed, round pillar array as an example

Figure 2.2 illustrates the dimensions used to describe the geometry of a piezocomposite that consists of a square array of circular pillars. Obviously, with different geometry pillars and different packing, further dimensions will be required to describe the array effectively. The width of the pillars depends on their required height, or thickness, of the piezocomposite, and their aspect ratio. The gap between the pillars, or kerf, depends on the packing geometry of the array and the required volume fraction; which in turn depends on the required properties of the piezocomposite [12, 13]. Typically the kerf is smaller than the width of the pillars and

is significantly smaller than the thickness of the piezocomposite. One final dimension used to describe a piezocomposite is the pitch, which is the sum of the pillar diameter and the kerf.

The array of pillars has its own resonances associated with it. These resonances cause noise in the image and are therefore undesirable. In particular, the most common resonances occur between neighbouring pillars, creating a wave that propagates laterally through the composite. This is illustrated in Figure 2.3. The resonances occur at wavelengths that correspond to the pillar spacing, such that the kerf should be adjusted so that the resonances do not occur near the operating frequency [10, 14].

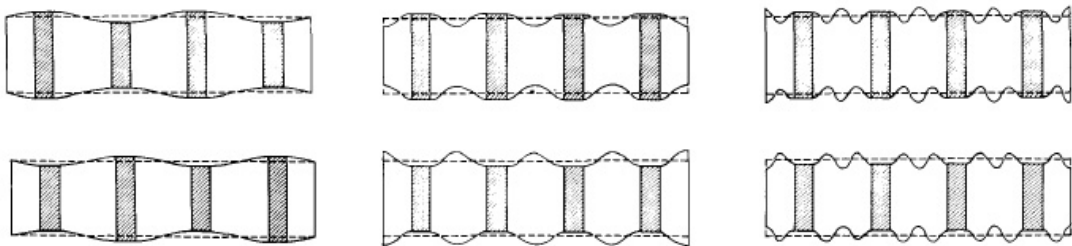


Figure 2.3 surface resonance waves propagating along the surface of the piezocomposite. These waves are related to the spacing of the pillars and should not occur at frequencies near the operating frequency [10]

In simple terms, the design of a piezocomposite is achieved by selecting the operating frequency and the volume fraction. The volume fraction affects the acoustic impedance, the electrical impedances, and the velocity of sound through the composite. Typically, a compromise is made between the properties such that the volume fraction is normally between 40 and 70% ceramic [15].

Once a compromise between the properties has been found, the velocity of sound and the operating frequency can be used to calculate the required thickness of the piezocomposite. The pillar width can then be calculated using the required height and the selected aspect ratio.

An aspect ratio of > 2 will give the correct pulse response and an aspect ratio of > 5 will maximise the k_t [15]. The volume fraction and the pillar width are then used to calculate the kerf, making sure that any resonances from it occur at greater than twice the operating frequency [10, 14]. If a more accurate design of the piezocomposite is required, finite element analysis methods such as PZFlex are used.

Following this simple approach we can estimate the dimensions of a piezocomposite. Table 2.1 shows the dimensions of a 1-3 piezocomposite with square packed, circular pillars that has a volume fraction of 50%. The speed of sound is required to be approximated, and is done so by the rule of mixtures, as shown in Equation 2.8. Here, V is the volume fraction, c is the velocity of sound, and the subscripts p , c and E denote the piezocomposite, ceramic and the epoxy matrix respectively.

$$c_p = V_c c_c + V_E c_E \quad \text{Equation 2.8}$$

By substituting in the velocity of sound of PZT to be $\sim 4000 \text{ ms}^{-1}$ and for epoxy $\sim 2000 \text{ ms}^{-1}$, the speed of sound through the piezocomposite can be approximated to be 3000 ms^{-1} .

Table 2.1 indicates that for a 10 MHz piezocomposite the thickness must be $\sim 150 \mu\text{m}$, and for a 30 MHz piezocomposite it must be $50 \mu\text{m}$. This means that for a relatively low aspect ratio pillar of 2.5, the pillar width and the kerf must be $70 \mu\text{m}$ and $23 \mu\text{m}$ respectively. Furthermore, the smallest feature in a 1-3 piezocomposite is the kerf and for a 10 and 30 MHz piezocomposite this is 30 or $10 \mu\text{m}$ respectively. It then follows that the largest aspect ratio,

and most challenging feature for fabrication of the piezocomposite, is actually the kerf rather than the pillars.

Table 2.1 The dimensions and aspect ratios of a 50% volume fraction 1-3 Piezocomposite *after lapping*. The calculations assume a velocity of 3000 ms^{-1} and square packed circular pillars

Frequency	Thickness (μm)	Pillar Diameter (μm)	Kerf (μm)	Pillar Aspect Ratio	Kerf Aspect Ratio
5 MHz	300	120	50	2.5	6.0
10 MHz	150	70	30	2.5	6.0
> 30 MHz	< 50	< 23	< 10	2.5	6.0

2.2.5 Piezocomposite Summary

A 1-3 piezocomposite consists of an array of piezoceramic pillars upstanding in a passive polymer matrix. They have a significant advantage over monolithic piezoelectric elements because neither PVDF nor PZT have exactly the right properties for a medical ultrasound transducer. PVDF has an acoustic impedance near ideal for imaging the human body, but is limited by a low k_t , whilst PZT has a high electromechanical coupling constant but is mainly limited by a high acoustic impedance. Piezocomposites, however, allow both the acoustic and electrical impedances to be tailored to the application and show an improved k_t over both monolithic materials [4, 5, 16].

The spatial scale of a piezocomposite is important because although the thickness affects the operating frequency, the size, shape, separation, and distribution all affect the performance of the device. The required thickness for a 30 MHz piezocomposite is around $50 \mu\text{m}$, with the kerf and width of the pillars being much smaller than this. The piezocomposite should be designed so that resonances that are not associated with the thickness should occur at more than twice the operating frequency, so that they do not affect the performance of the device.

2.3 Piezocomposite Fabrication Routes

1-3 Piezocomposites offer an improved performance over monolithic piezoelectric elements made from either PZT or PVDF. However the fine-scale of the piezoelectric elements represents a significant challenge for their fabrication. In order to appreciate the challenging dimensions of a piezocomposite it is necessary to introduce an intermediate structure called a ‘bristle block’, which is shown in Figure 2.4. All piezocomposite fabrication routes aim to produce this structure, which consists of the active piezoceramic pillars on a base, or ‘stock’. The bristle block is then transformed into a piezocomposite by infiltrating it with epoxy and then removing the stock by lapping. The piezocomposite can then be made active by applying a large electric field across the lapped faces in a process known as poling.

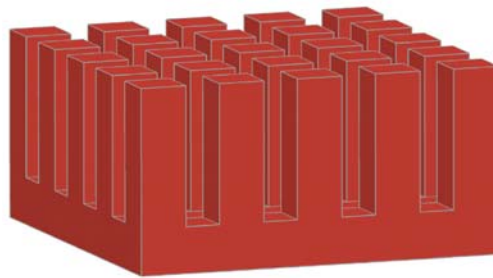


Figure 2.4 A bristle block that consists of piezoceramic pillars upstanding from a stock

In the lapping stage the two broad faces of the infiltrated bristle block are ground to expose the pillars and to ensure they are parallel. This removal of material means that the pillars must be made taller than required for the piezocomposite, and as a result the required aspect ratio increases. The minimum quantity of material that is removed during the lapping process is independent of the size of piezocomposite, and is dependent on the accuracy of the equipment and the operator’s skill. In the author’s experience a total of 100 μm is typically removed from the faces. This means that for higher frequency piezocomposites, not only

does the feature size decrease, but the aspect ratio also increases. Table 2.2 shows the dimensions of the bristle block before lapping has been completed, and demonstrates that an aspect ratio as high as 16 is required for a 30 MHz piezocomposite.

Table 2.2 The dimensions and aspect ratios of a 50% volume fraction bristle block *before* lapping. The calculations assume a velocity of 3000 ms^{-1} and square packed circular pillars

Frequency	Thickness (μm)	Pillar Diameter (μm)	Kerf (μm)	Pillar Aspect Ratio	Kerf Aspect Ratio
5 MHz	400	120	50	3.3	8
10 MHz	250	70	29	3.6	9
> 30 MHz	< 150	< 23	< 9.5	>6.5	>16

2.3.1 Dice and Fill

The dice and fill technique is the industry standard for piezocomposite fabrication for transducers operating at frequencies $<20 \text{ MHz}$, and is shown schematically in Figure 2.5. A sintered block of piezoceramic material has parallel grooves cut into it using a dicing saw. The block is then rotated by 90° and a further set of parallel grooves are cut into it. At this stage a bristle block has been produced and it can then be backfilled with epoxy resin and lapped ready for electroding [14, 15].

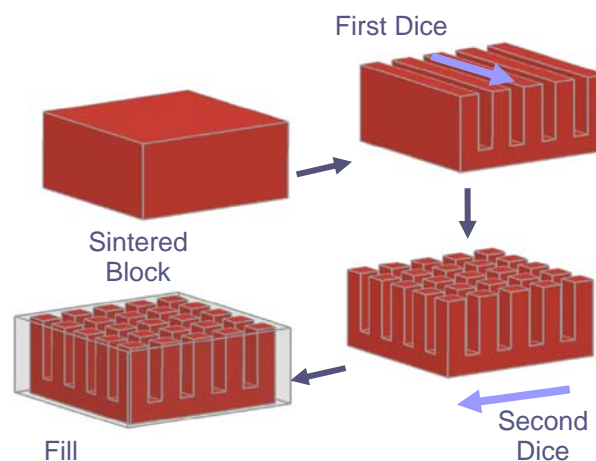


Figure 2.5 The industry standard, dice and fill, whereby a sintered ceramic block is sliced, rotated 90° and sliced again before backfilling with epoxy to make the piezocomposite [adapted from 14].

Dice and fill can routinely produce pillars that are 100 μm wide, but below this it becomes significantly challenging. The minimum pillar size is a function of the kerf and the ability of the ceramic to survive the dicing process [24, 17]. This is because conventionally processed ceramic contains defects of the order of 50 μm [15, 16], such that taking slices through the block often results in broken pillars, or defects that occupy the majority of the pillar.

The bristle blocks made by dice and fill are also limited to square sided pillars and certain array patterns [24]. The kerf is limited to the width of the saw blade ($\sim 15\mu\text{m}$) [14, 15] and at such small kerfs many grooves are required, which makes the process time consuming. As the pillar size and the kerf decrease, the achievable pillar aspect ratio tends towards one [14]

2.3.2 Ceramic Injection Moulding

A commercial alternative to dice and fill is ceramic injection moulding. The bristle blocks are produced by mixing the piezoceramic with a thermoplastic binder and are injection moulded under heat and pressure. Once removed from the mould, the green structure is then heated to remove the binder and is sintered [14]. The mould is reusable; however the lengthy and expensive production of the mould restricts the flexibility of the process [14]. The process can produce different shaped, sized and spaced pillars, however, at pitches $< 50 \mu\text{m}$ the transducer is easily destroyed during demoulding [14].

With smooth sided walls and a significant taper on each pillar, 40 μm diameter pillars have been demoulded [21]. However, the pillar arrays have a low volume fraction of ceramic in comparison to what can be produced by dice and fill [21, 22]. Producing finer scale arrays with high aspect ratios is difficult and further work has focused on higher volume fractions

rather than reducing the pillar width [22]. A bristle block with a volume fraction as high as 80% has been produced, however, the pitch was 150 μm [22] and this is much larger than what is required for the purpose of this work.

2.3.3 Viscous Polymer Embossing as a Lost Mould Technique

To overcome the difficulties of demoulding fine-scale ceramic structures the mould can be dissolved or pyrolised. The lost mould technique is the most suitable laboratory based processes for fabricating bristle blocks and is capable of producing pillars as small as 20 μm [17]. Figure 2.6 illustrates this process, whereby a mould with the negative of the desired bristle block structure is filled by a piezoceramic / binder based system, such as a slurry, paste or dough [14-20, 23, 24]. Once the system has dried, the mould can be removed. This is achieved by either thermal or chemical processes and can be carried out either before or after sintering [14, 15]. The lost mould process can produce pillars of any size, shape or spacing. However, the geometry and size of the bristle blocks is dependent on the mould, and a new mould is required each time a bristle block is made [14].

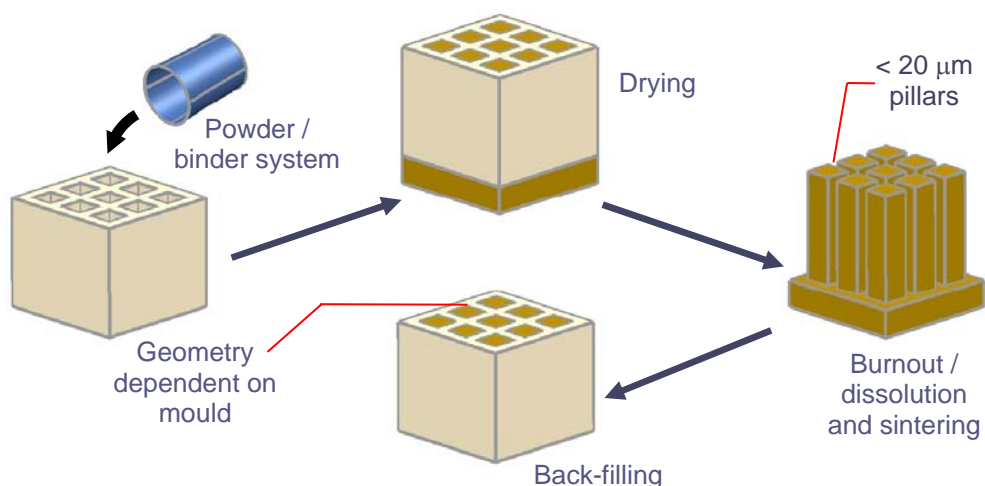


Figure 2.6 The stages of the lost mould process for the manufacture of piezocomposites: filling, drying, demoulding and backfilling with epoxy [adapted from 14]

Removal of the mould can be achieved by burn out [14-20, 23, 24]. However, when the pillars are as small as 20 μm , they can be distorted by the polymer flow [20, 23]. To avoid damage to the pillars a plasma etch process can be used to remove the mould [20, 23]. The stage in the process where the plasma etch is carried out is dependent on the mould material. When an acrylic mould is used it is necessary to etch the mould before sintering [23], but if a silicon mould is used the structure can be sintered within the mould and etched afterwards [20]. The silicon process produced very fine structures and was highly successful in replicating the mould. However, a reaction was detected at the pillar / mould interface, and both deep reactive ion etching and plasma etching were required for each transducer [20], and made the process expensive. In the case of acrylic moulds, only the plasma etch process was required because the moulds were manufactured via injection moulding; however, the pillars that were produced were wider and had a lower aspect ratio [23].

An alternative method to prevent the distortion and destruction of the pillars during demoulding is to increase the green strength of the dried ceramic. Viscous polymer processed (VPP) material shows a high green strength [15, 18, 19, 25-28] and can be formed by conventional plastic forming techniques such as extrusion, calendaring and embossing [18, 26-28]. Viscous polymer processed material is produced in the form of a ceramic dough, using a twin roll mill. The dough consists of ceramic powder, polymer binder, solvents, lubricants and a plasticizer to achieve the require rheology [26, 28]. VPP material can be made using a selection of binder systems, which allows a greater choice in mould materials and provides the potential to dissolve the mould without dissolving the green ceramic [15, 26, 27]. Finally, the high solids loading, and good homogeneity leads to uniform

shrinkage and therefore the ability for the process to be used for net shape processing [15, 19, 26-28].

The high green strength is derived from the high shear mixing achieved by the twin roll mill. In this stage of the process the roughly mixed components are placed between two counter rotating rollers. These rollers rotate at different speeds and generate a high shear stress which causes good agglomerate breakdown of the ceramic powder [26, 27]. The good agglomerate breakdown leads to a reduction in defects, which results in an improvement in the properties of the ceramic [18, 19, 25, 28]. Thus initially work focused on producing high strength ceramics [18, 29, 30], but more recently has led to the use of them for electroceramic applications and net-shape processing [15, 18, 19, 26-28].

The plastic forming, improved properties, net-shape processing and flexibility in mould materials has lead to previous researches producing 1-3 piezocomposites by embossing VPP material into polymer moulds. This process is called viscous polymer (VP) embossing but the method of mould removal can vary, from either a burn-out method [31] or a dissolution technique [15].

When piezocomposites have been produced by these different lost mould techniques the results vary. The pillars in the piezocomposites produced by the burn-out method had a much lower aspect ratio compared to the dissolution process, but did achieve a greater volume fraction [15, 31]. However, the lower volume fraction of the piezocomposite could easily have been caused by the mould not being specifically designed for transducer applications, rather than it being a function of the mould dissolution process itself. The burn-out process

produced relatively large pillar widths of 135 μm , whilst the dissolution process produced much smaller structures with heights of 50 μm and aspect ratios of greater than 2 [15, 31]. The authors of the dissolution process did comment that for the work to be advanced further, specialist moulds were required that could take advantage of standard composite design techniques [31].

2.3.4 Piezocomposite Fabrication Summary

The industry standard dice and fill struggles to make ceramic pillars smaller than 100 μm due to the size of the defects found in the sintered block. The commercial alternative to dice and fill is injection moulding, but this has poor flexibility and is limited to low volume fractions and larger scales than dice and fill. A promising technique called viscous polymer embossing has emerged and is based on the lost mould process. Small pillars of around $\sim 25 \mu\text{m}$ have been produced by this method but the aspect ratio and the volume fraction is low. It was commented by the researchers that the process was limited by a poor availability of suitably designed moulds.

2.4 Chapter References

- [1] G. R Lockwood et al “Beyond 30 MHz: Applications of High Frequency Ultrasound Imaging” *IEEE Engineering in Medicine and Biology* 15 (1996) 60-71
- [2] K. K. Shung and M Zipparo “Ultrasonic Transducers and Arrays” *IEEE Engineering in Medicine and Biology* (1996) 20-30
- [3] J. F. Tressler et al “Functional Composites for Sensors, Actuators and Transducers” *Composites: Part A* 30 (1999) 477-483
- [4] W. A. Smith “The Application of 1-3 Piezocomposites in Acoustic Transducers” *IEEE 7th International Symposium on Applications of Ferroelectrics* (1990) 145-152
- [5] W. A. Smith “Modelling 1-3 Composite Piezoelectrics: Thickness Mode Oscillations” *IEEE Transactions on Ultrasonics, Ferroelectrics and frequency Control* 38 (1) (1991) 40-47
- [6] T. R. Gururaja “Piezoelectrics for Medical Ultrasonic Imaging” *American Ceramic Society Bulletin* 73 (5) (1994) 50-55
- [7] J. W. Hunt et al “Ultrasound Transducers for Pulse-Echo Medical Imaging” *IEEE Transactions on Biomedical Engineering* BME-30 (8) (1983) 453-480
- [8] Opamp Electronics “AC Theory Tutorial” (2003)
http://www.opamp-electronics.com/tutorials/ac_theory.htm
- [9] T. A. Ritter et al “A 30 MHz Piezo-Composite Ultrasound Array for Medical Imaging Applications” *IEEE transactions in Ultrasonics, Ferroelectrics and Frequency Control* 49 (2) (2002) 217-230
- [10] W. A. Smith “The Role of Piezocomposites in Ultrasonic Transducers” *Ultrasonics Symposium* (1989) 755-766
- [11] Krautkramer J, Krautkramer H. “Ultrasonic Testing of Materials 4th Edition” *Springer-verlag, Berlin.* (1990)
- [12] V. F. Janas, A. Safari “Overview of Fine-Scale Piezoelectric Ceramic/Polymer Composite Processing” *Journal of the American Ceramic Society* 78 (11) (1995) 2945-2955
- [13] R. J. Meyer Jr. S. Yoshikawa, T. R. ShROUT “Processing and Properties of 15-70 MHz 1-3 Fiber/Polymer Composites” *Materials Research Innovations* 3 (2000) 324-331
- [14] A. safari, V. F Janas, A. Bandyopadhyay “Development of Fine-Scale Piezoelectric Composites for Transducers” *Ceramics Processing* 43 (11A) (1997) 2849-2856
- [15] A. Abrar et al “1-3 Connectivity Piezoelectric Ceramic-Polymer Composite Transducers made with Viscous Polymer Processing for High Frequency Ultrasound” *Ultrasonics* 42 (2004) 479-484

- [16] J. M Cannata et al “Design of efficient, Broadband Single-Element (20-80 MHz) Ultrasonic Transducers for Medical Imaging Applications” *IEEE Transactions on Ultrasonics, Ferroelectrics and Frequency Control* 50 (11) (2003) 1548-1557
- [17] K. Lubitz, A. Wolff, G. Preu “Microstructuring Technology” *Ultrasonics Symposium 1* (1993) 515-524
- [18] P.A. Smith et al “Ferrite helical devices” *IET microwave, antennas and propagation* 1 (4) (2007) 839-842
- [19] S Cochran et al “Net-shape ceramic processing as a route to ultrafine scale 1-3 connectivity piezoelectric ceramic-polymer composite transducers” *IEEE International Ultrasonics, Ferroelectrics, and Frequency Control Joint 50th Anniversary Conference* (2004) 1682-1685
- [20] S. Wang et al “Lost Silicon Mold Process for PZT Microstructures” *Advanced Materials* 11 (10) (1999) 873-876
- [21] L Bowen et al “Injection Molded Fine-Scale Piezoelectric Composite Transducers” *IEEE Ultrasonics Symposium 1* (1993) 499-503
- [22] B. G. Pazol et al “Ultrafine Scale Piezoelectric Composite Materials for High Frequency Ultrasonic Imaging Arrays” *IEEE Ultrasonics Symposium 2* (1995) 1263-1268
- [23] Y. Hirata “Effects of Aspect Ratio of Lead Zirconate Titanate on 1-3 Piezoelectric Composite Properties” *Japanese Journal of Applied Physics* 36 (1997) 6062-6064
- [24] Y. Hirata “Piezocomposite of Fine PZT Rods Realized with Synchrotron Radiation Lithography” *IEEE Ultrasonics Symposium 2* (1997) 877-881
- [25] B. Su et al “Embossing of 3D ceramic microstructures” *Microsystems Technologies* 8 (2002) 359-362
- [26] N. J. Porch et al “Net shape processing of piezoelectric ceramics and novel devices” *Processing of Electroceramics Conference, Aug-Sept 3, 2003, Bled, Slovenia* (2003) 293-312
- [27] B. Su, D. H. Pearce and T. W. Button “Routes to net shape electroceramic devices and thick films” *Journal of the European Ceramic Society* 21 (2001) 2005-2009
- [28] B. Su and T. W. Button “A comparative study of viscous polymer processed ceramics based on aqueous and non-aqueous binder systems” *Journal of Materials Processing Technology* 209 (2009) 153-157
- [29] N. McN. Alford, J. D. Birchall and K. Kendall “High-strength ceramics through colloidal control to remove defects” *Nature* 330 (1987) 51-53

[30] J. H. Song and J.R. G. Evans “The Assessment of Dispersion of Fine Ceramic Powders for Injection Moulding and related Processes” *Journal of the European Ceramic Society* 12 (1993) 467-478

[31] J-S. Park et al “Acoustic and Electromechanical Properties of 1-3 PZT Composites for Ultrasonic Transducer Arrays Fabricated by Sacrificial Micro PMMA Mold” *Sensors and Actuators A* 108 (2003) 206-211

Chapter 3

Micro Replication and Fabrication

3 Micro Replication and Fabrication

3.1 Micro Replication Processes for Polymer Moulds

3.1.1 Process Requirements

The poor availability of specifically designed moulds is a major factor that has limited the development of VP embossing as a piezocomposite fabrication route [1]. Not only is the aspect ratio and feature size of the moulds a challenge to fabricate, but the moulds must also be made in a cost effective way because a new mould is required for each piezocomposite. Therefore there is a need to identify a micro replication process that can cost effectively produce moulds in a material that can be dissolved without damaging the VP embossed structure. By carrying out a review of the most suitable micro replication techniques it will be possible to identify a suitable route for producing piezocomposites cost effectively.

To define the requirements of the micro replication process it is important to first define the mould that must be made. The mould must have the negative structure of the bristle block, and must therefore take the form of an array of cavities or a 'mesh' structure. This mould should be replicated from a master tool, which has the same, positive, pillar array structure, as the 1-3 piezocomposite. The VPP material will shrink during drying and sintering, such that the mould and master tool will be required to be larger. Typically this shrinkage occurs linearly by 20%, such that the required dimensions can be calculated from Table 2.2 and are shown in Table 3.1. Table 3.1 indicates that the feature sizes of the mould become larger, whilst the aspect ratios remain the same.

Table 3.1 The dimensions of a mould that is required to be produced by micro replication for fabricating 1-3 Piezocomposites

Frequency	Depth (µm)	Cavity Width (µm)	Wall Thickness (µm)	Cavity Aspect Ratio	Wall Aspect Ratio
5 MHz	480	144	60	3.3	8
10 MHz	300	84	35	3.6	9
30 MHz	125	28	11	6.5	16

As the dimensions of reported structures vary widely, and to help review the capability of the micro replication processes to achieve the dimensions required here, it is helpful to define some size ranges. Thus, the categories for the feature sizes have been grouped into large, intermediate, small and very small, and the aspect ratio values have been grouped into low, intermediate, high and very high. The actual values for the ranges are defined in Table 3.2 (a) and (b), and they have been cross referenced with Table 3.1 to give Table 3.3.

Table 3.2 The size-range of the terms used to describe feature size (a) and the aspect ratios (b) of structures in this work.

Feature Size (µm)	Description
< 15	Very small
15 – 34.9	Small
35 – 64.9	Intermediate
> 64.9	Large

(a)

Aspect Ratio	Description
<3	Low
3 – 5.9	Intermediate
6 – 9.9	High
> 9.9	Very High

(b)

Figure 3.1 The descriptions used of the required feature size and aspect ratio for different frequency piezocomposites

Frequency	Feature Size Description	Aspect Ratio Description
5 MHz	Intermediate	High
10 MHz	Small	High
30 MHz	Very Small	Very High

It can be seen from Table 3.3 that with increasing piezocomposite frequency the challenge of replicating the structure increases. Whilst studying Table 3.3 it should be remembered that whilst a structure with a small feature size, or a high aspect ratio, is challenging, it is even more challenging to produce a structure that combines the two.

Not only must the micro replication process be capable of achieving these dimensions, it must also be able to produce the structure in a material that has sufficient mechanical properties to ensure that it can withstand both demoulding from the master tool and the forces exerted during VP embossing, without fracture or yielding. This material must also be dissolvable in a solvent that does not affect the VP embossed structure and must be cost effective enough that it can be lost during mould dissolution.

It will be seen throughout the review of micro replication processes that polymethyl methacrylate (PMMA) appears frequently. This material is relatively cost effective, has good mechanical properties (tensile strength: ~50 to 70 MPa; Young's modulus: ~2.5GPa) [2], and is dissolvable in organic solvents such as ...(*Censored for commercial reasons*).... VPP material can be made using a binder system based on...(*Censored for commercial reasons*)..., which does not dissolve in organic solvents. It is therefore possible to use ...(*Censored for commercial reasons*)...to dissolve the PMMA mould without damaging the VPP material.

When selecting a micro replication process both the residual stress and the shrinkage should be considered. It is important to minimise both of these, not only because this will lead to more replicas being demoulded successfully, but also because minimising the shrinkage will

ensure accurate replication of the master tool, and minimising the residual stress will improve the survival of the mould during VP embossing.

The cost of the process should also be considered, in terms of the quantity required to be cost effective and the initial capital cost. It is important that the process is flexible because a single design of a 1-3 piezocomposite is specific to an application, and is therefore not required in quantities of hundreds to thousands, but in the tens to hundreds. A different master will be required for different designs, such that the process must be flexible, with short set-up times and low equipment costs. The small quantity of replicas required means that short cycle times are less important.

3.1.2 Micro Replication Process Outlines

Polymer moulds for fabricating piezocomposites should be replicated from a master tool with a suitable structure. The three common ways of producing a polymer replica are: micro injection moulding (μ IM); reaction injection moulding (RIM); and hot embossing. The following section outlines the processes so that an understanding of the characteristics of each process can be made and the most suitable micro replication process can be selected.

Micro injection moulding is adapted from injection moulding on the macroscopic scale, where a polymer melt is injected into a cold mould under heat and pressure. The process needs adapting because the shot size is much smaller and the polymer melt can solidify early, causing defects and incomplete mould fill. The machine must be adapted so that it is capable of controlling the pressure when only a small quantity of polymer is injected into the mould [3]. The master tool is also required to be warmed prior to injection. This is achieved by a

‘varotherm’ that reduces the viscosity of the melt and prevents early solidification [4, 5] by heating the master tool to between the glass transition temperature and the melt temperature of the polymer [3, 6 - 8]. The injection temperature is dependent upon the polymer used, the required flow characteristics, and the required mechanical properties of the replica [4, 5]. The injection temperature for PMMA is around 170°C [9] and the mould temperature can vary from 120 to 150°C [3].

Reaction injection moulding is similar to micro injection moulding, except a two component resin is injected at low pressure (< 1 MPa) rather than a polymer melt. The two resins are stored separately and are only mixed just before injection. This means that polymerisation does not occur too early, and the low viscosity of the resin means that it can fill the mould cavity easily. The reaction typically occurs at room temperature and is commonly photo- or thermo-initiated [9, 10 - 12].

Unlike micro injection moulding and reaction injection moulding, hot embossing is an open die process that operates at lower temperatures and pressures. A schematic diagram of a hot embossing machine is shown in Figure 3.2, and consists of a force frame with two heated and water cooled platens attached to it [13]. One platen has the master tool attached to it and a polymer substrate is attached to the other. The machine also has data acquisition equipment mounted onto the platens and the force frame, to gather information on temperature, displacement and load [14].

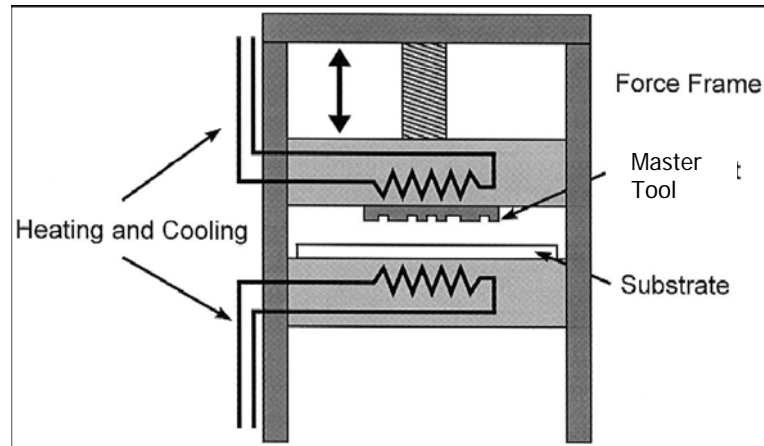


Figure 3.2 Schematic diagram of the hot embossing equipment, which shows the heated and cooled platens, the force frame and the polymer substrate [13]

The platens are heated to just above the glass transition temperature (T_g) of the polymer before being pressed together. For PMMA the T_g is $\sim 110^\circ\text{C}$ so that the platens typically operate in a range between 135°C and 150°C [13, 14]. The platens are pressed together and held at a constant load, until the master tool is fully embossed into the polymer substrate. Finally, the two are cooled to below the T_g of the polymer before retracting the platens in a stage known as de-embossing [9, 13-15].

3.1.3 Characteristics of Micro Replication Processes

Each micro replication process uses a different approach to achieve the micron scale structure, and leads to very different characteristics of each process. In both micro injection moulding and reaction injection moulding the polymer is injected at a low viscosity, either as two resins that will polymerise later, or as a melt that is exposed to higher mould temperatures. By contrast, the hot embossing process uses a polymer in a much more viscous state that slowly surrounds the features of the tool. The advantages and disadvantages of all three processes are summarised in Table 3.3, whilst a description of the main characteristics of each process is discussed below.

The rapid injection and solidification of the polymer in micro injection moulding leads to a high residual stress in the replica [9, 5]. By comparison, hot embossing has a slow flow rate which allows the polymer to relax and relieve the internal stresses [9, 5]. Furthermore the shrinkage in hot embossing is low, because the temperature difference between the forming temperature and the de-embossing temperature is smaller than in μ IM [9, 5]. The residual stress is not as high in RIM as it is in μ IM, but the shrinkage can be as large as 20% because the polymerisation occurs in the mould [4, 9].

Table 3.3 The advantages and disadvantages of reaction injection moulding, micro injection moulding and hot embossing compiled from [1] and other sources.

Advantages		
Micro Injection Moulding	Reaction Injection Moulding	Hot Embossing
Excellent dimensional Control	Generally an intermediate between μ IM and hot embossing.	Short set-up time [4, 5, 13, 16]
		Simple, relatively inexpensive equipment
		High molecular weight polymers with improved mechanical properties
		Internal and external mould release available

Disadvantages		
Micro Injection Moulding	Reaction Injection Moulding	Hot Embossing
High productivity required	Medium to high cost	Longer cycle times (~30 min)
Expensive equipment [13]	High shrinkage (20%) [4]	
High residual stress on replica [5]	Internal mould release only [5]	
High stress on master tool [5]		
Only low molecular weight polymers		

The nature of each process results in different cycle and set-up times. Hot embossing has a relatively long cycle time of around ~ 30 min because the platens are required to be heated up

and cooled down in each cycle [4, 5, 13, 16]. However, in μ IM the polymer is injected under pressure and the mould is not required to be heated and cooled as much. This leads to a cycle time that is of the order of tens of seconds [9, 15]. For UV-initiated RIM the process is dependent upon the time to cure the resin and there is no thermal cycling, such that the cycle time is around 10 minutes [13, 12]. Although μ IM and RIM have relatively short cycle times their set-up times are much longer than in hot embossing, [4, 5, 13, 26] and they have high equipment costs [9, 13]. This means that hot embossing is a much more versatile technique than both μ IM and RIM and is therefore much more suitable for the production of small to medium quantities (up to several thousand) than micro injection moulding [5, 13, 16, 17].

3.1.4 Achievable Feature Sizes, Aspect Ratios and Materials

A range of structures that have been replicated using micro injection moulding, reaction injection moulding, and hot embossing have been reviewed and are shown in Table 3.4, Table 3.5 and Table 3.6 respectively. These tables identify the dimensions, aspect ratio and material of each structure, along with additional comments made by the researchers. When a '~' symbol has been used in front of a dimension this indicates the dimension has been estimated from an image and has not been specifically mentioned in the literature. For ease of discussion the structures are numbered, and the structures highlighted in bold correspond to an image below the table. In Table 3.6 this nomenclature also contains a letter with the number which is used later in section 3.1.7. The process review tables are discussed in sections 3.1.4.1 to 3.1.4.3 and the achievable aspect ratios and feature sizes are related back to the size ranges shown in Table 3.2 (a) and (b). The tables also note the master tool fabrication process, which will be discussed later in section 3.2.

3.1.4.1 Micro Injection Moulding

The aspect ratio and feature size that is achievable by micro injection moulding can be identified by the example structures shown in Table 3.4 and Figure 3.3 to Figure 3.6. From this table it can be seen that micro injection moulding is therefore only capable of replicating a structure with low to medium aspect ratios. Structures with aspect ratios > 5 have not been seen in the literature, and in one paper the researchers have discussed the unsuccessful demoulding of a structure with an aspect ratio of 6 (#4) [7].

Feature sizes of $40\ \mu\text{m}$ have frequently been achieved, and examples are seen in structure #3 (Figure 3.4), #6 (Figure 3.6) and #7. Structure #1 has a smaller feature size, but these are ripples that are not part of a self supporting structure and it is unlikely that such small features will be achievable in a mould.

The structures that have been achieved by micro injection moulding have been replicated in a variety of materials. However, the researchers in [15] have commented that that a structure with a feature size of $40\ \mu\text{m}$ and an aspect ratio of 2.5 was not possible in PMMA.

Table 3.4 A summary table of structures that have been replicated by micro injection moulding. The structures highlighted in bold correspond to Figure 3.3 to Figure 3.6

No.	Description	Dimensions (μm)			Aspect Ratio	Material	Mould Tool	Comments	Ref
		Height	Width	Kerf					
#1	Multi fibre connector for optical fibres	287.5	110	140	2.61	PMMA	Micromilled / LIGA	The structures states have designed rippled features ~ 20 μm. aspect ratio ~ 14	[18]
#2	Leading structure for optical fibres	~265	~130	~130	~2	-	-	-	[19]
#3	Pillar structure	174	40	~143	4.35	316L / polyacetal based binder	DRIE etched silicon	Similar process to ceramic injection moulding of 1-3 piezocomposites, and is more difficult than polymer μIM	[8]
#4	Pillar test samples	350	100	230	3.5	Poly-oxymethylene, polypropylene	Micromilled	Micro fingers were also produced with aspect ratios up to 6 (feature sizes, 50 μm), however some fingers were damaged.	[7]
#5		400	150	180	2.6				
#6	Mesh Structure	100	40	40	2.5	Cyclo olefin polymer	LIGA	Flouropolymer release agent. Was not possible in PMMA or PC	[15]
#7		200	200	100	2				

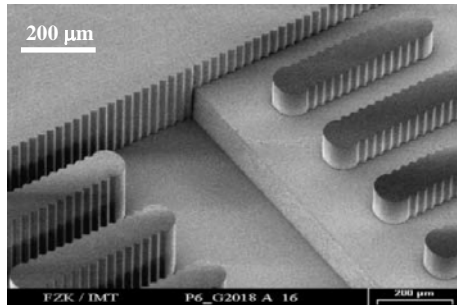


Figure 3.3 Multi fibre connector for optical fibres (#1) [18]

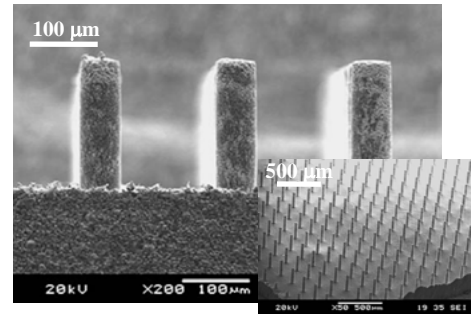


Figure 3.4 Metal micro injection moulded pillar structure (#3) [8]

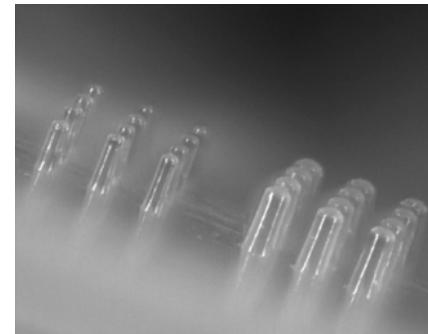


Figure 3.5 Injection moulding pillar test samples (#4) [7]

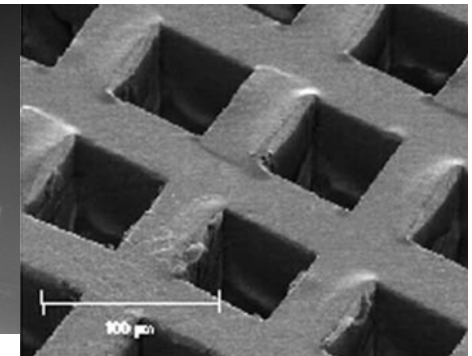


Figure 3.6 Mesh structure (#7) [15]

3.1.4.2 Reaction Injection Moulding

Table 3.5 shows a range of structures found in the literature made by reaction injection moulding. All of the structures are made from PMMA and are compatible with the mould dissolution process. The table demonstrates that reaction injection moulding is capable of replicating very small feature sized structures, and a range of aspect ratios from low to very high. The lowest feature size achieved is 6 μm (#5), and the highest aspect ratio is 10 (#5, #6). Not only are these very small feature sizes and very high aspect ratios, but they have been achieved in the same structure.

3.1.4.3 Hot Embossed Structures

Figure 3.11 to Figure 3.16 summarise the hot embossed structures found in the literature. The table demonstrates that hot embossing is capable of producing a broad range of feature sizes, with most of the structures being either small or very small. The process is also capable of producing a range of aspect ratios, from low to very high. Hot embossing can replicate structures in either PMMA or a similar material, such as polycarbonate (PC).

The smallest achieved feature size is 0.8 μm , from a structure that also had an aspect ratio of 5 (#1A). The highest aspect ratio was achieved by #2A and #4H, which had aspect ratios of 12 and 19 respectively. Furthermore, structure #4H has the second smallest feature size seen in the literature which was 8 μm . Not only does this demonstrate that hot embossing can produce structures with both very high aspect ratio and a very small feature sizes, but also that it is capable of producing structures with aspect ratios that are nearly twice as large as those achieved by reaction injection moulding.

Table 3.5 A summary table of the structures that have been replicated by reaction injection moulding. The structures highlighted in bold correspond to Figure 3.7 to Figure 3.10

No.	Description	Dimensions (μm)			Aspect Ratio	Material	Master Tool	Comments	Ref
		Height	Width	Kerf					
#1	IMF Test structure	~32	~8	~21	4	PMMA	KrF excimer Laser machined PI insert		[11]
#2	Free standing wall test structure	66	10	~250	6.6	PMMA	KrF excimer Laser machined PSU insert		[11]
#3	Varying height wall array	~60	~27	~70	~2.2	PMMA	KrF excimer Laser machined steel mask		[11]
#4	Array of walls	100	10	~33	10	PMMA	KrF excimer Laser machined PI insert		[10]
#5	Pillar array	61	8	6	10	PMMA	As above		[10]
#6	Varying height wall array	~72	~13	~22	~5.5	PMMA	As above		[10]

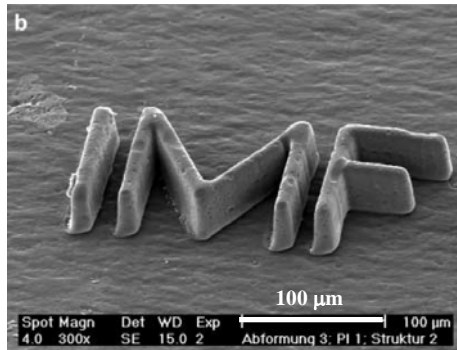


Figure 3.7 IMF test structure in PMMA (#1) [11]

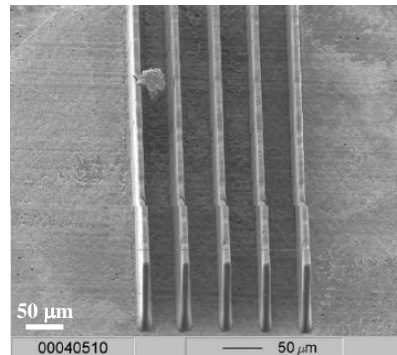


Figure 3.8 Array of walls (#4) [10]

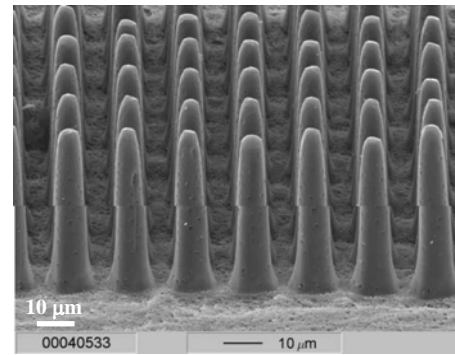


Figure 3.9 Array of pillars (#5) [10]

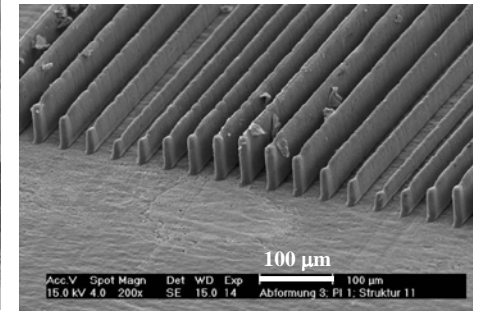


Figure 3.10 Array of walls with varying heights (#6) [10]

Table 3.6 Summary of the hot embossed structures found in the literature. The rows in bold correspond to Figure 3.11 to Figure 3.16

No	Description	Dimensions (μm)			Aspect Ratio	Material	Master Tool	Embossing System	Comments	Ref
		Height	Width	Kerf						
#1A	Array of Microfluidic Grooves	5	0.8	4.2	> 5	PMMA	Silicon, Advanced Silicon Etched (ASE)	Unknown	Demoulded by Hand. Some distortion of the in the size range of 50 – 100nm	[20]
#2A	Electrostatic Comb Drive	60	10	10	12	PMMA	Silicon, Inductive Coupled Plasma Dry Etching	HEX01¹	Minimum Feature Size 5 μm	[22]
#3A	Cavities for Electroplating of Seismic Masses for an Acceleration Sensor	150	100	8 and 13	19 and 12	PMMA	Nickel, LIGA	HEX01	Additional Plasticizers and release agents were required to obtain this aspect ratio	[13]
#4H	Line of Crosses	155	8	-	> 19	PMMA	Nickel, LIGA	HEX01		[22]
#5H	Groove in a Circular Test Structure	140	20	-	7	PC	Nickel, LIGA	HEX01		[13]
#6H	Single Cross	140	20	-	7	PC	Nickel, LIGA	HEX01		[13]
#7H	Cross in the Centre of a Gear	150	27	-	5	PMMA	Nickel, LIGA	HEX01		[23]
#8M	Low Aspect Ratio Pillar Array	150	Base > 100 Top < 100	15 – 40	3 - 10	Unknown	Unknown	HEX01		[24]
#9A	Microfluidic Channel Array	90	300	200	2.2	PMMA	PDMS master tool replicated from an SU-8 mould	MTP-10 ²	Depth from 5 μm to 250 μm with width of over 40 μm and aspect ratios of 2. However, the images are not shown	[25]

¹ From Jeniptik Microtechnik, Jena, Germany

² Tetrahedron Associates Inc., San Diego CA

No	Description	Dimensions (μm)			Aspect Ratio	Materials	Master Tool	Embossing System	Comments	Ref
		Height	Width	Kerf						
#10A	Microfluidic Channel	20	50	-	0.4	PMMA	Epoxy Mould tool replicated from a PDMS mould	HEX01	Demoulded by Hand. No Release agents were required	[26]
#11M	Square Hole Array	Unknown	90	25	~ 5	PS	Ni-Co electrodeposited into SU-8 Mould	See Foot Note¹	Master tool dimensions: 85x85x120 with kerf 24 μm . Aspect ratio 5 Master tool was coated in PDMS	[27]
#12M	Micro Lens Array	Unknown	80	40	~ 3	PC	Nickel, LIGA	Procedure only	The dimensions were taken from the mould (tool). The lenses were not embossed fully but the mould tool was 200 μm thick	[28]
#13M	Square Hole Array	Unknown	200	83	> 2	PMMA	Nickel, LIGA	See Foot Note ²	The Master tool was coated in a fluorocarbon to aid demoulding	[29]
#14M	Square Hole Array	200 100	200 40	100 40	2 2.5	PMMA and PC	Nickel, LIGA	As Above	The Master tool was coated in a fluorocarbon to aid demoulding. Injection moulding was also attempted but was only successful in Cycloolefin Polymer not PMMA or PC	[15]
#15M	VP Embossed Hexagonal Pillars	400 75	75 40	~ 55 30	7.2 2.5	PMMA	Nickel, LIGA	HEX01	The structures are green after VP embossing into hot embossed moulds	[1]
#16M	Micro Lens Array	160	69	14.5	11	PC	DRIE	Unknown	The demoulding method is not recorded nor is the use of a vacuum. The array may also only be linear.	[31]

¹ The embossing system used a hotplate in an evacuated bell jar to heat the mould tool. Whilst the tool was still cold the polystyrene and a steel weight was placed on top of the tool and then the hotplate switched on.

² The embossing system was developed at the National Institute of Advanced Industrial Science and Technology

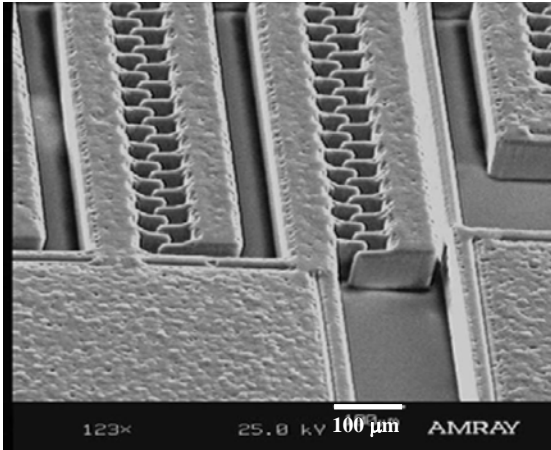


Figure 3.11 Electrostatic comb drive (#2) [21]

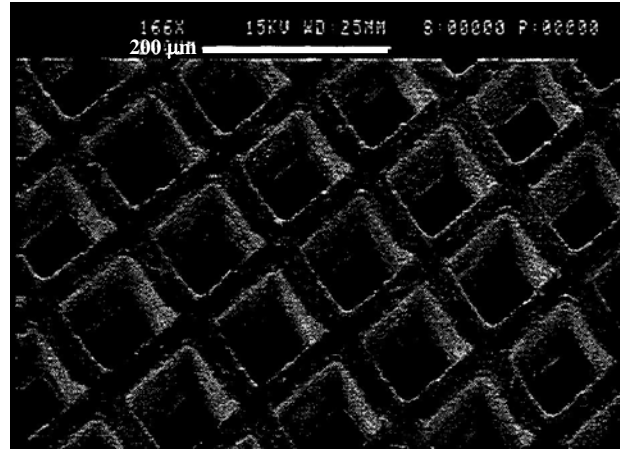


Figure 3.14 Square hole array (#11) [20]

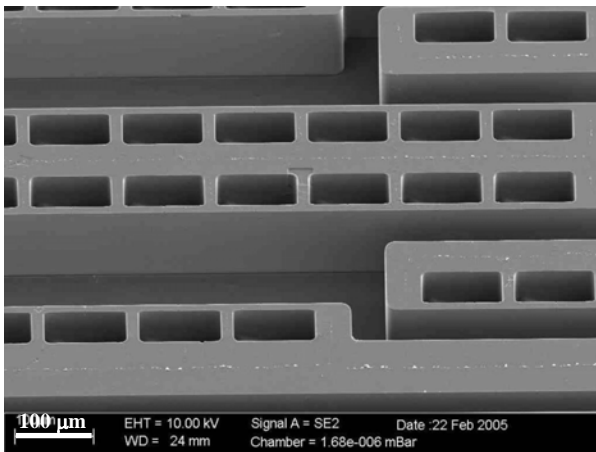


Figure 3.12 Cavities for electroplating of seismic masses for an acceleration sensor (#3) [13]

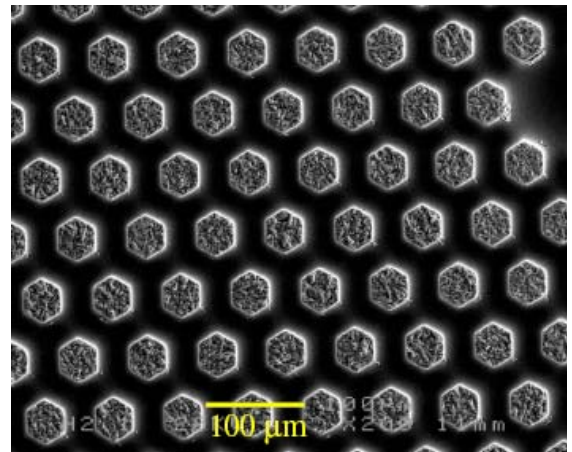


Figure 3.15 Green pillars produced by VP embossing into hot embossed moulds (#15) [1]

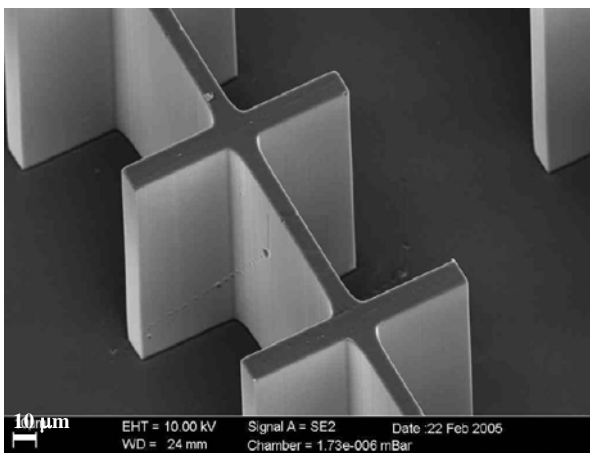


Figure 3.13 Line of crosses as a test structure (#4) [26]

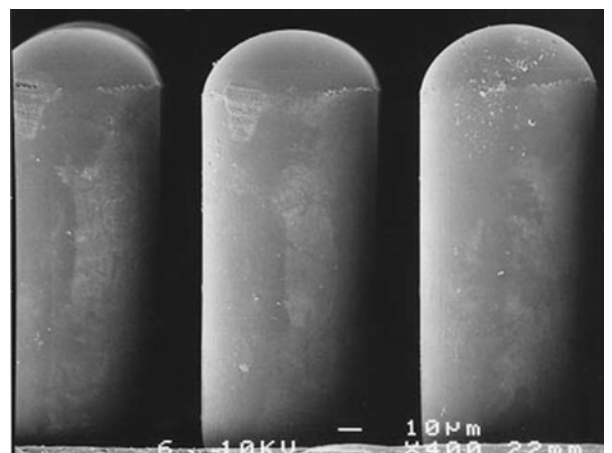


Figure 3.16 An array of micro lenses (#16) [11]

3.1.5 Geometry of the Replicated Structures

All three micro replication processes are capable of producing structures in a material that is compatible with the mould dissolution process of VP embossing, and in particular PMMA frequently occurs in both RIM and hot embossed structures. It has been demonstrated that micro injection moulding is only capable of producing large feature size, low aspect ratio structures, whilst reaction injection moulding and hot embossing are able to produce very small and very high aspect ratio structures, which are more desirable for 1-3 piezocomposite moulds. However, a micro replication process may be capable of producing certain aspect ratios and feature sizes in one structure, but it may not be capable of doing so in another. A good example of this is the ripples on the structure shown in Figure 3.3. Whilst the ripples are around 20 μm , they form part of a much larger feature that is 110 μm wide that provides structural support for these features. Furthermore, the very high aspect ratio and very small feature size seen in #4H and Figure 3.13 have been produced in a line of crosses, which is an inherently stable structure. By comparison, mesh structures, like the ones required for 1-3 piezocomposite moulds, show lower aspect ratios and higher feature sizes. It is therefore important to consider structures that are the most similar to what is required for a piezocomposite mould, such as mesh and pillar array structures.

Injection moulding can produce both mesh and pillar array structures. However, the aspect ratio is limited to below 5 and the feature size is limited to 40 μm . This feature size would be suitable for a 5 MHz piezocomposite but the aspect ratio is still some way from the required 8 in Table 3.1. Furthermore, the process is not able to produce replicas successfully in PMMA without further reducing the aspect ratio or increasing the feature size.

Reaction injection moulding has been able to produce pillar structures and arrays of walls, but not a mesh structure. However, the pillar array that has been produced has a minimum feature size of $6\ \mu\text{m}$ and an aspect ratio of 10 (#5), and therefore correlates to a 10 MHz piezocomposite. These feature sizes are of the order required for a 30 MHz piezocomposite but the aspect ratio would need to be increased by 1.6.

Hot embossing is also able to produce pillar structures. The pillars shown in Figure 3.16 are $69\ \mu\text{m}$ wide and $160\ \mu\text{m}$ high. The smallest feature size is the kerf that measures $14.5\ \mu\text{m}$ wide and hence gives an aspect ratio of 11. Comparing these features to Table 3.1 indicates that it would match a 30 MHz piezocomposite.

Hot embossing is also capable of replicating mesh structures with aspect ratios as high as 7.2 and feature sizes of $55\ \mu\text{m}$ (#15M). This represents a tripling of the aspect ratio compared to the mesh structure made by micro injection moulding (#6). Whilst the mould cannot be seen in Figure 3.15, the VP embossed pillars are shown and would nearly correspond to a 5 MHz piezocomposite.

The most appropriate mesh and pillar structure has been produced by hot embossing. Reaction injection moulding is able to produce a pillar structure that is similar to that made by injection moulding. The few mesh structures that have been seen in the literature serve to highlight the comment made in [1] that the lost mould process is limited by the availability of suitable moulds. For example, Figure 3.12 shows a structure replicated by hot embossing that was designed as a mould for seismic masses. This structure has mould walls that measure 8 and $13\ \mu\text{m}$ and have aspect ratios of 19 and 12 respectively. This structure

demonstrates that it is possible to produce feature sizes and aspect ratios that are able to make a 30 MHz piezocomposite but the structure is not suitable because it does not form an array geometry.

3.1.6 Selection of the Replication Process

Based on the geometry, aspect ratio and feature size, micro injection moulding is not suitable for the replication of moulds for piezocomposites. Reaction injection moulding has demonstrated pillar structures that indicate it is possible, whilst hot embossing has produced pillar structures that are as good as in RIM, and mesh structures that could be used to produce a 5 MHz piezocomposite. Hot embossing also appears more promising because it is able to produce structures that have an aspect ratio nearly twice as large as those produced by reaction injection moulding. It is therefore useful to consider some of the other characteristics of the micro replication processes discussed in section 3.1.3.

One particular consideration indicated in Table 3.3 was the initial expense and levels of through-put required to be cost effective. Micro injection moulding requires the highest productivity, RIM second and hot embossing requires the least. Similarly, the processes can be ranked in the same order in terms of the shortest cycle time, and the longest set up time. Hot embossing provides a flexible process that does not require a high productivity to break even. Most importantly, the number of moulds required for piezocomposites is low and the short set up time allows for the master tool to be change frequently.

Reaction injection moulding and μ IM require similar equipment [12, 13]. The injection pressures are not as large but RIM does require the replica to be exposed to UV light [9, 12,

13]. RIM requires the mould cavity to be evacuated [9, 12, 13] to prevent the formation of bubbles within the structure [9]. However, in the case of hot embossing, a vacuum is only need if air is likely to become trapped in the cavities. The open die nature of the process means that when an array of pillars is pressed into the polymer substrate the air will flow out laterally, so that no vacuum system is required. For these reasons hot embossing has been selected as a micro replication route for 1-3 piezocomposite moulds.

3.1.7 Improving the Aspect Ratio & Feature Size of Hot Embossed Structures

At present it has not been demonstrated that any micro replication process is capable of producing mesh structures that have the correct aspect ratio and feature size for a 30 MHz piezocomposite. One way to improve the feature size and aspect ratio is to add a taper onto the cavity walls of the mesh. However, the reason why this approach has not been used by other researchers can be found by considering why the structures have been replicated. The structures in Table 3.6 can be organised into three groups based on why they have been replicated. These groups are: structures designed for *specific applications*; structures used to demonstrate *high aspect ratios*; and structures designed to demonstrate *mesh*, or pillar, structures. These groups can be identified in Table 3.6 by either an A (application), H (high aspect ratio) or a M (mesh) after the structure number.

The structures that have been designed for specific applications could have the complete opposite design criteria to what is required for 1-3 piezocomposite moulds. Examples of these structures are #1A, #9A and #10A. However, in some cases, the structures show both a high aspect ratio and a small feature size, despite not being specifically designed for a 1-3 piezocomposite mould. Figure 3.11 and Figure 3.12 do have high aspect ratios and small

feature sizes, but in both cases the feature is attached to a much larger supporting structure. This supporting structure may be there only to help de-emboss the smaller feature or it may be required to help the replica perform its function. This argument suggests that the small features are difficult to de-emboss, but despite this the small features and high aspect ratios have been achieved without a taper to aid de-embossing. The most likely cause for this is that a taper could not be tolerated by the design of the structure.

The high aspect ratio demonstration structures produce some similar observations, and Figure 3.13 is a good example of this. The aspect ratio of this structure is nearly 20, with a feature size of 8 μm . However, the cross geometry is relatively stable and provides the same effect as the larger supporting structure in Figure 3.11 and Figure 3.12. This means that, as a whole, the structure has a relatively low aspect ratio and a much larger size. As before, the structure shown in Figure 3.13 has parallel walls such that no taper has been used to help de-embossing. This time the structure has no application other than to demonstrate the feasibility of moulding high aspect ratio structures. Therefore if the structure was to show a taper it would defeat the point of moulding it.

The mesh and pillar demonstration structures have a similar geometry to what is required for 1-3 piezocomposites. These structures were replicated with the intention of showing that this type of geometry can be produced, but they were not specifically designed for this application. Often they have the potential to produce a suitable volume fraction in a piezocomposite because they have the correct ratio of cavities to walls, but they do not have the required feature size or aspect ratio. As with the other two categories, these structures do

not show a taper. The structures have been designed to demonstrate that this type of structure can be made, and to add a taper would undermine this demonstration.

It is believed that mesh structures are capable of higher aspect ratio and smaller feature sizes than has been seen in the literature. This has been demonstrated when a mesh structure was used as a 1-3 piezocomposite mould and is shown in Figure 3.15. The mould had an aspect ratio as high as 8 and cavities as wide as 60 μm [1]. This particular master tool was not originally made for moulding 1-3 piezocomposites and showed a volume fraction at the lower end of the spectrum, parallel walls, and a rough surface on the top of the pillars. It is anticipated that, if a master tool is specifically made for hot embossing piezocomposite moulds, much higher aspect ratios and feature sizes can be produced.

The review has demonstrated that it is possible to produce piezocomposite moulds by hot embossing. A taper has not been added to many of the structures seen in this review because it would undermine the purpose of replicating them. However, a small taper can be tolerated by 1-3 piezocomposites in injection moulding [32] and as such provides a valid route to improve both the aspect ratio and the feature size. Furthermore, whilst hot embossing is able to produce moulds similar to 5 MHz piezocomposites, there is a need to increase this frequency. As the frequency increases the aspect ratio and the feature size become much more demanding, and therefore the need for a taper becomes much more important. There is a need to investigate what size of taper is required to improve the de-embossing of the structures, and what size of taper can be tolerated by the piezocomposite. Thus an investigation into the ease of demoulding different master tools is proposed, followed by the VP embossing into the moulds to identify the optimum taper for both roles.

3.1.8 1-3 Piezocomposites with Tapered Pillars

The ability of 1-3 piezocomposites to tolerate a taper is demonstrated by the taper exhibited on the pillars of a fine-scale ceramic injection moulded 1-3 piezocomposites [32]. Researchers in [33] investigated the effect of taper on a piezocomposite. To simplify the problem, the researches investigated a taper on piezoelectric walls rather than pillars. Thus, a sintered block was diced with slots in one direction rather than two. Two piezocomposites, both with walls 1530 μm deep and either 500 μm or 750 μm wide, with a taper angle of 5° , were fabricated.

Modelling was carried out on these two designs over a taper range of 0 to 10° . The researchers observed that the operating frequency was unaffected by the taper because this resonance is mainly dependent on the height of the wall. However, the taper did affect the higher frequency, lateral resonances. As the taper was increased the resonances began to split and shift. At a critical taper, these resonances began to interfere with the harmonics of the operating frequency, and limited the size of the taper that could be tolerated [33].

The modelling indicated that high aspect ratio walls were more affected by the taper than lower ones. This is because for tall, or narrow, walls the change in width is much greater for a specific taper angle. It was found that for the 500 μm wall, with an aspect ratio of 3, the largest taper that could be tolerated was 5° . By comparison, the 750 μm wall, with an aspect ratio of 2, showed much less pronounced shifting and splitting of the lateral resonances and was able to achieve larger tapers [33].

The exact size of the taper that can be tolerated by the piezocomposite is dependent on the array geometry [34, 35], pillar shape [11], volume fraction, pillar aspect ratio [33] and taper angle [33]. Therefore, 5° only provides a rough figure as to the size of taper that can be considered. Furthermore, it has been discussed elsewhere that a taper of 2° is beneficial in hot embossing [5, 13], and therefore offers the opportunity to increase the aspect ratio and reduce the feature size of the mould. However, this is an empirical observation, and the ease at which a master tool can be de-embossed is dependent on many factors, such that the de-embossing process is difficult to model [20, 21]

It is proposed that the best way to investigate the effect of the taper is to emboss using several master tools with different tapers ranging from 0° to 5° . The de-embossing force required to remove the tool can be recorded, and the moulds used to produce piezocomposites, so that data about the resonances of the piezocomposites can be obtained. However, the first stage before this is to identify a micro fabrication process that can produce the required dimensions, aspect ratios and taper.

3.2 Micro Fabrication Techniques for the Master Tool

A micro replication process for producing a master tool that can be replicated into many moulds need to be identified. The shrinkage that will occur during the hot embossing process depends on many factors, and is difficult to anticipate. For the sake of comparing the micro fabrication techniques it is assumed that the required dimensions and aspect ratios of the master tool are the same as the mould that was discussed in section 3.1.1.

For hot embossing it is favourable to use a metal master tool because it tends to be more durable than silicon or SU-8 tools. If the micro fabrication process is not capable of producing a metallic master tool it is possible to electroform a pillar array structure from the negative structure. Thus, the micro fabrication process has been considered with both an array of cavities and an array of pillars in mind.

In reviewing these processes consideration to the feature size, aspect ratio and achievable taper are important. In addition, the surface roughness should be considered, as this provides areas where the polymer can become mechanically locked into the master tool. Researchers have empirically found that a root mean square (RMS) roughness of 80 nm is required to successfully remove a structure with aspect ratios greater than 0.5 [14]. It is generally accepted that the RMS roughness can be converted to the arithmetical mean roughness (Ra) by multiplying the RMS by 1.11, such that acceptable roughness in terms of Ra should be < 90 nm. However, it is doubted that this is a strict rule, and therefore only provides a rough figure for comparison purposes.

3.2.1 UV Lithography

UV lithography is commonly used to fabricate integrated circuits. The example shown in Figure 3.17 shows the stages of lithography on a silicon wafer. The first stage is to coat the substrate with a photoresist and is typically achieved using a spin coater. Then, a mask is positioned over the photoresist that consists of an optically flat, transparent sheet of glass with an opaque, absorber pattern on it. The photoresist is then exposed to UV light through the mask and, depending on the type of resist, the light can either make the exposed areas soluble or insoluble to the developer. A negative photo resist, such as SU-8, becomes insoluble in the developer because the UV light causes cross linking of the exposed photo resist [9].

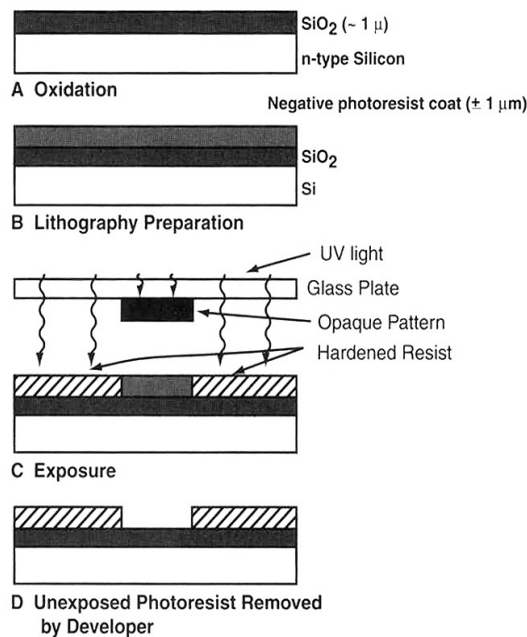


Figure 3.17 The stages of UV lithography [9]: Spin coating of the photoresist, followed by exposure to UV light through a mask, and then development of the structure by dissolving the unexposed photoresist.

Common difficulties of UV lithography are the depth of structures, control of the taper angle and the resolution of the features. However, all of these problems can be overcome to some

degree. This is demonstrated by the structures in Figure 3.18 to Figure 3.20 which show a range of; deep, very small feature size, very high aspect ratio structures.

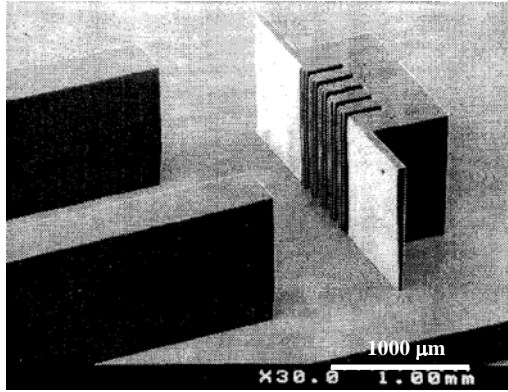


Figure 3.18 Grooved structure SU-8 which is 1200 μm thick with 16 μm grooves [36]

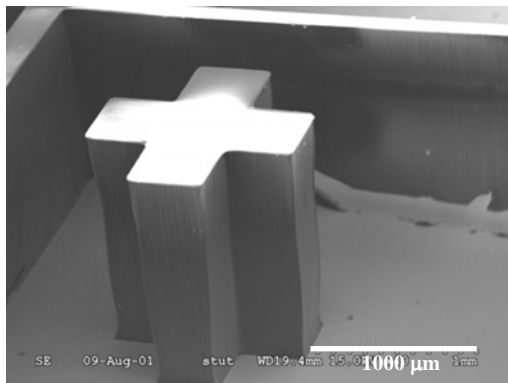


Figure 3.19 1500 μm tall cross SU-8 cross [37]

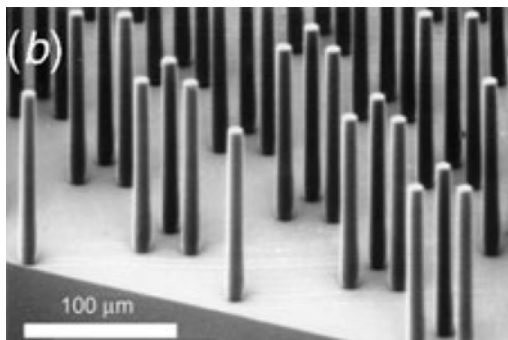


Figure 3.20 clusters of SU-8 pillars that are 10 μm wide and 220 μm tall [38]

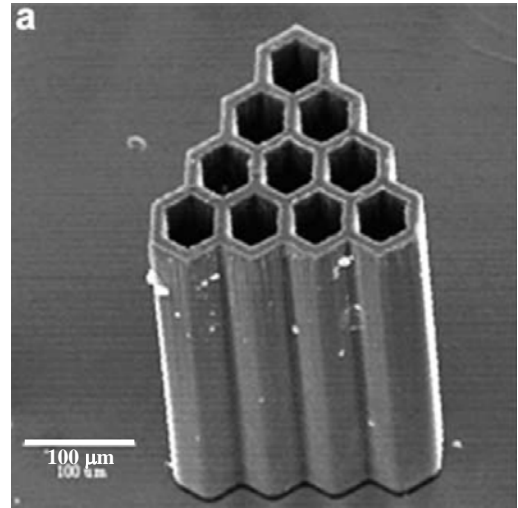


Figure 3.21 SU-8 honeycomb structure with a 10 μm wall thickness and aspect ratio 21 [39]

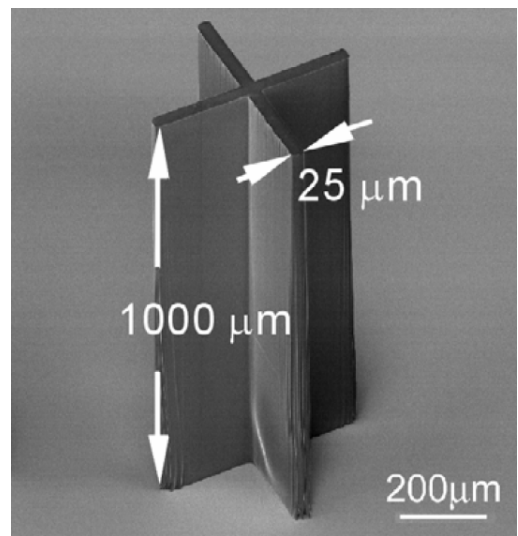


Figure 3.22 SU-8 cross with an aspect ratio of 40 [40]

Typically the photoresists are used to produce structures to depths of 500 μm . This is mainly because it is difficult to spin coat a wafer with a greater thickness than this, and because the optical absorbency of the resist means that the UV light cannot penetrate deeply enough. Thicker layers of photo resist can be applied by either multiple spin coats [36, 41] or by other methods such as direct casting [40, 42, 43, 44].

Compared to other negative photoresists SU-8 has a relatively low optical absorbency in the near UV range [40, 42, 43, 45]. SU-8 is transparent in colour, which enables a much more uniform cross linking of the structure when exposed to UV radiation. However SU-8 still absorbs a proportion of the radiation, such that the intensity of the radiation that reaches the thicker layers is reduced. This effect becomes particularly more obvious when producing structures greater than 500 μm [40]. Thus, for thicker structures, it is beneficial to maintain the transparency of the SU-8.

The optical absorbency can be maintained by an additional baking step before exposure, known as the soft bake, and is carried out at around $\sim 100^\circ\text{C}$ for SU-8. Researchers investigated the effect of soft bake time on optical transmittance [40], and showed that a short soft bake time improves the transmission of the UV radiation through the photo resist. In addition, the researchers found that there was an increased residual stress in the structure when the resist was held at higher temperature. Whilst the researchers presented evidence to suggest that the transmittance, and thus the structure, improves with a reduction in the soft bake time, they presented tall structures (700 μm and 1000 μm) with high aspect ratios (15 and 40 respectively) that had longer bake times compared to the other literature. The coated wafer was heated to 65°C and held for 2 hours and then heated to 95°C for 15 hours, whereas

it is more typical to simply bake for 3 hours at 95°C [36]. Further consideration of the literature reveals that a longer bake time per micron of depth is required for structures with high aspect ratios, or a greater depth than 500 µm. It is also possible to reduce the baking time per micron if higher temperatures are used [37], but can result in cracking of the structure due to the residual stresses [40]. It may be possible to improve the transparency of the resist through a shortened soft bake time, however this is not the sole mechanism for improved deep structures and it is clear that an optimised process is necessary for each structure.

Diffraction of the light by the mask and the resist is still a problem if vertical side walls are required [46, 47]. For this project we do not require vertical side walls, yet this does not reduce the complexity of the fabrication process. Since we wish to study a range of tapers, some control over the taper angle is required. Of the literature reviewed, only four studies commented upon the taper of the structure [41, 46, 47, 48], and of these four, two studies did not demonstrate a taper that was suitable for piezocomposites [41, 47].

SU-8 is a negative tone resist, and therefore upon exposure the resist becomes insoluble in the developer. This means that if a pillar is produced from the photo resist using the conventional exposure techniques, described by Figure 3.17, the pillars are larger at the top than at the bottom. If this was used as a master tool it would cause a dovetail effect, and lock the master tool into the moulding [41, 46, 47, 48]. Similarly, this problem still remains for producing an array of holes in photo resist that can be electroformed to produce a metallic master tool. It is therefore necessary to produce tapers in SU-8 using a backside exposure technique that is illustrated in Figure 3.23. The dovetail effect can be clearly seen Figure 3.23(a) which shows

the conventional method next to the backside exposure technique in Figure 3.23(b). When using the backside exposure technique, the silicon substrate is replaced with an optically transparent substrate such as glass [41, 46, 47, 48] that allows the resist to be exposed through the substrate. The taper angle is controlled by the distance that the mask is from the resist [46, 48], such that the distance is simply the thickness of the glass substrate.

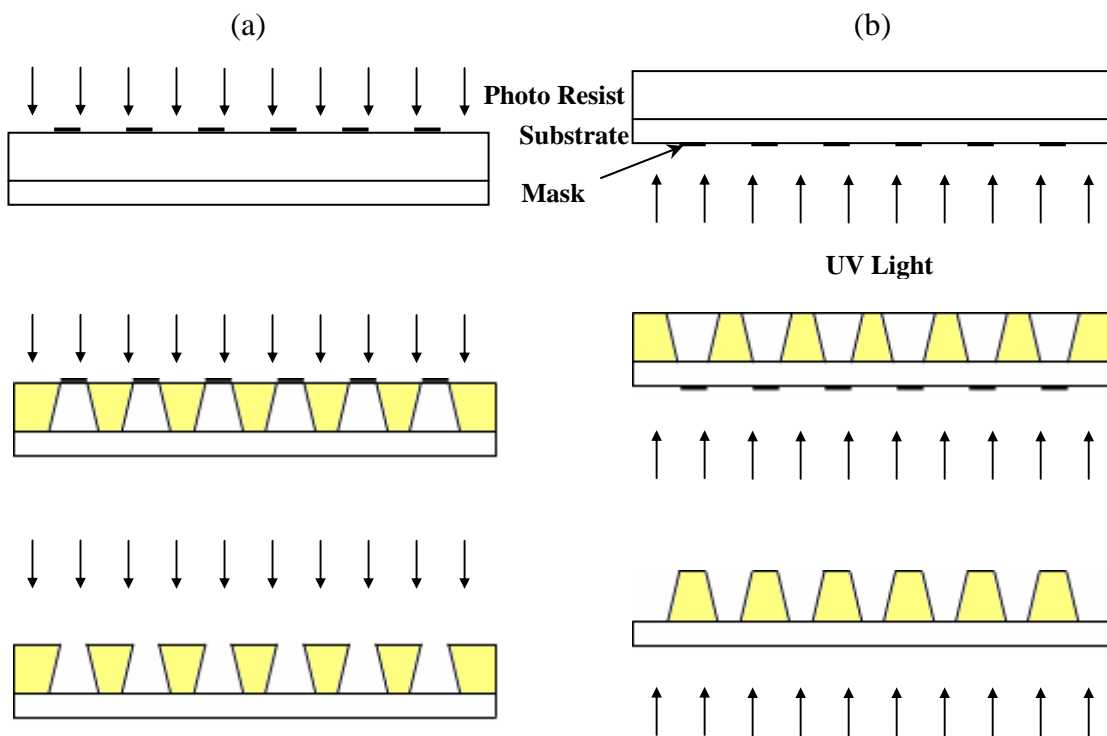


Figure 3.23 The conventional exposure (a) and backside exposure (b) techniques for UV lithography. The diagram illustrates that the required taper can only be formed using the backside exposure technique

An example of a tapered structure can be found in [17]; where two sets of tapered pillars were produced in SU-8. One pillar array had a pillar width of 250 μm , and a kerf of 150 μm , whilst the other had 150 μm wide pillars with a 250 μm kerf. Both sets of pillars measured 400 μm in height, such that the largest aspect ratio achieved was 2.5, which is somewhat lower than required for this project. The taper was not recorded, but was clearly visible in Figure 3.24 and looked close to what is required for the master tool.

In another study, a range of tapers were produced [48]. The aim was to produce a structure with a taper in SU-8 that could then be electroformed for use in hot embossing. These structures had an aspect ratio of < 1 and a height of $65\ \mu\text{m}$. The tapers produced measured 18° , 16.8° and 2.7° , and were obtained by using different process set-ups. It has been acknowledged that the distance that the mask is away from the photo resist is the controlling factor [17, 31], and by using the different set-ups this was varied [48]. The experimental set-up could also be combined such that a more complicated pillar structures could be produced, with different taper angles on the internal and external walls. Examples of these structures are shown in Figure 3.24 to Figure 3.. The pillars are approximately $80\ \mu\text{m}$ wide and have an aspect ratio of 2 [48]

In a third study the limitations of parallel walls were discussed [47]. In this study the aim was to produce a 0° taper. Two structures were commented on. The first structure was a trench that was $6.5\ \mu\text{m}$ wide and $105\ \mu\text{m}$ deep, that had a taper angle of 0.55° . The second structure was a wall that was $11\ \mu\text{m}$ wide, $700\ \mu\text{m}$ tall with a taper angle of 0.16° [47]. These structures had very high aspect ratio, and were also deep, however the work focused on eliminating the taper, rather than controlling it.

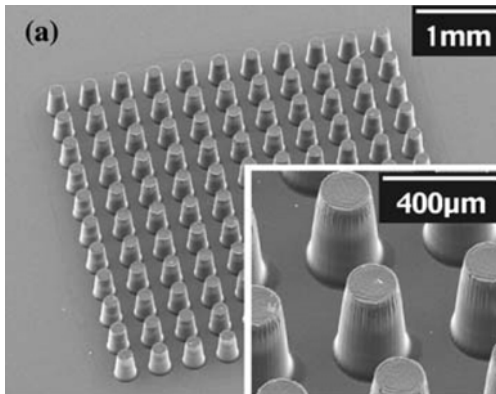


Figure 3.24 SU-8 tapered pillar array with 250 μm pillars and a kerf of 150 μm [46]

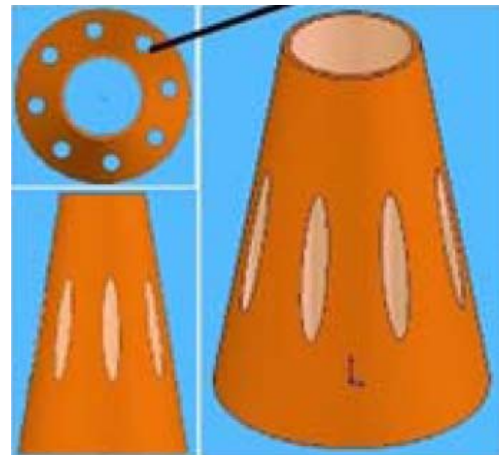


Figure 3.27 CAD drawing of hollow pillar structure with side holes [48]

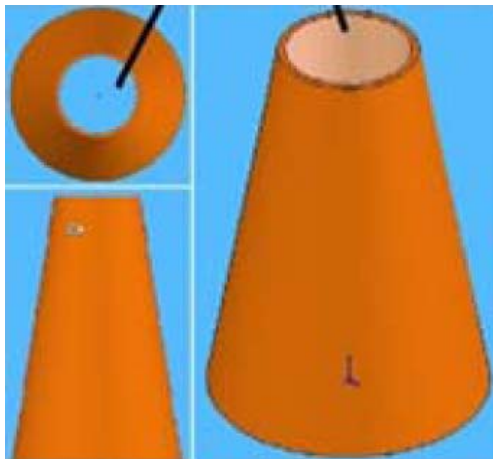


Figure 3.25 CAD drawing of hollow pillar structure produced by a combination of experimental set-ups [48]

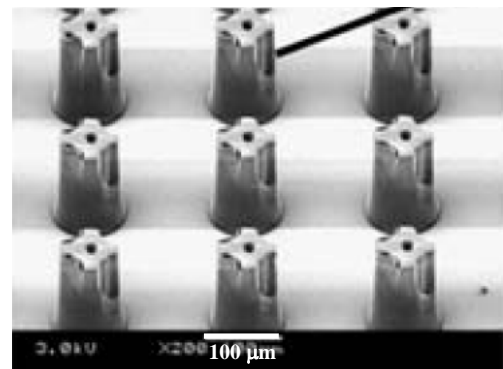


Figure 3.28 SU-8 hollow pillar structure with side holes produced by a combination of experimental set-ups [48]

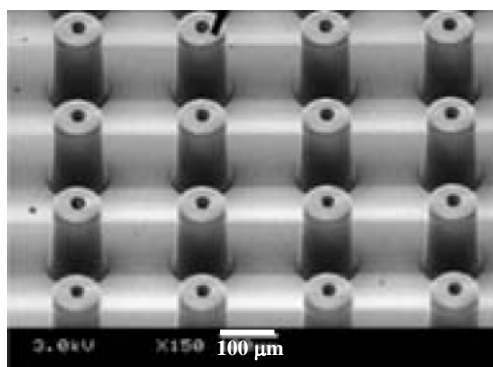


Figure 3.26 SU-8 hollow pillar structure produced by a combination of experimental set-ups [48]

More structures produced by UV lithography are shown in Table 3.7. The structures in bold have corresponding figures and have already been discussed. The table demonstrates that there are a broad range of structures possible by UV lithography, with depths ranging from 65 μm [48] to 1500 μm [37], aspect ratios as high as 66 [37], and with some control over the taper angle [46, 48, 41]. The surface finish is rarely mentioned, but it is typically smooth, and in one case has been reported to have an arithmetical mean roughness (Ra) of 7 nm [46]; which is considerably smoother than required for hot embossing. Figure 3.18 and Figure 3.22 show some example structures that have been fabricated using UV lithography. They are a range of structures that are either deep, have a high aspect ratio, or are of a similar geometry to that required for a piezocomposite. The figures feature two crosses, an array of trenches, pillars, and a honeycomb structure.

The review has indicated that very small feature size and very high aspect ratio structures can be produced. Tapered structures have also been achieved, but a tapered structure with an aspect ratio as high as 8 has not. In addition, researches have recognised that the natural tapering of the structures, caused by the diffraction of the light, can be used to produce a taper to help de-embossing. It has also been reported that the taper can be controlled by varying the proximity of the mask from the resist, however fine control over the taper has not been demonstrated. When using the backside exposure technique, the proximity of the mask is limited by the thickness of the glass substrate. In addition this is further complicated by an increase in stress between the resist and the glass if either of them becomes too thick.

Table 3.7 A review of the structures produced by UV Lithography

Process	Structure	Material	Feature Size (μm)	Depth (μm)	Aspect Ratio	Surface Finish (μm)	Structure Number / Reference	Comments
UV Lithography	Rotor for Micro Engine	SU-8	80	500	6.3	-	#1 [49]	Spin coated, no work with tapers
	Letters	SU-8	16	160	10	-	#2 [45]	Spun, no tapers
	Comparison structure with #10 in Table 3.10	SU-8	400		> 2 (depth > 900)	46.5 S.D. 33.6	#3 [50]	
	Right Angle Structures	SU-8	16	270	17	-	#4 [36]	Single spin, no taper
	Stars	SU-8	-	500	-	-	#5 [36]	Double Spin Coated
	Grooves	SU-8	65	1200	18	-	#6 Figure 3.18 [36]	
	Grooves	SU-8	43	700	17	-	#7 [36]	Double Spin Coated, limitation of feature size is 4 μm due to developer flushing.
	Cross	SU-8	494	1500	3.0	-	#8 Figure 3.19 [37]	Constant volume injection method
	Nozzle	SU-8	100	1500	15	-	#9 [37]	Single spin coated
	Pillar Array	SU-8	40	210	5.25	-	#10 [37]	
	Honeycomb	SU-8	70	400	5.7	-	#11 [51]	
	Microgear	SU-8	57	1000	17.5	-	#12 [42]	Direct casting on level wafer, optimised soft bake process
	Small Honeycomb array	SU-8	10 walls	210	21	-	#13 Figure 3.21 [39]	Single spin coating
Wall	SU-8	10	210	21	-	#14 [39]		

Process	Structure	Materials	Feature Size (μm)	Depth (μm)	Aspect Ratio	Surface Finish (μm)	Structure Number / Reference	Comments
UV Lithography	Block array	SU-8	100	65	0.5	-	#15 [48]	3° taper, other samples had features sizes of 20 μm and 50 μm but are shown. Single spin coat. Back-side exposure technique on glass wafer
	Hollow Pillar	SU-8	~ 80	~ 160	~ 2	-	Figure 3.25 to Figure 3. [48]	
	Pillar array	SU-8	150 kerf, 250 posts	~ 400	2.5	Ra 0.007	#16 [46]	Backside exposure technique on glass wafer. Unknown taper.
		SU-8	250 kerf, 150 posts	~ 400	2.5		#17 [46]	
	Variable focus micro lens	SU-8	700	-	-	-	#18 [41]	Double spin coated, Backside exposure, production of 36° angle
	Trench	SU-8	6.5	105	16	-	#19 [47]	Taper 0.55° (not specified in the design)
	Line / wall	SU-8	11	700	66	-	#20 [47]	Coating not described. "Average groove width" Taper 0.16° (not specified in the design)
	Cluster of Pillars	SU-8	10	220	22	-	#21 Figure 3.20 [38]	Spin coated, Pulsed backside exposure
	Channels	SU-8	9.2	92.2	10	-	#22 [52]	Spin coated
	Walls	SU-8	9.2	92.0	10	-	#23 [52]	
Cross	SU-8	25	1000	40	-	#24 Figure 3.22 [40]	Optimised soft bake process, direct casting	

3.2.2 LIGA

It will be seen from Table 3.6 that many of the master tools were made by the LIGA process. LIGA is a German acronym for three processes used together, X-ray Lithographie (X-ray lithography), Galvoformung (electroforming) and Abformtechnik (moulding). The process is similar to UV lithography, as explained in section 3.2.1, but uses X-rays rather than UV light and thus has a greater resolution, better penetration and undergoes less scattering. It is, therefore, frequently used for producing master tools for hot embossing because it is very good at producing very small feature sized and very high aspect ratio structures that are also smooth. However, the process requires access to energetic X-rays made using synchrotron orbital radiation, which is not only very costly, but difficult to access. Furthermore, LIGA was designed to produce parallel structures such that the ability to achieve a taper on the pillars is limited [9].

3.2.3 Laser Ablation

Laser ablation for micro-scale devices uses two types of laser, excimer lasers and femtosecond lasers. Both types of lasers aim to machine the material through ablation, whereby a large amount of energy is applied locally to the work piece such that material is removed by the breaking of chemical bonds, in the form of a plasma [9, 53].

Excimer lasers commonly transmit laser light through a mask to achieve the required geometry of the micro-scale device. The wavelength of the light is in the UV range and is dependent upon the gas source, with wavelengths ranging from 157 nm to 308 nm. The pulse length is of the order of nanoseconds, and has a peak power 3 MW to 50 MW. The key

feature of excimer lasers is that at these wavelengths, the laser strongly interacts with the chemical bonds of organic materials, such as polycarbonate or PMMA.

Femtosecond (10^{-15} s) lasers focus a spot onto the work piece to produce a laser cut. The laser can produce a peak power of between 5 and 10 GW in a laser pulse that lasts a millionth of the time that a pulse from an excimer laser lasts. The laser produces a power density that is far greater than any material can withstand, such that even hard or high melting point materials can be ablated. The key feature of these lasers is that the laser pulse is so short that the energy from the pulse can not diffuse away from the work spot in time, leading to a build up of energy at the working spot, which causes a plasma regime [9].

Laser ablation requires a threshold fluence to be exceeded. The fluence is the pulse energy per area and is thus dependent upon the area, such that increasing the pulse energy or decreasing the spot size will increase the fluence. In addition, the threshold fluence is dependent upon the material being ablated, and depends largely on the material structure and the absorption coefficient of the material at the wavelength of the laser. When the laser fluence is below the threshold value, the temperature of the work spot is directly proportional to the fluence, and etching occurs at a relatively slow rate. However, once the etch threshold value is exceeded, the temperature increase is much slower, and a plasma plume is generated. The highly energetic particles, such as ionised atoms and free electrons, expand away from the machining site, such that the energy around the spot does not build up any further. The process requires chemical and atomic bonds to be broken, and an increase in highly energetic particles increases the reaction rate and aids ablation [9, 53].

Femtosecond and excimer lasers generate an ablation plume by different mechanisms. In a femtosecond laser, there is sufficient energy to exceed the threshold of all materials. In an excimer laser, the absorption coefficient in the UV range is high so that less energy is required to ablate an organic material [a]. In general, machining by femtosecond laser produces a better quality product. However their use is limited by a low throughput, small machined areas and their high cost; which can reach a six to seven figure sum [9].

Table 3.8 describes some of the structures produced by laser machining. Of the structures described in the table, the most applicable to the project is a comb structure shown in Figure 3.29 [54]. This structure has an aspect ratio of 30, which is the highest of the reviewed structures. The height of the structure is 300 μm and the minimum feature size is 10 μm . The same researchers also produced another comb structure with an aspect ratio of 15 and a height of 150 μm . Both these structures were produced by an excimer laser [54]. These aspect ratios are suitable for hot embossing of piezocomposite moulds and are particularly notable because several authors have stated that aspect ratios do not typically exceed 10 for excimer machining [54, 55].

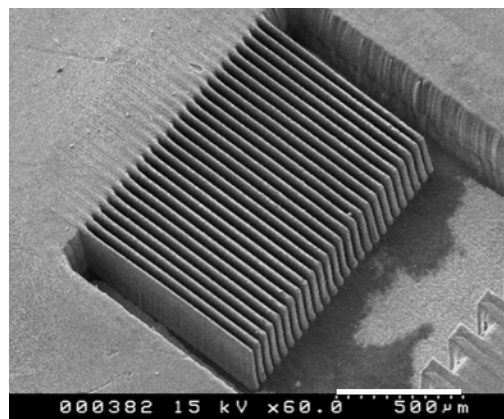


Figure 3.29 Comb structure with 10 μm fingers and 300 μm depth produced in polyimide by an excimer laser [54]

A femtosecond laser has produced a 40 μm hole with an aspect ratio of 10 and with parallel sides. At aspect ratios larger than this it was noted that the hole had a taper. A hole with an aspect ratio of 25 was also produced that had a taper but it also began to curve away from the central axis. Other structures have been produced but their aspect ratios do not exceed 5 [53, 54, 56].

The geometry closest to a bristle block is the micro probe array and is shown in Figure 3.30. This figure shows metallic needles, created by electroforming into a laser ablated glass mould. The aspect ratio of this structure is about 2 and the feature size is estimated to be 15 μm . Nonetheless, the microprobe array is still an array of tapered pillar-like structures. The actual size of the taper is not discussed, but the taper angle can be approximated from the images to around 15° [53] and is much larger than the angle required for hot embossing of piezocomposite moulds. The authors of the study commented that an increase in repetition rate of the pulse would result in a probe with a larger taper angle and a blunt needle tip. They also commented that an increase in shot number would result in an increase in depth [53].

Table 3.8 A review of the structure produced by laser machining

Process	Structure	Material	Laser	Feature Size (μm)	Depth (μm)	Aspect Ratio	Surface Finish (μm)	Reference	Comments
Laser Ablation	Unspecified	Polymers, ceramics, some metals	Excimer	6				[57]	
	Unspecified	Any	Femtosecond	1				[57]	
	Unspecified	steel	Excimer				Metallic mould 0.2-0.3	[58]	
	Holes			< 1		-		[9]	
	Hole			-		50		[9]	
	Hole	PMMA	Femtosecond	40	400	10		[55]	Good quality hole.
	Gear	Synthesised polyimide	Excimer	~ 21	~ 127	6	-	[54]	Projective mask. 0° taper, but possible to control taper from > 25° to ~ 0°
	Comb Structure			10	150	15	-	[54]	
	Comb Structure			10	300	30	-	[54]	
	Micro probe array	Glass	Excimer	13	26	2	-	[53]	Projective mask. Taper ~ 15°.
	Rotor	PMMA	Excimer		150		< 0.1	[56]	Projective mask
Trenches	Positive Photo resist	Excimer	25	100	4	-	[56]	Projective mask. Taper angles from -10° to 10°	

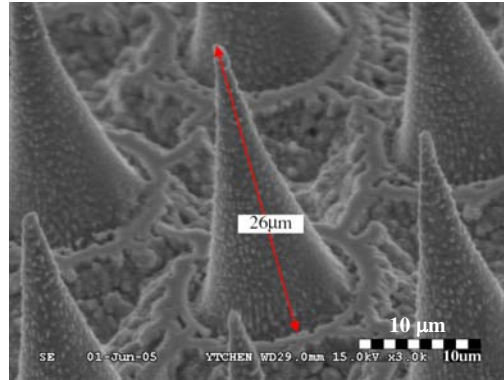


Figure 3.30 Electroformed micro probe array made from an excimer laser ablated glass mould [53]

Other authors have commented more comprehensively about taper control. Whilst producing the comb structure [54], the researchers discussed the effect of several machining parameters on the taper of the structure. It was found that a taper range of $> 25^\circ$ to 0° could be produced, depending on the number of pulse shots and the laser fluence. The authors concluded that the taper angle could be reduced by an increase in laser fluence, but noted that an increase in fluence caused severe thermal damage [54]. Increasing the number of shots also decreases the taper angle, but an excessive number can degrade the quality of the structure [54]. These comments were further reinforced by similar comments made by researchers who machined $25\ \mu\text{m}$ wide, $100\ \mu\text{m}$ deep trenches in a positive photoresist, LM5000 [56].

Some very small feature size, very high aspect ratio structures have been produced by laser ablation. Some researchers have attempted to control the taper on the holes and in a micro probe array with some success. The surface finish of the holes, and subsequent electroformed pillars, is a concern and it is suggested that a brief feasibility study is required to confirm the suitability of the micro fabrication technique for a master tool, and is described in section 7.1.

3.2.4 Micro Electro Discharge Machining (μ EDM)

Micro electro discharge machining (μ EDM) is a process that uses an electrical spark to vaporise the surface of any conducting work piece. The work piece is submerged in an electrolytic fluid that is typically either de-ionized water or oil. When the electrode is brought to within $\sim 1 \mu\text{m}$ of the surface of the work piece a spark is discharged that erodes both the electrode and the work piece. The discharge vaporises the material leaving a crater and debris that is removed by the circulating electrolyte. The surface finish is strongly influenced by the shape of the craters which, in turn, are related to the size and shape of the discharge pulse. Micro EDM does not require a mask and therefore has a high design freedom. It is non-contact, such that any conducting material can be machined regardless of its hardness or mechanical properties; it has low set up costs [59] and will avoid the need for an electroforming step.

The two main μ EDM methods discussed here are wire μ EDM and μ EDM drilling. In wire μ EDM the electrode is a long wire that is continually transferred between two spools. Cutting is achieved as the wire is transferred between the two spools, and sparks are generated along the length of the wire. The main benefit of this method is that the electrode is continuously changed, such that the accuracy of the process is not affected by the erosion of the electrode during the process. However, in μ EDM drilling, the electrode is not continuously changed and is used vertically, like a drill bit. It can be used to produce holes of different shapes, by simply using a different shaped electrode. However, because the electrode is not changed, the continual wear makes accuracy more difficult and the process must be optimised with the consideration of minimising the electrode wear.

Wire μ EDM can use wires with a diameter as small as 20 μm , but at this size the wire is particularly susceptible to vibration [60, 61]. Machining small feature size or high aspect ratio structures can be problematic because they can become distorted by heat building up within them, and it is therefore necessary to minimise the spark energy used to machine them [61]. The small energy used means that the wire must be brought closer than 1 μm to the surface, which results in more short circuits, when the wire vibrates or due to any unremoved debris [60]. These problems have led researchers [60, 61] to modify a wire EDM machine to overcome the problems of wire vibration and spark generation. The modifications have resulted in the structures shown in Figure 3.31 to Figure 3.33 [60, 61].

In the modified machine the wire tension was magnetically controlled [60, 61], and a wire guide with a vibration dampener [60] and a low energy circuit was fitted. In addition, the machine was also modified to cut horizontally and vertically to reduce the set-up times. The structures shown in Figure 3.31 and Figure 3.32 were able to be cut from underneath, in a process named reverse EDM, which allowed debris to be removed more easily from the structure and avoided short circuits caused by them [61]. The pagoda shown in Figure 3.33 demonstrates the geometrical complexity that can be achieved by the process.

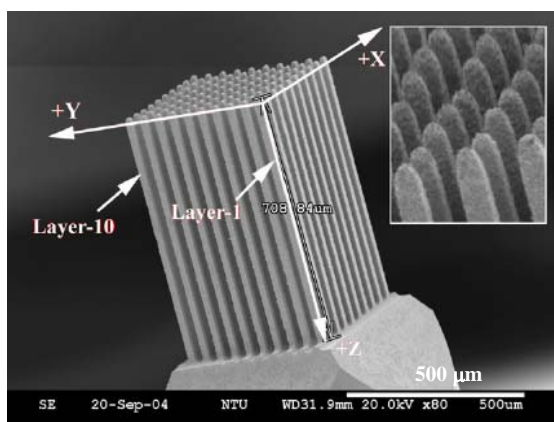


Figure 3.31 Beryllium copper pillar array with an aspect ratio up to 33 [61]

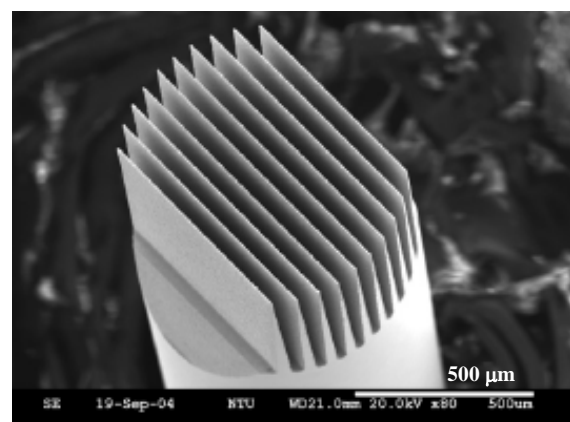


Figure 3.32 Beryllium copper array of tapered walls [61]

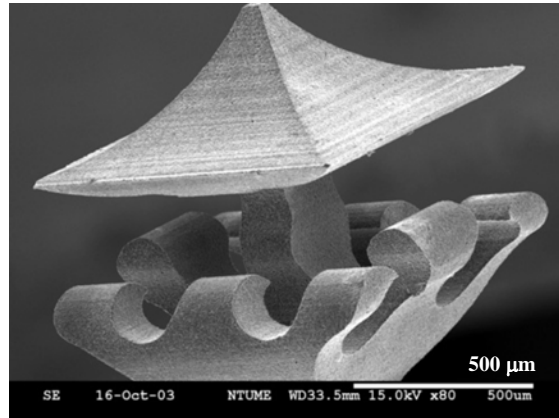


Figure 3.33 Magnified view of a copper pagoda machined by μ EDM [60]

The dimensions of many example structures and the structures shown here can be found in Table 3.9. The two arrays are particularly interesting because they reach aspect ratios in excess of 24 and have a kerf of 24 μm . To produce such a high aspect ratio at such a low feature size is impressive, but it is unlikely that the feature size can be reduced any further because the smallest electrode wire that can be used for μ EDM is 20 μm . Therefore, this method of master manufacture could be suitable for a 10 MHz piezocomposite with 84 μm pillars, and a kerf of 35 μm , but is not suitable for scaling any smaller. Furthermore, a common problem with μ EDM structures is the surface finish. It is recommended that, for polymer replication, the surface roughness, R_a , must be $< 0.09\mu\text{m}$. However in these images the best surface finish is 0.2 μm [5], which is twice as rough as the recommended roughness for polymer replication.

Rather than producing positive structures by wire μ EDM it is also able to produce negative structures using μ EDM drilling. This method can be used to produce tapered holes, which are often a by-product of the eroding electrode. An EDM machine has been modified to cut tapered holes [62]. The machine was modified so that the electrode could be tilted and rotated to drill the hole. The modifications were successful for producing tapered holes, and a hole with a taper of $\sim 2^\circ$ was produced.

However, a limiting factor in using this type of μ EDM is that many of the holes are $\sim 100\ \mu\text{m}$ in diameter, and it is unlikely that smaller electrodes can be used.

Table 3.9 shows a range of structures that have been fabricated by wire μ EDM and μ EDM drilling. It can be seen that the surface roughness described previously is fairly typical of the process, and that the feature sizes discussed for both μ EDM processes are also fairly typical. It is therefore possible to conclude that whilst μ EDM offers the opportunity to directly produce a metallic master tool without an electroforming stage, the size of the wire and the surface roughness limits the process for fabricating a master tool for the replication of 1-3 piezocomposite moulds.

Table 3.9 Example structures produced using micro electro discharge machining

Process	Structure	Material	Feature Size (µm)	Depth (µm)	Aspect Ratio	Surface Finish (µm)	Structure Number / Reference	Comments
µEDM	Unspecified	Conductive materials	5 - 300		3 - 5	Ra 0.1	[9]	
	Unspecified	-	15-25			0.1	[61, 63, 59, 57]	
	Tapered Fin Array	Tungsten carbide	Top 10, bottom 40, kerf at bottom 22	600	24		Figure 3.32 [61]	
	Fin array		10 kerf 21	300	12	Rmax 0.45	[61]	
	Pillar Array		Pillar width 21, kerf 24	700	33	Rmax 0.44, Ra ~0.2	Figure 3.31[61]	
	Pillar Array	Steel	Pillar width 80, Kerf 400		6.5	-	[63]	
	Gear tooth		Tooth 50.2	6000	120	-	[63]	Attached to supporting structure
	Pyramid Array	Stainless steel	Kerf at base 125		~ 1	Ra 0.12	[63]	
	Rachet Gear	Beryllium Copper	Tooth 175	884	~ 18	-	[57]	
	Gear	Copper	~ 35		~ 7	Ra 0.16	[60]	
	Pagoda		~ 160		-		Figure 3.33[O]	
	Silicon electrode imprint	-	50		10.5	Ra 0.074	[64]	
	Hole	Case hardened steel	115		~ 8	Ra 0.3	[62]	2° taper
	Triangular hole	Copper : tungsten alloy (25:75)	~ 180		~ 1.1	-	[65]	2° taper
	Rectangular hole		~ 130		~ 1.5	-	[65]	
	Tapered circular hole		~ 110		~ 1.8		[65]	
	Circular Hole	Ni-Mo alloy	~ 170		~ 3	Rmax reduced from 2.11 to 0.69	[66]	Electropolishing removes recast layer that exhibits cracks and a heat effected zone.
	Triangular Hole		~ 130		~ 2.0		[66]	
	Square Hole		~ 120		~ 2.9		[66]	
	Circular hole	304 stainless steel	~ 106	500	4.7	-	[67]	Very straight hole 0.12°
Circular hole	steel	~110	1000	~ 9	-	[67]	Straight and deep hole 0.4 °	

3.2.5 The Bosch Process

The Bosch process is used to anisotropically etch silicon wafers through a sequence of alternating etch and passivate cycles, as illustrated in Figure 3.34. The structure to be machined is defined by a mask that can typically be made from photoresist [68, 69, 70], or chromium [69, 71]. The wafer is placed on a stage in an inductively coupled plasma (ICP) reactor and the chamber is evacuated. The etchant gas, typically sulphur hexafluoride (SF_6), is pumped into the chamber before a radio frequency (r.f.) coil is used to generate the plasma.

A second r.f. source is used to bias the stage, such that the positively charged ions in the plasma are accelerated vertically towards the wafer. These ions impact on the exposed silicon, and assist the chemical etching by fluorine radicals and other reactive species. Etching by these species is isotropic and causes an elliptical cavity to form beneath the mask [68, 70, 72, 73] as shown by the second image in Figure 3.34.

A typical etch phase lasts around 5 s. After this, the etchant gas is replaced by the passivating gas, which can be any perfluorinated monomer [72], typically C_4F_8 [74, 68, 71, 69, 70, 75]. The r.f. coil is used a second time to transform the gas into another plasma. In this plasma state, polymerisation occurs and a Teflon-like film is deposited on the newly exposed silicon. If the stage remains biased, an ion flow is present during the passivation stage and the polymer preferentially forms on the sides of the cavity where the ion flow is at its weakest [70, 72, 73]. The benefit of this is that during the second etch step the polymer does not need to be removed from the base of the cavity before further silicon etching can start, thus increasing the etch rate and the anisotropy of the process [72].

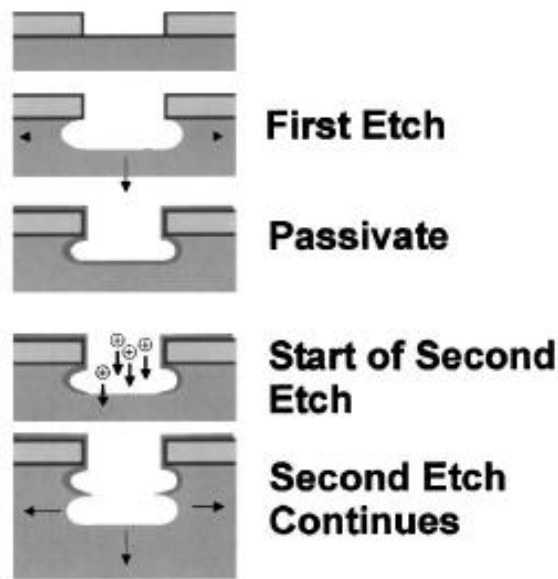


Figure 3.34 The stages in the Bosch Process: the initial isotropic etch phase, followed by a passivation phase, then an anisotropic etch of the passivation layer, before isotropic etching of the silicon [16]

The fourth image in Figure 3.34 shows the second etch phase, where the ion current is assisting the removal of the passivating polymer at the base of the cavity. The passivating polymer has a high chemical resistance, such that physical sputtering by the ions is required to aid removal of the polymer. The incident ions affect the removal of the passivating film, and therefore which areas of silicon are exposed to the reactive species. This means that the speed and angular distribution of these ions can affect the anisotropy, selectivity and the etch rate of the Bosch process [68, 69, 70, 72, 75].

The resultant structure from the Bosch process is dependent upon a combination of many variables. The process was developed so that the user can optimise the combination of parameters to etch structures with a rapid etch rate, good selectivity, and without the loss of anisotropy [72].

Control over the etch rate is dominated by the power applied to the plasma coil. Increasing this power increases the degree of ionisation and therefore the ion flux to the wafer. In some cases the SF₆ flow can limit the etch rate, and therefore the rate is further improved by an increase in the etchant gas. This ensures that the etchant species are replenished and limits the redeposition of the etch product [70, 75]. However, too much SF₆ and the number of collisions can become too great, reducing the energy of the ions such that they are not capable of etching the silicon [70].

The applied electrode power can improve the etch rate, but to a lesser degree. The bias on the electrode is typically required to accelerate the ions vertically towards the wafer. Increasing the bias increases the acceleration of the charged species, such that they strike the passivating film with greater force and increase the rate of removal. Unfortunately, the ions also strike the mask and increase its rate of removal, leading to a decrease in the selectivity of the process [69, 70, 75]. The vertical velocity of the ions means that very few strike the side walls of the cavity; thus the polymer on the side walls is etched more slowly relative to the base.

The w/d ratio describes the anisotropy of a single etch cycle. It is the ratio of the width to the depth of an ellipse formed by a single etch phase. The aim is to minimise the ratio, such that the width of the ellipse is at a minimum such that the etch is made more anisotropic. The depth of the ellipse is caused by a combination of ion-enhanced etching and isotropic etching, whilst the width is caused solely by isotropic etching. Increasing the power of the plasma coil increases the number of ions and causes the vertical etch to become more dominant, and, therefore improves the w/d ratio [70, 75]. The anisotropy is also improved by increasing the

applied electrode power. This causes the ions to be accelerated in a more vertical direction and results in fewer collisions with the sidewalls, and more at the base of the structure.

It would be expected that increasing the pressure, or flow rate, of SF₆ would increase the w/d ratio because this would increase the amount of isotropic etchant, atomic fluorine. However, the opposite occurs and the ratio is minimised due to a more even covering of reactive species at higher pressures [75]. Increasing the pressure further leads to an increase in the ratio because the ion energy is reduced by an increased number of collisions [70].

The switching between the isotropic etching stage and the passivation stage in the Bosch process causes scalloping, which is illustrated in Figure 3.34 and demonstrated in Figure 3.35. This characteristic of the process obviously has an effect on the surface finish, however it is possible to keep the depth of these oscillations to low values by controlling various process parameters. The cycle time of each step is commonly used to control the depth of the scalloping; however, if the cycles are alternated too rapidly the etch rate is reduced significantly. The w/d ratio also describes the scallops that will develop on the side of the structures. The width of the ellipse is related to the peak to valley height of the scallops, as illustrated in Figure 3.35. It is also favourable to minimise the w/d ratio in order to improve the surface roughness.

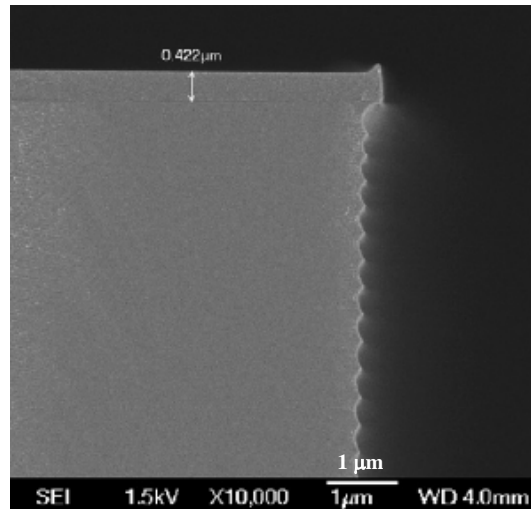


Figure 3.35 Scalloping caused by the etch and passivate cycles of the Bosch process [76]

Other forms of surface roughness can manifest themselves on the sidewalls of the structures. A common type of roughness is vertical striations, which are caused by surface damage to the passivating polymer, or mask. The surface damage means that the polymer is no longer able to protect the silicon beneath it and therefore the silicon can be etched readily by reactive species [70]. A second problem that can occur is the formation of micro grass. This is caused by a phenomenon that is called micro masking, whereby the pieces of the mask, or passivating polymer, is redeposited and masks a small area from the etchant. A small column, similar in appearance to grass, is formed because the etchant cannot remove this area of silicon [69, 70]. Micro grass can be avoided by increasing the bias on the electrode, which helps to complete removal of etching by-products, by increasing the incident energy of the ions.

Table 3.10 A review of the structures produced by the Bosch process

Process	Structure	Feature Size (μm)	Aspect Ratio	Surface Finish (μm)	Structure No. / reference	Comments
Bosch	Array of Holes	20	30	0.05	#1[9]	Much more accessible and less expensive than LIGA [a] Balance between etch rate and surface roughness [a] slow etch rate 4-10 μm / min
	Array of Holes	Cavity width 10, kerf ~3	10?	-	#2 Figure 3.36 (B) [77]	These structures demonstrate that high aspect ratio features can be achieved by etching low aspect ratio features around them
	Array of Pillars	Width ~ 9, kerf ~ 12			#3 Figure 3.36 (A) [77]	
	Array of Holes	Width ~ 12, kerf ~ 1.5 Depth ~ 18	13		#4 Figure 3.36 (C)[78]	
	Concentric Circles	Wall Width ~1 Gap ~14 Depth ~ 5 μm	5		#5Figure 3.36 (D) [78]	
	Comb Structure	Wall Width ~9 Kerf ~ 12	~ 11	0.01 to 0.07	#6 Figure 3.37[79]	
	Trench	Width ~ 13 Depth 314	~ 24		#7 Figure 3.38 [80]	These structures demonstrate the depth the can be achieved by the Bosch process
	Trench	Width 13 Depth 515	~40		#8Figure 3.38 [80]	
	Tapered Trenches	100	1.08 (1°) 0.94 (3°) 0.97 (3.5°) 0.69 (4.5 °) 0.73 (5°)	< 1 μm	#9 Figure 3.40 and Figure 3.41 [74]	Modified Bosch process, using a combination of isotropic and anisotropic etching.

Process	Structure	Feature Size (μm)	Aspect Ratio	Surface Finish (μm)	Structure No. / Reference	Comments
Bosch	Comparison with UV lithography (#3 in Error! Reference source not found.)	~ 1.1 Depth > 450 μm		Rrms 0.5 to 0.2 μm	#10[50]	
	Tapered (5°) Block array	Depth 45			#11 [71]	Blocks show tapered angle of 5°
	Tapered (38°) Block array	440	0.16	-	#12 [71]	
	Silicon electrode for imprinting	50	10.5	Rz 0.02	#13 [64]	
	Array of Pillars	Width ~ 4 Kerf ~ 6	~ 4		#14[78]	
	Trench	~ 4	~ 26		#15 Figure 3.39 [80]	
	Trench	~36	~ 5		#16 [80]	
	Array of Holes	Width 62 Depth 257	4		#17[76]	
	Array of Holes	Width at Bottom ~75 Kerf at Bottom ~ 40 Depth 235	~ 5.9		#18 Figure 3.42[76]	Taper only half way down
Trench	~ 12	34		#19[70]		

The types of structures that are possible by the Bosch process are shown in Table 3.10 and the following paragraphs discuss the some structure of particular interest.

Figure 3.36 shows examples of mesh, pillar and trench structures that have been produced using the Bosch process. In these examples, the structures are very small, and have feature sizes of around 1 to 10 μm and aspect ratios of around 10. However, these features have been formed by etching relatively large, low aspect ratio features, to leave a small feature size, high aspect ratio feature. Thus, whilst etching a silicon master tool is possible, it is preferable to etch a mesh structure that can be electroformed into.

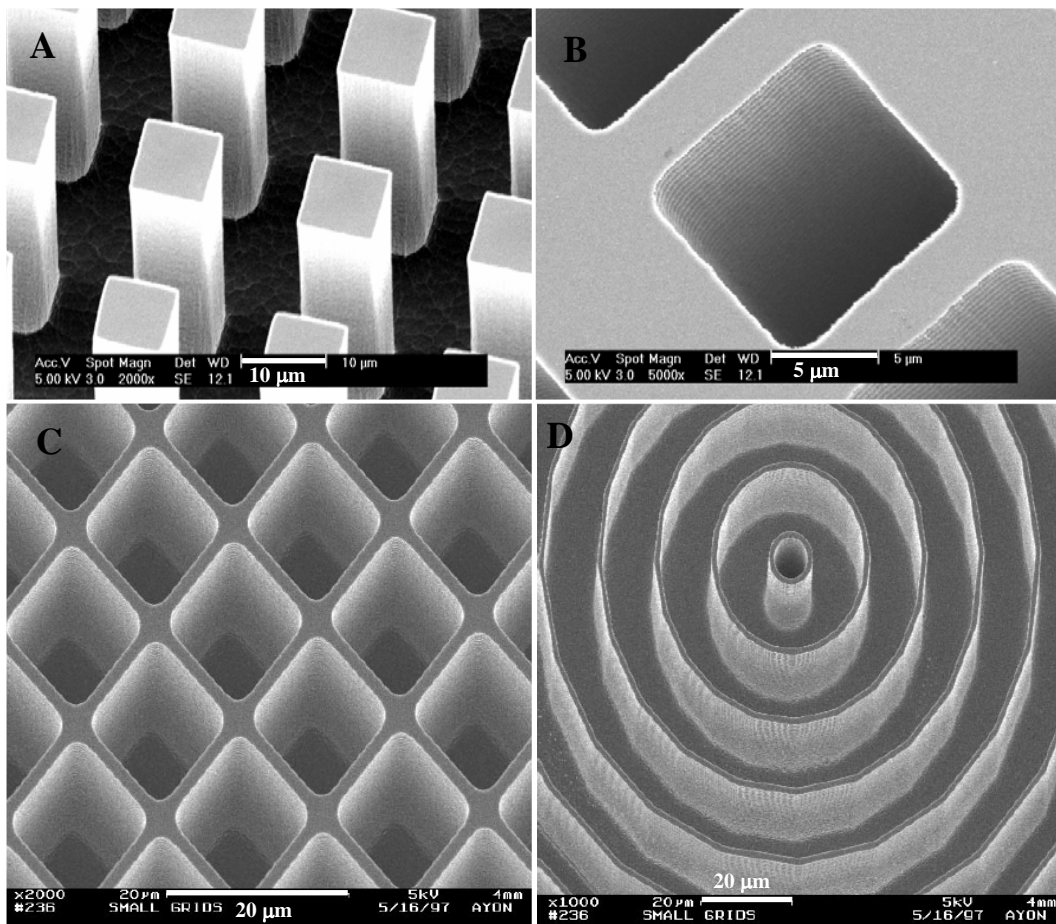


Figure 3.36 High aspect ratio structures produced by etching lower aspect ratio structures such that the kerf in (B) is much smaller than the kerf in (A) [77], similarly the cavities etched away compared to the remaining feature in (C) and (D) [78]

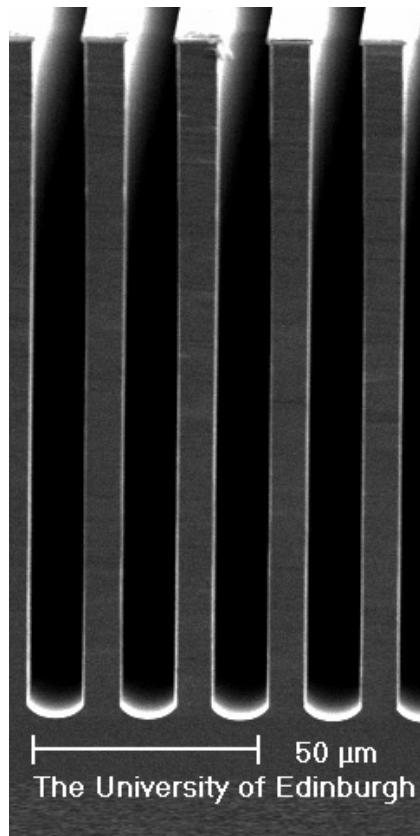


Figure 3.37 High aspect ratio comb structure [79]

Other high aspect ratio and deep structures have also been produced by the Bosch process, and are demonstrated in Figure 3.38 and Figure 3.39. Of particular interest is Figure 3.38 that shows particularly deep structures with very high aspect ratio. The trenches shown in the figure are approximately 13 μm wide and one trench has a depth of 515 μm [80]. This trench is of a greater depth to that required for thick a master tool for a 5 MHz piezocomposite, and is a depth that is not commonly found in the literature. It demonstrates that such a depth is possible by the Bosch process, but it is important to note that the profile of the trench has not been controlled. The trench also has an aspect ratio of 40, which is an order of magnitude greater than the aspect ratio of the cavities required to electroform a master tool. Such a large depth was achieved by increasing the neutral flux reaching the bottom of the trench. As the etch progresses, typically the amount of neutral ions reaching

the bottom of the trench decreases. Therefore, the loss of flux could be compensated for by increasing the flow rate of the SF₆, this increases the number of collisions and therefore increases the number of etching species [80]. However, increasing the number of collisions can widen the angular distribution of the ion flux, and increase the side wall etching of the cavity and cause bowing of the side wall [68].

Good profile control is obtained in Figure 3.39 where a trench ~ 4 μm wide has been etched to a depth of 104 μm and an aspect ratio of 26. The aspect ratio is not as high as in Figure 3.38, but the profile is significantly better and the aspect ratio is still 6 times greater than what is required by for the master tool. In addition, the trench has been etched next to a larger trench which is particularly difficult to do because the larger trench tends to locally deplete the available etching species [68].

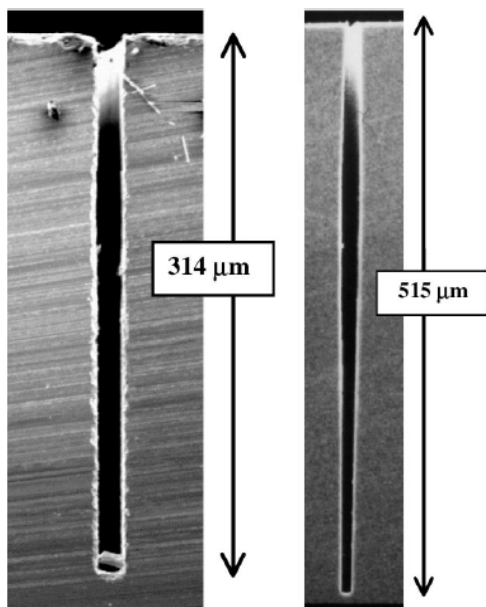


Figure 3.38 Deep trenches etched by the Bosch process [78]

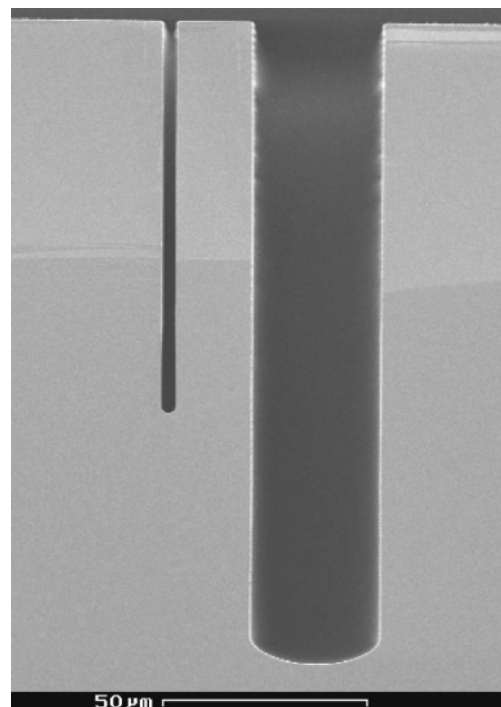


Figure 3.39 Straight sided, high aspect ratio trench [78]

Tapered walls can be obtained using several methods. For very small tapers $< 5^\circ$ the process parameters of the Bosch process itself can be varied to obtain the required wall angle [68]. However, other groups have used the directionality of the whole Bosch process coupled with the isotropic nature of the fluorine etch, to obtain a greater wall angle [74, 76].

The simplest of these methods to control is the a method used in [74], where a few cycles of the Bosch process, typically 3-20, were followed by a few seconds of isotropic etching, typically 15-60 s. Thus, the cavity was etched vertically by the Bosch process, then vertically and laterally by the isotropic process. Cavities created by this method are shown in Figure 3.40 and Figure 3.41. The obvious ridges on the sidewalls of the cavities are caused by the switching between the Bosch process and the isotropic etching. These ridges, named taper scallops by the researchers, are caused by the development of a narrow cavity by the anisotropic process that is then widened by the isotropic process. They are different to the normal scallops seen in Bosch etching because they are caused by the switching between anisotropic and isotropic etching rather than switching between the etch and passivate cycles of the Bosch process [74] and they are much larger.

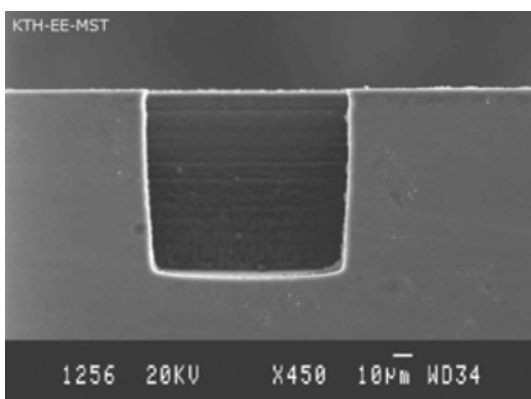


Figure 3.40 Bosch etched cavity with 3° taper and $<1 \mu\text{m}$ surface roughness [74]

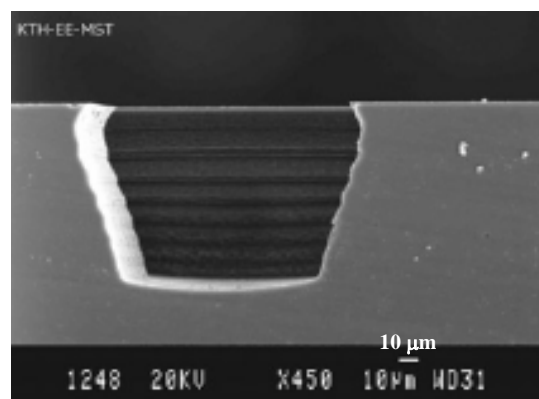


Figure 3.41 Bosch etched cavity with 18° taper and $3.3 \mu\text{m}$ surface roughness [74]

The wall angle can easily be predicted by the ratio of the vertical to lateral etching, which makes this process simple to control. The method has produced a broad range of tapers, ranging from 0° to 36° , and all to a depth of approximately $100\ \mu\text{m}$. However, it is recognised that the taper scallops do restrict this process, and in some cases the scallops have reached sizes of $3.5\ \mu\text{m}$. The scalloping is much smaller when the two processes are switched more frequently, such that several cavities with tapers $< 5^\circ$ have been produced with scallops smaller than $1\ \mu\text{m}$ [74]. This means that the taper scalloping is less of a concern for the manufacturing of a master tool. However, it will also be noted from Figure 3.41 that a further feature of the process is that, the mask is considerably undercut by the isotropic etching process, and although this is a feature that is more pronounced in larger tapered structures it will cause mechanical locking during de-embossing [74].

A similar method was used by another set of researchers [76], this technique used both anisotropic and isotropic etching, but did not use them in alternating steps. Rather, the authors etched a much deeper cavity, and then used an isotropic etch to create a taper. The aim was to break the process down into two stages and therefore achieve a high etch rate without sacrificing taper control. Thus the cavity would be etched to a depth using the Bosch process and then finished off using an isotropic etch stage.

The process produced cavities that were up to $340\ \mu\text{m}$ deep and had tapers ranging from 13° to 4° . However Figure 3.42 illustrates that process control was difficult to obtain by this method, and shows the cavity that was produced with only a taper on the upper part of its wall. This type of tapering is caused by the neutral fluorine radicals being present in much higher concentration towards the top of the cavity compared to the bottom.

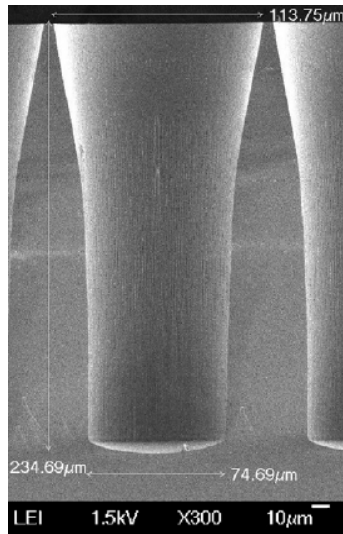


Figure 3.42 An array of cavities produced by the two stage process that is only tapered towards the upper half [76]

A further method for tailoring the side wall profile was developed by a third group of researchers [69, 71]. The process did not use an isotropic and an anisotropic etch as discussed before but rather, the authors decided to modify the original Bosch process. They decided to control the taper by varying the ratio of the passivation and etching cycles. Unfortunately, the typical process time for each stage of the Bosch process is very short (~ 3 s passivate, ~ 5 s etch), providing little scope for controlling the taper. Therefore, the cycle time for each stage was increased to ~ 30 s passivate, ~ 60 s etch, which can potentially result in larger scalloping. However, an additional modification was made to the process by increasing the ion energy as the etch progressed. This modification resulted in a much smoother sidewall than was anticipated, and had a peak to valley height of 0.25 µm. A third modification was made to the conventional process, whereby a ‘pause’ was introduced between each etch and passivate phase. This pause avoided a mixed gas state whilst the etchant and passivation gases were exchanged. By avoiding this mixed state, additional polymerisation on the silicon was reduced [69, 71] and the anisotropy and etch rate were improved. The structure produced was an array of 500 µm wide squares with a shallow

depth of 45 μm and a uniform taper of 5°. This structure is shown in Figure 3.43 and was subsequently replicated.

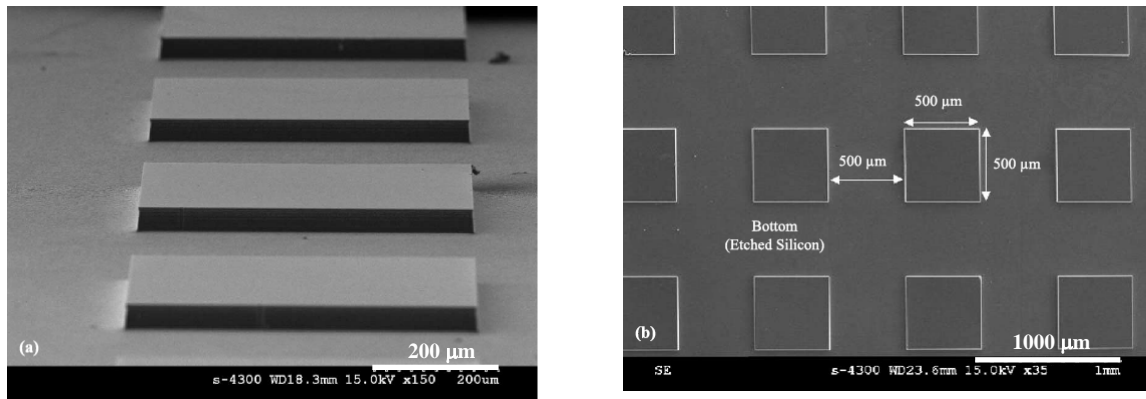


Figure 3.43 SEM images showing the array of blocks produced by the modified Bosch process: (a) tilted and (b) from above [70]

The conventional way of controlling the taper angle of a cavity is by controlling the ratio of the passivation to etch. This can be done by controlling the cycle time of both the etch and passivate cycles, as in the modified Bosch process [68, 70, 71], or it can be achieved by adjusting the flow rates of the two gases [68]. Adjusting the flow rate is a more precise method than just using the cycle time because the cycle time can only be adjusted in integers [68].

A fourth set of researchers [68] investigated both, cycle time and flow rate (of C_4F_8) as a method of increasing the thickness of the passivating layer. The passivating layer becomes thick when either the flow rate or the cycle times are relatively large. If the polymer thickness becomes a significant proportion of the trench width, it was found that the ion flux at the base of the trench is reduced. Therefore, a smaller amount of the passivating polymer is removed from the base of the trench at each cycle, and the trench narrows. This effect is obviously

dependent on the trench width, since the polymer thickness will quickly become more significant with narrower trenches [68].

When the polymer is thin, and the ratio favours etching, the trenches will widen. However, at particularly low passivation flow rates, or cycle times, the polymer is too thin and is etched by the off-incident ions. The sidewalls are therefore no longer protected from the fluorine radicals and are etched, causing the sidewalls to bow [68].

The taper of the trench can be made to be either positive, i.e. the funnel or trench narrows, or negative, i.e. a dovetail or trench that widens. However, the wall angle is influenced by not just the ratio of etch to passivate cycles, but by other parameters as well. In the positive taper case, the effect that the polymer thickness has on the wall angle is affected by the width of the cavity, and it is the relative thickness of the polymer that influences the ion flux and therefore taper angle. In the negative case, the widening of the trench is influenced by the etching of the trench sidewalls. This is not only affected by the polymer thickness but also by the ion angular distribution that has its own contributing factors [68].

The obtained taper angles plotted against flow rate and cycle time are shown in Figure 3.44 and Figure 3.45 respectively and are for 50 μm trenches. The flow rate curve used a passivation time of 10 s and the cycle time curve used a flow rate of 60 sccm. The taper can be calculated by subtracting 90° from the wall angle, such that value below the 90° line is negative and the trench will have a dovetail shape. In Figure 3.44 the wall angle is the curve increasing from 82° to 90.5° with increasing C_4F_8 flow rate. The figure shows a much broader taper range on the negative taper side of the curve. The taper decreases rapidly from

below 10 sccm to 30 sccm, but at values greater than this the curve begins to reach a plateau. At flow rates of less than 10 sccm bowing of the sidewalls was observed.

By varying the flow rate the required taper range can be achieved over a range of 10 sccm and 30 sccm, but the range is relatively narrow and does not vary linearly, requiring careful control of the flow rate.

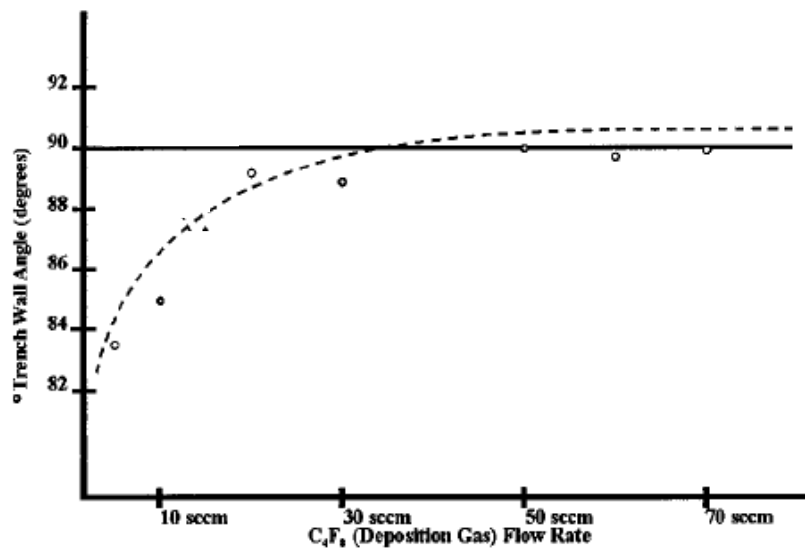


Figure 3.44 Trench wall angle as a function of C₄F₈ flow rate in a modified Bosch process [68]

In Figure 3.45 the taper varies linearly, and the wall angle from 88.5° to 90.5°, which is a much smaller range than in Figure 3.44. Therefore, it is easier to obtain different taper angles by varying the cycle time, but fewer angles are possible. The authors suggested that the cycle time method could be used to coarsely find the correct conditions and then the flow rate could be adjusted to ‘fine tune’ the taper.

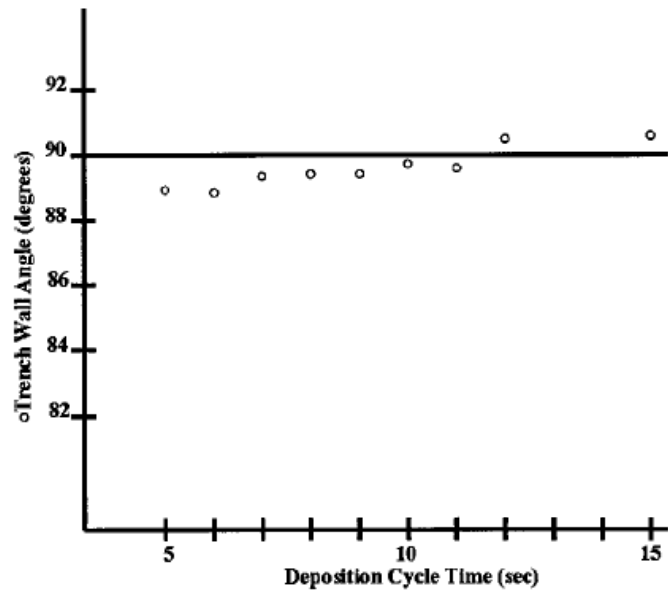


Figure 3.45 Trench wall angle as a function of cycle time in a modified Bosch process [68]

The Bosch process is capable of producing very small feature sized, very high aspect ratio structures, that have a similar geometry to what is required for the master tool. Many researchers have investigated taper control using a variety of approaches, indicating that the process is feasible for this work. The surface roughness is rarely discussed but a surface finish of 0.01 to 0.07 μm [79] has been achieved. There has been sufficient development to suggest that a feasibility study should be carried out and this is discussed further in section 7.2.

3.2.6 Electroforming

Electroforming can be used to produce a metallised part from a non-metallic structure. A negative structure in a polymer, or silicon pre-form, can be turned into an array of pillars made from either, copper, gold, nickel or a nickel based alloy [81].

For electroforming to begin, the non-metallic mould is required to be made conductive and is typically made so by coating with a seed layer. The process takes place in a bath, which contains an electrolyte solution and an anode connected to a d.c. power supply. When the pre-form is also connected to the power supply it acts as the cathode such that the metal ions in the electrolyte are reduced and are deposited onto the seed layer [81-86]. A typical electrolyte is nickel sulfamate ($\text{Ni}(\text{SO}_3\text{NH}_2)_2$) [82, 83, 84-86] and is used in conjunction with a sulphur-depolarized nickel anode [84, 86]. This chemistry is often used because it has a rapid deposition rate [85] and can produce a replica with low stress and distortion [82, 84, 85]. The electrolyte solution also contains a boric acid (H_3BO_3) buffer, [83, 84-86], surfactants to improve the wetting of the pre-form [83], and nickel chloride to maintain the dissolution of the electrode [87].

The important operating parameters used in electroforming include processing time [82, 83], operating temperature [81-83, 86], current density [82, 84, 86] and pH [81-84, 86]. An increase in the temperature results in a faster rate of diffusion and an increase in the deposition rate throughout the whole structure. An increase in the current density can also increase the deposition rate, however this can exaggerate local fluctuations, such that uneven film growth and coarse grains can occur [81, 83, 84, 86]. Furthermore, hydrogen is evolved during deposition, and, if the reaction rate is too fast, hydrogen bubbles can become trapped bubbles within the metal structure [84]. Therefore, the bath temperature is kept constant throughout plating, and is typically kept just above 50°C [81, 83-85]. The pH is a measure of the concentration of hydrogen ion in solution, and it is therefore important to maintain it at a constant value. The buffer solution is used to maintain the pH to one decimal place, which can have values ranging from pH 3.0 to 5.0 [81, 83, 84, 86].

A large advantage of electroforming is that the process is not limited by complex geometry, and is a true 3D process [82]. However, in practice the process has difficulty replicating some structures with deep or narrow cavities [81, 82]. Blind holes with aspect ratios up to 5 [84] can be fully filled by appropriately controlling the parameters of the process. The problem occurs in deep, or narrow, holes because the metal is deposited at different rates at the top and bottom of the hole [81, 83, 84-86]. Deposition occurs slowly at the base, because the electrolyte finds it difficult to penetrate into the cavity and replenish the depleted metal ions [85, 86]. At the entrance to the cavity, deposition occurs more rapidly because the ions can be replenished such that, the local current density is higher. The local fluctuations in current density can be reduced by reducing the voltage, and then compensating for the reduction in deposition rate by increasing the operating temperature [86]. However, for holes with aspect ratios greater than 5, this becomes difficult and an alternative approach is needed [83, 84, 85].

The simplest way of electroforming into deep, or narrow, cavities is to prevent deposition around the cavity entrance, or on the cavity walls. By preventing deposition here, the chance of the metal film growing over the entrance to the cavity is greatly reduced. It is, therefore, desirable for the nickel to grow from the base of the cavity upwards, and this can be achieved by only seeding the nickel at the base of the hole. A pre-form with through holes should be used that can then be attached to a conductive plate [83, 84, 85]. Thus, deposition can only occur at the bottom of the hole, and the nickel must be deposited from the base upwards.

3.2.7 Selection of Master Tool Fabrication Technique

The requirement of the micro fabrication process to produce very small, very high aspect ratio features can be met by UV lithography, laser ablation and the Bosch process. Micro EDM offers the ability to directly produce a metallic master tool, but cannot produce features smaller than 20 μm , and is therefore not capable of producing a master tool for a 30 MHz piezocomposite.

The control of the cavity taper is a particularly important parameter for this work since the project aims to identify the most suitable taper for both hot embossing and piezocomposite performance. It will require the development of a micro fabrication process that is capable of producing master tools that vary only by the pillar taper. UV lithography has not seen sufficient development into the control of this taper in high aspect ratio structures, whereas greater progress has been made in laser ablation and significantly more in the Bosch process. For both processes a target surface finish of $R_a < 0.09 \mu\text{m}$ is demanding. The Bosch process has produced surface finishes of 0.05 μm but a feasibility study of both processes is required. The feasibility studies and the master tool fabrication are discussed in section 7.

Neither the Bosch process nor laser ablation are available at The School of Metallurgy and Materials, Birmingham, such that several collaborations were arranged. A collaboration was developed with the Scottish Microelectronics Centre (SMC), Edinburgh, for the etching of the silicon, whilst a feasibility study was also carried out by the UK Laser Machining Centre, Bangor. Both laser ablation and the Bosch process produce non metallic structures such that electroforming is required. Therefore a collaboration with the Micro-engineering and Nanotechnology Research Group, Birmingham was also developed.

3.3 Chapter References

- [1] A. Abrar et al “1-3 Connectivity Piezoelectric Ceramic-Polymer Composite Transducers made with Viscous Polymer Processing for High Frequency Ultrasound” *Ultrasonics* 42 (2004) 479-484
- [2] W. D. Callister “Materials Science and Engineering: an Introduction 5th edition” *John Wiley and Sons, New York* (2000) ISBN 0-471-32013-7
- [3] A-C Liou and R-H Chen “Injection molding of polymer micro- and sub-micron structures with high aspect ratios” *International journal of Advanced Manufacturing Technologies* 28 (2006) 1097-1103
- [4] O Rotting et al “Polymer Microfabrication Technologies” *Microsystems Technologies* 8 (2002) 32-36
- [5] M. Hecke, W.K. Schomburg “Review on Micro Moulding of Thermoplastic Polymers” *Journal of Micromechanics and Microengineering* 14 (2004) R1-R14
- [6] N. S. Ong, H. Zhang and W H Woo “Plastic Injection Moulding of High Aspect Ratio Micro Rods” *Materials and Manufacturing Processes* 21 (2006) 824-831
- [7] B. Sha et al “Investigation of Micro-Injection Moulding: Factors Affecting the Replication Quality” *Journal of Materials Processing Technology* 183 (2007) 284-296
- [8] G. Fu et al “A varotherm mold for micro metal injection moulding” *Microsystem Technology* 11 (2005) 1267-1271
- [9] M. J. Madou “Fundamentals of Microfabrication: The Science of Miniaturisation Second Edition” *CRC Press London* (2002) ISBN-13: 978-0849308260
- [10] W Pflöging et al “Rapid fabrication and replication of metal, ceramic and plastic moulds inserts for application in microsystem technologies” *Proceedings of the Institute of Mechanical Engineers, Part C: Journal of Mechanical Engineering Science* 217 (2003) 53-63
- [11] W. Pflöging et al “Rapid fabrication of microcomponents - UV-laser assisted prototyping, laser micro-machining of mold inserts and replication via photomolding” *Microsystem Technologies* 9 (2002) 67-74
- [12] T. Hanemann et al “Laser micromachining and light induced reaction injection molding as suitable process sequence for the rapid fabrication of Microcomponents” *Microsystem Technologies* 7(2002) 209-214
- [13] H Becker, U Heim “Hot Embossing as a Method for the Fabrication of Polymer High Aspect Ratio Structures” *Sensors and Actuators* 83 (2000) 130-135
- [14] Y-J Juang, L J Lee, K W Koelling “Hot Embossing in Microfabrication. Part I: Experimental” *Polymer Engineering and Science* 42 (3) (2002) 539-550

- [15] H. Mekarū et al “Microfabrication by Hot Embossing and Injection Molding at LASTI” *Microsystems Technologies* 10 (2004) 682-688
- [16] M. Worgal et al “Large-Scale Hot Embossing” *Microsystems Technologies* 12 (2005) 110-115
- [17] S-C. Chen “Rapid Mold Temperature Variation for Assisting the Micro Injection of High Aspect Ratio Micro-feature parts Using Induction Heating Technology” *Journal of Micromechanics and Microengineering* 16 (2006) 1783-1791
- [18] U. Wallrabe et al “Micromoulded easy-assembly multi fiber connector: RibCon” *Microsystems Technologies* 8 (2002) 83-87
- [19] V. Piottter et al “Performance and simulation of thermoplastic micro injection moulding” *Microsystem Technologies* 8 (2002) 387-390
- [20] H. Becker, U. Heim “Silicon as a Tool Material for Polymer Hot Embossing” *MEMS '99. The Twelfth IEEE International Conference on Micro Electro Mechanical Systems* (1999) 228-231
- [21] Y. Zhao and T. Cui “Fabrication of High Aspect Ratio Polymer-based Electrostatic Comb Drives using the Hot Embossing Technique” *Journal of Micromechanics and Microengineering* 13 (2003) 430-435
- [22] Jenoptik Mikrotechnik GmbH “Application Aspect ratio 20, depth 155 μm ” *HEX01 Data Sheet* (2005) received 10/03/06 from G. Ungelenk at Jenoptik
- [23] Jenoptik Mikrotechnik GmbH “Application Aspect ratio 5, depth 150 μm ” *HEX01 Data Sheet* (2005) received 10/03/06 from G. Ungelenk at Jenoptik
- [24] Jenoptik Mikrotechnik GmbH *Example Images Sent via Email* (2005) received 10/03/06 from G. Ungelenk at Jenoptik
- [25] J. Narasimhan and I. Papautsky “Polymer Embossing Tools for Rapid Prototyping of Plastic Microfluidic Devices” *Journal of Micromechanics and Microengineering* 14 (2004) 96-103
- [26] T. Koerner, et al “Epoxy Resins as Stamps for hot embossing of Microstructures and fluidic Channels” *Sensors and Actuators B* 107 (2005) 632-639
- [27] K. Roberts et al “The Fabrication of an Array of Microcavities Utilizing SU-8 Photoresist as an Alternative ‘LIGA’ Technology” *University/Government/Industry Microelectronics Symposium, 1999. Proceedings of the Thirteenth Biennial* 23 (1999) 139 - 141
- [28] X. Shen and L. Lin “Microplastic Lens Array Fabricated by a Hot Intrusion Process” *Journal of Micro electro mechanical Systems* 13 (6) (2004) 1063-1071

- [29] Mekar H.; Yamada T.; S En and Hattori, T. "Microfabrication by Hot Embossing and Injection Molding in LIGA Process" *Digest of Papers. Microprocesses and Nanotechnology 2002 (2002) 192-193*
- [30] D. Zhang "Fabrication of Ceramic Microcomponents" *PhD Thesis, The University of Birmingham (2006)*
- [31] X.-J. Shen et al "Microplastic embossing process: experimental and theoretical characterisations" *Sensors and Actuators: A 97-98 (2002) 428-433*
- [32] L Bowen et al "Injection Molded Fine-Scale Piezoelectric Composite Transducers" *IEEE Ultrasonics Symposium 1 (1993) 499-503*
- [33] D. Powell et al "The Impact of element Taper and Inhomogeneous Material Properties on Ultrasonic Array Performance" *IEEE Symposium 2 (2002) 1161-1166*
- [34] C. Negreira "Lateral Modes and Diffracted Field Behaviour in Non-Periodical 1-3 Piezocomposite Transducers" *Proceedings of 1998 IEEE Ultrasonics Symposium 1 (1998) 641-644*
- [35] R. Steinhausen et al "Finite Element Analysis of the Thickness Mode Resonance of Piezoelectric 1-3 Fibre Composite" *2004 IEEE International Ultrasonics, Ferroelectrics and Frequency Control Joint 50th Anniversary Conference (2004) 1678-1681*
- [36] M. Despont "High aspect ratio, ultrathick, negative-tone near UV photoresist for MEMS applications" *Proceedings of the 10th Annual International Workshop on Micro Electro Mechanical Systems (1997) 518-522*
- [37] C-H. Lin et al "A new fabrication process for ultra-thick microfluidic microstructures utilizing SU-8 photoresist" *Journal of Micromechanics and Microengineering 12 (2002) 590-597*
- [38] M. C. Peterman et al "Building thick photoresist structures from the bottom up" *Journal of Micromechanics and Microengineering 13 (2003) 380-382*
- [39] J. Liu et al "Process research of high aspect ratio microstructure using SU-8 resist" *Microsystem Technologies 10 (2004) 265-268*
- [40] K. Jang et al "SU-8 Ka-band filter and its microfabrication" *Journal of Micromechanics and Microengineering 15 (2005) 1522-1526*
- [41] Y-J Chang, K. Mohseni, V. M. Bright "Fabrication of tapered SU-8 structure and effect of sidewall angle for variable focus microlens using EWOD" *Sensors and Actuators A 136 (2007) 546 -553*

- [42] Z. Zhu, X. Wei and K. Jiang “A net-shape fabrication process of alumina micro-components using a soft lithography technique” *Journal of Micromechanics and Microengineering* 17 (2007) 193-198
- [43] C. H. lee et al “Design and Fabrication of a micro Wankel engine using MEMS technology” *Microelectronic Engineering* 73-74 (2004) 529-534
- [44] A. Schneider et al “Comparison of PMMA and SU-8 resists moulds for embossing of PZT to produce high aspect ratio microstructures using LIGA process” *Microsystem technologies* 8 (2002) 88-92
- [45] K. Y. Lee et al “Micromachinig applications of a high resolution ultrathick photoresist” *Journal of Vacuum Science and Technology B* 13 (6) (1995) 3012-3016
- [46] I-H. Song, Y. Jin, P. K. Ajmera “Fabrication of a polymeric tapered HARMs array utilizing a low-cost nickel electroplated mold insert” *Microsystems Technologies* 13 (2007) 287-291
- [47] P. M. Dentinger et al “High aspect ratio patterning with a proximity ultraviolet source” *Microelectronic Engineering* 61-62 (2002) 1001-1007
- [48] C. Fu and H, Huang “Different methods for the fabrication of UV-LIGA molds using SU-8 with tapered de-molding angles” *Microsystems Technologies* 13 (2007) 293-398
- [49] C-H Ho et al “Ultrathick SU-8 mold formation and removal, and its application to the fabrication of LIGA-like micromotors with embedded roots” *Sensors and Actuators A* 102 (2002) 130-138
- [50] C. H. Lee, K. Jiang, G. J. Davies “Sidewall roughness characterization and comparison between silicon and SU-8 microcomponents” *Materials Characterization* 58 (2007) 603-609
- [51] W. Dai and W. Wang “Selective metallization of Cured SU-8 microstructures using electroless plating method” *Sensors and Actuators A* 135 (2007) 300-307
- [52] M. B. Chan-Park et al “fabrication of large SU-8 mold with high aspect ratio microchannels by UV exposure dose reduction” *Sensors and Actuators* 101 (2004) 175-182
- [53] Y-S Liao and Y-T Chen “Precision fabrication of an arrayed micro metal probe by the laser-LIGA process” *Journal of Micromechanics and Microengineering* 15 (2005) 2433-2440
- [54] C-R Yang et al “Photoablation characteristics of novel polyimides synthesized for high aspect ratio excimer laser LIGA process” *Journal of Micromechanics and Microengineering* 14 (2004) 480-489
- [55] Y. Zhang et al “High Aspect ratio micromaching of polymers with an ultrafast laser” *Applied Surface Science* 186 (2002) 345-351

- [56] A. S. Holmes “Laser processes for MEMS manufacture” *2nd International Symposium on Laser Precision Microfabrication RIKEN review 4* (2002) 63-69
- [57] G. L. Benavides et al “High aspect ratio meso-scale parts enabled by wire micro EDM” *Microsystems Technologies 8* (2002) 395-401
- [58] W. Pfleging et al “Laser micromachining of metallic mold inserts for replication techniques” *Material Research Society 617* (2000) J5.5.1 – J5.5.6
- [59] H.S. Lim et al “A study on the machining of high aspect ratio micro-structures using micro-EDM” *Journal of materials Processing Technology 140* (2003) 318-325
- [60] Y-S Liao, S-T Chen and C-S Lin “Development of a high precision tabletop versatile CNC wire EDM for making intricate micro parts” *Journal of Micromechanics and Microengineering 15* (2005) 245-253
- [61] Y-S Liao et al “Fabrication of high aspect ratio microstructure arrays by micro reverse wire-EDM” *Journal of Micromechanics and Microengineering 15* (2005) 1547-1555
- [62] C. Diver et al “Micro-EDM drilling of tapered holes for industrial applications” *Journal of Materials Processing Technology 149* (2004) 296-303
- [63] A. Schoth, R. Forster, W. Menz “Micro wire EDM for high aspect ratio 3D microstructuring of ceramics and metals” *Microsystems Technologies 11* (2005) 250-253
- [64] J-B Li, K Jiang and G J Davies “Novel die-sinking micro-electro discharge machining process using microelectromechanical systems technology” *Proceedings of the Institute of Mechanical Engineers Part C: Mechanical Engineering Science 220* (2006) 1481-1487
- [65] N. Ravi and H. Huang “Fabrication of symmetrical section microfeatures using the electro-discharge machining block electrode method” *Journal of Micromechanics and Microengineering 12* (2002) 905-910
- [66] J-C Hung et al “Micro-hole machining using micro-EDM combined with electropolishing” *Journal of Micromechanics and Microengineering 16* (2006) 1480-1486
- [67] D J Kim et al “Straight hole micro EDM with a cylindrical tool using variable capacitance method accompanied by ultrasonic vibration” *Journal of Micromechanical and Microengineering 16* (2006) 1092-1097
- [68] C. J. Cragie et al “Polymer thickness effects on Bosch etch Profiles” *Journal of Vacuum Science Technology B 20* (6) (2002) 2229-2232
- [69] S-B. Jo et al “Characterization of a modified Bosch-type process for silicon mold fabrication” *Journal of Vacuum Science Technology A 23*(4) (2005) 905-910
- [70] A. A. Ayon “Characterization of a Time Multiplexed Inductively Coupled Plasma Etcher” *Journal of the Electrochemical Society 146* (1) (1999) 339-349

- [71] S-B Jo et al “Fabrication and Surface treatment of silicon mold for polymer microarray” *Surface and Coatings Technology* 188-189 (2004) 452-458
- [72] F. Laermer and A. Scholp “Method of Anisotropically Etching Silicon” *US patent number 5,501,893* (1996)
- [73] F. Laermer et al “Bosch Deep Silicon Etching: Improving Uniformity and Etch Rate for Advanced Applications” *Proceedings of the IEEE Micro Electro Mechanical Systems (MEMS)* (1999) 211-216
- [74] N. Roxhed, P. Griss, G. Stemme “A method for tapered deep reactive ion etching using a modified Bosch process” *Journal of Micromechanics and Microengineering* 17 (2007) 1087-1092
- [75] A. A. Ayon et al “Influence of Coil Power on the etching Characteristics in a High Density Plasma Etcher” *Journal of the Electrochemical Society* 146 (7) (1999) 2730-2736
- [76] R. Nagarajan et al “Development of dual-etch via tapering process for through-silicon interconnection” *Sensors and Actuators A* 139 (2007) 323-329
- [77] Scottish Microelectronics Centre “Example images” *received February 2007*
- [78] A. A Ayon “Deep reactive ion etching: a promising technology for micro- and nano satellites” *Smart Materials Structures* 10 (2001) 1135-1144
- [79] Scottish Microelectronics Centre “Example images from Smart X-ray Optics” *received February 2007*
- [80] A.A Ayon, X. Zhang, R. Khanna “Anisotropic silicon trench 300-500 μm deep employing time multiplexed deep etching (TMDE)” *Sensors and Actuators A* 91 (2001) 381-385
- [81] R. Ruprecht et al “Various replication techniques for manufacturing three-dimensional metal microstructures” *Microsystems Technologies* 4 (1997) 28-31
- [82] S-J Lee “electroforming of metallic bipolar plates with micro-featured flow field” *Journal of Power Sources* 145 (2005) 369-475
- [83] R-H Chen, C-C Chang and C-M Cheng “Fabricating a micromould insert using a novel process” *International Journal of Advanced technology* 25 (2005) 678-684
- [84] J. Lorenz “Electroplating of micro-patterned tools via replication of silicone rubber forms” *Microsystems Technology* 12 (2006) 870-876
- [85] N. Holstein “Metallic microstructures by electroforming from conducting polymer templates” *Microsystems Technologies* 11 (2005) 179-185

[86] A. Thies et al “Chemical deposition of metals for the formation of microstructures: an alternative method to galvanofforming” *Electrochimica Acta* 42 20-22 (1997) 3033-3040

[87] G. A. DiBari “Nickel Plating” *Metal Finishing* 97 1 (1990) 289-290

Chapter 4

Aims and Objectives

4 Project Aims, Objectives and Approach

1-3 Piezocomposites offer improved performance over monolithic materials for use as piezoelectric elements for medical ultrasound applications. They can achieve this by providing better acoustic, and electrical impedance matching, and an increased conversion of electrical energy to mechanical energy. The drive to image smaller and smaller structures within the body means that piezocomposites must be operated at higher frequencies, and must therefore be fabricated with smaller features and higher aspect ratios than the industry standard can achieve.

Unfortunately the industry standard, dice and fill, is limited to fabricating pillars smaller than 100 μm and is therefore not suitable for fabricating piezocomposites with operating frequencies greater than 10 MHz. As has been presented in Table 2.2, a 10 MHz piezocomposite typically has pillar widths of $\sim 70 \mu\text{m}$, kerfs $\sim 30 \mu\text{m}$ and aspect ratios before lapping of 9.

Other piezocomposite fabrication techniques have been developed, but they have struggled to move out of the laboratory. Viscous polymer embossing offers an alternative fabrication route for piezocomposites by pressing ceramic dough into a PMMA mould, which is then dissolved before sintering. However, the loss of the mould per piezocomposite can make the process expensive and therefore requires the moulds to be replicated from a master tool to reduce the cost.

Hot embossing has been identified as a route to replicate these moulds from a specifically designed master tool. This designed tool will consider the requirements of the master tool

fabrication technique, the replication process and the performance of the piezocomposite. It has been identified from the literature review that if piezocomposites are to achieve higher frequencies in a process that is able to move out of the laboratory, then mesh structures with a smaller feature size, and a higher aspect ratio must be achieved by hot embossing. The addition of a taper of just 2° is known to improve de-embossing of the master tool significantly, and preliminary modelling by other authors has suggested that a taper of up to 5° can be tolerated by the piezocomposite. However, this tolerance is dependent on the array geometry, piezoceramic volume fraction, pillar shape, and pillar aspect ratio; such that the acceptable taper will depend on the final piezocomposite design. Furthermore, the de-embossing process is challenging to model, and it is necessary to carry out experiments that will determine the effect of the taper size on the de-embossing force.

The Bosch process and laser ablation have been selected as fabrication routes for the master tool. The aim is to develop a procedure to produce several master tools that are identical except for the pillar taper. This will allow the affect of taper angle on de-embossing and on the performance of the piezocomposite to be assessed. To make the master tools more achievable the aim will be to start with lower frequency piezocomposites, in the 5 to 10 MHz range that have a larger feature size and lower aspect ratio. Once this has been achieved, it will provide further knowledge both on hot embossing and the master tool fabrication process, and will provide a 'solid base' to produce more demanding, higher frequency piezocomposites.

The expertise and equipment for laser ablation and silicon etching are not available within The School of Metallurgy and Materials, Birmingham, such that several collaborations have

been arranged. The UK Laser Machining Centre (UK-LMC) will carry out feasibility trials with an excimer laser; investigations into the Bosch process will be carried out at the SMC; and electroforming will be achieved at the Micro-engineering and Nano-technology Research Group at the University of Birmingham.

The hot embossing of the polymer moulds, the VP embossing, and the piezocomposite fabrication will be carried out at the School of Metallurgy and Materials. However, a hot embossing rig is not available at The University of Birmingham, such that as part of the project it is necessary to modify a mechanical testing machine to carry out the micro replication. The micro fabrication review has indicated that the development of the master tool fabrication route may be difficult, particularly with tapered pillars. Therefore a master tool made using the LIGA process, which has parallel sides, has been acquired. This will allow the independent development and understanding of the hot embossing rig, and the characterisation of the hot embossed moulds, VP embossed bristle blocks and the functioning piezocomposite, whilst the master tool fabrication route is investigated.

The key milestones in the project are:

- 1) The design of master tool, considering all the process stages.
- 2) The fabrication of the designed pre-form and the electroformed master tool.
- 3) The specification, design and construction of the hot embossing rig.
- 4) The investigation of the hot embossing process leading to an understanding and optimisation of the process parameters, such that 1-3 piezocomposite moulds can be made.
- 5) The VP embossing of 1-3 piezocomposites from the hot embossed moulds

- 6) The characterisation of the whole process, from the master tool to the mould, from the mould to the bristle block, and from the bristle block to the performance of the piezocomposite
- 7) Identification of the most appropriate taper for hot embossing and piezocomposite performance, which will enable mesh structures to be produced that have an improved aspect ratio and feature size compared to the literature.
- 8) The demonstration of 1-3 piezocomposites whose pillar width is less than 100 μm , which cannot be made by the industry standard, dice and fill.

Chapter 5

Experimental and Analytical Procedures

5 Experimental and Analytical Procedures

This chapter outlines the methods and procedures used for hot embossing and VP embossing. It is divided into three subsections that discuss the procedures and techniques for the familiarisation of the hot embossing rig, the moulding of the piezocomposites, and the characterisation of the whole process.

5.1 Hot Embossing Rig Familiarisation

The aim of this section of work was to familiarise the author with the hot embossing rig after it had been fabricated. The design and fabrication of the rig is presented in section 8.1, and the effect of adjusting each major parameter on the process, and the replicated mould is discussed in section 8.2.

The success of the embossing was measured in three ways: the depth of penetration of the polymer between the pillars; the ease at which the master tool could be removed; and the severity of the defects seen on the embossing. The hot embossing parameters that were adjusted were: the temperature of the master tool and the substrate; the load applied to the master tool during embossing; and the length of time that the load was applied for. The information gathered in this process has led to the selection of the appropriate parameters for replicating PMMA moulds. These moulds can then be used to produce 1-3 piezocomposites by VP embossing. The procedure for replicating the moulds and the piezocomposites is presented in sections 5.2 and 5.3, and the results are discussed in section 9.

5.1.1 The Hot Embossing Process

The hot embossing cycle is illustrated by Figure 5.1, where a glassy polymer is heated and formed around a shape under heat and pressure. Here, the cycle is shown in terms of its main parameters, temperature, force, displacement and time. The polymer substrate and the master tool are heated to the embossing temperature which is just above the glass transition temperature of the polymer. Once at this temperature the master tool is slowly pressed into the polymer substrate, at a rate known as the embossing speed, and is then held at a constant force called the embossing load. During this hold the polymer flows around the features of the master tool, and the master tool moves further into the polymer substrate to maintain the pressure. After the load hold, the master tool and the polymer substrate are cooled at a constant rate to below the glass transition temperature of the polymer, before being separated from each other [1-3]. This phase has been called de-embossing to avoid confusion with the demoulding phase of VP embossing. Two parameters that are important during hot embossing are the de-embossing temperature and, the speed at which the master tool retracts from the substrate, the de-embossing speed.

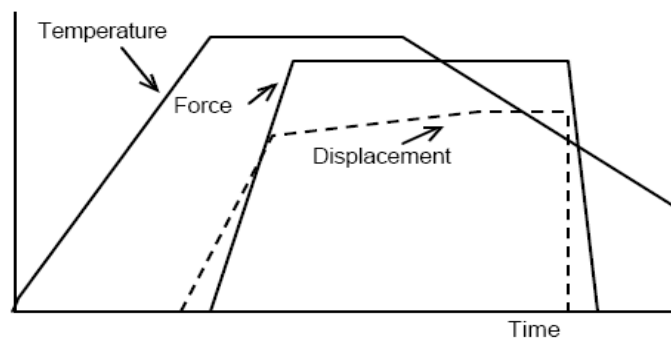


Figure 5.1 The hot embossing process illustrated by its force, temperature, and displacement profiles [4]. The platens are heated, pressed together and held under constant load, whilst the polymer deforms, before the platens are cooled and then separated.

5.1.2 Procedure for Investigating the Main Parameters

To study the effect of changing the main parameters, the master tool temperature, substrate temperature, embossing load and dwell time were each varied one at a time. The parameters that were not the subject of the investigation at the time were kept constant at approximately the centre of their ranges. A summary of the parameters used in the investigation is shown in Table 5.1. An example would be when the load was investigated, it was varied in 0.1 kN increments from 1 to 1.9 kN, the master tool temperature was kept at 145°C, the substrate temperature was 115°C, and the dwell time was kept at 6 min. Other parameters that were not investigated had their values chosen nominally, because it was considered that the other parameters required greater focus. However, if required, the hot embossing rig had the facility to investigate each of them. These process parameters were: the embossing speed (1 mm / min), the de-embossing speed (1 mm / min) and the heating and cooling rates (0.42°C / s). The de-embossing temperature was also investigated, but used a slightly different method for characterisation and has been included in Table 5.1 for completeness. The method used to investigate the de-embossing temperature is discussed later in section 5.1.3.4.

Table 5.1 A summary of the parameters used to familiarise the author with the fabricated hot embossing rig. The table includes the increments that each parameter was varied in, the investigated range, and the values of the parameters that were used when the parameter was not the subject of the investigation.

Parameter	Investigated Range	Increments	Parameter Value When Not Investigated
Master Tool Temperature (°C)	130 – 155	5	145
Substrate Temperature (°C)	110-130 or Constant	5	Constant
Embossing Load (kN)	1 – 1.9	0.1	1.25
Dwell Time	10 s – 12 min	1.5 min	6 min
De-embossing Temperature (°C)	60 – 90	1 (between 65-80) 5 (60-65, 80-90)	63

5.1.2.1 Isothermal vs. Non-isothermal Hot Embossing

The literature suggests that hot embossing should be carried out with a temperature range of $T_g + 25^\circ\text{C}$ to $T_g + 40^\circ\text{C}$ [2, 5]. The temperature should be high enough to allow sufficient flow that residual stress is minimised, but cool enough to obtain a stable structure [6]. The PMMA sheet that was used in these experiments was Perspex cast, from Lucite International, Darwen, Lancashire¹ and was 2 mm thick. The T_g of the polymer was estimated to be 105°C , but was later measured using differential scanning calorimetry and was found to be 113°C ². Therefore, the embossing temperatures for investigation should have been 138°C to 153°C but were 130 to 155°C .

Initially, the master tool and the substrate temperature were kept the same, in a process called isothermal hot embossing. The temperature was increased from 130°C to 155°C , in increments of 5°C . But it was found that a large proportion of the load went into deforming the bulk polymer, at its free surface, rather than between the pillars. To overcome this, the substrate temperature was reduced to just above the T_g , whilst the master tool temperature remained similar to the temperatures used in isothermal embossing. This process is known as non-isothermal hot embossing [5] and resulted in localised deformation of the polymer around the master tool, rather than in the bulk, and showed reduced damage during de-embossing.

Non-isothermal embossing was first investigated relatively coarsely, to try and identify approximately the right combination of substrate and master tool temperature. The highest tool temperature was first investigated with the lowest substrate temperature, and then the tool

¹ Bought from Perspex Distribution Ltd., (<http://www.perspex.co.uk/products/cast-acrylic/details>)

² See appendix, section 11.1

temperature was decreased by 5°C, whilst the substrate temperature was increased by 5°C for the next sample. Thus, the investigated temperatures were: 150:110; 145:115; 140:120; 135:125; and 130:130, where the first number represents the temperature, in °C, of the master tool, and the second number is the temperature of the substrate in °C. The results are discussed in detail in section 8.2.2, but a substrate temperature of 115°C was selected for a more thorough investigation of non-isothermal hot embossing.

5.1.3 Characterisation Methods

5.1.3.1 Percentage Mould Fill Method and Errors

The percentage mould fill is a measure of the penetration of the polymer between the pillars. It expresses how close the polymer has come to completely filling the gaps between the master tool pillars, and is illustrated in Figure 5.2. The percentage mould fill can be calculated by the ratio height of the embossed cavities to the maximum possible height, limited by the length of the pillars.

To measure the mould fill the embossed samples were de-embossed, cross-sectioned, mounted in plasticine and measured with a travelling microscope. Care was taken to ensure the sample was vertical, because any tilt would affect the accuracy of the results. In addition to this, the mounting and measuring process was repeated for each sample to try and identify any error from a poorly mounted sample.

The most significant error in the measurement of the cavities is likely to be the microscope because the Vernier scale could only be read to 20 µm. The effect of this error is best

explained using the diagram shown in Figure 5.2 that shows the pillars and substrate during the dwell phase of the hot embossing process.

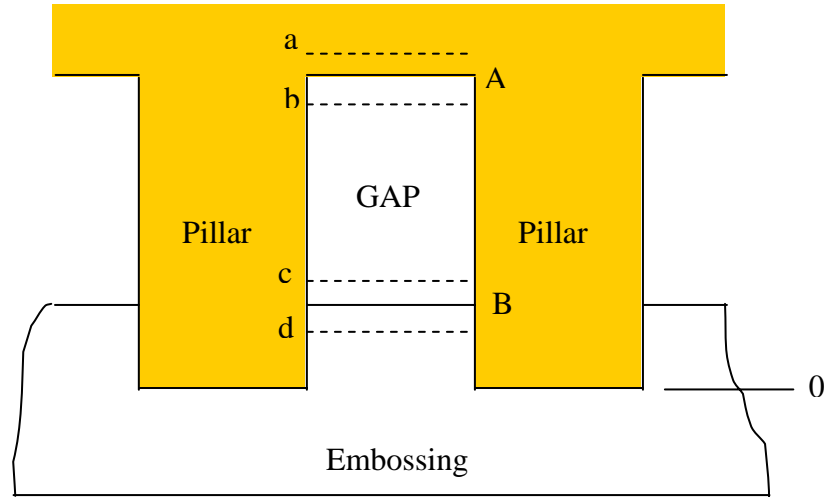


Figure 5.2 An illustration of the percentage mould fill with annotations to help describe the error attributed to the Vernier scale

After a hot embossing cycle the polymer has partly embossed and has flowed between the pillars up to line B. The maximum distance that the polymer could fill the mould to is the base of the pillars shown by line A. When measuring with a travelling microscope, line B could either be 20 μm above or below the central position, at dotted lines c or d. Similarly, line A could actually be at positions a or b. The Percentage mould fill is calculated by:

$$\text{Percentage Mould Fill} = \frac{\text{Height of the Embossed Polymer}}{\text{Height of the Pillars}} \times 100 \quad \text{Equation 5.1}$$

When there is no error:

$$\text{Percentage Mould Fill} = \frac{B - 0}{A - 0} \times 100 = \frac{B}{A} \times 100 \quad \text{Equation 5.2}$$

The lowest value of percentage mould fill will occur when measured position A is actually at position a, and when B is in position d. At their maximum error these positions are 20 µm away from the measured point, such that:

$$\frac{d}{a} \times 100 = \frac{B - 20}{A + 20} \times 100 \quad \text{Equation 5.3}$$

And the highest value of percentage mould fill occurs when A = b, and B = c,

$$\frac{c}{b} \times 100 = \frac{B + 20}{A - 20} \times 100 \quad \text{Equation 5.4}$$

The actual value of the error varies according to the measured value of line B such that the actual error must be calculated for each measurement. For a low percentage mould fill the absolute error is 5%, but for higher mould fill it is 9%.

5.1.3.2 De-embossing Force Method and Error

The force required to remove the master tool from the embossing can be measured using the load cell of the hot embossing rig. The peak load that occurs during de-embossing was used to study the effect that the embossing temperature, embossing load and dwell time would have on the ease of withdrawing the master tool from the embossing.

The master tool is often de-embossed with some degree of damage to the embossing, such that the de-embossing force does not only relate to how easily the master tool can be ‘pulled out’ but also the strength of the polymer embossing; i.e. if de-embossing occurs at low load, but with lots of damage, then this relates to a weaker embossing rather than a low adhesion.

The de-embossing force was measured using an Instron 2525 series, 30kN load cell. This load cell is accurate to either "...0.025% of the rated output of the load cell or 0.25% of the indicated load, whichever is the greater..." [7]. Thus, the load cell is accurate to:

$$30,000 \times 0.025\% = 7.5N$$

Or, taking the maximum measured value of the de-embossing force to be ~500N, the error could be:

$$500 \times 0.25\% = 1.25N$$

Therefore the load cell is accurate to ± 7.5 N. The minimum de-embossing force value is 300 N and represents a maximum percentage error of 2.5%.

5.1.3.3 Severity of Defects Method

Frequently some form of defect is seen in the embossing, but the severity of the defect varies according to the parameters used. There are two types of defect seen on the embossing, which is either an area of damaged cavities, or cracks. The frequency of these defects means that they deserve some consideration. Within each investigation the defects were arranged in order of their severity using a chart with the x-axis showing the severity of the cavity damage and the y-axis showing the severity of the cracking. An example of such a chart can be seen on page 219. These charts are rather qualitative and should only be used to observe general trends.

5.1.3.4 Curvature of the Substrate during De-embossing

Whilst the hot embossing procedure was the same, the method of characterising each embossing was not. Adjusting the de-embossing temperature will not affect the penetration of the PMMA between the pillars. However, it was anticipated that it would affect the force required to remove the master tool, and the severity of the defects seen on the embossing. In addition, the higher de-embossing temperature caused the initially flat substrate to deform into a dome shape.

The curvature of the embossing that occurs during de-embossing is shown in Figure 5.3. The amount of deformation can be quantified by measuring the displacement of the underside of the embossing from its initial flat position to its curved position. The embossings were cross-sectioned, mounted in Plasticine, and a line representing the initial position of the substrate was drawn between the undeformed edges of the embossing. A second line marking the largest displacement from the original position was also drawn, and the distance between these two lines was used to quantify the deformation. The largest error in measuring the deflection can be attributed to the width of the pixel used in the photograph, which is 0.05 mm.

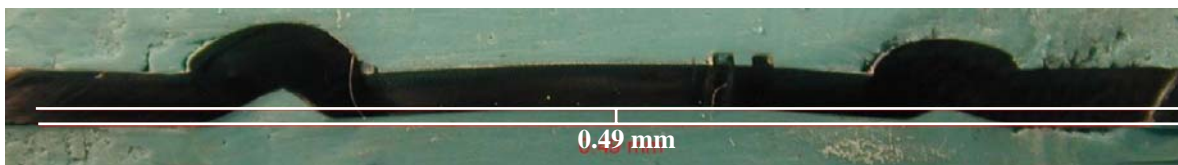


Figure 5.3 An image showing the curvature of the embossing after withdrawal from the master tool. The curvature was quantified by measuring the distance between the original position of the substrate and the final position of the embossing's underside.

5.2 Fabrication of Moulded Piezocomposites

Once the author had familiarised himself with the hot embossing rig it was possible to characterise the whole fabrication process, from the master tool to the fully functioning piezocomposite. This section outlines the procedure used to replicate a PMMA mould using hot embossing, and the fabrication of a piezocomposite by viscous polymer embossing of the mould. The whole process is shown in Figure 5.4 and indicates the process steps, and the point at which the pillar and cavity arrays are characterised. These characterisation methods are presented in section 5.3.

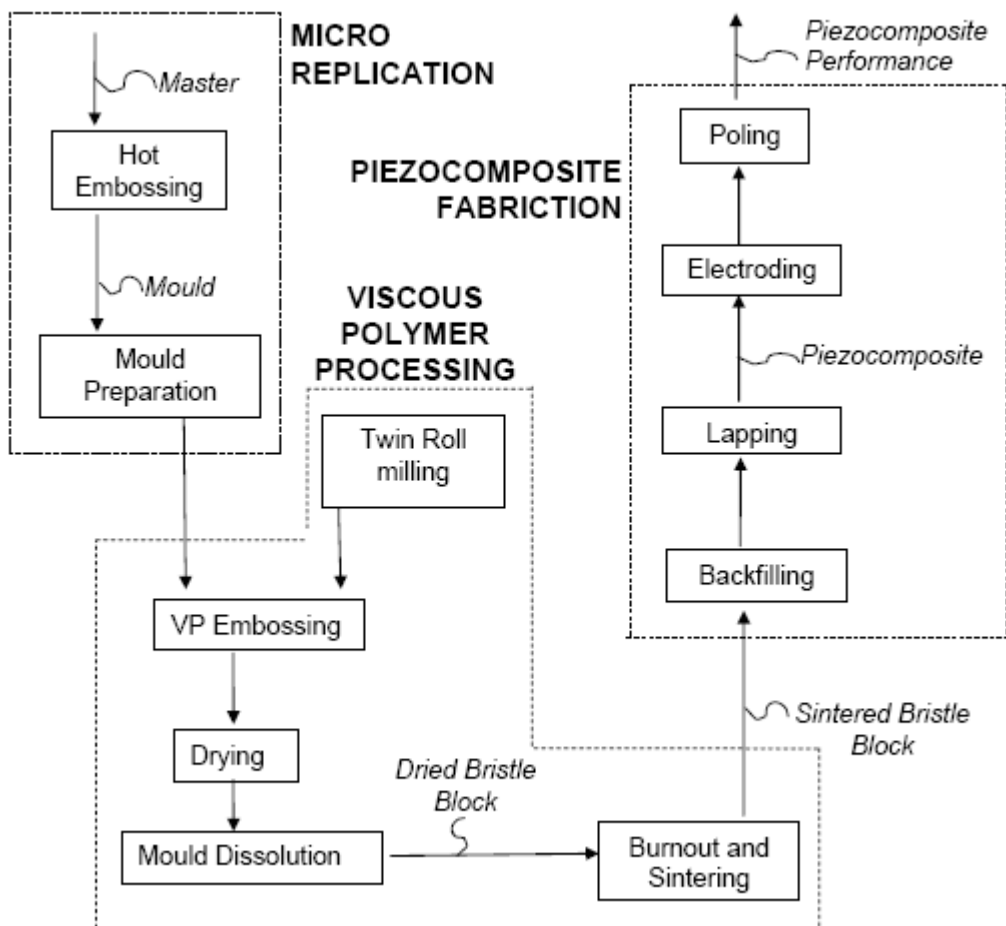


Figure 5.4 A schematic diagram of the process steps for producing piezocomposites from hot embossed moulds, showing the points at which the samples were characterised in the process.

5.2.1 Hot embossing Procedure

The PMMA mould was fabricated using a hot embossing cycle which is shown in Table 5.2. The development of the hot embossing cycle and the reasons for selecting these values is shown in section 8.2. These parameters were derived with the aim of maximising mould fill, whilst minimising the de-embossing force and the severity of the defects.

Table 5.2 The hot embossed parameters used for the replication of the polymer moulds

Stage	Parameter	Value
Embossing	Master Tool Temperature	153°C
	Substrate Temperature	118°C
	Load	1.2 kN
	Dwell	11 min
De-embossing	Master Tool Temperature	66°C
	Substrate Temperature	66°C

The master tool, whose dimensions have been characterised in section 9.1, was mounted onto the platens as discussed in section 8.1.1.4. The platens were then heated to their set temperature before being held at their set point for 3 minutes, to allow the temperature to stabilise. The platens were then pressed together at 1 mm / min to the set load and then held at the set hold time. The platens were cooled, at 0.42 °C / s, to their de-embossing temperature whilst the platens remained in their position. The temperature was held for a further 3 minutes after the set temperature was reached and before retracting the master tool at 1 mm / min.

5.2.2 Mould Preparation Procedure

The hot embossed mould did not show uniform embossing and only a fully embossed area measuring 5 mm x 5 mm, out of the total 10 mm x 10 mm, was achieved. However, this area was more than enough to VP emboss a piezocomposite. Thus, the fully embossed area was

removed using an Accutom-50, precision diamond saw, from Struers, Solihull, and is shown in Figure 5.5.

The thickness of the embossing is 1.66 mm, of which the cavities represent only 0.4 mm. This low ratio of useable depth to surplus depth had two detrimental consequences. The thick mould requires a large amount of ceramic dough to be used during embossing, which leads to a large excess ceramic stock that can cause cracking and deformation in subsequent process stages. Secondly, as shown in Figure 5.6, the large amount of swelling that occurs in such a thick piece of polymer destroys the pillars, and shows little sign of full dissolution ...*(Censored for commercial reasons...)*

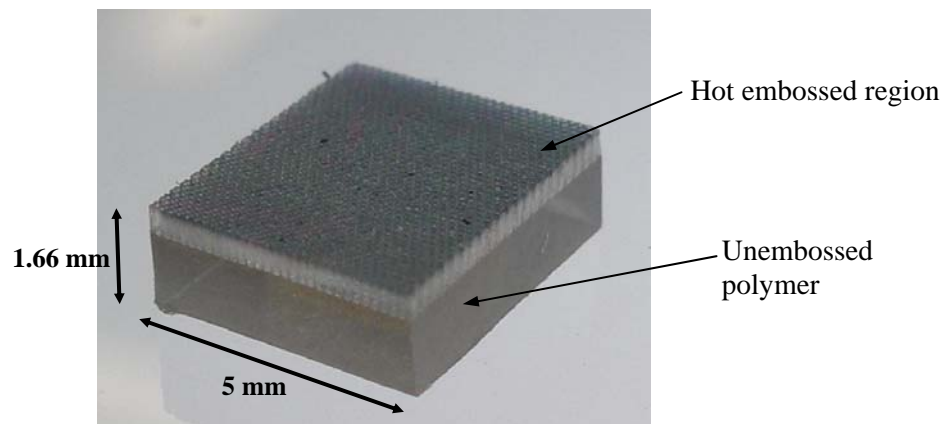


Figure 5.5 The polymer mould before lapping, showing the large proportion of unembossed polymer that needed removing

The mould was reduced down to $\sim 500 \mu\text{m}$ by lapping which is discussed in more detail in section 5.2.8. The mould was lapped only to make dissolution easier, and a thin section remained at the base of the mould, such that the holes remained blind. There was no need for the holes to be through-holes as the VPP dough filled the holes without trapping air.



Figure 5.6 An example of an undissolved thick mould after ...(*Censored for commercial reasons*)...

5.2.3 Twin Roll Milling

A sheet of PZT based VPP dough was produced by twin roll milling. The process allows a high viscosity dough to be produced that is macro defect free and has a high green strength. The twin roll mill, Winkworth Machinery, UK, uses two rollers that counter rotate at different speeds to generate a high shear stress that breaks down agglomerates in the ceramic powder and reduces the size of the defects in the sintered ceramic. A typical composition of the VPP dough is shown in Table 5.3, along with the function of each constituent.

Table 5.3 A typical composition of the VPP dough including the supplier and the function of the constituent

(*Censored for commercial reasons*)

5.2.4 VP Embossing

VP embossing was carried out in a 13 mm standard die from Specac, Kent. Circles were cut, to fit the die, from a 1 mm thick sheet of VPP dough. The mould was placed in the die with the pieces of dough placed on top of the mould. A load ...(*Censored for commercial reasons*)..., by a mechanical testing machine, s250 from ESH testing, Dudley.

The embossed mould was then removed from the die and dried ...(*Censored for commercial reasons*).

5.2.5 Mould Dissolution

The moulds were removed from the dried bristle block by polymer dissolution ...(*Censored for commercial reasons*). Each dried bristle block and mould ...(*Censored for commercial reasons*).

5.2.6 Burnout and Sintering

Sintering and burnout of the binder were carried out in the same heating cycle. The dried bristle blocks were arranged in a rectangular crucible ...(*Censored for commercial reasons*). Volatile lead oxide loss and creep are common problems in sintering PZT, particularly when sintering net shape components [8]. Thus, the bristle blocks were sintered in ...(*Censored for commercial reasons*)...to maintain the stoichiometric composition. ...(*Censored for commercial reasons*)...

Figure 5.7 A schematic illustration of the arrangement of the furnace furniture for the sintering and burnout of the bristle blocks ...(*censored for commercial reasons*).

The thermal profile for the sintering and burnout is shown in Figure 5.8. Slow heating rates (1°C / min) are required in the initial stages of heating to avoid excess pressure within the bristle block whilst the binder is decomposing. A heating rate that is too fast will lead to the pressure exceeding the green strength of the bristle block and hence cause fracture of the ceramic. Once all of the burnout gases had been removed the heating rate ...(*Censored for commercial reasons*)...

Figure 5.8 The thermal profile for sintering and burnout of the binder

5.2.7 Backfilling

The sintered bristle blocks were backfilled with Epofix mounting resin from Struers, Solihull. The sintered bristle block was placed in a silicone rubber mould and the Epofix was mixed according to the manufacturers instructions. The sintered bristle block was then covered with the epoxy resin and placed in a vacuum chamber for degassing. After the gasses were removed from the resin the silicone mould was placed in a cool room overnight to allow the sample to cure.

5.2.8 Lapping

Lapping of the piezocomposites and the PMMA moulds was carried out on a PM5 auto-lap precision lapping machine, from Logitech, Glasgow. The piezocomposite / mould were mounted on a glass substrate using quartz wax, supplied by Logitech, Glasgow. It was then lapped at 40 rpm to the required thickness using a 9 μm alumina grinding solution. Periodically the mould / piezocomposite would be measured using micrometers and lapped further. The lapping machine was fitted with a PP5 / PLJ sample monitor, from Logitech, which stopped the machine after the required thickness of material had been removed.

5.2.9 Corona Poling

The poling process applies a high voltage to the piezocomposite to make it piezoelectrically active. The piezocomposites in this work were poled using a process called corona poling. This was achieved in a bespoke jig shown in Figure 5.9, and an expanded technical drawing is

shown in section 11.3. In the corona poling process the high voltage is applied by using an air-based corona discharge. The corona is generated in the chamber from a copper pin connected to a high voltage power supply, and the chamber is heated to aid the poling process. The process is non-contact and therefore does not require electroding prior to poling.

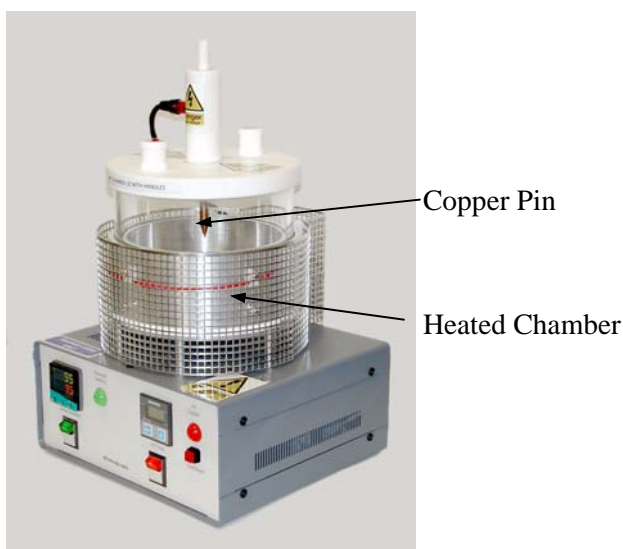


Figure 5.9 The bespoke corona poling jig

The poling jig was connected to a Brandenburg Alpha III, 30 kV high tension power supply and was heated to 95°C. The piezocomposite was placed inside the corona poling jig, and was clamped between a copper plate and a silica ring to prevent the piezocomposite from curling up during the process. Once the piezocomposite was at the set temperature, the voltage was increased to 30 kV and was held for 10 minutes to ensure complete poling.

5.2.10 Electroding

Electroding was carried out after corona poling since electrodes are not necessary for the poling process. Chrome and gold electrodes were sputtered onto the piezocomposites using a K575X Turbo Sputter Coater, from Emitech, Kent. An initial chrome electrode was sputtered

at 20 nm / min by applying a 100 mA current for 2 minutes. Then, a second gold electrode was sputtered in two, two minute cycles at 80 mA to give a second electrode thickness of 200 nm. The piezocomposite was then turned over before repeating the process for the other side.

5.3 Characterisation of Moulded Piezocomposites

This section outlines the method used to characterise the pillar, and cavity, arrays at each of the process stages and covers: the master tool; the moulds; the dried bristle blocks; the sintered bristle blocks; and the piezocomposites. A second master tool was used in this work compared to the master tool discussed in section 8.2.1, because it enabled a higher aspect ratio and a smaller feature sized structure to be achieved. The accurate dimensions of the master tool are presented in section 9.1, and the characterisation of the whole process is covered throughout section 9. The master tool and the moulds in these sections had hexagonal features such that when describing the width of these features, it should be noted that the width refers to the distance between parallel sides rather than opposite corners.

5.3.1 Dimensions of the Master Tool, Mould and Dried Ceramic Pillars

The kerf and pillar width of the dried ceramic pillars were imaged in a Joel 6060 scanning electron microscope (SEM), Joel, Hertfordshire. The same method was used for measuring the cavity width and the cavity wall width of the PMMA moulds, but only the dimensions of the dried bristle block are discussed here for ease of reading. The images were calibrated using a sample of known feature size (50 μm grid pattern). Four images per sample were taken at a magnification of x400, and each image showed five pillars for measuring. Thus, twenty measurements of the pillar width were measured for each sample. The images also showed sixteen cavity walls on each image such that a total of sixty-four measurements could be taken of each dried bristle block. The median, first quartile and third quartile were used to describe the size distribution, as they are less susceptible to values that occur vastly different to the bulk of the data. A large sample size proved useful for the kerf because distortion of

the periodicity in the array manifests itself as variation in the kerf, rather than the pillar width. An example of some of the distortion seen in the array can be seen on page 264.

The master tool was measured in a similar way to the moulds and dried pillars, but used thirteen images to provide a sample size of sixty-five for the pillar width and a sample size of two hundred and eight for the kerf. It was felt that such a large sample should be used for the tool, as it was important to establish the variation already in the array before replication began.

The images were measured using image analysis software, ImageJ (<http://rsbweb.nih.gov/ij/notes.html>). The measuring process either requires the user to manually draw a bounding rectangle, which can then be used to measure the pillar width, or can automatically draw the rectangles itself based on the contrast between the pillars and the background. It was found by a brief experiment that the method which produced the least scatter was the user defined rectangles. The resolution of a x400 magnification image was 0.25 μm per pixel, whilst the resolution of the SEM was ~ 0.4 nm [9]. Thus, the major error in the measurement of the pillars was considered to be the resolution of the image rather than the SEM.

The estimation of the error was demonstrated to be accurate when the master tool was measured. The master tool used here was fabricated using the LIGA process, which is known for its accurate, parallel sided features [10]. The edges of the pillars were well defined such that the rectangle for measurement could be easily drawn; and it was found, as discussed in section 9.1, that 80% of the pillar widths were within 0.25 μm of the median value, such that

this could be considered to be an accurate measure of the error. Furthermore, it will be seen in sections 9.2 and 9.3 that the error bars correspond to the interquartile range of each sample, and demonstrates again the accurate estimate of the error.

5.3.2 Dimensions of the Sintered Bristle Block

During sintering the dried ceramic pillars shrink, resulting in a smaller array, such that a high magnification can be used to capture five pillars. The magnification used was x450 magnification rather than x400, and improved the absolute error to $\pm 0.22 \mu\text{m}$

5.3.3 Master Tool, Dried and Sintered Pillar Height

The master tool and the sintered pillars were measured by tilting the stage in the SEM by 25° . An angle of 45° would have been preferred but was not used to avoid damaging the filament. The error here would be estimated to be caused by the resolution of the image, but is then increased by the trigonometry used to calculate the actual height from the measured value. For example, when measuring the pillars of the master tool using a magnification of x330 the error due to the pixel size is $\pm 0.31 \mu\text{m}$, but the actual error was is then increased to $\pm 0.74 \mu\text{m}$ ($\pm 0.31 / \sin 25$). In practice the error is greater than this because the edges of the pillars are not as well defined as in the plan view images used to measure the kerf and pillar width. Thus, it becomes harder to define where the measurement should be, such that if the measurement is out by three pixels, then the error increases to $3.0 \mu\text{m}$ ($0.31 \times 4 / \sin 25$).

Measuring the height of the pillars in the dried ceramic bristle block required a different approach to the pillars in the master tool, because it was not possible to get a full length image of the pillars by tilting the sample in the SEM. However after dissolution, broken pillars were

present on the top of the pillar array (shown on page 262), which could be imaged and measured at x270 to allow an estimate of the height of the pillars. Obviously the accuracy of the estimate is dependant on the position of the fracture, and whilst the pillars did not break at the absolute bottom of the pillar it was very near. Thus, the error can not be attributed solely to the resolution of the image, but provides a reasonable estimate. The validity of which is discussed in section 9.3.

5.3.4 Mould Height

The depth of the hot embossed moulds was measured by using optical microscopy. A reference image of one of the moulds was acquired, and the measurements obtained from the SEM images were used to establish a scale. The edges of the moulds were then photographed using the same magnification to measure the depth of the moulds. The reference image and results are shown in section 9.2.

5.3.5 Comparisons between Process Stages

The experimental error increases when comparing the dimensional changes between each stage. This can be explained by considering a comparison between the cavity width of the mould and the width of the dried ceramic pillars. The error for measuring both of these is $\pm 0.25 \mu\text{m}$, but since we are using two measurements to calculate another, the error value increases; i.e. if the master tool is actually $0.25 \mu\text{m}$ larger than measured, and the mould is $0.25 \mu\text{m}$ smaller than measured, the maximum error when comparing them is $0.5 \mu\text{m}$. Similarly when comparing the sintered to the dried pillars the maximum error is $0.47 \mu\text{m}$ ($0.25 + 0.22 \mu\text{m}$).

The shrinkage of the pillars is calculated by the difference between the width of the pillars (or cavity) of each stage, divided by the original dimension. For example, in the case of dried ceramic pillars to sintered pillars this is calculated by Equation 5.5

$$\frac{\text{Dried pillar width} - \text{sintered pillar width}}{\text{Dried pillar width}} \quad \text{Equation 5.5}$$

The absolute error for the shrinkage can be calculated using a similar method to Equation 5.5, whereby the absolute error between the two stages is divided by the original size of the pillar or kerf. Therefore, the absolute error in expressing the shrinkage is 0.6 % for both drying (mould to dried pillars) and sintering (dried pillars to sintering).

5.3.6 Determination of the Velocity of Sound in PZT

To determine the velocity of sound through the PZT of the piezocomposite it was necessary to measure the velocity of sound through PZT itself. Five PZT discs were made using the steps outlined in section 5.2.3 to 5.2.10, but a mould was not used. Thus after a sheet of VPP dough had been made discs were cut using a 15 mm hole borer. The discs were then dried, sintered, lapped, poled and electroded before calculating the velocity of sound.

The thickness of the discs was measured six times on different positions on the disc using a micrometer. The resonance frequency was measured using an Agilent 4294A impedance analyser, Agilent, West Lothian, and the velocity of sound was then calculated by making c the subject in Equation 2.6. The thickness of the discs varied by $\sim \pm 2 \mu\text{m}$ on a $450 \mu\text{m}$ disc, such that the mean maximum, mean minimum and grand mean velocities were 4780, 4670 and 4700 m / s respectively.

5.4 Chapter References

- [1] D. Yao, V L Virupaksha, B. Kim “Study on Squeezing Flow During Nonisothermal Embossing of Polymer Microstructures” *Polymer Engineering and Science* 45 (5) (2005) 652-660
- [2] H Becker, U Heim “Hot Embossing as a Method for the Fabrication of Polymer High Aspect Ratio Structures” *Sensors and Actuators* 83 (2000) 130-135
- [3] M G Alonso-Amigo “Polymer Microfabrication for Microarrays, Microreactors and Microfluidics” *Journal of the Association for Laboratory Automation* 5 (6) (2000), 96-101
- [4] D. Hardt et al “Process Control in Micro-Embossing: A Review” *Innovation in Manufacturing Systems and Technology* (2004) *Massachusetts Institute of Technology, USA*
<http://hdl.handle.net/1721.1/3917>
- [5] Y-J Juang, L. J. Lee and K W Koelling “Hot Embossing in Microfabrication. Part 1: Experimental” *Polymer engineering and Science* 42 (2002) 3 539-550
- [6] D. Yao, V. L. Virupaksha and B. Kim “study on squeezing flow during nonisothermal embossing of polymer microstructures” *Polymer Engineering and Science* (2005) 652-660
- [7] Instron “2525 drop in load cells”
http://www.instron.co.uk/wa/acc_catalog/prod_list.aspx?cid=480&cname=2525%20Series%20Drop-through%20Load%20Cells as viewed 05/07/09
- [8] N. J. Porch et al “Net shape processing of piezoelectric ceramics and novel devices” *Processing of Electroceramics Conference, Aug-Sept 3, 2003, Bled, Slovenia* (2003) 293-312
- [9] The centre for Electron Microscopy, The University of Birmingham “Microscopes and Ancillary Equipment: Joel JSM-6060 LV: Specifications”
<http://www.cem.bham.ac.uk/je6060.htm> as viewed 05/07/09
- [10] M. J. Madou “Fundamentals of Microfabrication: The Science of Miniaturisation Second Edition”. *CRC Press London* (2002) *ISBN-13: 978-0849308260*

Chapter 6

Master Tool and Piezocomposite Design

6 Master Tool and Piezocomposite Design

A detailed discussion and comparison of piezocomposite fabrication, micro replication and micro fabrication processes has been given in Chapter 3. However, as yet only the approximate dimensions of the piezocomposites have been discussed, rather than an actual design. The minimum feature size and maximum aspect ratio of a micron scale structure is dependent upon the array geometry, in terms of the shape of the pillars, their packing, their aspect ratio and the volume fraction. This chapter describes the design of a piezocomposite and a master tool based on the achievable aspect ratio and feature sizes of both the hot embossing process and the micro fabrication process.

The most suitable array geometry for hot embossing and micro fabrication will have the largest minimum feature size, and the smallest aspect ratio for a specific volume fraction. Geometry has been used to derive equations relating the kerf, to the pillar width, and to the volume fraction, whilst also considering the pillar taper. Combined with the procedure outlined in section 2.2.4 it has been possible to develop a spreadsheet in Microsoft Excel to calculate the required dimensions of the master tool, which is illustrated in an example screenshot shown in section 11.4 in the Appendix.

From the data supplied by the spreadsheet and the literature review, it is possible to select a design that is reasonable for micro replication, micro fabrication and for the piezocomposite. It has been considered that Microsoft Excel was sufficient for this design since we are only considering the geometry of the micron scale structures, and using the minimum feature size and maximum aspect ratio to viability of it being fabricated and replicated.

6.1 Considered Array Geometries

There are six array designs that have been considered for use as a master tool and piezocomposite which are shown in Figure 6.1. The designs consider four pillar shapes; square, hexagonal, circular, and triangular, which have each been packed into an hexagonal array; and a further two arrays that have been formed by packing the square and circular pillars into square arrays. The most common array fabricated for 1-3 piezocomposites is the square packed, square pillar array, because this is the easiest array to fabricate using dice and fill. Circular pillars, hexagonal pillars, and hexagonally packed square pillars, are not possible by dice and fill because the process is only able to cut straight grooves in the sintered ceramic block.

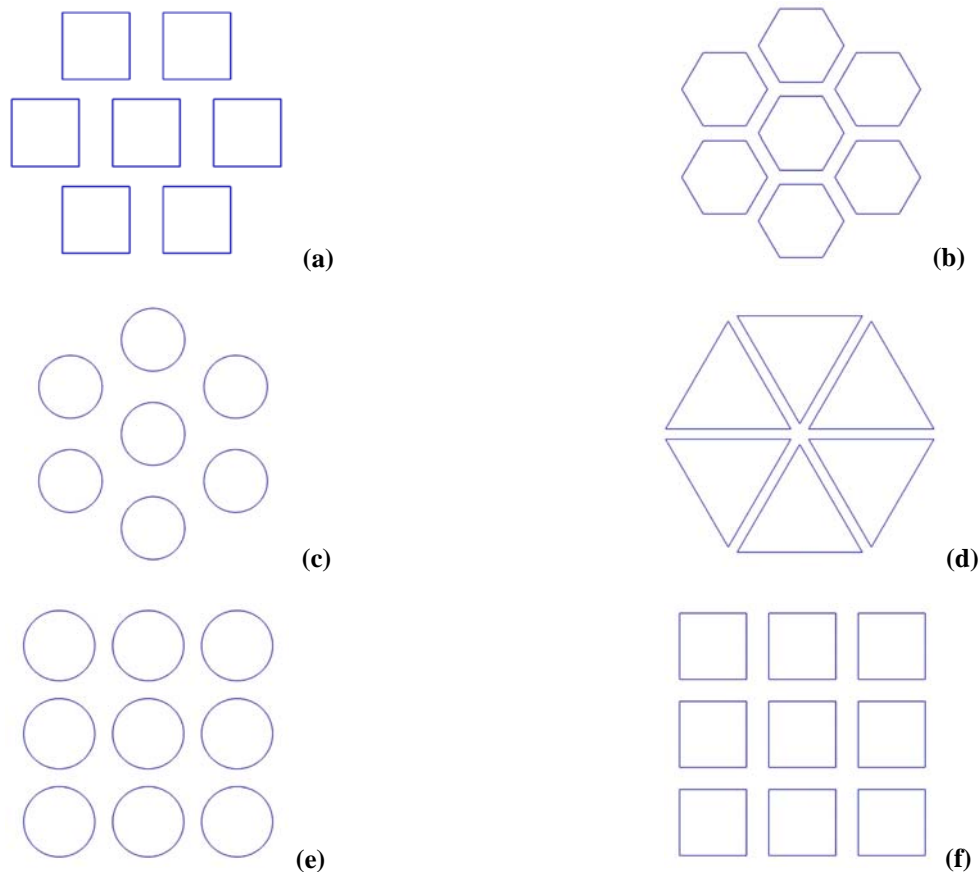


Figure 6.1 The various pillar array designs that were investigated, Hexagonally Packed: Square (a), Hexagonal (b), Circular (c), Triangular (d) Pillars and Square Packed: Circular (e) and Square (f) Pillars

6.2 Dimensions of Pillar Arrays

The important dimensions of a pillar array are shown in Figure 6.2, and are: the average pillar width; the minimum feature size; the absolute height; the taper; and the maximum aspect ratio. The kerf is responsible for two of these dimensions, the minimum feature size and the maximum aspect ratio. However, the kerf is also dependent upon the volume fraction, pillar width, taper, and the pillar packing.

To produce identical pillar arrays that are the same except for the taper, it is necessary to design the array such that sides of the pillars pivot about a point that is at half the absolute height of the pillar. This will result in the same volume fraction between each array, because the increase in kerf at the top of the array is countered by a decrease in kerf at the bottom. However, increasing the taper results in a decrease in the minimum feature size, and an increase in the maximum aspect ratio, which are both defined by the kerf at the bottom of the array.

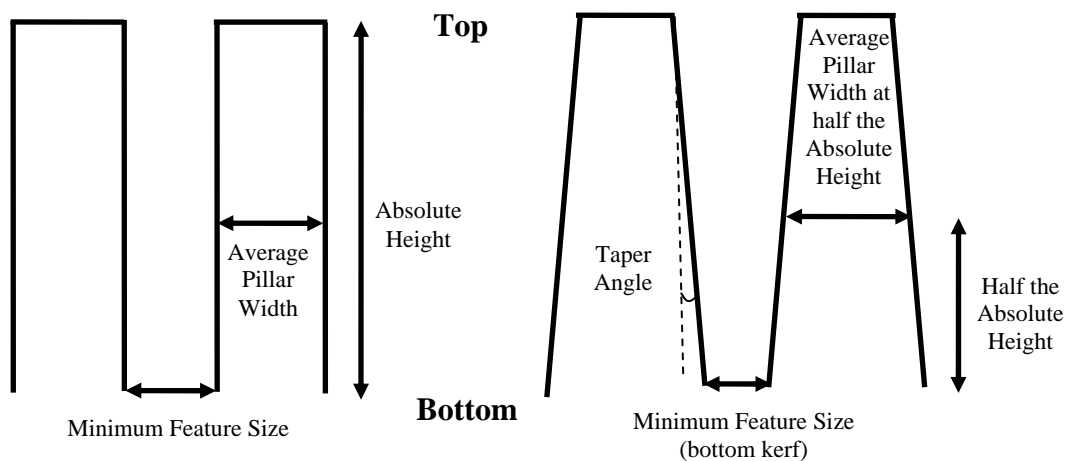


Figure 6.2 The important dimensions of the pillar arrays; which highlights the decrease in minimum feature size and the increase in maximum aspect ratio as the taper is increased

6.3 Selection of Taper Range

The taper will have an effect on the geometry of each pillar array and in turn this will affect the master tool manufacturing process, the master tool during hot embossing, and the behaviour of the final piezocomposite. The implications and the severity of this effect will vary between the different geometries, such that the selection of the taper range must consider all three of the functions of the pillar array.

To demonstrate the effect of the taper range an example master tool has been selected. The following figures demonstrate the effect of adding a taper onto a pillar array. For all the figures the same design, based on the 5 MHz piezocomposite that was shown in Table 2.1 and Table 3.1, has been used to illustrate the effect. This means that a piezocomposite with a volume fraction of 0.5, pillar aspect ratio of 2.5 and a pillar width of 120 μm has been used. A lapping depth of 100 μm and an approximate shrinkage of the VPP dough by 20% has been assumed such that the master tool used will have a pillar width of 144 μm and an aspect ratio of 3.3.

The effect of the taper on the volume fraction at the top and bottom of the piezocomposite is shown in Figure 6.3. The curves are for the different geometries discussed in section 6.1 and indicate that for square and circular pillars the effect is the same, hence not all are visible as some of the data are overlaid. The figure indicates that volume fraction behaves linearly with taper angle, and that square or circular pillars in either packing are least affected by the taper. For hexagonal pillars there is a slightly larger effect on the volume fraction, whilst for triangular pillars it is much more pronounced.

To compare the geometries more quantitatively, we should look at the difference in volume fraction between the top of the piezocomposite and the bottom. For triangular pillars this difference is greater than 50%, for hexagonal pillars this difference is 40% and for circular or square pillars this is 35%. The aim is to minimise the variation between the volume fraction at the top and at the bottom of the piezocomposite, because this will affect the performance of the piezocomposite, whilst still maintaining a sufficient taper to help de-emboss the master tool.

Figure 6.4 shows how the minimum feature size, the kerf at the bottom of the master tool, reduces with an increase in taper angle. The figure illustrates that the minimum feature size is reduced significantly from 0° taper to a 4° taper, even without considering a 5° taper. The aim is to minimise the effect that taper has on the minimum feature size. Obviously, a larger feature size is easier to replicate and to fabricate. The figure shows that square pillars are least affected, in both packing geometries. This is then followed by hexagonal pillars, and hexagonally packed circular pillars, whilst square packed circular and triangular pillars show even smaller feature sizes. To highlight this difference further we can compare square pillars to triangular pillars with a 4° taper. This shows that for 144 µm wide triangular pillars the kerf diminishes to zero, whilst the kerf for square pillar remains at 26 µm, which is achievable for hot embossing, the Bosch process and laser ablation.

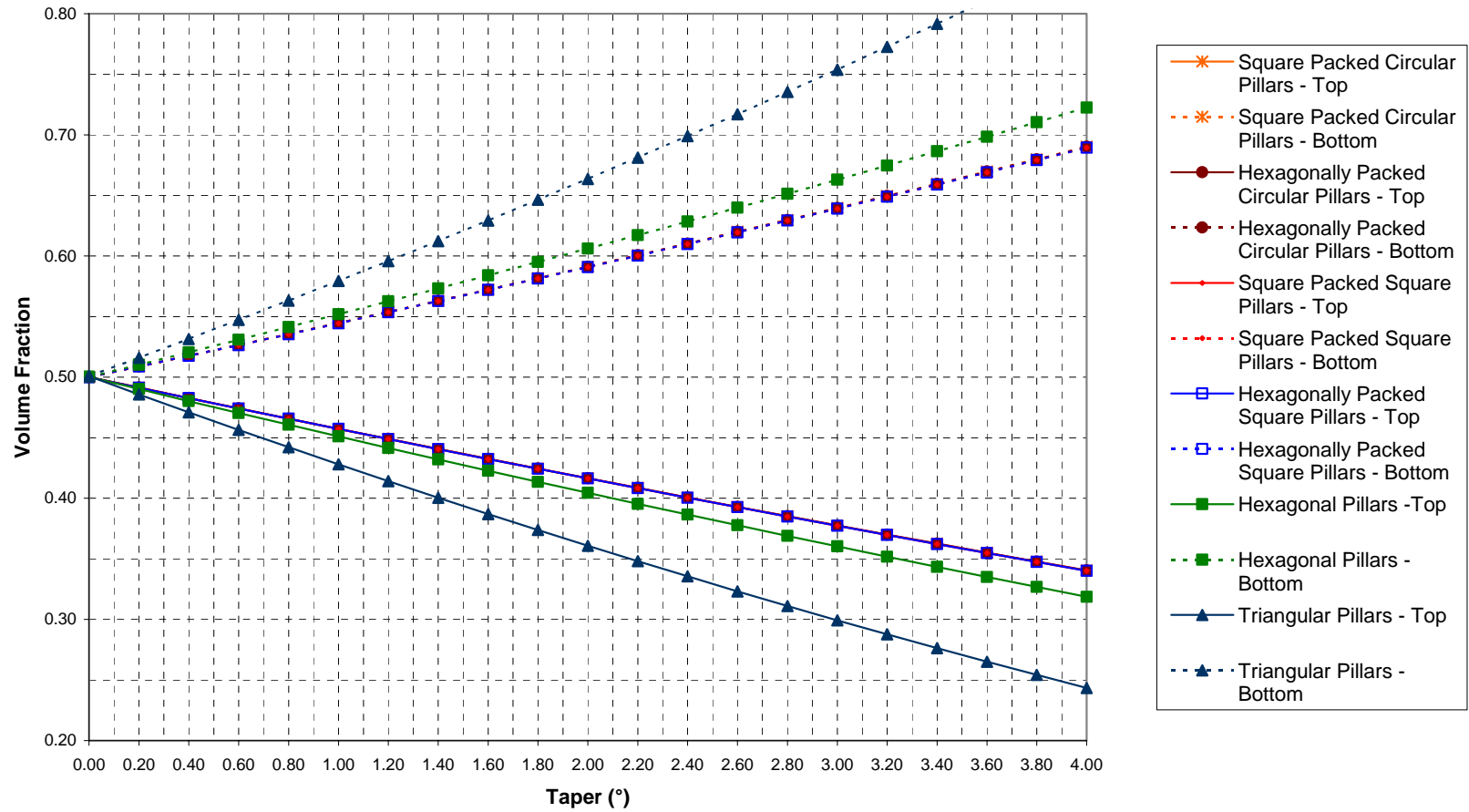


Figure 6.3 The effect of taper on the volume fraction for various array geometries with an a master tool of volume fraction 0.5, and a pillar width of 144 μm at half the absolute height

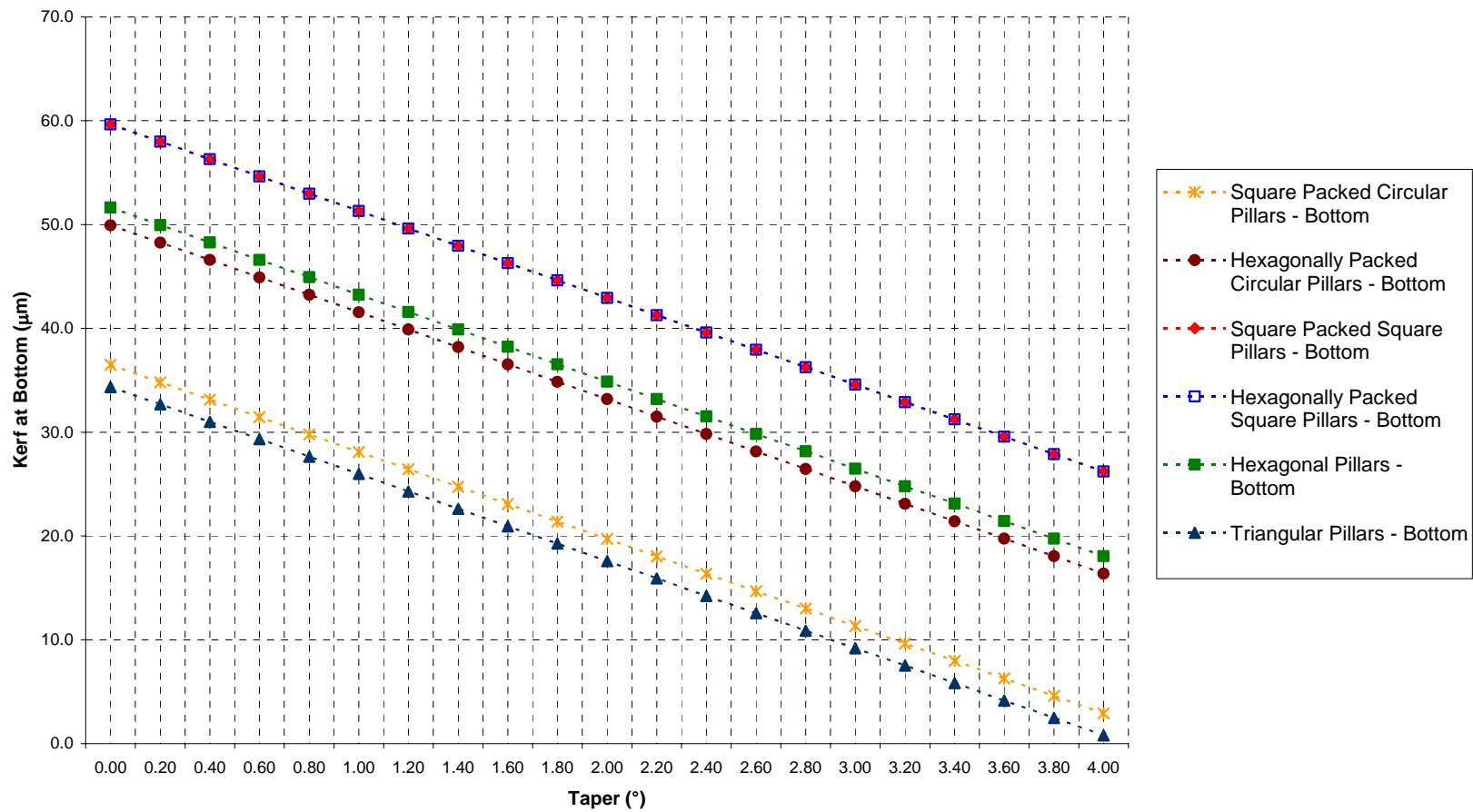


Figure 6.4 The effect of taper on the minimum feature size of a master tool with 144 μm wide pillars and a volume fraction of 0.5, for various array geometries.

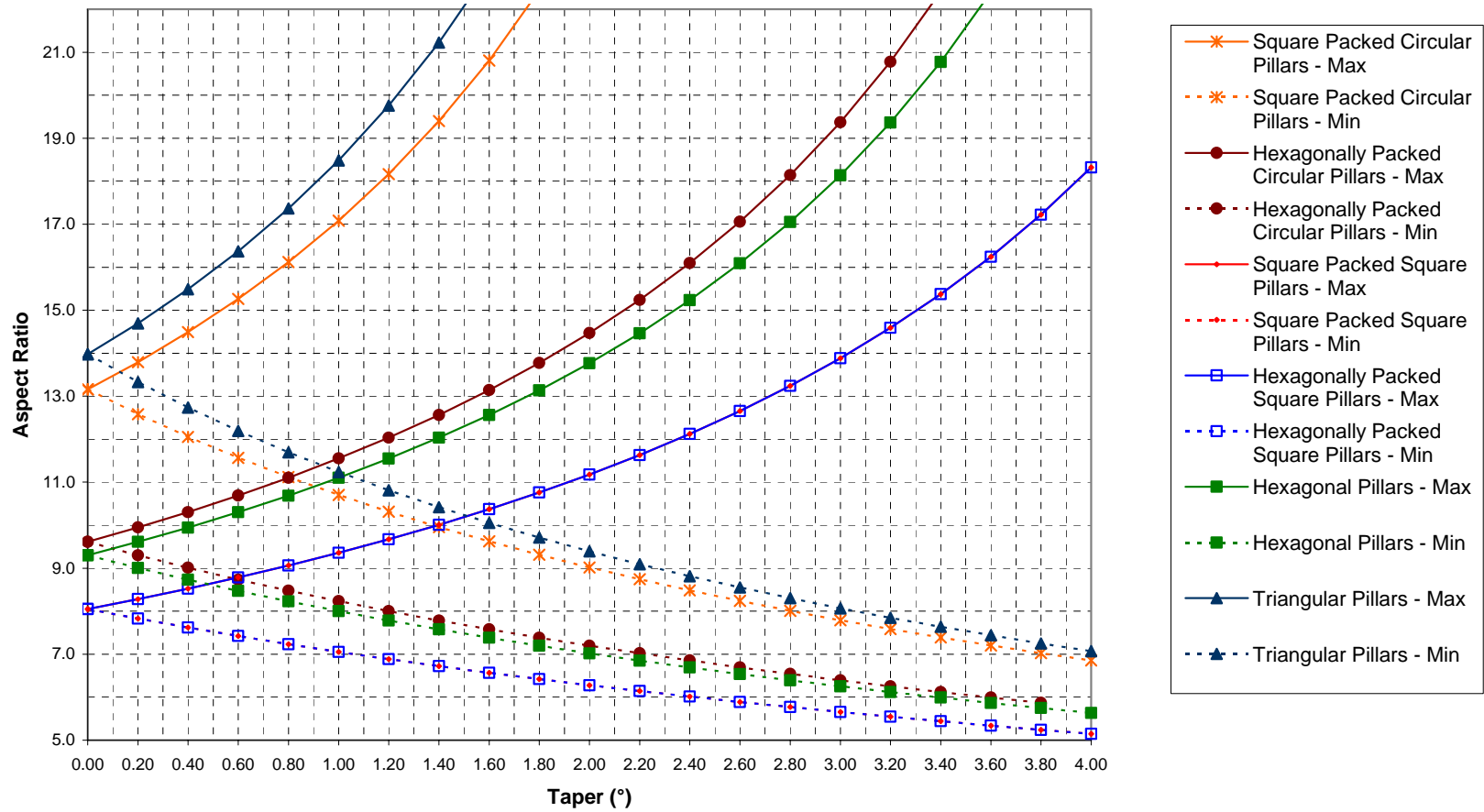


Figure 6.5 The effect of taper on the maximum and minimum aspect ratios of the mould wall for various array geometries. The master tool considered here had a volume fraction of 0.5 and pillar width of 144 μm .

The effect of taper angle on the maximum aspect ratio is illustrated in Figure 6.5. It is evident from the figure that whilst the maximum aspect ratio increases, the minimum aspect ratio also decreases. However, it is this maximum aspect ratio that is important for both micro replication and micro fabrication. As before, it can be seen from Figure 6.5 that the aspect ratio of square pillars is least affected, and shows the same behaviour for both forms of packing. Furthermore, square pillars show the lowest aspect ratio overall due to their larger feature size. In a similar way to Figure 6.4 the hexagonal pillars and the hexagonally packed circles are affected more by the taper, whilst the triangular pillars and the square packed circular pillars show a large effect.

The maximum aspect ratio increases rapidly in all of the pillar array geometries. However, it should be remembered that as this aspect ratio increases with taper it is not quite the same as the aspect ratio being high in a parallel sided feature, since the tip of the feature will be supported by the base. The important thing to acknowledge is that the square pillars show the least increase in aspect ratio, and that the aspect ratio of 18 has been achieved by hot embossing, the Bosch process and laser ablation, if not in mesh structures.

Figure 6.3 to Figure 6.5 indicate that square pillars offer the best opportunity to investigate the effect of taper on hot embossing and piezocomposite performance, because the volume fraction, aspect ratio, and feature size are least affected by taper angle. A taper range of 0° to 4° has been presented because it was felt that 5° would present an even greater challenge in terms of aspect ratio and feature size. In addition, the recommended taper angle for hot embossing, 2° , lies in the centre of this range, and it is thought that this provides a suitable range for micro replication, micro fabrication and piezocomposite performance.

6.4 Selection of Size Range

The aim of this approach is to lay a foundation to develop smaller piezocomposites with higher operating frequencies. Therefore, it is important to understand how the designs developed here apply to being scaled down. As a result, the spreadsheet has been developed to visualise how the minimum feature size and aspect ratio will change according to the change in pillar width and taper.

The size range that has been considered is from a master tool pillar width of 204 μm to 12 μm , which corresponds to piezocomposite pillar width of 170 μm to 10 μm . The graphs were generated based on a piezocomposite with a specified pillar width that had an aspect ratio of 2.5 and a volume fraction of 50 %.

6.4.1 Minimum Feature Size

Figure 6.6 shows the decrease in the minimum feature size as the pillar width of the master tool decreases. The figure has been split into 5 sub figures from (a) to (e) to show the effect on an array with a 0, 1, 2, 3 or 4° taper. In all cases the minimum feature size decreases with the pillar width. The geometries are affected in the same way as described in Figure 6.4 and Figure 6.5, with the square pillars showing the largest feature size, which have a kerf of 5 μm for a pillar width of 12 μm . However, when the taper is increased some of the designs are not achievable because the kerf cannot be negative.

Triangular pillars are the worst affected by increasing the taper. When a taper of 2° is added to the array even 204 μm wide pillars cannot be produced with a positive kerf. Even square packed circular pillars require an 8 μm kerf for a pillar width of 204 μm with a 4° taper. By

comparison square pillars are least affected, and all designs can be made up to 12 μm at 2°. A taper of 4° can be achieved in a master tool with 36 μm wide pillars.

By comparing the figures it can be seen that square pillars are the most suitable for scaling down because they are capable of producing the highest minimum feature size for a given pillar width. Several designs are not possible, particularly the triangular pillars, or the pillars with a larger tapers and smaller pillar widths. The reason for this is explained in section 6.4.3.

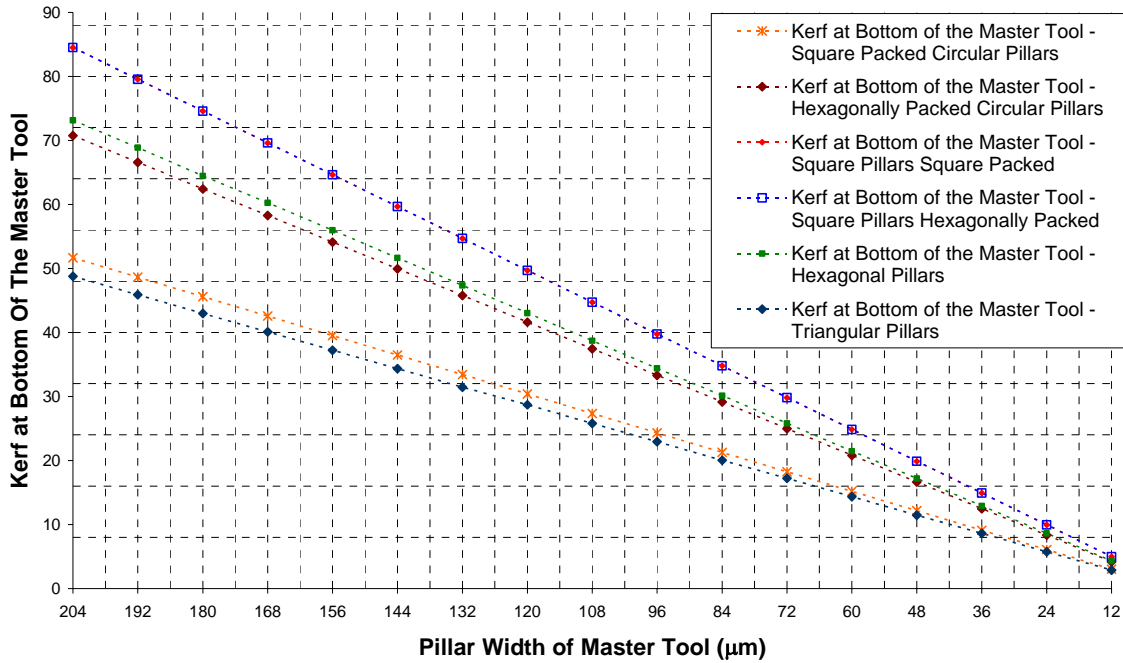


Figure 6.6 (a)

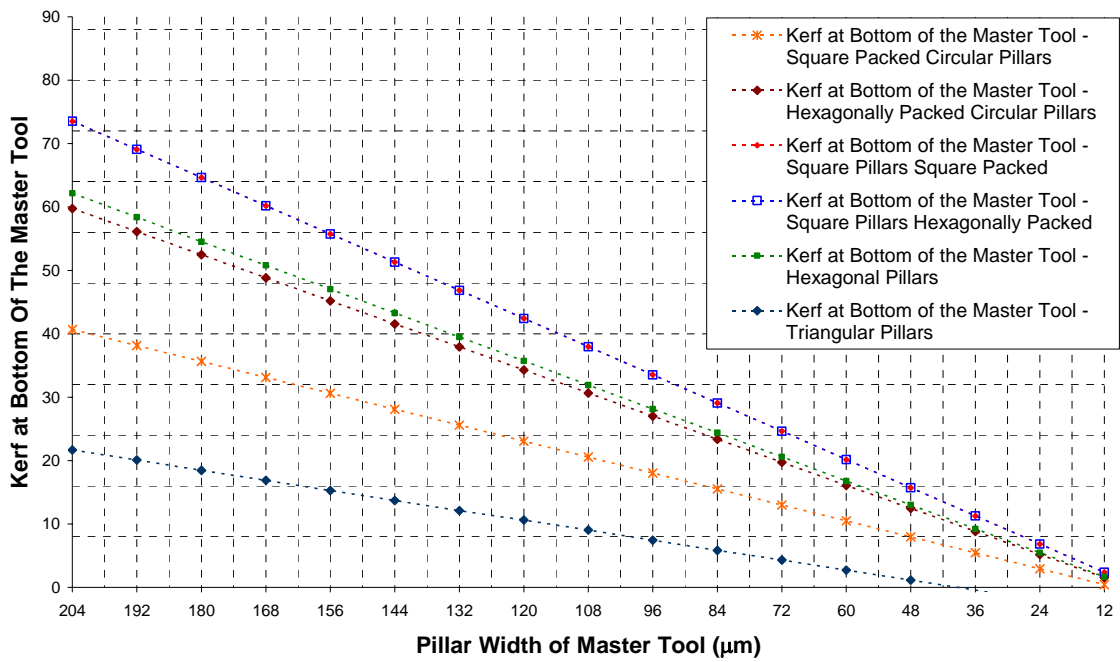


Figure 6.6 (b)

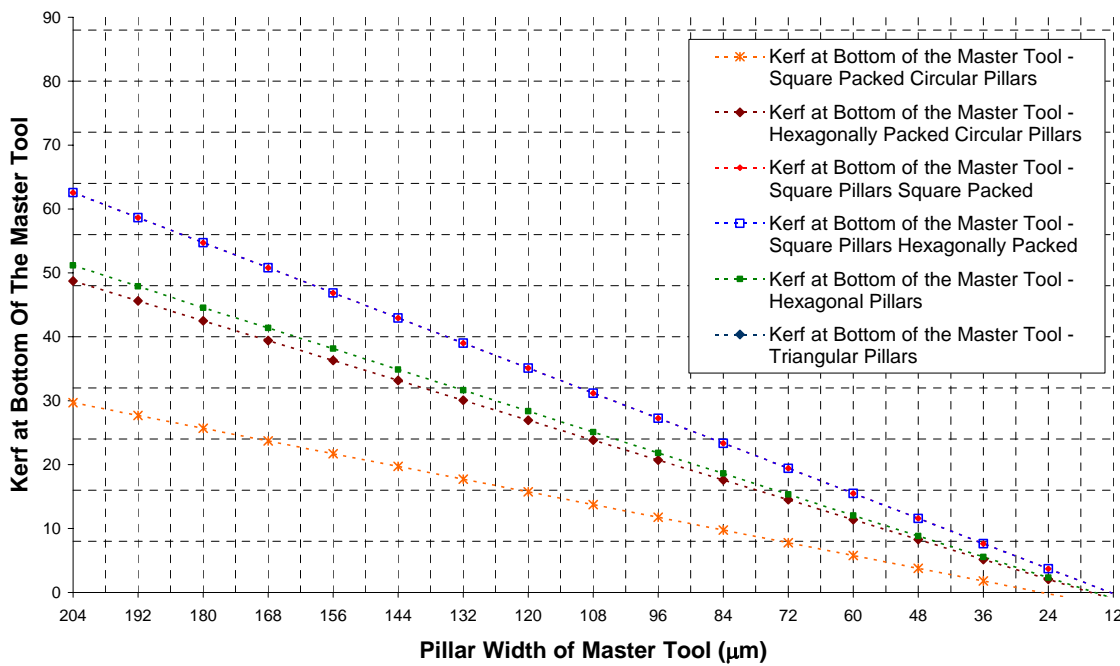


Figure 6.6 (c)

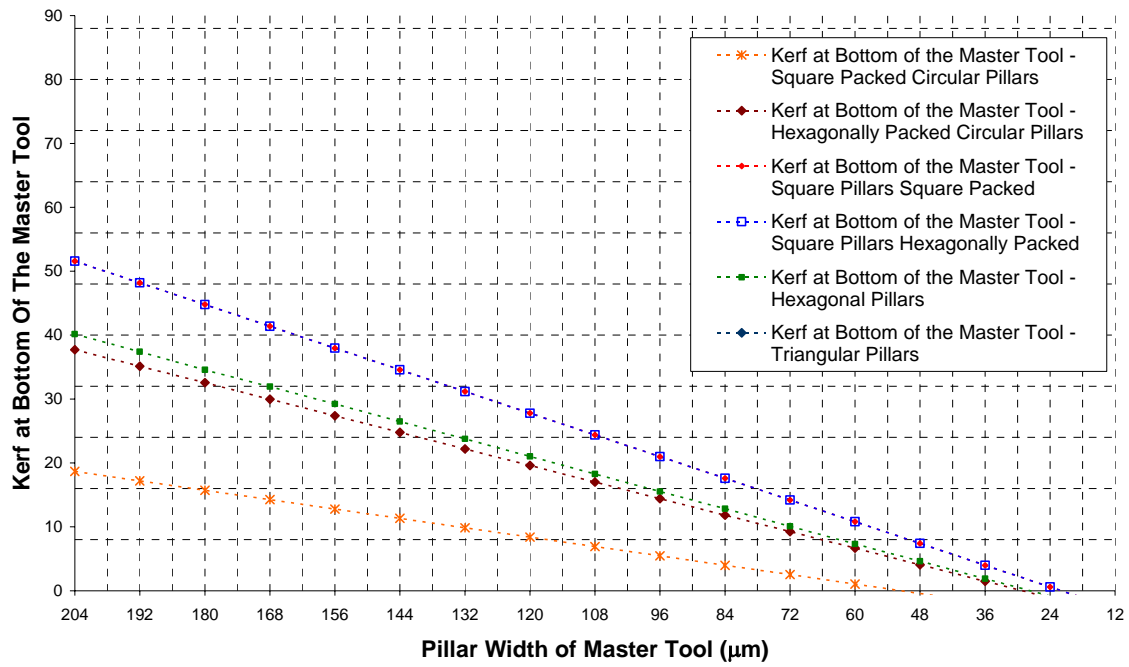


Figure 6.6(d)

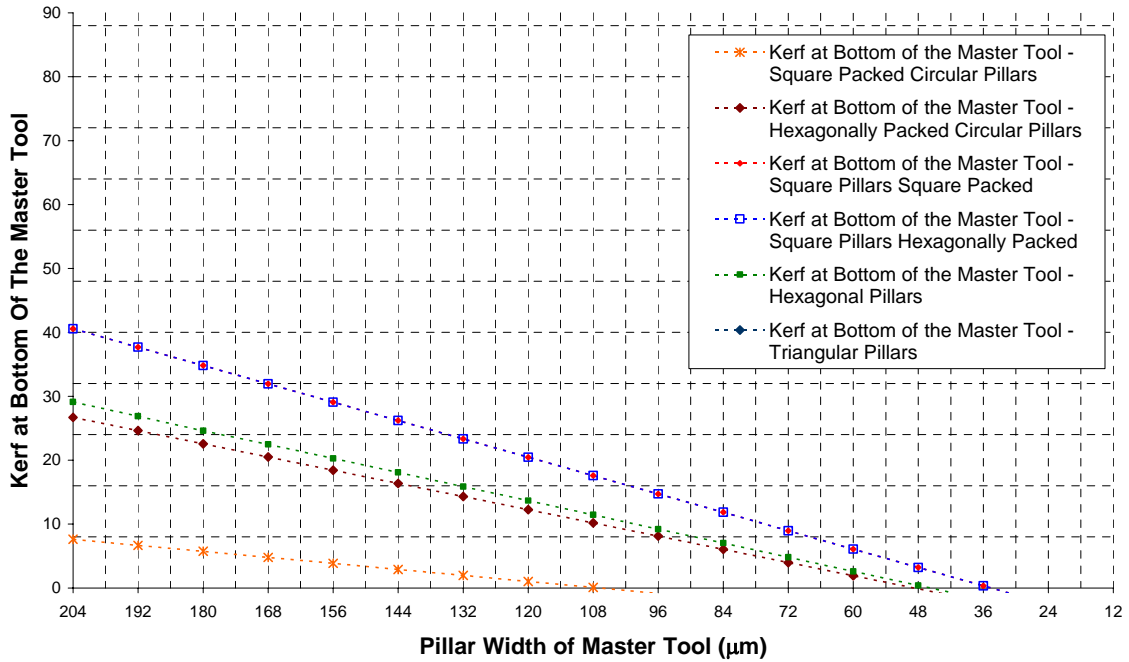


Figure 6.6 (e)

Figure 6.6 The graphs (a) to (e) show the change in minimum feature size (the kerf at the bottom) of the different pillar arrays with respect to the decrease in pillar size. The taper used for each graph is (a) 0° , (b) 1° , (c) 2° , (d) 3° and (e) 4°

6.4.2 Aspect Ratio

Figure 6.7 shows how the aspect ratio changes, for all the geometries, from a master tool with a pillar width of 200 μm to 20 μm . Each figure from (a) to (e) shows this change for arrays with taper angles from 0° to 4° respectively. For a constant taper angle the figures show a sharp increase in the aspect ratio as the pillar width is reduced. The most affected are the triangular pillars and the least affected are the square pillars in either packing, with the remaining geometries in the same order as in sections 6.3 and 6.4.1.

In the case of the square pillars with no taper, the aspect ratio is at 7 for 200 μm pillars, 9 at around 100 μm pillars and then doubles to 18 at 24 μm . The other geometries, without a taper, show similar behaviour but start at higher aspect ratios. When the effect of the taper is considered, similar behaviour to the feature size occurs, whereby the curves are shifted off the scale of the graph to abnormally high aspect ratios. This behaviour is seen because we are considering the maximum aspect ratios rather than aspect ratios based on the average pillar width as illustrated in Figure 6.2.

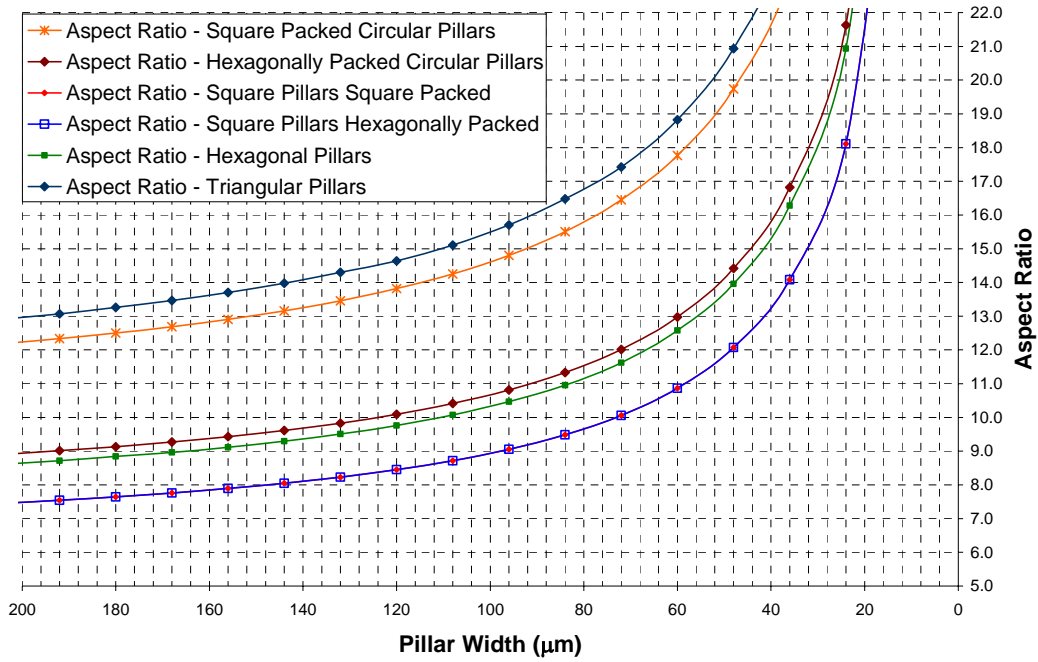


Figure 6.7 (a)

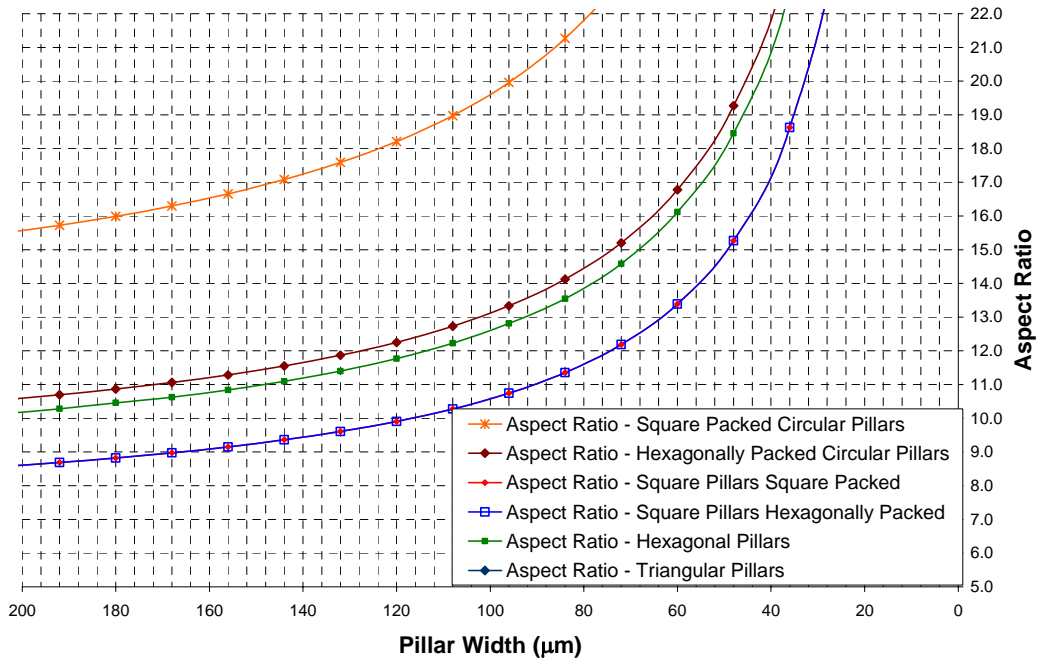


Figure 6.7 (b)

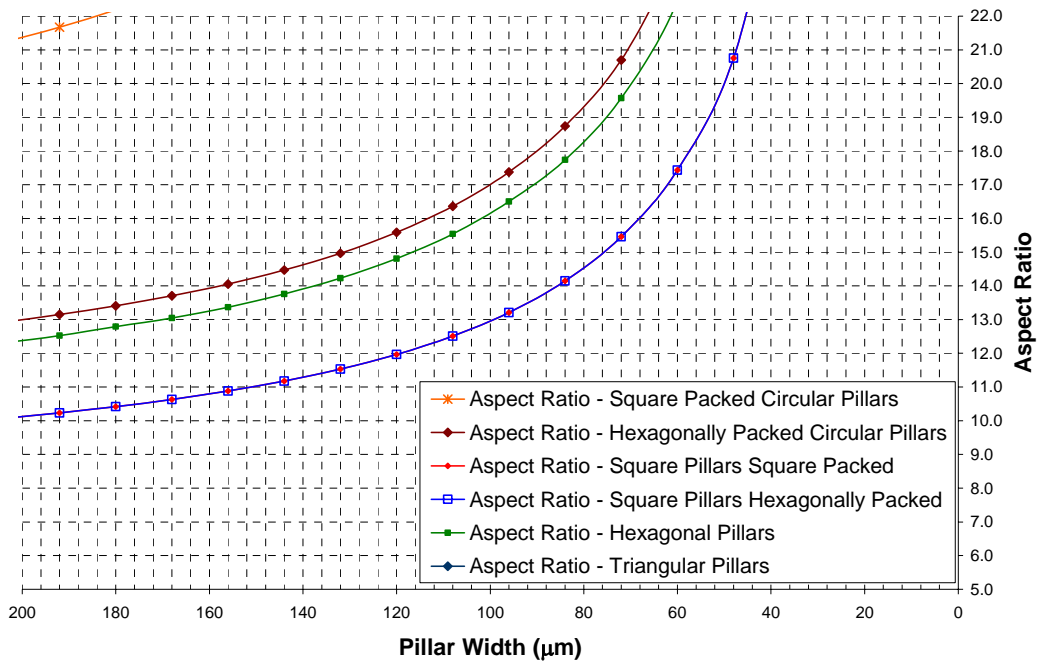


Figure 6.7 (c)

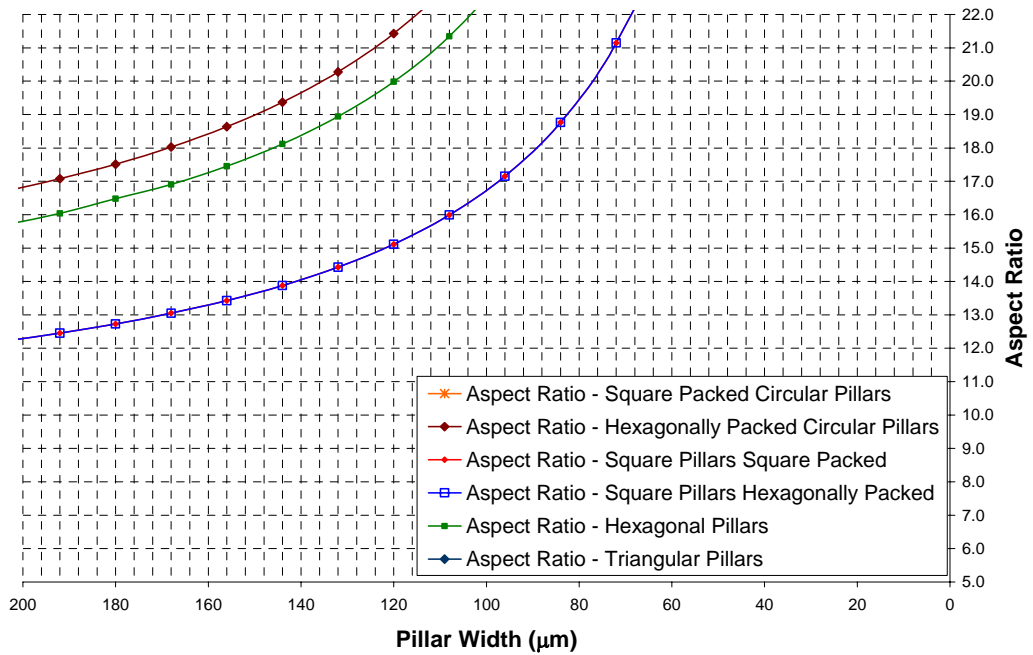


Figure 6.7 (d)

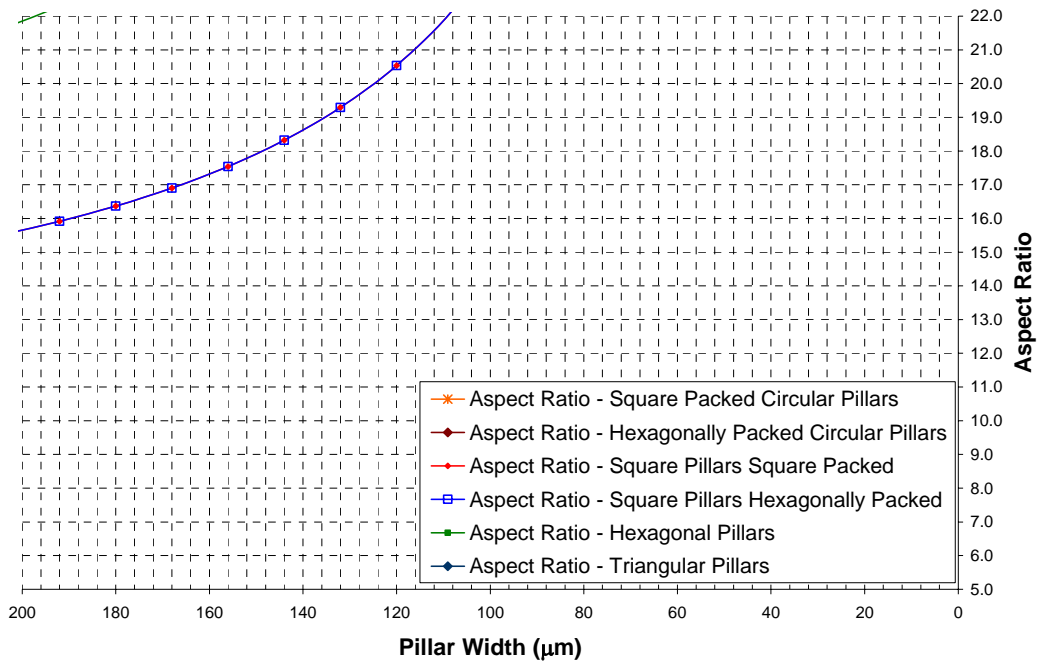


Figure 6.7 (e)

Figure 6.7 The graphs (a) to (e) show the change in aspect ratio of the different pillar array with respect to the decrease in pillar size. The taper used for each graph is (a) 0°, (b) 1°, (c) 2°, (d) 3° and (e) 4°

6.4.3 Lapping Depth

The rapid increase in aspect ratio at around a pillar width of 85 μm is caused by the 100 μm lapping depth being more significant at smaller scales. This is illustrated in Figure 6.8 by comparing two extremes of the scale, a master tool with a 400 μm pillar width and a master tool with a 15 μm pillar width. The master tool is shown in yellow, the sintered piezocomposite is shown in transparent orange, and the lapped piezocomposite is shown in cream and green. The figures illustrate the relative amounts of material that is required to be removed by lapping to a lapping depth of 100 μm.

The rapid increase in aspect ratio seen in section 6.4.2 can be reduced by removing a smaller quantity of material. This will depend on the skill and experience of the operator, but if it is

possible to reduce the lapping depth to 50 μm for example the required aspect ratio will be reduced and the feature size will be increased. This will make the micro replication and fabrication steps much easier and will provide a route to higher frequency piezocomposites without a compromise in piezocomposite performance.

The effect of reducing the lapping depth is shown in Figure 6.9. The square packed square pillars curve is used to ‘trace out’ the curve of aspect ratio vs. pillar width for a lapping depth of 100 μm while the hexagonally packed square pillars, which would ordinarily follow the same curve, show the effect when the lapping depth is reduced to 50 μm at pillar widths $< 85 \mu\text{m}$. It is suggested that this change occurs at this point because, after this width, the increase in aspect ratio becomes quite rapid. Figure 6.9 shows that for a master tool with 0° taper, and 36 μm wide square pillars, the maximum aspect ratio can be reduced from ~ 14.5 to ~ 10.5 .

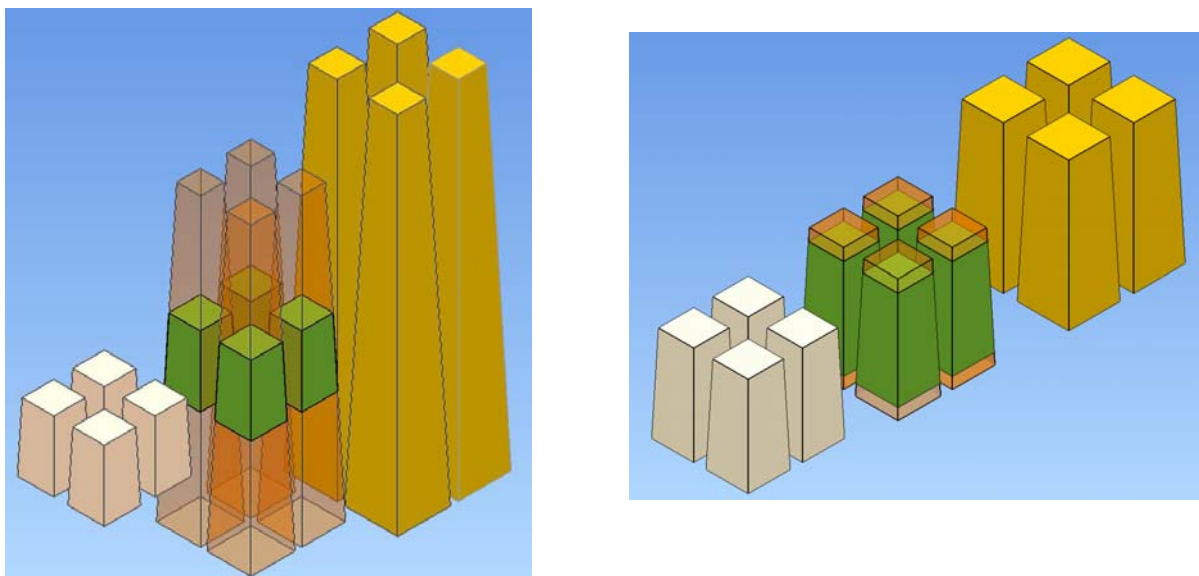


Figure 6.8 The significance of lapping depth as the size scale reduces. The master tool (yellow), sintered piezocomposite before lapping (orange) and the final composite (green / cream) are shown for a 15 μm (left) and a 400 μm (right) piezocomposite.

Figure 6.10 shows the results when all of the geometries are considered with a 4° taper and with the same step change in lapping depth. In this case the aspect ratios of the arrays are > 22 such that they can not be seen on a graph with this scale. However for the square pillars the lapping depth has been reduced, so that for a pillar width of $84 \mu\text{m}$ the aspect ratio becomes 17, and is now visible on the graph. When this aspect ratio is related back to the structures seen in the section 3.1.4.3, it can be seen that an aspect ratio of > 17 has been achieved by hot embossing but not in a mesh structure.

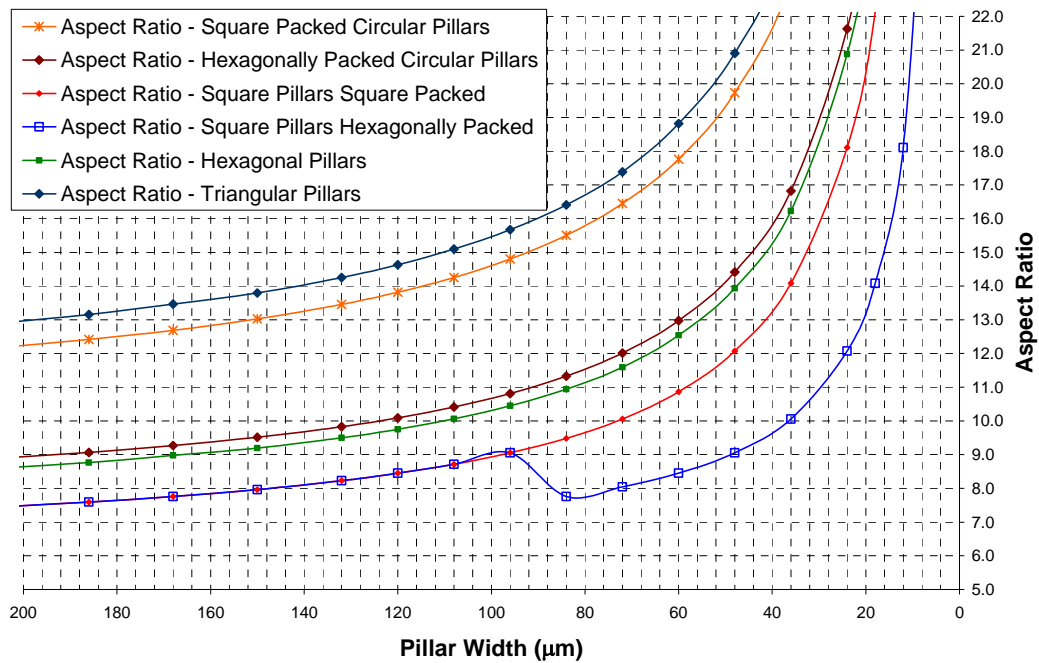


Figure 6.9 The effect of a reduction in lapping depth. All curves show the change in aspect ratio as the pillar width is reduced on a pillar array with 0° taper. All curves have a lapping depth of $100 \mu\text{m}$, except for the hexagonally packed square pillars which have the lapping depth reduced to $50 \mu\text{m}$ after a pillar width of $84 \mu\text{m}$.

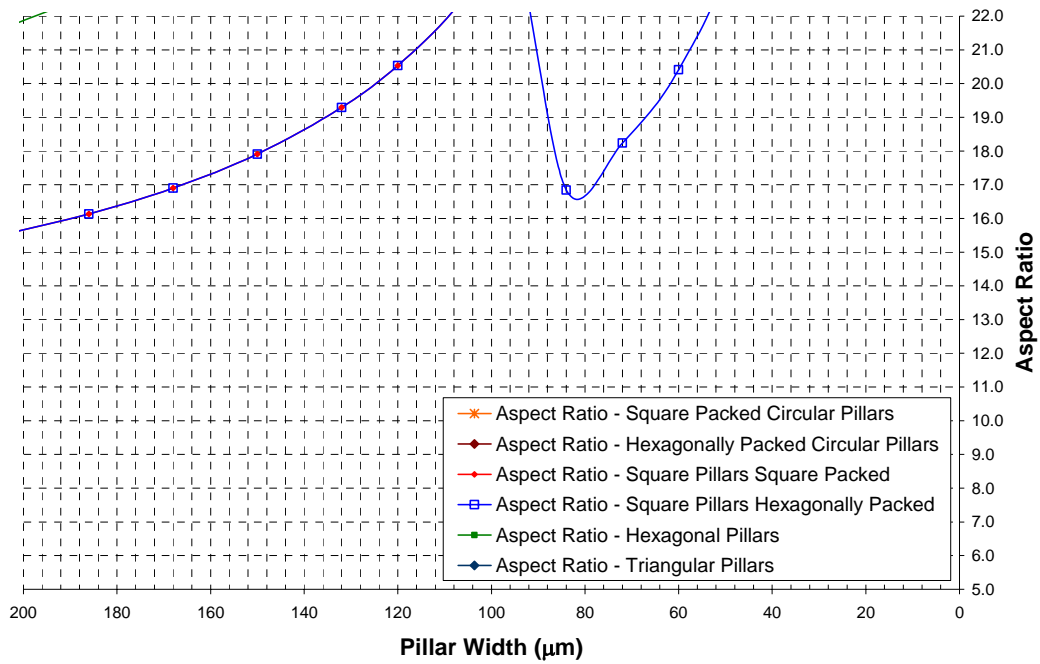


Figure 6.10 The change in aspect ratio with respect to the decrease in pillar width for pillar arrays with 4° taper and a change in lapping depth at 84 μm

6.5 Array Design and Summary

Square, circular, hexagonal and triangular pillars have been reviewed in square and hexagonal packing. The affect of taper on the minimum feature size, aspect ratio and volume fraction has been investigated, as has the ability of the pillar array to be made into smaller sizes.

Throughout the investigation, square and hexagonally packed, square pillars have repeatedly produced favourable results. The aspect ratio is the smallest and the feature size is the largest out of all of the arrays, and both are least affected by the taper. This makes the square pillars the most likely to be replicated and fabricated successfully out of all of the geometries. Further, the volume fraction varies the least with taper, such that the variation of the piezocomposites properties through the thickness will be minimised.

The calculations have identified a problem with reducing the size of the piezocomposite. This problem is inherent in all 1-3 piezocomposite fabrication processes where a bristle block structure is formed, backfilled and lapped. The minimum amount of material that can be removed by lapping is constant, regardless of the size of the bristle block. Thus, the proportion of the material that is required to be removed increases with a smaller target thickness. As the target thickness decreases so does the feature size; but the height does not reduce as rapidly, which leads to a rapid increase in aspect ratio. The minimum amount of material that is removed by lapping can be reduced with operator skill and experience, but represents an important problem in all piezocomposite manufacture techniques.

The chosen design will use square pillars because this geometry is most easily fabricated and replicated. The array will be hexagonally packed, because this illustrates that VP embossing

is not restricted by array geometry like dice and fill. The pillar width of the master tool will be around 100 μm because at values lower than this, the aspect ratio begins to rapidly increase. The Bosch process uses stock silicon wafers, such that to achieve cavities through the entire thickness of the wafer, the master tool will be required to have pillars 400 μm high after electroforming. Therefore for piezocomposite with a 50% volume fraction, and an aspect ratio of 2.5, the design with no taper will have 112 μm pillars and 46 μm kerf; giving an aspect ratio of 8.7. The other designs are shown in Table 6.1 and show the increase in aspect ratio and decrease in feature size.

Table 6.1 The chosen dimensions for the master tool fabrication

Taper ($^{\circ}$)	Pillar Width (μm)		Kerf (μm)		Aspect ratio	Minimum feature size (μm)
	at pillar top	at pillar bottom	at pillar top	at pillar bottom		
0	112	112	46	46	8.7	46
1	105	119	53	39	10.3	39
2	98	126	60	32	12.5	32
3	91	133	67	25	16	25
4	84	140	74	18	22.2	18

The aspect ratios and feature sizes shown in the table may appear challenging. However, it is important to remember that the maximum aspect ratio depends on the minimum feature size, which is based on the smallest distance between the pillars. However, the distance between the pillars varies with the height of the pillar array, so that one should also consider the aspect ratio based on the kerf at half the absolute height. This aspect ratio is equivalent to the aspect ratio of a pillar with a 0° taper. Therefore, by adding a taper, we may not increase the aspect ratio to a point where it makes it harder to de-emboss. In addition, lowering the aspect ratio by designing an array with larger pillars was also considered. But it was found that for 150 μm wide pillars, it was not possible to achieve the required 500 μm depth using the Bosch process. Further detail is given in section 7.3, but this illustrates that compromises must be

made in the process chain so that by making one process easier another step is not made more difficult.

Chapter 7

Master Tool Fabrication

7 Master Tool Fabrication

Not all of the work in this project was able to be carried out at the School of Metallurgy and Materials, Birmingham, and therefore a number of collaborations were required. Throughout this project, the work carried out by other parties was on a collaborative basis with the ideas and problems being discussed at each stage of the research, and whenever possible characterisation was completed at the school.

This chapter describes the work carried out on this collaborative basis, which has focused on developing a master tool fabrication route that would enable the control over the pillar taper, and enable an investigation into the effect of the taper on both hot embossing and piezocomposite performance. The chapter aims to fabricate a master tool to the designs discussed in section 6.

7.1 Feasibility Study of Laser Ablation

7.1.1 Direct Fabrication of the Master Tool

A brief investigation into the feasibility of directly producing a master tool was carried out by the UK-LMC. This study aimed to produce a positive, pillar array structure that could be used immediately as a master tool. The investigation studied 316 stainless steel and glass as master tool materials, and aimed to produce 50 μm pillars, with a kerf of 20 μm . Four different combinations of parameters were tried on the stainless steel, and a fifth set of parameters were tried on the glass using an excimer laser. The machining parameters that were varied were spot size, laser power, the number of passes over a particular site, and the change of focus during machining [1]. An excimer laser was used in this study because it was

this type of laser that was able to produce 10 μm fingers, with an aspect ratio of 15, as shown in Figure 3.29.

The results of the study are shown in Table 7.1 and indicate the difficulty in machining both stainless steel and glass with an excimer laser, as only A1 and A2 produced measurable results. Furthermore, it can be seen that long process times were necessary because only a low power could be used to avoid damaging the arrays [1].

Table 7.1 The dimensions and process time for each set of machining parameters [1]

Sample Number (Material)	Array Size	Border Width	Pillar Pitch	Depth	Process Time
A1 (316)	1mm x 1mm	0.5mm	50 μm	~ 80 μm	55 min
A2 (316)	1mm x 1mm	0.5mm	50 μm	~ 50 μm	135 min
A3 (316)	1mm x 1mm	0.05mm	50 μm	N/A	170 min
A4 (316)	1mm x 1mm	0.5mm	50 μm	N/A	40 min
A5 (glass)	1mm x 1mm	0.25mm	50 μm	N/A	30 min

Example images of the arrays are shown in Figure 7.1 and Figure 7.2 and correspond to sample numbers A1 and A4 respectively and are considered representative of all of the samples. It can be seen from Figure 7.1, the highest aspect ratio sample, that the dimensional accuracy is poor and shows pillars with curved tops. Figure 7.2 shows pillars with flatter tops but it was not possible to produce pillars with an acceptable height. The results presented here indicate that a 50 μm pillar width and 20 μm kerf are not achievable in these materials.

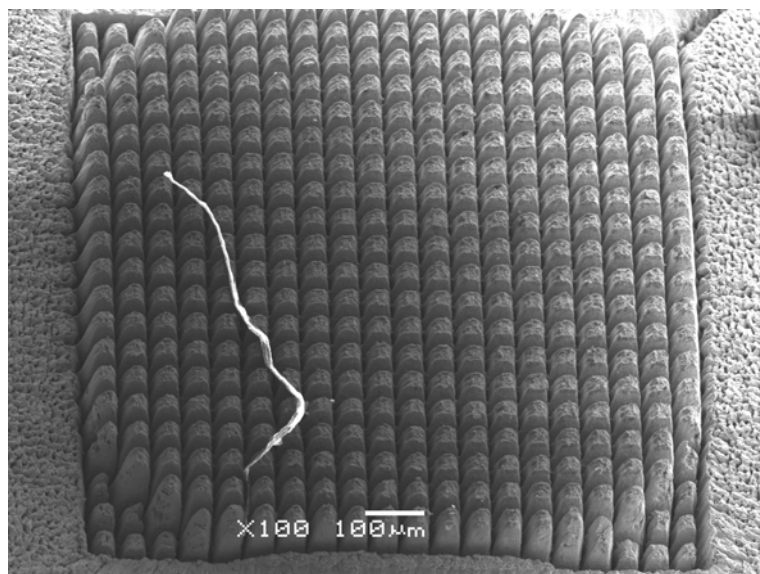


Figure 7.1 Highest aspect ratio laser machined pillars in stainless steel (A1)

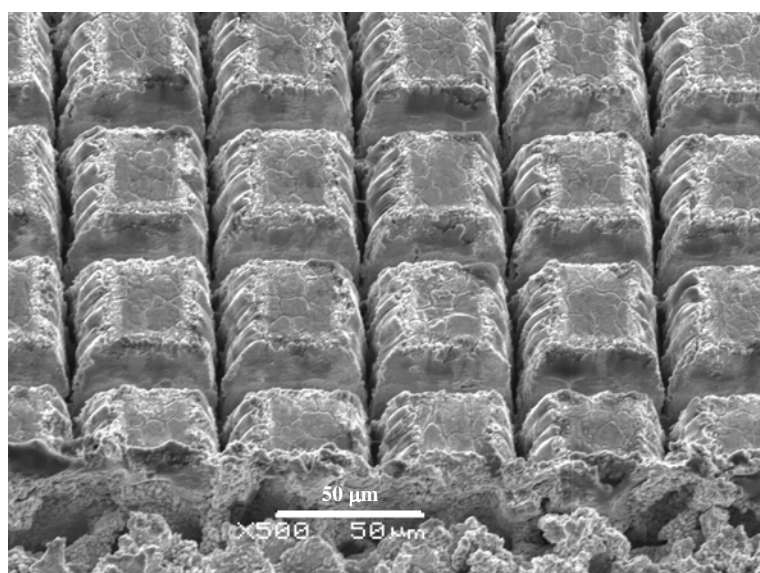


Figure 7.2 More defined pillars laser machined in stainless steel (A4)

7.1.2 Indirect Fabrication of the Master Tool

From the first feasibility study it was obvious that machining high aspect ratio structures with a pillar width of 50 μm and a kerf of 20 μm is difficult, not only because of the small feature size but also because of the choice of material. The literature review indicates that excimer lasers are more successful with organic materials such as polycarbonate. Machining of a

polycarbonate perform was carried out that could then be electroformed into a master tool. To this effect a second study was carried out which aimed to machine 200 μm diameter holes in 200 μm thick polycarbonate to investigate the control over the taper.

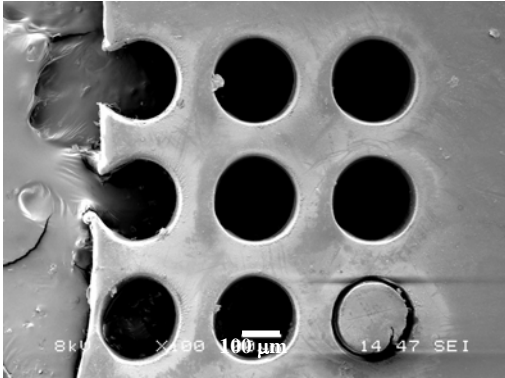


Figure 7.3 Plan view of 200 μm diameter holes laser machined into 200 μm thick Polycarbonate

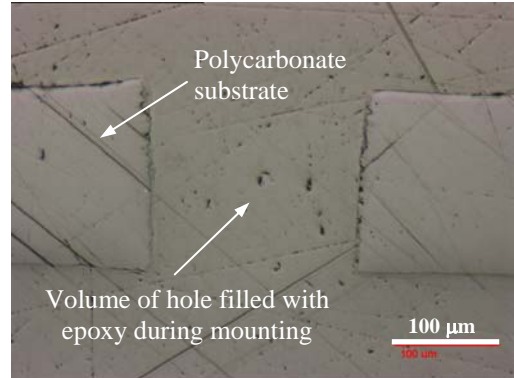


Figure 7.4 Cross section view of polycarbonate hole showing the taper and the rough surface

As in section 7.1.1, the work was carried out by the UK-LMC at a range of parameters to produce the small array of holes shown in Figure 7.3. The holes were also mounted and cross-sectioned using standard metallographic techniques and are shown in Figure 7.4.

It can be seen in Figure 7.3 that the base of the holes in the array are not visible, and therefore the most appropriate way to measure the taper was to mount and cross-section the array. However, because the holes are cylindrical, the amount of material removed affected the accuracy of the method. By assuming the holes are perfectly circular, and drawing them in the visualisation software PowerSHAPE, Delcam, Birmingham, we can calculate the accuracy of the measurements.

Figure 7.5 shows a 200 μm tapered hole with lines indicating the shape of the hole after a proportion of the material is removed. These lines correspond to 5 % increments, and can then be used to calculate the size of the taper, as shown in Figure 7.6. Thus, if exactly 50% of the hole was removed, the taper would measure 3.68° , if 60% was removed the taper would be 3.76° and if 70% was removed the taper would be 4.05° . In addition, the results are symmetrical such that if 30% to 70% of the material is removed the taper would be $3.68^\circ + 0.37^\circ$.

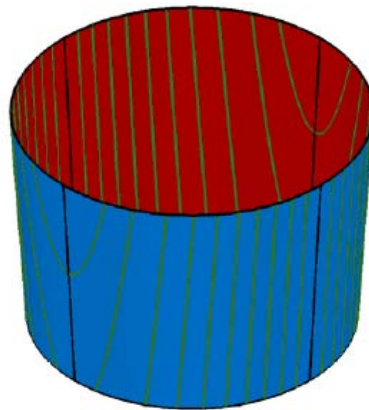


Figure 7.5 200 μm diameter tapered hole with lines indicating the shape of the hole if 5 % of the material was removed at a time

The cross-sectioning problem was only realised after machining, so that there was no way to determine how close to the centre of the hole the imaged face of the sample was. Therefore, it was assumed that between 30 and 70% of material had been removed, such that sample A was found to have a taper of $1.83^\circ + 0.18^\circ$, and sample B was found to have a taper of $3.68^\circ + 0.37^\circ$ region.

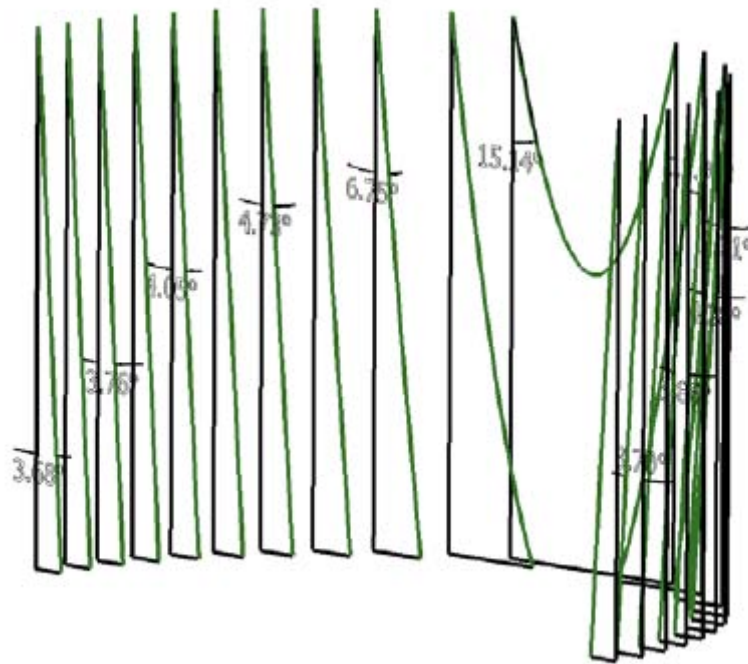


Figure 7.6 The taper measured after different proportions of the hole have been removed. The lines show 5% increments

The tapers demonstrate that tapers can be produced within the 0° to 4° range. However, the investigation does not demonstrate that a suitable aspect ratio, feature size or surface finish could be obtained. The surface finish of the hole in Figure 7.4 does not look smooth. However, the undulations correspond to a roughness of $\sim 1.5 \mu\text{m}$ to $5 \mu\text{m}$, which could easily be caused by the grinding media. The smoothest structure in Table 3.8 was a rotor [2] which had a surface roughness of $0.1 \mu\text{m}$, but did not have the high aspect ratio, nor a particularly small feature size [2].

The two feasibility studies demonstrated that the most feasible way to obtain a master tool would be by indirect fabrication, whereby a polymer preform is machined before electroforming a master tool. The required taper angle is achievable using excimer laser ablation. However a good surface finish has not been demonstrated in these studies, or in the

literature. Furthermore, the holes will be required to have a higher aspect ratio than has been demonstrated here, which was not thought to be achievable by the UK-LMC whilst maintaining an adequate surface finish.

7.2 Feasibility Study of the Bosch Process

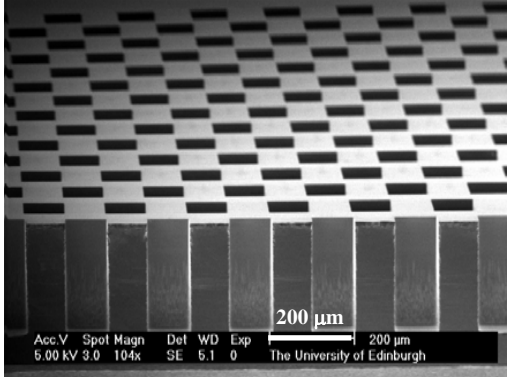
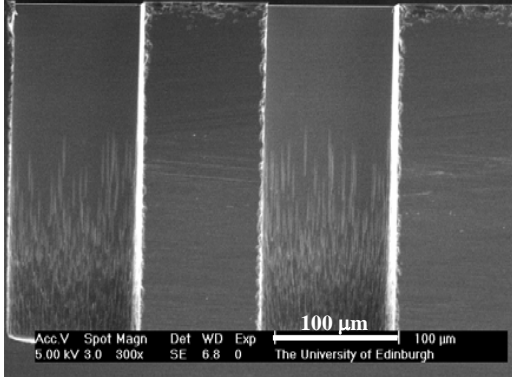
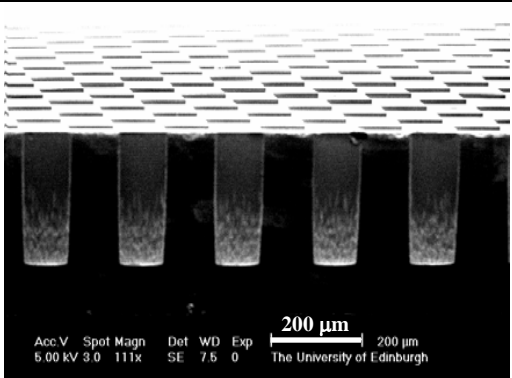
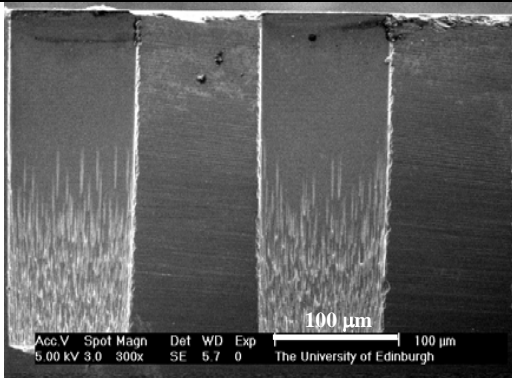
The Bosch process was also investigated as a means of producing a master tool for hot embossing. The approach aimed to fabricate the master by an indirect approach, aiming to etch an array of cavities rather than pillars. The process is capable of producing a positive structure, as shown Figure 3.36, but this would only be possible in silicon and would not be sufficiently durable. In addition, the smaller feature size and lower aspect ratio of the cavities is a more achievable challenge than trying to etch the high aspect ratio, small feature sized grooves. In order to assess the feasibility of the process, an existing mask was used at the SMC to etch 275 μm deep features. The mask had 100 μm , hexagonally packed, square holes and a kerf of 50 μm . The aim was to identify if the appropriate size, aspect ratio, taper and surface finish could be achieved using different etching parameters.

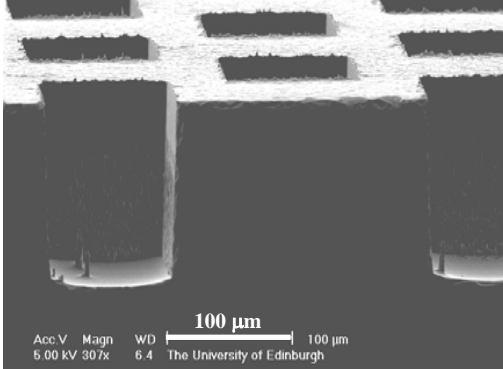
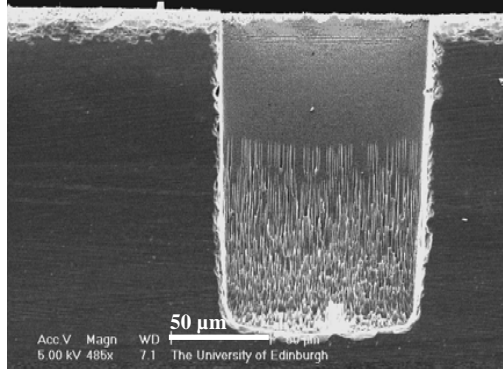
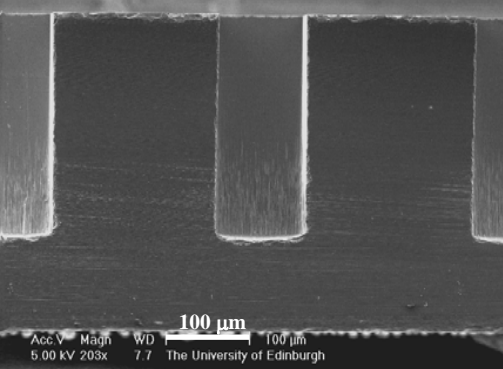
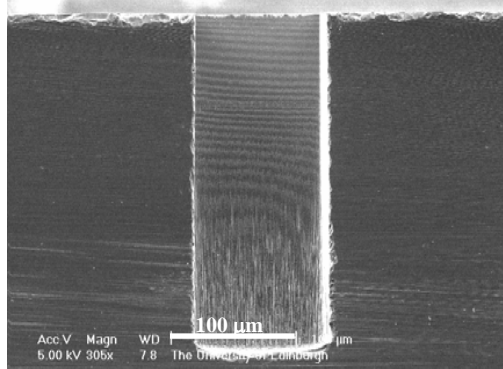
The results of the feasibility study are shown in Table 7.2 [3] and it can be seen that by varying the different process parameters, tapers ranging from -0.2° to 2.6° , aspect ratios of 1.3 to 2.4, and cavities ranging from 98 to 109 μm can be etched. This demonstrates that the target aspect ratio of the cavities can be achieved, as can the feature size and cavities within the specified taper range.

It will also be observed from the table that the size of the cavities varies by $\sim 25\%$. However, this represents the variation between arrays across the wafer, rather between neighbouring cavities. Therefore, it is not thought to be a problem during master tool fabrication, as only one array will be used rather than the whole wafer.

The Ra was found to be 0.015 to 0.025 μm at the top of cavities and $> 0.045 \mu\text{m}$ at the bottom [4]. These values are significantly less than the 90 nm required for master tools as described in section 3.2. In addition, it was felt by the SMC that the surface finish could be improved further by reducing the amount of passivation, or by other post processing techniques. However, the feasibility study concluded that the process was repeatable but the taper could not be predicted [3].

Table 7.2 The results of the feasibility study into the etching of silicon performs for producing a master tool [3]

Etch Cycle	Results	Etched Structures		Comments
SCUBA_61	<p>Depth: $274\mu\text{m} \pm 3\mu\text{m}$ Cavity width: $99\mu\text{m} \pm 25\mu\text{m}$ Taper: 1.12° Aspect ratio: 2.77:1</p> <p>Time: 2hrs 5mins Etch rate: $2.2\mu\text{m} / \text{min}$ Etch uniformity: 98.8% Selectivity Si to oxide: 500:1</p>	 <p style="text-align: center;">Top of the wafer</p>		<p>Measurements on 15 chips</p> <p>$1\mu\text{m}$ of oxide as mask was enough</p>
		 <p style="text-align: center;">Bottom of the wafer</p>		

XR_7	<p>Depth: $151 \mu\text{m} \pm 8 \mu\text{m}$ Cavity width: $98 \mu\text{m} \pm 17 \mu\text{m}$ Taper: 2.6°</p> <p>Time: 2hrs Etch rate: $1.26 \mu\text{m} / \text{min}$ Uniformity: 94.5%</p>			<p>Measurements on 9 chips</p> <p>The oxide mask was etched away before reaching target etch time of 2hrs 36mins</p>
XR_5	<p>Depth: $265 \pm 4 \mu\text{m}$ Cavity Width: $109 \mu\text{m} \pm 2 \mu\text{m}$ Taper: -0.2° Aspect ratio: 2.43:1</p> <p>Time: 2hrs 13mins Etch rate: $2 \mu\text{m} / \text{min}$ Etch uniformity: 98.7%</p>			<p>Measurements on 8 chips</p> <p>Oxide plus photoresist mask were just enough</p>

7.3 Master Tool Fabrication via the Bosch Process

The feasibility study has demonstrated that the Bosch process is capable of providing a route for the fabrication of the master tool. It was identified that several issues remained, including the ability to predict the size of the taper and the variation in the size of the cavities. The aim was to fabricate these master tools according to the designs described in section 6.5, such that five master tools would be produced that had the same pillar width, at half the absolute height, and only varied according to their taper.

The variation in the size of the cavities, which is seen across the wafer, was accounted for by placing the five designs (denoted 1-5) in a staggered formation as shown in Figure 7.7. By arranging the designs in this method the fluctuations in etching can be reduced because there is a design in each position.

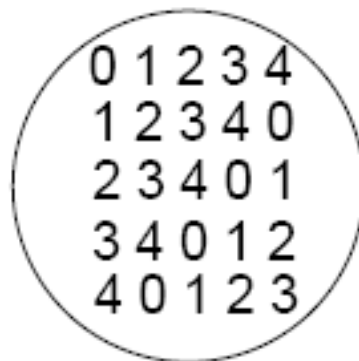


Figure 7.7 The arrangement of the mask designs on the wafer for Bosch etching

The nature of the Bosch process means that the size of the features are defined by the mask, thus as the taper angle changes, the size of the pillars at the top and the bottom change. If the taper could not be predicted it is difficult to design a mask accordingly. Fortunately, the size of the master tool is small relative to the size of the wafer. This means that a range of designs, corresponding to taper angles of 0° , 1° , 2° , 3° and 4° , can be used on the same mask.

The designs for the mask are described in Table 6.1 and aimed to etch fully through a 400 μm wafer.

By using the approach described above, it was felt that there would be a good chance of achieving a range of master tools that could be used to study the effect of taper on de-embossing and piezocomposite performance. However, the size and the depth of the design proved difficult to achieve, whilst also maintaining the uniformity of the holes and surface roughness. Originally, as described in section 6.5, it was hoped that a larger feature sized master tool could be produced that had 150 μm wide cavities and a depth of 500 μm , which would have made hot embossing and lapping easier.

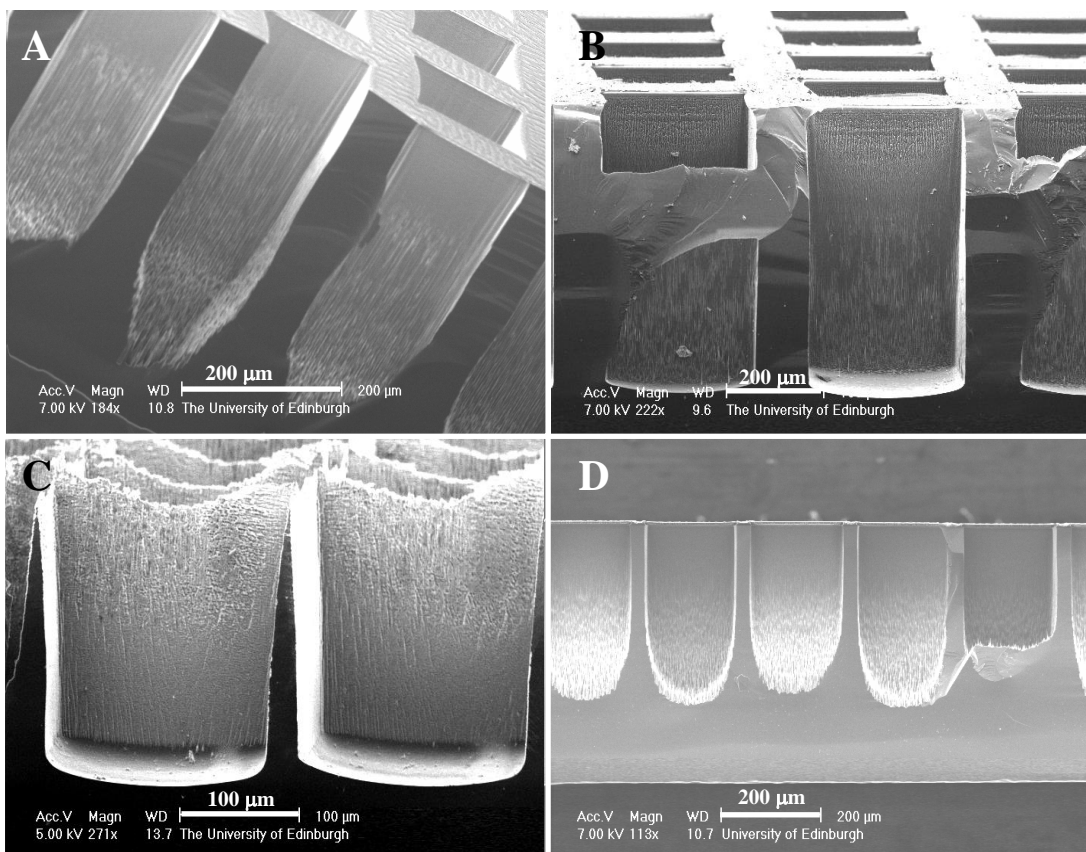


Figure 7.8 Example images of the failed attempts to produce pillars of depth 500 μm and width 150 μm

Several established etching programmes were used, and the most successful programme was then modified to try and improve on these results. However, no improvement was seen when this approach was used. The SMC were then advised by the manufacturers of the etching equipment on three possible procedures to use. These all did not produce satisfactory results. Some examples of the failed attempts to achieve the 500 μm depth are shown in Figure 7.8. Typical issues involved: the loss of the cavity shape at deep depths (A and D); etching of the mask before the required depth was reached (B); and the undercutting of the mask which led to the destruction of the cavity walls (C). The difficulties seen in achieving these depths are unsurprising, as similar behaviour of deep structures has been observed in the literature review.

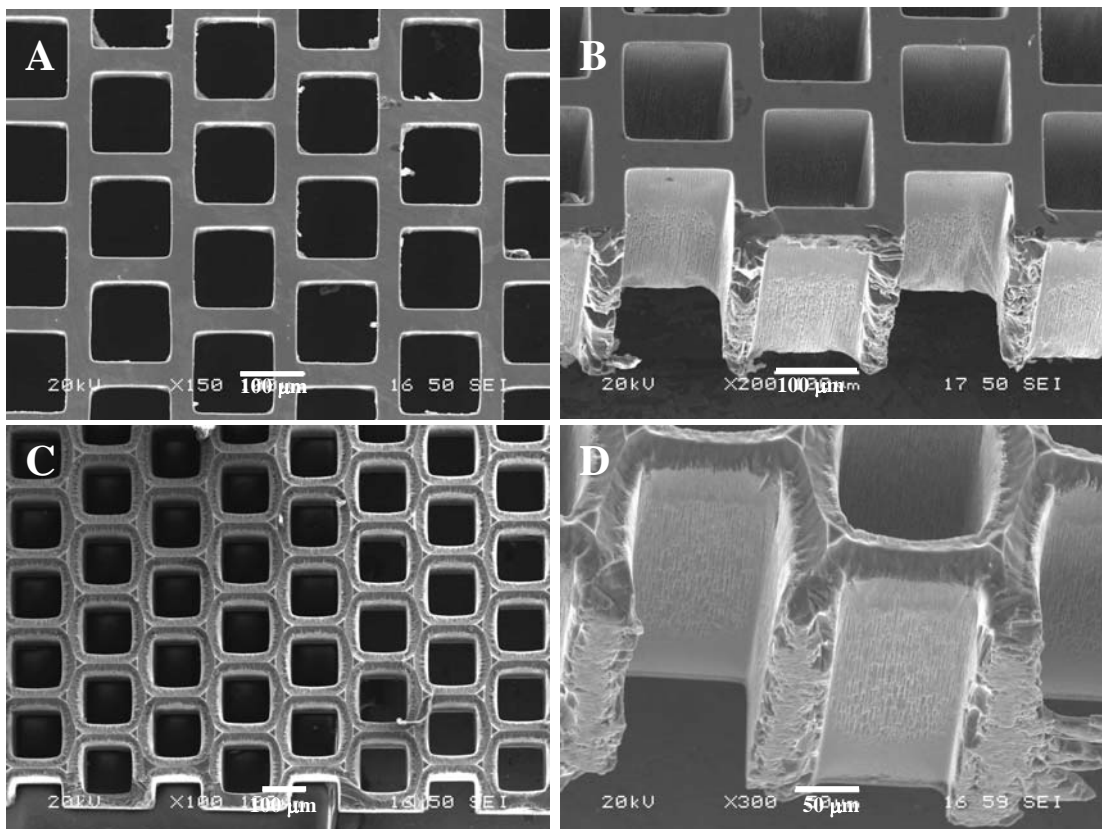


Figure 7.9 Images of successfully etched silicon

The largest problem was achieving a depth of 500 μm without the loss of the surface finish, or cavity geometry. The solution to this was twofold. The first was to reduce the depth to 400 μm and the width of the cavities to 112 μm , as discussed in section 6, and the second approach was to use a different etching procedure.

Previously, all etching had been carried out using a mask whose dimensions corresponded to the bottom of the pillars of the master tool. Thus, at the top of the silicon wafer, the etched cavity would be at its largest, and at the bottom the cavity it would be at its smallest. This approach is the conventional method of etching, and provides easier access for the plasma, and etching and passivating gases. However, the Bosch process is also capable of producing a negative taper, such that the cavity starts at a narrow opening and widens. Since we aimed to etch all of the way through the wafer, it is possible to use this approach, whereby the top of the wafer now corresponds to the top of the pillars of the master tool. Examples of the structures produced by this approach are shown in Figure 7.9 where images A and B are from the 3° design and C and D are from the 1° design. The depth is $\sim 400 \mu\text{m}$, however the taper and actual feature size is difficult to measure from these images. A more accurate approach is to measure the master tool after it has been electroformed from the silicon performs, which is discussed in section 7.4.

7.4 Electroforming of Silicon Pre-forms

Electroforming was carried out by the Micro-engineering and Nano-technology Research Group, The University of Birmingham. The cavities etched by the Bosch process present a challenge due to their $\sim 100 \mu\text{m}$ cavity width, and aspect ratio of ~ 4 . The problem is caused by the nickel film on the top of the wafer, which can grow over the cavity entrance before it has been fully filled. The solution, as previously discussed in section 3.2.6, was to attach the silicon perform to a conductive, gold coated wafer. Thus, the growth front of the nickel would move upwards from the conductive plate, and fill the cavities from the bottom upwards.

The width of the cavities means that the penetration of the electrolyte into the cavities was important. Thus the electrolyte contained sodium dodecyl sulphate, a surfactant to improve the wetting of the silicon, and also contained Saccharin and Coumarin, which are useful additives for forming fine scale structures, and a uniform morphology of nickel [5].

Silicon is a semi-conductor, and it does not conduct as well as gold, but does allow some nickel to be deposited on the surface of the silicon. Therefore, growth of the nickel does occur in areas other than at the base of the cavities. The growth is at its highest where there is a large current density. Unfortunately, due to the geometry of the silicon perform, the current density is at its highest at the top surface, near the entrance of the holes. Thus, the current density must be reduced to make growth at the base of the cavities more favourable than at the top. This of course affects the growth rate of the nickel, such that there is a balance to be made with time. The maximum limiting current density was calculated to be $30 \text{ mA} / \text{cm}^2$, but to ensure the cavities were fully filled this was reduced to $20 \text{ mA} / \text{cm}^2$. The total time to

fill the cavities was 24 hours, and once the cavities had been fully filled the current density was increased to rapidly produce a stock for the pillars.

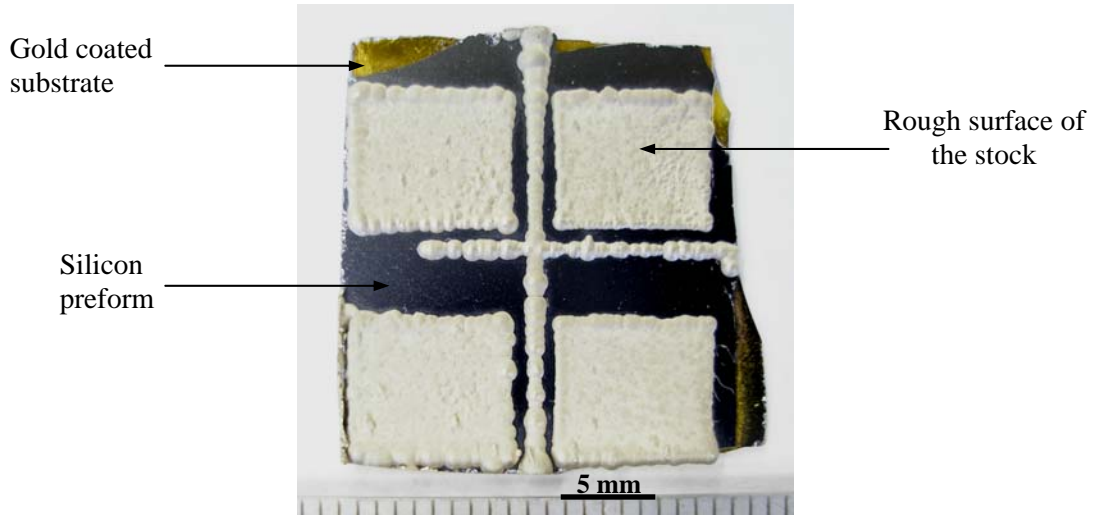


Figure 7.10 A photograph showing four master tools after electroplating. The conductive silicon plate is visible, as well as the rough surface of the electroformed nickel

An example image of the fully electroplated pre-form is shown in Figure 7.10, with the conducting gold coat coated wafer visible, as well as the rough surface of the stock. The surface of the stock was lapped, as described in section 5.2.8, to ensure that it was flat and level for hot embossing before the silicon preform was dissolved in potassium hydroxide. A selection of images of the fabricated master tool is shown in Figure 7.11. This figure shows a good uniformity of both the individual pillars and the array itself.

Three different designed pre-forms were electroformed and measured from their SEM images in a similar way to that outlined in section 5.3. Table 7.3 shows the mean dimensions of the pillars that were measured, with the calculated error shown in the bottom row of the table. The size of the pillars varies from array to array because of the mask design, and because they were lapped to ensure parallelism.

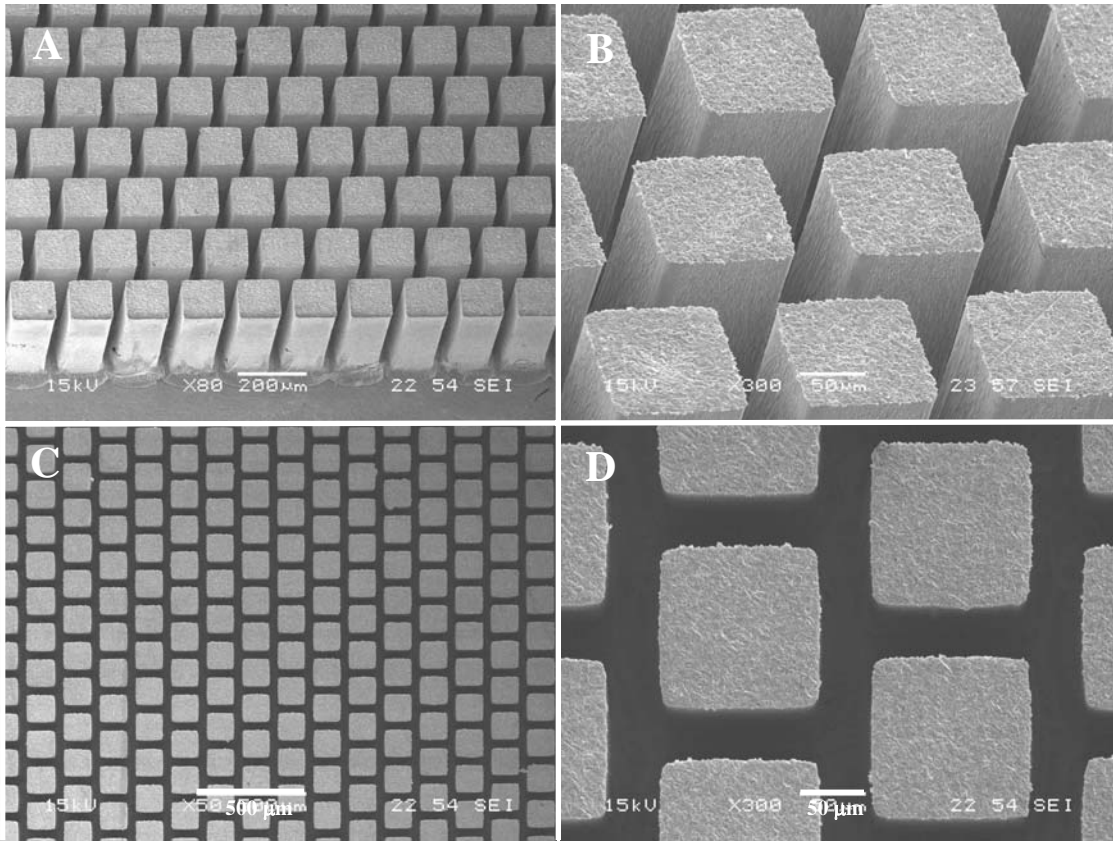


Figure 7.11 A selection of images showing the uniformity of the electroformed pillar arrays.

Table 7.3 The dimensions of the electroformed master tools

Design (°)	Pillar Width at Top (μm)	Pillar Width at Bottom (μm)	Kerf at Top (μm)	Depth (μm)	Pillar Aspect Ratio	Kerf Aspect Ratio	Taper (°)
0	121	124	42	346	2.9	8.2	0.27
2	104	108	48	318	3.1	6.6	0.34
3	99	102	55	299	3.0	5.4	0.22
Error	± 0.76	± 0.76	± 0.76	± 5.4	± 0.07	± 0.07	± 0.14

The size of the pillars varies according to the designs on the mask. It was originally planned that the same mask would be used for every etch. Thus, once a suitable set of parameters were found for a certain angle of taper, the pre-forms with the correct mask design could be set a side and another set of parameters could be used to achieve another taper. Unfortunately, due to time constraints, only one run could be carried out, with only one set of parameters, such that all of the designs had a taper of 0.3°. However, this has demonstrated

the proof of principle that the Bosch process and electroforming can be combined to produce tapered pillars. It has also demonstrated that pillars with an approximate width of $\sim 100 \mu\text{m}$, kerf $\sim 50 \mu\text{m}$, depth $\sim 320 \mu\text{m}$, pillar aspect ratio ~ 3 , kerf aspect ratio of ~ 6.5 , and a taper $\sim 0.3^\circ$ can be produced.

The dimensions of the pillars can be related back to the original mask design shown in Table 6.1. When these results are cross referenced back to the designs it can be seen that width at the top of the pillars has increased and the kerf at the top has decreased. The width at the top of the pillars has increased by between 6 and 9 μm , whilst the width of the kerf has decreased by 4 to 12 μm . This effect is mainly caused by lapping, which ensures the master tools are flat and parallel. As layers of material are removed, the taper means that the pillar gets wider and the kerf gets smaller. The larger difference between the designed and actual kerf, compared to the difference between the pillars, is also an effect of the pillar taper, which is caused by the Bosch process and not the mask design, i.e. the taper is caused by the parameters of the Bosch process. For this same reason the base of the pillars are much smaller than they were designed, and whilst the original design considered the lapping stage of the piezocomposite, it did not consider the lapping step that was necessary to ensure a parallel master tool.

The surface finish of the pillars is also a key consideration of the process, which is mainly defined by the surface finish of the Bosch process. The surface finish often degrades with the depth of the etching, such that the deeper the structure the greater the challenge. Figure 7.12 shows the surface roughness of a typical pillar, which has been estimated from the image to be a peak-to-valley height of $\sim 1 \mu\text{m}$.

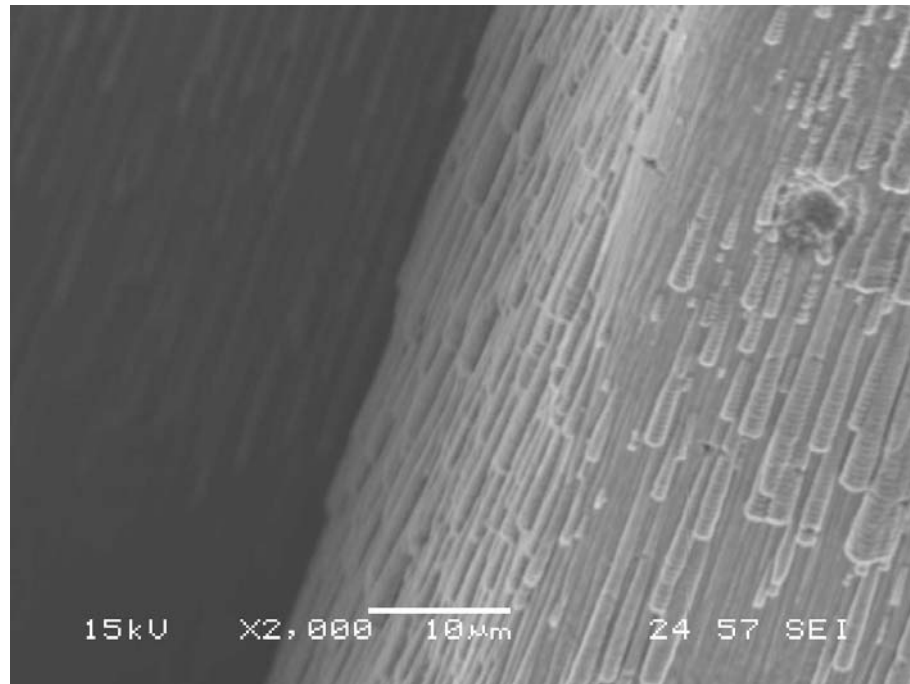


Figure 7.12 The surface finish of the electroformed pillars, estimated to be 1 μm .

7.5 Master Tool Fabrication Summary

Feasibility studies of directly and indirectly producing a master tool by laser machining have been carried out. They have concluded that the excimer laser ablation is not capable of producing a master tool with the desired requirements, because the combination of surface finish, aspect ratio, feature size and taper is too demanding.

A feasibility study into using the Bosch process to fabricate silicon pre-forms before electroforming has also been carried out. The study demonstrated that pre-forms with various tapers from -0.2° to 2.6° can be produced, with cavity widths of $98\ \mu\text{m}$ to $109\ \mu\text{m}$ and depths of $274\ \mu\text{m}$. The surface finish of these cavities was found to be $> 45\ \text{nm}$, but is almost half of the empirical limit.

Master tools have been produced using a combination of the Bosch process and electroforming. The processes have produced pillar array structures, after lapping, with a taper of $\sim 0.3^\circ$. The master tools showed a kerf and a pillar width that matched reasonably well to the original designs. The kerfs at the top ranged from $42\ \mu\text{m}$ to $55\ \mu\text{m}$, and the pillar width at the top ranged from $99\ \mu\text{m}$ to $121\ \mu\text{m}$. The depth of the master tools after lapping ranged from $299\ \mu\text{m}$ to $346\ \mu\text{m}$, which gave a pillar aspect ratio of ~ 3 , and a kerf aspect ratio which ranged from 5.4 to 8.2.

The authors that were reviewed in section 3.2.5 and Table 3.10 have been able to produce structures that have aspect ratios of greater than 6 (structure #2, #4, #6-#8, #15) [6-11], are over $300\ \mu\text{m}$ deep (structure number #7 and #8) [7] and are in hole or pillar array geometry (structure number #1-4, #14, #17, #18) [10, 11, 12]. However, none have been able to

combine all three. Often deep structures are in the form of trenches, or high aspect ratio structures are very shallow and have small feature sizes. The structures presented in this work, however, do combine all three aspects and are much improved over the literature. In particular the 0° design has shown an array with a minimum feature size of $42\ \mu\text{m}$, a depth of $346\ \mu\text{m}$, and an aspect ratio of 8.2. This represents the deepest array structure, the second deepest structure reviewed, and the third highest aspect ratio array of holes or pillars. It is also important to note that the array structures with a high aspect ratio are all very small structures and do not have depths of greater than $30\ \mu\text{m}$. Furthermore, it should also be remembered that these structures were not fully measured until the electroformed positives were produced, thus the lapping which occurs prior to this will have reduced the depth and aspect ratio. Prior to lapping, these structures can be estimated to have a height equal to the wafer thickness ($\sim 400\ \mu\text{m}$) and therefore have an aspect ratio of 9.5.

7.6 Chapter References

- [1] UK Laser Machining Centre “Laser machining of pillars in stainless steel” (26/01/06)
- [2] A. S. Holmes “Laser processes for MEMS manufacture” *2nd International Symposium on Laser Precision Microfabrication RIKEN review 4 (2002) 63-69*
- [3] C. C. Dunare “Test Wafers for Birmingham” *Scottish Microelectronics Centre, Edinburgh (2007)*
- [4] C. C. Dunare (Camelia.Dunare@ee.ed.ac.uk) “100 micron windows” *email to T J Clipsham (tjc152@bham.ac.uk) (04/05/07 14:47)*
- [5] Xueyong Wei “Nickel Electroforming for Tim” *Micro-engineering and Nano-technology Research Group, The University of Birmingham (2008)*
- [6] Scottish Microelectronics Centre “Example images from Smart X-ray Optics” *received February 2007*
- [7] A.A Ayon, X. Zhang, R. Khanna “Anisotropic silicon trench 300-500 μm deep employing time multiplexed deep etching (TMDE)” *Sensors and Actuators A 91 (2001) 381-385*
- [8] A. A. Ayon “Characterization of a Time Multiplexed Inductively Coupled Plasma Etcher” *Journal of the Electrochemical Society 146 (1) (1999) 339-349*
- [9] J-B Li, K Jiang and G J Davies “Novel die-sinking micro-electro discharge machining process using microelectromechanical systems technology” *Proceedings of the Institute of Mechanical Engineers Part C: Mechanical Engineering Science 220 (2006) 1481-1487*
- [10] A. A Ayon “Deep reactive ion etching: a promising technology for micro- and nanaosatalites” *Smart Materials Structures 10 (2001) 1135-1144*
- [11] Scottish Microelectronics Centre “Example images” *received February 2007*
- [12] R. Nagarajan et al “Development of dual-etch via tapering process for through-silicon interconnection” *Sensors and Actuators A 139 (2007) 323-329*

Chapter 8

Design, Fabrication and Optimisation of the Hot Embossing Rig

8 The Hot Embossing Rig

A hot embossing machine was not available at The University of Birmingham, and to purchase one was beyond the budget of the project. However, the simple nature of the machine meant that it was possible to study the parameters required for hot embossing, and to identify the limits of other machines such that a hot embossing rig could be developed.

This chapter describes the hot embossing process, the design considerations, and the necessary modifications made to a mechanical testing machine. The chapter then discusses the familiarisation process that was used to understand the inter-related effects of each parameter; so that an optimised hot embossing cycle could be developed for the embossing of the polymer moulds.

8.1 Design Considerations and Optimisation

The essential components of a hot embossing machine have already been described in section 3.1.2, and the hot embossing cycle that has been described in section 5.1.1. The machine is required to accurately control force, displacement and temperature profiles; in terms of both set points and rate.

Hot embossing machines are commercially available, and the most popular is the HEX 01 from Jenoptik, Jena, Germany [1-8]. Hot embossing machines consist of heated platens, which are also water or oil cooled, and have force - displacement control and a vacuum system. Due to the cost of such a system, some research groups have modified either a pneumatic press or a materials testing machine for hot embossing [9-13]. Of particular

interest to this study is work done at the Massachusetts Institute of Technology (MIT), where an Instron mechanical testing machine has been successfully converted to a hot embossing rig [12, 13].

The intention in this project is to modify a 5507 Instron materials testing machine using water cooled heated platens that were purchased from Specac Ltd, Kent. The aim of this section is to describe the work completed and the considerations involved in modifying an Instron into a hot embossing rig. The Instron can be used to control and obtain force – displacement data, whilst the platens and control box will control the temperature of the master tool and polymer substrate. The use of a vacuum system has not been investigated because of the anticipated cost and difficulty in sealing the moving parts. Furthermore, it is believed that a vacuum is only necessary for geometries [9, 10, 14], such as micro-lenses, where the air is required to be removed before embossing the polymer into a closed, hemispherical cavity.

8.1.1 Heated and Water Cooled Platens

8.1.1.1 Embossing Temperature and Pressure

The temperature and pressure that the polymer is exposed to, and the rate at which they are applied, is very important in obtaining a satisfactory micro scale structure because they influence the way the polymer flows. Complete viscous flow is not necessary for hot embossing. However, the temperature should be sufficient for the polymer to flow without inducing large amounts of stress into the embossing and be cool enough to maintain a stable structure [11]. The actual values of the load and temperature are dependent upon the size and geometry of the master tool as well as the polymer used. Table 8.1 shows the range of parameters used to replicate the different structures, and specifies what machine was used.

These parameters can be used to get an idea of the range and accuracy of the parameters required for a hot embossing rig.

It has been stated in [9, 10] that the embossing pressure should be between 0.5 and 2 kN / cm² (5 to 20 N / mm²) and in the majority of cases the table agrees. In some of the procedures in the table only the load is given, and the pressure cannot be calculated. Some procedures do show much higher operating pressures, such as the micro fluidic grooves that used an embossing force of 4.4 kN over a 50 mm². However, this high pressure is used in conjunction with a very short embossing time of 1 to 25 s, whilst the other times presented in the table are of the order of minutes. The master tools used throughout this work have an area of ~1 cm² such that the required load of the hot embossing rig is up to 2 kN.

Table 8.1 A summary of the parameters and capabilities of the hot embossing machine used in the literature, including the replicated structure and material

Ref	Structure (and material)	Temperature	Applied Load	Hold Time	Vacuum	Other comments
[9]	Low aspect ratio, 5 μm pitch optical diffraction wave structure (PMMA & PC)	Up to 205°C	80 bars (8 N / mm ²)	Unknown	Unknown	Pneumatic Cylinder Press , (optimum temp of PMMA 140°C)
[15]	Microfluidic Grooves (PMMA)	146°C (+40°C)	Touch force, Emboss force 4.45 kN	15 min	To avoid air entrapment	MTP-10 (press with vacuum attachment) Force still applied when cooling and held just below T _g for 5 min, to avoid shrinkage problems. Whole process took 1hr. De-embossed at room temperature
[10]	Microfluidic Grooves (PMMA-like photo resist)	Up to 300°C	Up to 4.4 kN +- 1N over an area of 50 mm ²	1-25 s	Unknown	One ton force sensing arbour press Total embossing time 30 – 65 s
[14]	Micro Lens Array (PC)	Unknown	Touch force 100 N, Emboss load 300 N to 1.3 kN	20 min	Unknown	Procedure Only Heat rate 10°C/min, cooling rate 4°C/min, load should be kept on during cooling to reduce shrinkage. De-embossed at 80°C
[11]	Mesh structure. Aspect ratio 2.5 and 40 μm wall. (PMMA)	140°C	1 kN	60 s	Unknown	Machine developed at AIST Fluoride and phlorocarbon release agents, de-embossed at 95°C
[1]	High aspect ratio comb drive (PMMA)	130°C	Touch force 300N, emboss force 3.5 kN	Touch 5 min Emboss 1 min	3 mTorr	HEX 01 Whole process 20 min. De-embossed at 85°C
[2]	Microfluidic channels (PC)	115°C	Touch force 250N, Emboss 2.5 kN	Touch 30 s, Emboss 5 min	Yes	HEX 01 Demoulded by hand (de-embossed at 45°C)
[3]	Variety of high aspect ratio, low feature sized structures. (PMMA & PC)	100 – 180°C (T _g +25 °C to T _g +40 °C \pm 1 °C)	20 – 30 kN 5 to 20 N/mm ² \pm 0.1 N/mm ²	-	10 ⁻¹ mbar	HEX 01 , sensor feedback controlled force, high heat capacity oil used for cooling – can achieve same heating rate as heating stage. Cooled under load. De-embossed at 95°C for PMMA and 135°C for PC
[4]	Grooves and wells (PC, PMMA & Polyvinyl butyral)	(T _g +25 °C to T _g +40 °C \pm 1 °C)	5 to 20 N/mm ² \pm 0.1 N/mm ²	-		Pneumatic cylinder pump , constant compression force, cartridge heaters to heat plates, air or water based cooling system, thermocouples in insert and polymer substrate.
[5]	VP Embossed Pillars (PMMA)	T _g +25 °C to T _g +35 °C	2.5 to 3.5 N/mm ²	30 to 60 s	Yes	HEX 01 De-embossed at room temperature
[12]	MIT letters, 0.9 μm depth, 2 μm wide bars (PMMA)	Up to 150°C, typically 135°C	90N, Touch force 10N	240s	None	Modified Instron Cross-head speed 0.075 mm/min, cooling rate 150°C to 50°C in 5 min (de-embossed at 60°C)

Polymethyl methacrylate (PMMA) and polycarbonate (PC) are commonly used in hot embossing because they are fully amorphous and can be easily formed at temperatures just above their T_g. The T_g of PMMA and PC is ~ 100°C and ~ 150 °C respectively, which means that forming can be completed at easy to achieve temperatures that minimise energy, cycle time and shrinkage. Typically, hot embossing is carried out at temperatures that are 20°C to 40°C above the glass transition of the polymer such that the typical operating temperature required is from 120°C to 200°C [9, 10]. It can be seen from Table 8.1 that these operating temperatures are fairly typical. Therefore the heated platens for the rig must be able to achieve an operating temperature of > 200°C, so that either PMMA or PC can be hot embossed.

Obviously it is favourable to have the heating elements capable of achieving a higher temperature such that the heating elements are not operating at their maximum capacity. However, the temperature that the hot embossing was achieved at is often quoted rather than the capacity of the machine. In some cases though, the maximum temperature has been quoted, and, for one machine, it is up to 300°C [10]. The highest temperature noted on the commercial machine, the HEX 01, data sheet is 220°C ± 2°C, but can be upgraded to 320°C [16]. In the case of the Instron that was modified by the Massachusetts Institute of Technology (MIT) the maximum temperature reported was 150°C ± 1°C [12]. The maximum temperature for the Specac platens is 300°C ± 1°C [11], and will operate comfortably at the maximum PMMA embossing temperature of ~ 150°C.

8.1.1.2 Cooling Rate

Once the polymer substrate has been embossed it is cooled to below the glass transition temperature of the polymer. At this point the master tool and embossing are separated in a de-embossing phase. Table 8.1 shows that this can be carried out at range of temperatures ranging from 60°C to 95°C for PMMA. In some instances, de-embossing has been carried out at room temperature. However, this has only been achieved for low aspect ratio, microfluidic grooves, or the authors have struggled to achieve high aspect ratios [5]. It is not favourable to de-emboss high aspect ratio structures at room temperature for several reasons. Firstly, the polymer will shrink more when there is a large difference between the embossing and de-embossing temperatures. This leads to a greater de-embossing force at lower de-embossing temperatures. Secondly, the polymer will have greater flexibility close to the glass transition point, and therefore is less likely to crack. Thirdly, using a higher de-embossing temperature will minimise the cooling, and therefore the cycle time.

The cooling rate is important to control because if the rate is rapid, the shrinkage will be minimised and so will the de-embossing force. However, the mould will have a high residual stress, which may weaken the embossing and thus cause fracture during de-embossing. It is therefore necessary to find a balance between these two factors, and to have the ability to use a large range of cooling rates during de-embossing. The effect of the cooling rate is also dependent on the geometry, such that the best cooling rate for all structures is difficult to define and is often found experimentally. Furthermore, the cooling rate is rarely reported in the literature, and the best approach is to be able to study a broad range of cooling rates. Thus, a rapid maximum cooling rate is necessary because the rate can then be slowed to other rates by using the heating element and the thermal controller.

In the literature, where the cooling rate has been reported, it has been said that the cooling rate should be similar to the heating rate [3]. Therefore, from section 8.1.1.3, the cooling rate should be between $0.16\text{ }^{\circ}\text{C} / \text{s}$ and $0.46\text{ }^{\circ}\text{C} / \text{s}$. In another paper, a cooling rate as low as $4\text{ }^{\circ}\text{C} / \text{min}$ ($0.07\text{ }^{\circ}\text{C} / \text{s}$) has been reported [14]. Commercial hot embossing machines such as the HEX 01 offer a cooling rate from 180°C to 60°C in less than 7 minutes ($0.29\text{ }^{\circ}\text{C} / \text{s}$) [16]. The Instron modified by MIT has a reported cooling rate of $1.3\text{ }^{\circ}\text{C} / \text{s}$ [3, 13]. However it is likely that this is a peak cooling rate, caused by the cooling water being introduced to the hot platen at the start of the cooling sequence. The cold water will flow through the cooling channels and produce high pressure steam, causing the rapid cooling. Once the platens have cooled sufficiently, the cooling water will flow in a more conventional way. The overall time taken to cool the system from $150\text{ }^{\circ}\text{C}$ to $50\text{ }^{\circ}\text{C}$ was 5 min, giving a cooling rate of $0.33\text{ }^{\circ}\text{C} / \text{s}$ [12].

Figure 8.1 shows a drawing of the Specac platens, and shows the press plate, in the shape of an aluminium disc, on top of a water cooled block. The press plate contains the heating element and the water block is designed to thermally isolate the platens from the load frame of the Instron [18]. This means that cooling was a function of the room conditions and the platen temperature only such that the cooling rate was required to be estimated before purchasing the platens. An aluminium disc of the same dimensions as the press plate was made and heated to 150°C on a Bibby HC502 thermostatically controlled hot plate, from Bibby Scientific, Stone. The time taken for the disc to cool down was measured when it was on the bench top and when it was on a large heat sink. The cooling rate could be defined as between $0.50\text{ }^{\circ}\text{C} / \text{s}$ to $0.13\text{ }^{\circ}\text{C} / \text{s}$, which was a range either side of the commercial machine.

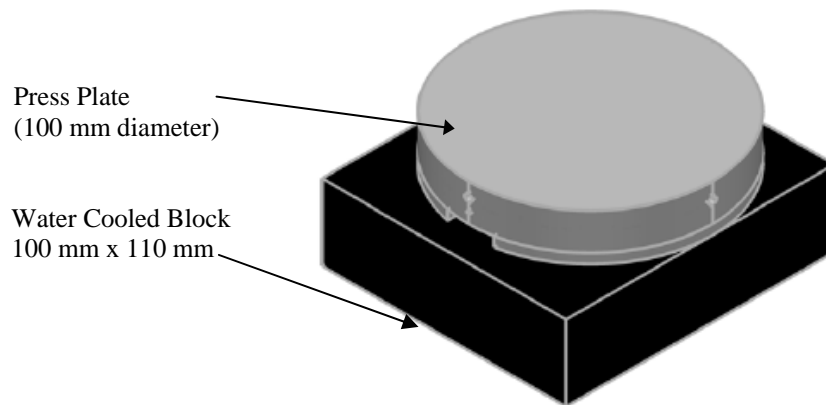


Figure 8.1 3D drawing of the Specac platen

The platens were purchased, and on delivery were tested using the mains water supply. A comparison between the performances of the platens with other machines is shown in Table 8.2, where it can be seen that the actual cooling rate before modification is very slow and was outside of the estimated range given by the experiments. It had been assumed that the press plate would be in direct contact with the water cooling block. However, upon visual inspection, it was obvious that various thermal insulating layers separated the hot press plate from the water cooled block and prevented any active cooling.

Table 8.2 The performance of the platens before and after modification and comparison to the MIT and the HEX01 hot embossing machines.

Parameter	MIT	HEX01	Unmodified Platens	Modified Platens
Maximum Temperature °C	150 (reported)	220 (320 option)	300	240 (Thermal fuse)
Heating Rate °C / s	0.46	0.29	0.92	0.82
Cooling Rate °C / s	0.33	0.29	0.11	0.44

To improve the cooling rate the platens were modified by milling an aluminium ring. This ring would fit exactly between the press plate and the water block, to provide a route for thermal conduction directly into the block. A cross-section of the platen before and after the

modification is shown in Figure 8.2. The diagram on the left shows the unmodified platen, whereby the heat is received into the aluminium press plate from the heating element, but then can only leave the plate by convection at the surface. The diagram on the right hand side shows the aluminium ring that has been clamped between the water block and the press plate. This modification allows a conduction path for the heat to leave the aluminium disc, and although the cross sectional area of the ring is small, the cooling rate is improved to $0.44\text{ }^{\circ}\text{C} / \text{s}$, which is 33 % higher than the fastest reported cooling rate [3] shown in Table 8.2.

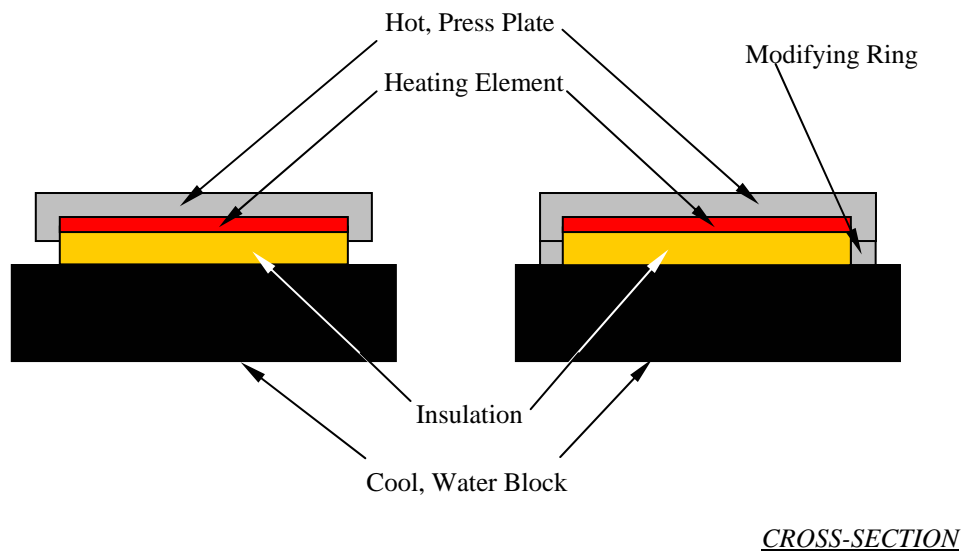


Figure 8.2 A schematic diagram of the modifications made to the Specac platens. An aluminium ring is clamped between the press plate and the water block to provide a thermal conduction away from the press plate.

8.1.1.3 Heating Rate and Temperature Control

It has already been established that the platens should be capable of achieving temperatures $> 200^{\circ}\text{C}$ and unmodified they are capable of achieving 300°C . The heating rate is not as important as the cooling rate, but in terms of cycle time it can have an important effect. The heating rate is scarcely reported in the literature, mainly because heating takes place before a load is applied to the polymer. One reported heating rate in the literature is $10\text{ }^{\circ}\text{C} / \text{min}$

(0.16 °C / s) [14]. The HEX 01 can achieve 180°C from 60°C in less than 7 minutes, which approximately corresponds to a heating rate of 0.29 °C / s [16].

The MIT embossing machine was capable of achieving 150°C in 10 minutes; using 2 x 200 W cartridge heaters and used a proportional integral controller that avoided over temperature. Assuming that the initial temperature was room temperature, this corresponds to an approximate heating rate of 0.21 °C / s [12, 13]. The Specac platens are reported to reach 300 °C in 10 minutes and use a 600 W heating element; the heating rate is approximately 0.46 °C / s [17]. The platens have the fastest heating rate reported and are more than adequate for achieving the required temperatures.

Unlike the MIT platens, water in the Specac platens is circulated during the whole hot embossing cycle. This has the advantage of avoiding pressurised steam, and provides accurate control over the cooling rate and full thermal isolation between the Instron and the platens.

Table 8.2 shows the heating rate of the platens before and after modification. It can be seen that the heating rate was reduced by 11%, but was still nearly twice the rate of the MIT platens. In reality, the modification has resulted in no loss of performance to the embossing machine because the heating rate is not critical compared to the improved cooling rate. A measurement of the cycle time was carried out by heating the platens from room temperature to 150°C and then cooling them to 80 °C. This showed that the modifications had reduced the minimum cycle time from 22 min to 7.5 min.

8.1.1.4 Clamps and Mounting Stage

After embossing, the master tool is required to be removed from the PMMA. Some research groups chose to do this by hand [2, 5, 19] but it is recommended that high aspect ratio structures are de-embossed by an automated process [9, 10]. Not only is this more convenient, but automated de-embossing provides improved control over the load, and removal rate, and allows the master tool to be removed much closer to the glass transition temperature of the polymer.

For automated de-embossing, the master tool and the polymer are required to be securely mounted and clamped to the platens. Little is mentioned in the literature about the clamping method, and it has only been recorded in [13]. The clamping method may seem trivial, but it is important to remember that adding additional thermal mass to the platens will affect the performance of the platens, particularly if the controlling thermocouple is not mounted close enough to the polymer or master tool.

Of primary concern was making sure that the additional thermal mass would not cause a reduction in the performance of the hot embossing rig. Therefore the size of the clamp was minimised, and the effect of the clamp was estimated experimentally. The experiments were conducted as in section 8.1.1.2, by heating an aluminium disc to 100°C and 150°C. In addition to the disc that represented the press plate, a smaller disc that was the same size as the clamp was placed on top. The temperatures at the surface of the large and small discs were both measured.

It was found that there was no change in the gradient of the cooling rate, but there was a delay before a change in the surface temperature could be detected. The clamp took 40 s longer to reach 100°C and 160 s longer to reach 150°C. These preliminary results indicated that there was a noticeable delay between the surface of the plate and the surface of the clamp, but both could be managed with a 3 minute dwell. In addition, a thermocouple could be mounted in the clamp to ensure that the master tool and the substrate were at the correct temperature. A second thermocouple is mounted in the platens to monitor the status of the element.

The clamp design for the polymer substrate is shown in Figure 8.3. The clamp is attached to the platen using eight bolts, which, once screwed into the platen, sit below the surface of the clamp. The clamp accepts 46.0 x 46.0 mm squares of polymer into a cavity, and has a 27.0 x 27.0 mm window so that the master tool has access to the surface of the polymer.

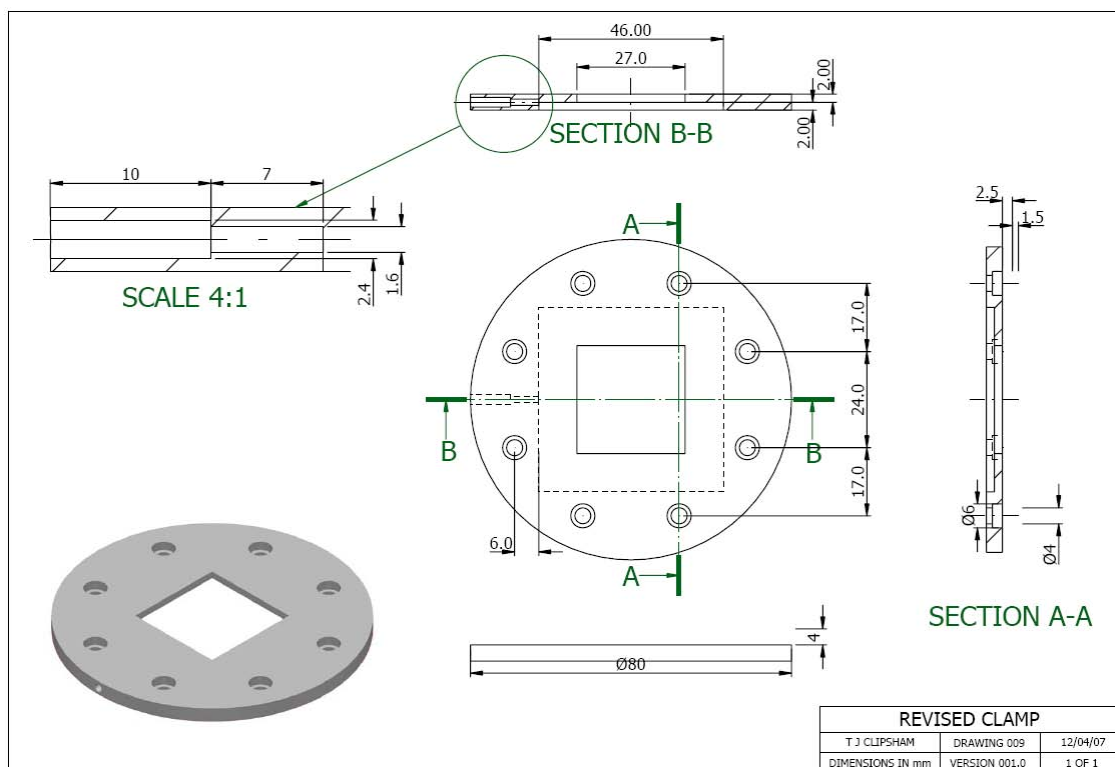


Figure 8.3 Technical drawing of the clamp for mounting the PMMA substrate

The clamp for the master tool is very similar to the clamp for the polymer substrate, but uses a slightly smaller window of 25.0 x 25.0 mm, and is used to clamp a master tool mounting stage that is shown in Figure 8.4. The mounting stage fits tightly into the cavity of the clamp such that it can not move, and the stage extends out through the window of the master tool clamp. When the hot embossing rig is in operation the raised part of the stage allows the master tool to access the clamped PMMA substrate, as shown in Figure 8.5.

The master tool is attached to the mounting stage by a thermal tape, called ‘die bonding tape’, which was supplied by Dalesway Print and Promotions. This tape allows the master tool to be attached at 80 °C, can be removed at 180 °C, and is stiff and strong for de-embossing at 65 °C. Further information on the auxiliary components of the hot embossing rig is provided in section 11.4 in the appendix.

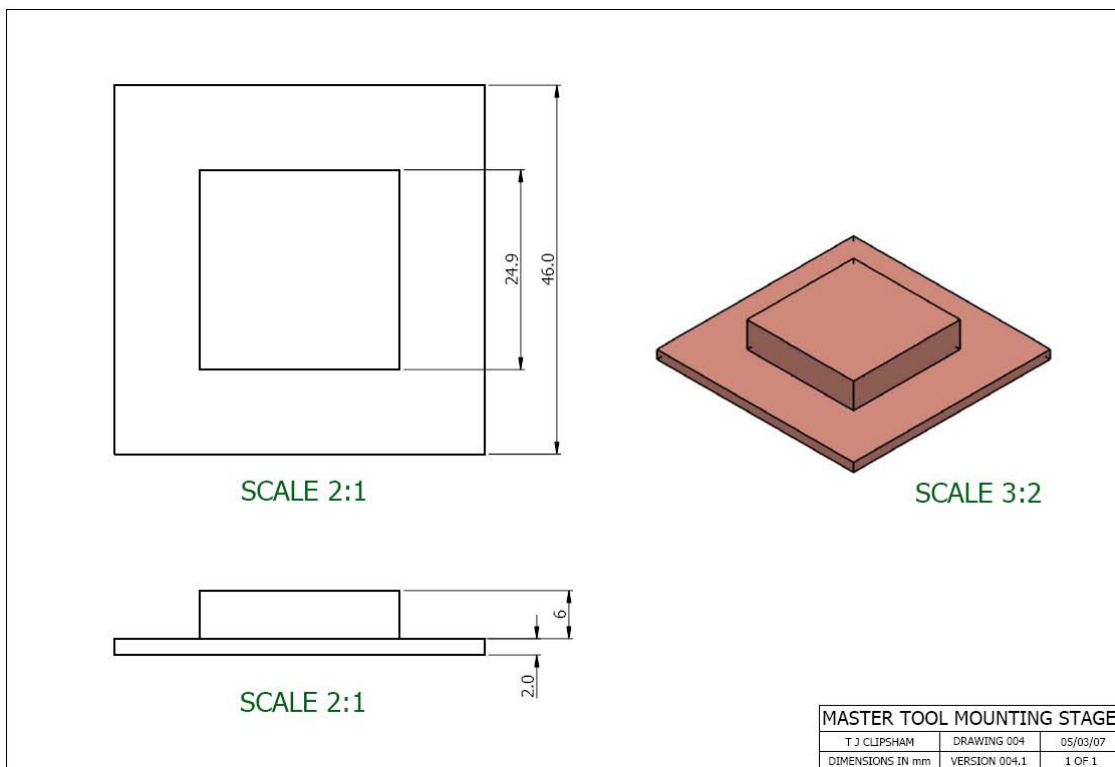


Figure 8.4 Technical drawing of the master tool mounting stage that slots through the window of the clamp

8.1.1.5 In Situ Testing

The tests after modification resulted in improved performance of the hot embossing rig. However, for these peak temperatures, heating and cooling rates were achieved using mains water. Using mains water for water cooling is not only wasteful, but the temperature fluctuation throughout the year can affect the heating and cooling rates. To solve this problem a HLA S05 chiller by Tricool, Hampshire, was introduced into the cooling system. The chiller was able to maintain the water temperature at 10°C, offering significant improvement over the mains water that had been entering the platens at ~18°C during the summer.

The cooling and the heating rate were measured with the chiller as part of the cooling system, and with the platens mounted onto a 5507 Instron. This meant that the hot embossing rig achieved a cooling rate of 0.60 °C / s and a heating rate of 0.51 °C / s. These rates are comparable to those of the commercial hot embossing machine and the modified machine made at MIT in Table 8.3. These results are favourable, and show a cooling rate that is twice the speed of the commercial machine, and a heating rate that is 76 % quicker. The cycle time was also measured, and resulted in a small increase in the cycle time from 7.5 min to 8.2 min. This increase in cycle time is not very significant compared to the ability of the hot embossing rig to achieve a greater range of cooling rates than is possible with the commercial machine.

Table 8.3 The maximum temperature, cooling and heating rates of the hot embossing rig compared to a commercial machine, the HEX01, and the materials testing machine modified at MIT

Parameter	MIT	HEX01	Modified platens with Chiller
Maximum Temperature °C	150 (reported)	220 (320 option)	240 (Thermal fuse)
Heating Rate °C / s	0.46	0.29	0.51
Cooling Rate °C / s	0.33	0.29	0.60

A photograph of the platens mounted onto the Instron is shown in Figure 8.5. The photograph shows the water block, press plate and modifying ring discussed in section 8.1.1.2 and 8.1.1.3. The mounting bars, clamps, and master tool mounting stage are also shown in the figure and are discussed in sections 8.1.1.4

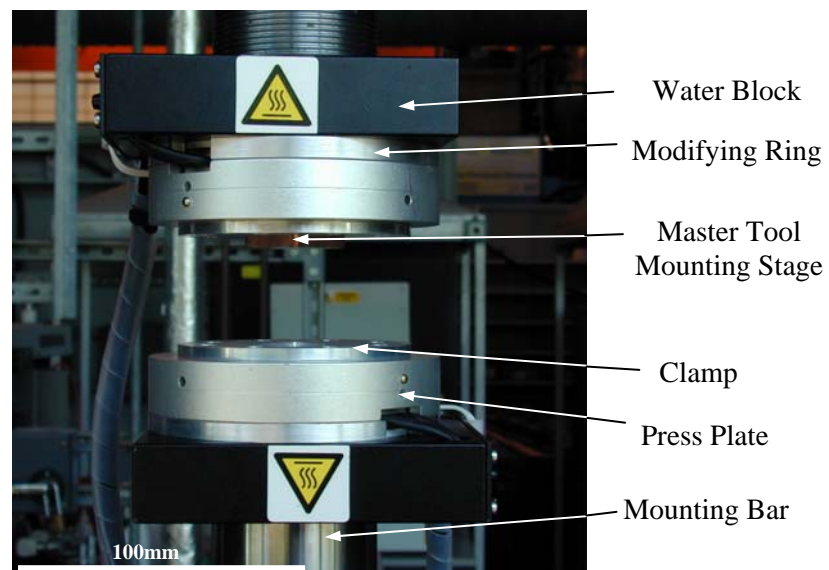


Figure 8.5 The platen assembly of the hot embossing rig

8.1.2 Control Box Specification and Design

The previous discussion has focused on the limits of the hot embossing rig, whilst the actual temperature, heating and cooling rates are controlled by the control box. There was an option

to use the control box supplied with the platens but there are several disadvantages to using it. Firstly, the supplied control box cannot control the heating or cooling rate of the platens, and, since the cooling rate affects the residual stress and shrinkage of the polymer, using this controller would limit the de-embossing conditions. Secondly, the supplied control box is designed to control the temperature using only one thermocouple mounted in just one of the platens. The design means that only one platen is accurately controlled, and the control over the second platen is made worse, the further the platens are apart. Further, the design also means that the platens are not controlled independently of each other and would limit the available embossing parameters. Therefore, it was necessary to design and build a bespoke control box for use with the platens.

8.1.2.1 Control Box Specification

The control box is required to:

- Control the temperature of each platen independently of the other;
- Control the heating and cooling rate of each platen;
- Monitor the temperature of each platen and at the surface of the tool (or substrate);
- Be safe.

In addition it is also beneficial if the control box:

- Is capable of operating just one platen;
- Will allow the temperature to be controlled by either the thermocouple mounted in the platen or the thermocouple mounted near the master tool;
- Is capable of providing feedback to the operator via Light Emitting Diodes (LED) and digital displays;

- Has a logical layout such that the information can be correctly interpreted;
- Is part of an easily removable embossing system to allow normal use of the mechanical testing machine.

8.1.2.2 Control Box Design

The temperature control of the rig is provided by two proportional integral derivative (PID) controllers. These devices use a feedback loop to adjust the actual temperature to the set temperature. These controllers are able to control a set temperature profile, with a series of set points, heating or cooling rates and temperature holds. One PID controller has been used per platen, providing independent control of the thermal profile of each platen. As will be discussed in section 8.1.1.4 the feedback is received from a thermocouple mounted in the clamp to ensure accurate temperature control. In addition, to monitor the temperature of the element a second thermocouple is mounted in the platen and is displayed, but is used for control. The control box and platens have been designed so that if necessary these thermocouples can be exchanged such that the temperature is controlled by the thermocouple closer to the element.

To ensure the safe operation of the hot embossing rig other indicators and safety devices have been incorporated into the design. The two main safety features are a water flow switch and a thermal fuse. If the water cooling is not flowing sufficiently, there is the potential of heat escaping into the load cell. Therefore, if insufficient water flow occurs the power supply to the heating elements is cut off. The thermal fuses prevent any overheating of the platens, such that they should not exceed 240°C. To help the diagnosis of either of these problems

LEDs have been added to identify if the water is flowing sufficiently and if power is being supplied to the platens.

A schematic diagram of the electrical components required for the control box is shown in Figure 8.7 and a key to the diagram is shown in Figure 8.6. The schematic diagram is split into two, the left hand side shows the schematics required for the top platen and the right hand side shows the schematics for the bottom platen. An explanation of the schematic diagram is provided below:

The latching relay is powered by 24 V and a control signal is sent through two thermal fuses (one for each platen) and a flow switch. Provided that the platens do not exceed 240°C, and that the water is flowing through the platens at a faster rate than 0.2 L / min, the relay will be switched to allow the 240 V power to the solid state relays (SSR).

The temperature controller receives an input from the thermocouple. If the temperature of the platen is less than the set value on the controller a control signal is sent to the solid state relay. The control signal then allows power to be supplied to the heating elements via the heating element socket.

	240 V Power Supply		Mains Power Input
	24 V Power Supply		Interacts with user; mounted on front of box
	Control Signal		No interaction with user; component contained in box
	24 V Control Signal		No interaction with user; Component external to box
	K –type Compensating Cable		Interaction with user whilst setting up (socket); mounted on back of box

Figure 8.6 Key to the schematic diagram shown in Figure 8.7

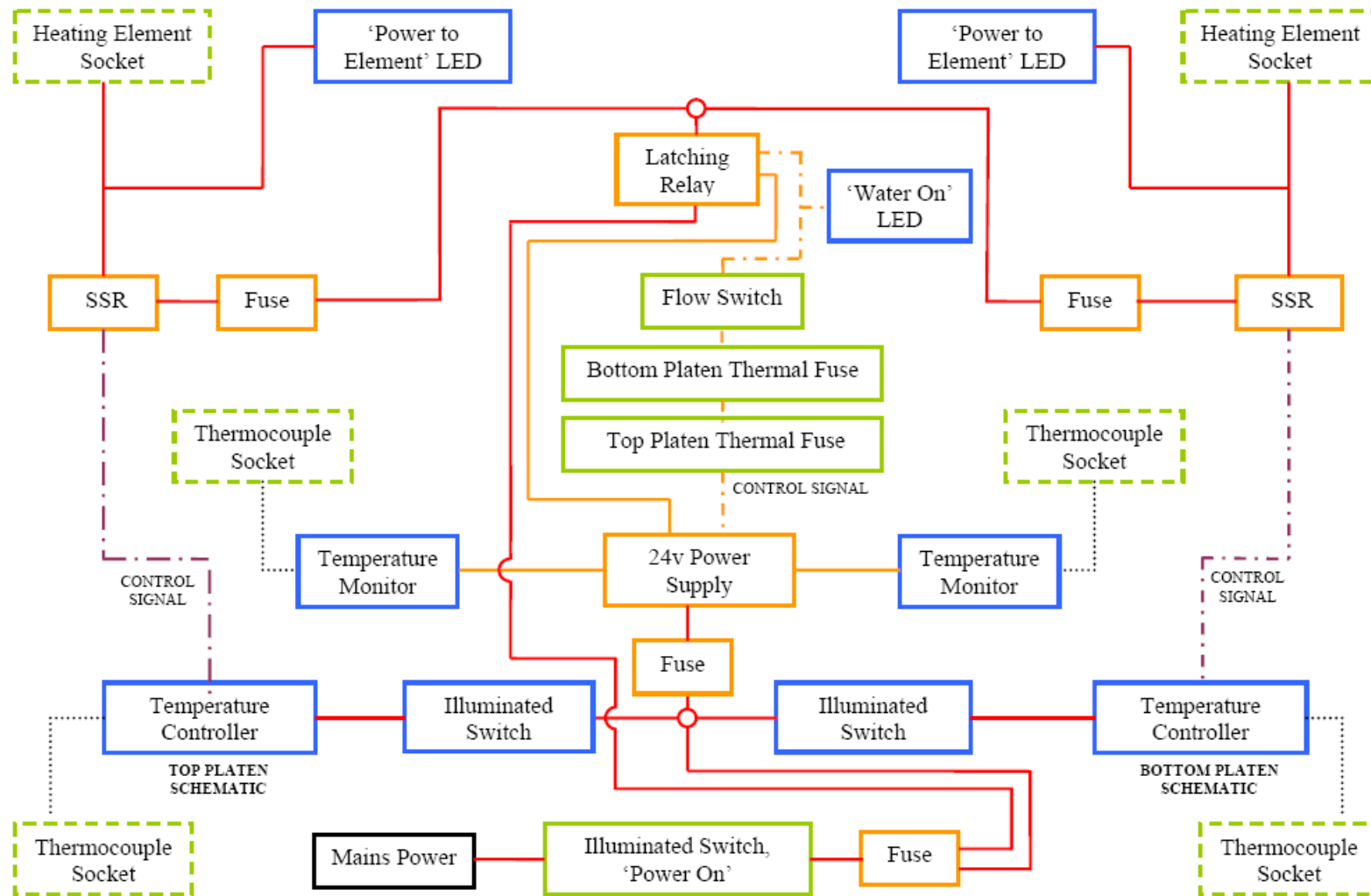


Figure 8.7 Schematic diagram of the circuit and electrical components used in the control box

8.1.3 Design and Modification Summary

A materials testing machine has been modified into a hot embossing rig. The materials testing machine will allow the control and collection of force and displacement data whilst a control box will control the thermal profile of the platens.

Section 8.1 has identified the important parameters of load, temperature and time; along with the importance of cooling rate. Heated and water cooled platens have been purchased and modified such that they are capable of operating at temperatures in excess of what is required, and are capable of heating and cooling rates that are significantly better than the machines described in the literature, including the commercial machine the HEX01. In addition, the modifications have led to a decrease in the cycle time such that more investigations and moulds can be made.

A control box has been specified, designed and fabricated to allow the independent control of each platen, in terms of rate, set point and hold time. The control box design has considered the failure of the water cooling system or over heating, whilst additional displays have been added for accurate temperature monitoring, and fault diagnosis. A diagram summarising the hot embossing rig is shown in Figure 8.8

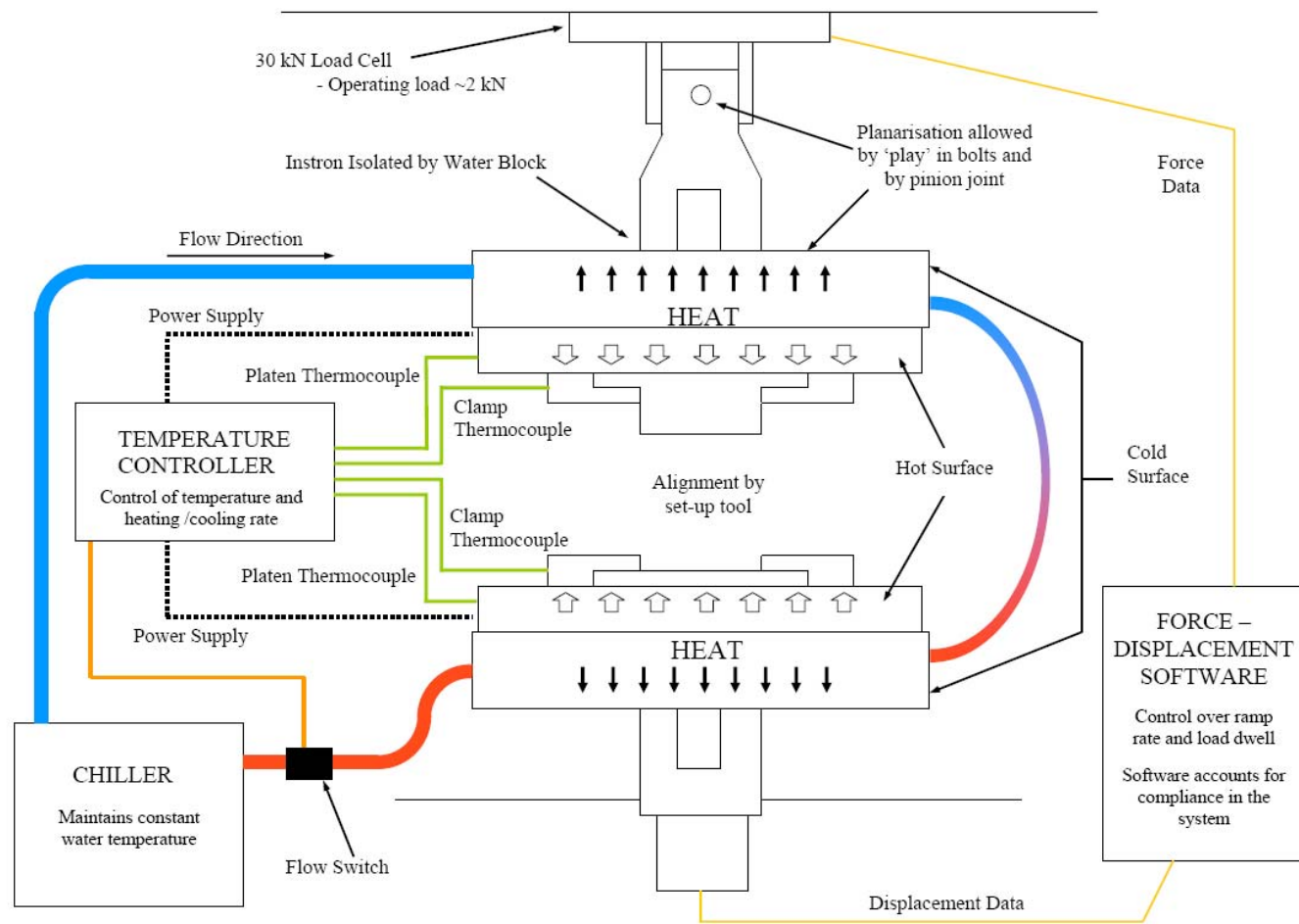


Figure 8.8 A schematic diagram illustrating the issues involved in the modification of a materials testing machine into a hot embossing rig

8.2 Hot Embossing Rig Familiarisation

The aim of this section was to familiarise the author with the hot embossing process and the bespoke rig, as well as to identify a combination of parameters to successfully hot emboss moulds suitable for the fabrication of piezocomposites. The embossing load, embossing temperature, dwell time and de-embossing temperature were all changed individually to study the effect on the quality of the embossing. Patterns in behaviour have been observed and reasons have been suggested, but not conclusively solved, since the aim was only to establish an understanding of the rig, and to develop a suitable cycle for replicating the polymer moulds. Details of the experimental procedures, and the master tool used, are given in section 5.1

The quality of the embossings was assessed in terms of the percentage mould fill, the de-embossing load and the severity of the defects seen in the embossed structure. The percentage mould fill refers to the depth that the polymer has penetrated between the pillars as a percentage of the maximum penetration possible. The de-embossing load was measured using the load cell of the Instron. It is a measure of how much force is required to remove the master tool from the embossed structure, but is also limited by areas of cavity damage or complete fracture of the PMMA mould. The third method of assessment was the severity of the defects seen in the embossed mould, which have been displayed graphically to show general trends as a result of changing the embossing load, temperature, or dwell time.

8.2.1 Master Tool Used for Hot Embossing Rig Familiarisation

The master tool used for the familiarisation of the hot embossing rig was not one fabricated by the author. The time taken to achieve the deep array structures via the Bosch process

meant that another master tool, which was supplied by the Institut für Mikrotechnik Mainz GmbH, Germany, was used to maintain momentum in the project. The master tool was made by the LIGA process, which has already been described in section 3.2.2, and inherently gives parallel walls such that it cannot be used for fabricating tapered structures to improve the ease of de-embossing. The dimensions of the master tool are: pillar width (between parallel sides) 100 μm ; kerf 40 μm ; height 450 μm ; which gives a pillar aspect ratio of 4.5, and a kerf aspect ratio of 11.3.

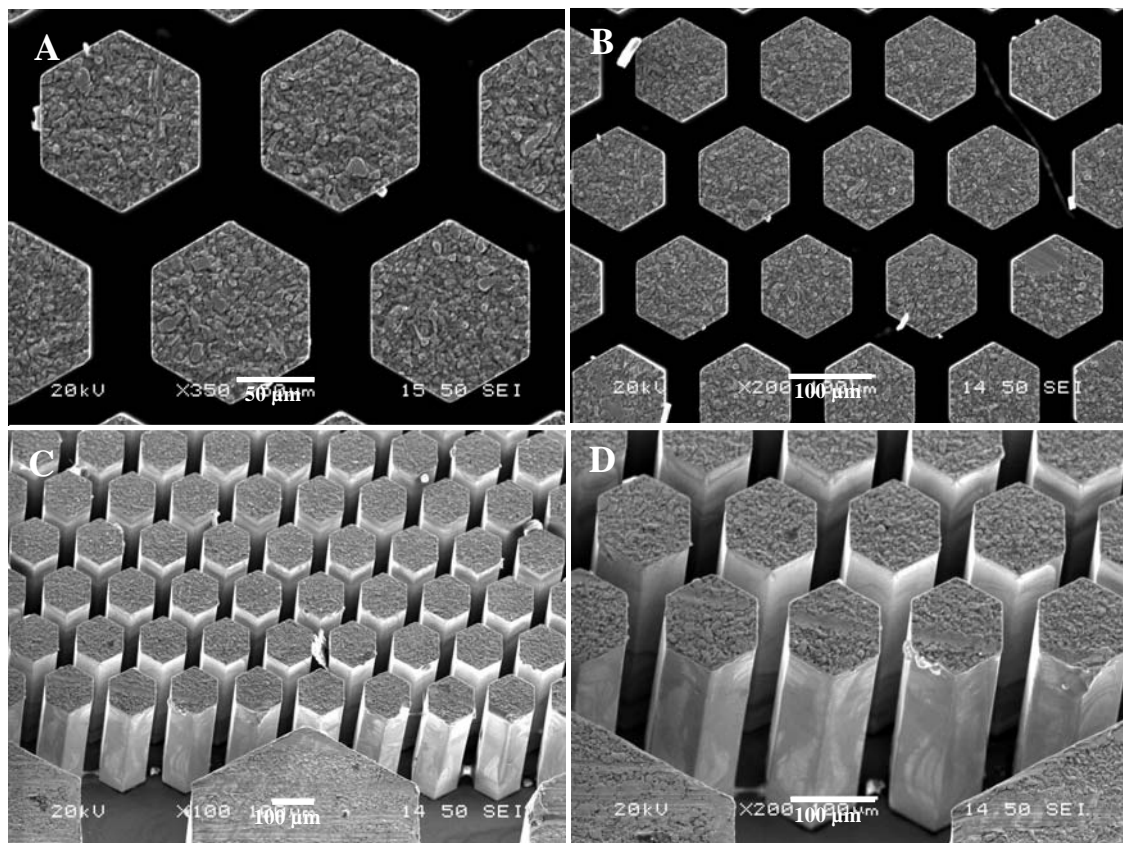


Figure 8.9 Plan (A & B) and perspective views at 25° (C & D) of the master tool used for familiarisation

The master tool used here is similar to the master tool produced in chapter 7. Although, the pillars are hexagonal, the structure is made from nickel and has a similar kerf to the pillars in the Bosch fabricated tool. This LIGA mould has a significantly smoother surface finish

compared to the Bosch process; however it also has parallel, rather than slightly tapered, pillars. The LIGA tool has a higher aspect ratio than the tool made by the Bosch process, such that it is difficult to definitively say which tool would be easier to hot emboss. Therefore it is considered that the LIGA tool is a good alternative to the tool produced by the Bosch process.

8.2.2 Embossing Temperature

The first parameter for investigation was the embossing temperature. As was previously described section 5.1.2.1 both isothermal embossing and non-isothermal embossing has been investigated, in a temperature range from 130°C to 155°C in 5°C increments. The embossing load and the dwell time were kept constant, at near the centre of their ranges, at 1.25 kN and 6 min respectively.

8.2.2.1 Percentage Mould Fill

The percentage mould fill verses temperature is plotted in Figure 8.10, and shows both the non-isothermal and the isothermal experiment. The x-axis indicates the temperature of the master tool, whilst the temperature of the polymer varies according to the experiment conducted. Further information is given in section 5.1.2.1.

The substrate did not emboss uniformly, and produced a region of cavities that were much deeper in some areas. Thus, the percentage mould fill is a mean value that was calculated by measuring the deepest and shallowest cavities, and represents the ease that the gap between the pillars can be filled with PMMA. However, since this is a mean of the deep and shallow cavities, 100% mould fill was not achieved because the master tool did not emboss uniformly;

such that the deep cavities in the 155:155 experiment obtained 100%, but the shallower cavities meant that the mould fill was only 83%. The error bars in Figure 8.10 are absolute values and their origins have previously been discussed in section 5.1.3.1.

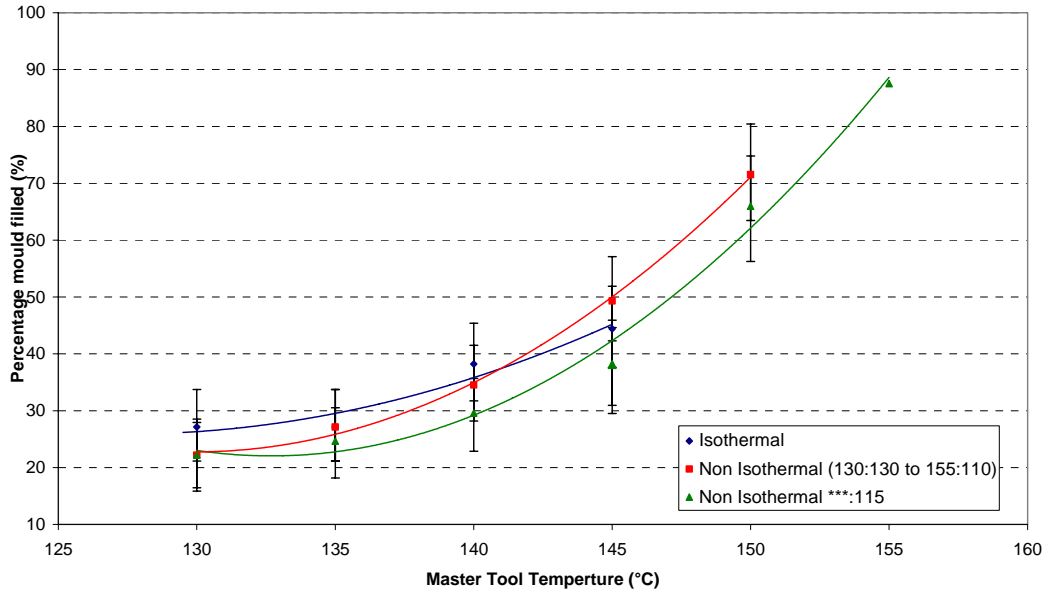


Figure 8.10 Curves indicating the percentage of the master tool that was filled by the polymer for different master tool temperatures during isothermal and non-isothermal hot embossing

The best fit lines have been calculated using the ‘trendline’ function in Microsoft Excel. The curves in Figure 8.10 are very similar, with both the mould fill and the gradient increasing with an increase in temperature. Thus, higher temperatures have a larger effect on the percentage mould fill. For example, when non-isothermal hot embossing was carried out with a substrate temperature of 115°C, the mould fill increased by around 10% between 130°C and 140°C, but then by nearly 60% from 140°C to 155°C.

The two non-isothermal curves are very similar, but the isothermal curve appears to have a slightly different shape. It shows the highest mould fill at lower tool temperatures, but it does not increase as rapidly as the non-isothermal curves. This behaviour is caused by the higher

substrate temperature compared to the non-isothermal cases, such that deformation is not focused around the pillars of the master tool, but instead, occurs in the bulk of the substrate and flows around the outside of the master tool instead. The isothermal curve is much shorter than the non-isothermal curves because at temperatures above 145°C it was not possible to de-emboss the mould.

Further observations are difficult to make because the error bars of each line fall within each other. However, the key observations are that the effect of temperature is more significant at higher temperatures, and isothermal embossing showed less mould fill at these temperatures, and was difficult to de-emboss.

8.2.2.2 De-embossing Force

The de-embossing force is plotted against the master tool temperature in Figure 8.11. The figure shows that the de-embossing force increases linearly with the master tool temperature, but the rate of this increase is significantly different for each experiment. Most of the lines of best fit correlate to the data points well, and are close to or within the error bars of each data point. The non-isothermal curve at a constant substrate temperature does show a slightly poorer correlation than the other two curves. This is because of the high value at the 145°C data point that has raised the best-fit line upwards and out of the error bar range of the 150°C data point. However, overall it has not affected the gradient of the best-fit line significantly.

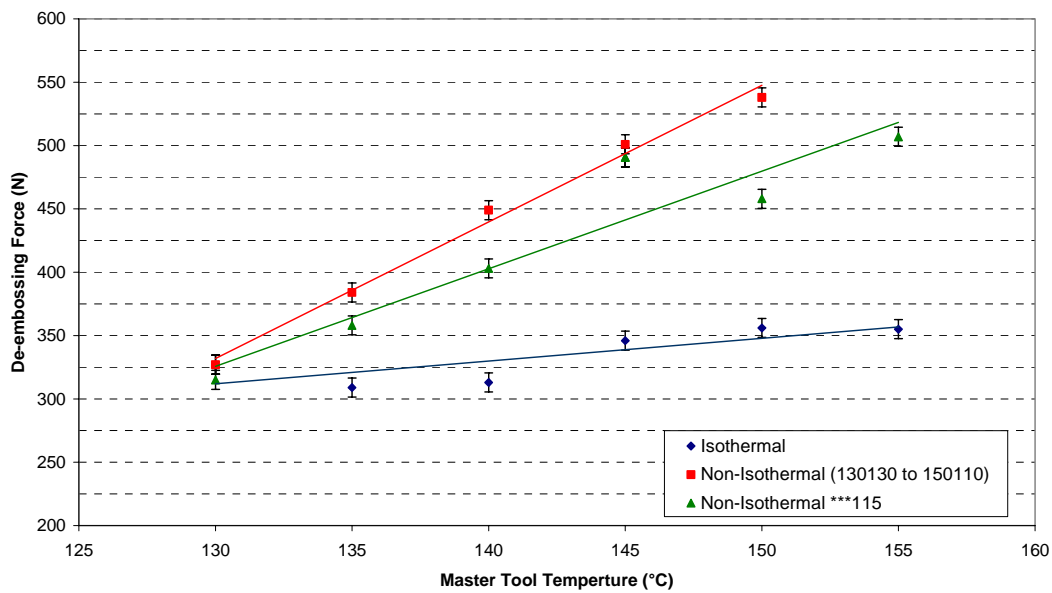


Figure 8.11 The force required to de-emboss the master tool after hot embossing at different temperatures. The force increases linearly with embossing temperature and is more prominent in non-isothermal embossing

This behaviour was to be expected since the de-embossing force is not only dependent on the adhesion between the master tool and the embossing, but also on the friction at the interface, which is increased by the lateral forces from the shrinking polymer [20]. The cooling rate will affect the shrinkage that can occur in the polymer. However, in this case, the cooling rate has been maintained at a constant rate throughout the experiments such that the difference in shrinkage will depend upon the temperature change, ΔT , between the embossing and the de-embossing temperature [3, 20, 21]. Thus, increasing the embossing temperature results in a greater shrinkage, and therefore a greater de-embossing force.

Shrinkage can be described by Equation 8.1, and shows the relationship between the change in length, or volume, and the change in temperature. Where Δl is the change in length, l_0 is the original length, α is the coefficient of linear expansion, and ΔT is the change in temperature.

$$\frac{\Delta l}{l_0} = \alpha \Delta T \quad \text{Equation 8.1}$$

During cooling the polymer can be considered to be elastic [21], such that the left hand side, which represents the strain, can be replaced by Hooke's law. Equation 8.2 can then be derived by rearranging the equation to make the stress, σ , the subject. By recognising that the Young's modulus, E and the linear expansion coefficient are constants over this temperature range, it can be seen that the stress and the change in temperature have a linear relationship.

$$\sigma = E \alpha \Delta T \quad \text{Equation 8.2}$$

The force that is exerted on the master tool pillars can then be calculated if the area of the polymer – master tool interface is known, and can be written as:

$$F = E \alpha A \Delta T \quad \text{Equation 8.3}$$

The force calculated by Equation 8.3 only describes the force perpendicular to the pillar / polymer interface and cannot be used to calculate the de-embossing force directly from it. Instead the coefficient of friction, and the adhesion, is required to be known plus the other residual forces that remain in the polymer. However, given that the experiment kept all of the other parameters the same, such as the master tool geometry, materials and cooling rates, the linear behaviour remains.

It is also visible from Figure 8.11 that the gradient of the isothermal curve is much less than the non-isothermal curves. In the isothermal curve the de-embossing force only increases

from 315 ± 7.5 N to 355 ± 7.5 N, whereas in the non-isothermal case this increases to over 500 N. This difference is likely to be caused by the shrinkage of the non-isothermal embossing occurring mainly in the region between the pillars, because this is the region with the largest temperature range. Conversely, in isothermal hot embossing, the shrinkage can occur throughout the whole substrate, such that not all of the force is exerted onto the pillars.

The literature also demonstrates that residual stresses occur through the whole substrate in isothermal hot embossing; whereas in non-isothermal hot embossing the residual stress is confined to the embossed area [4]. The greater force required to remove the master tool meant that the isothermal samples fractured during de-embossing at 140°C and completely failed to de-emboss at 150°C . Therefore, it is likely that the de-embossing force would have been higher if the substrate had been able to withstand the de-embossing stresses. Nevertheless the gradient is still significantly less than the other two non-isothermal experiments.

It could also be argued that the amount of mould fill will increase the adhesion between the master tool and the embossing. Figure 8.12 plots the relationship between mould fill and de-embossing force. No relationship can be seen between the de-embossing force and the mould fill in isothermal hot embossing because the data has been affected by the moulds failing to de-emboss successfully.

A best-fit line can be drawn for non-isothermal hot embossing, whereby the de-embossing force increases with the mould fill and then reaches a plateau. It would be expected that if the mould fill was more strongly linked to the de-embossing force then the plateau would not

occur. Furthermore, this shape of the curve is more likely to have occurred because of the non-linearity between the mould fill and the embossing temperature.

This subject is discussed further in section 8.2.3.2, where a graph with the same axis is presented but has been derived by a change in embossing load. Regardless of the cause, it can be concluded that the de-embossing force is strongly linked with the de-embossing temperature; such that increasing the temperature will increase the forces that the substrate must withstand during de-embossing.

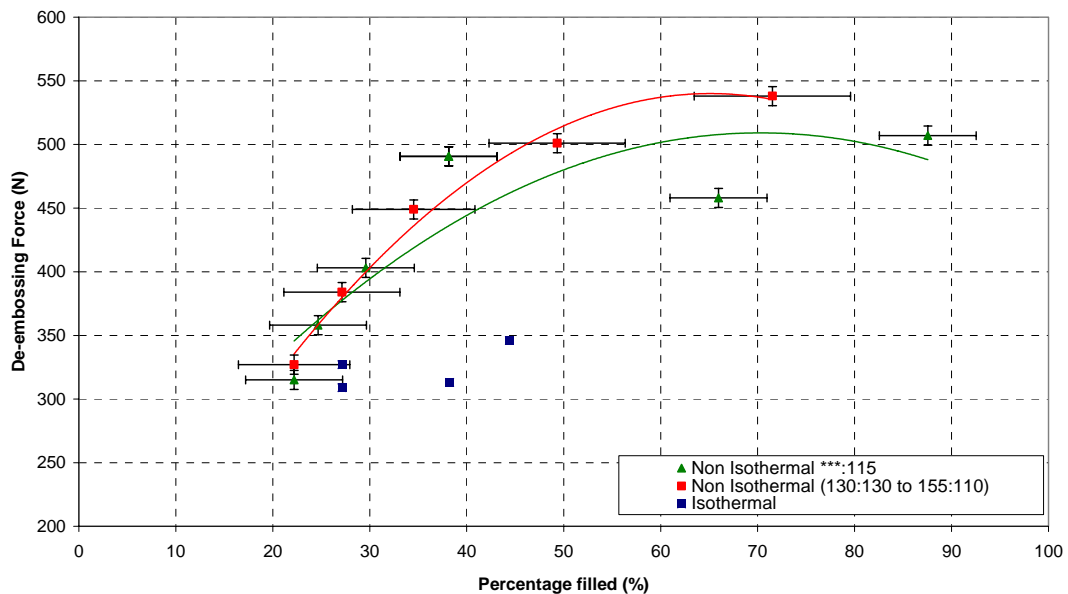


Figure 8.12 The relationship between the de-embossing force and the mould fill, which is likely to be caused by the nonlinear behaviour of the percentage mould fill in Figure 8.10

8.2.2.3 Common Defects

An isothermal sample is shown in Figure 8.13 and two non-isothermal samples are shown in Figure 8.14. Comparing the two sets of images shows some clear differences. The isothermally embossed sample shows a large amount of bulk polymer deformation compared

to the non-isothermally embossed samples. This is due to the bulk polymer, in the isothermal sample, having a sufficient temperature to deform rather than being forced between the pillars. In the non-isothermal samples the bulk polymer is much cooler and the heat is applied directly to the polymer near the pillars, so that the deformation occurs around the master tool, rather than the bulk polymer.

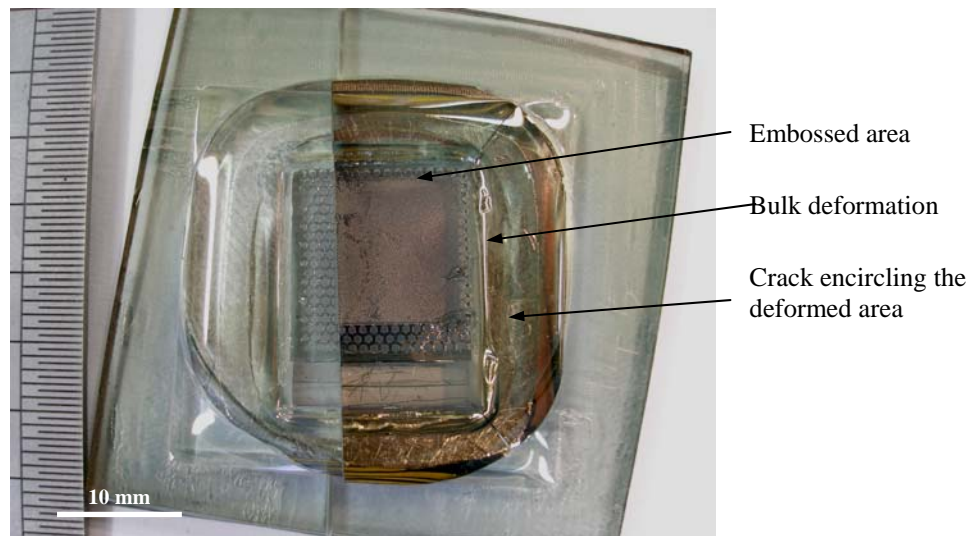


Figure 8.13 An isothermally embossed sample (145°C, 1.25 kN, 6 min) that shows the bulk deformation and the crack around the deformed area

Cracking is present in both types of sample, but occurs in different places. In Figure 8.13, cracking is visible around the outskirts of the deformed bulk polymer; whilst in Figure 8.14 cracks are visible in the actual embossed area. The cracks in the isothermally embossed experiments limit the potential of the process above 150°C because the crack completely encircles the embossing and prevents the full withdrawal of the master tool. In non-isothermal hot embossing cracking does occur but does not fully encircle the embossed area. Therefore the master tool can be removed before complete failure of the substrate.

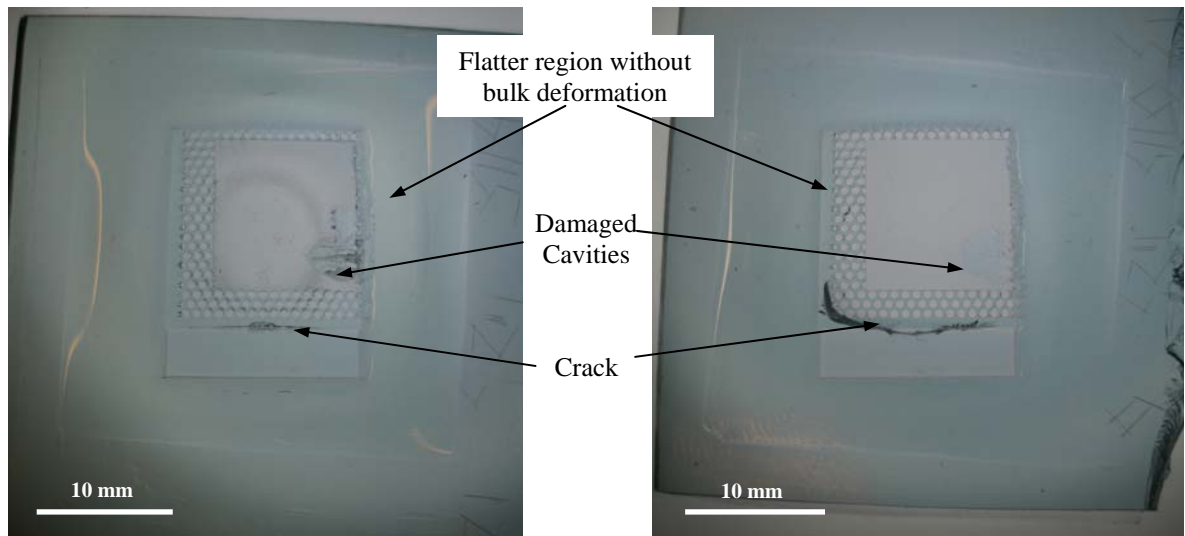


Figure 8.14 Non-isothermally embossed samples showing damaged cavities, cracks and a flatter region around the embossed area where less bulk deformation has occurred compared to the isothermally embossed sample in

For successful de-embossing, without fracture, the stress that the embossing experiences must be less than the fracture strength of the polymer. The de-embossing force that the polymer can withstand is influenced by the residual stresses in the embossing. The different cracking behaviour seen in the isothermal samples compared to the non-isothermal samples indicates that the distribution of the residual stress is different. Birefringence patterns in the literature agree with this [4, 22], such that the residual stresses are confined to the areas of polymer that can deform. Thus, in isothermal embossing, where the whole of the substrate can deform, the cracking occurs in the bulk polymer, but in non-isothermal embossing, the deformation, and the residual stress, is restricted to the embossed area such that cracking occurs here.

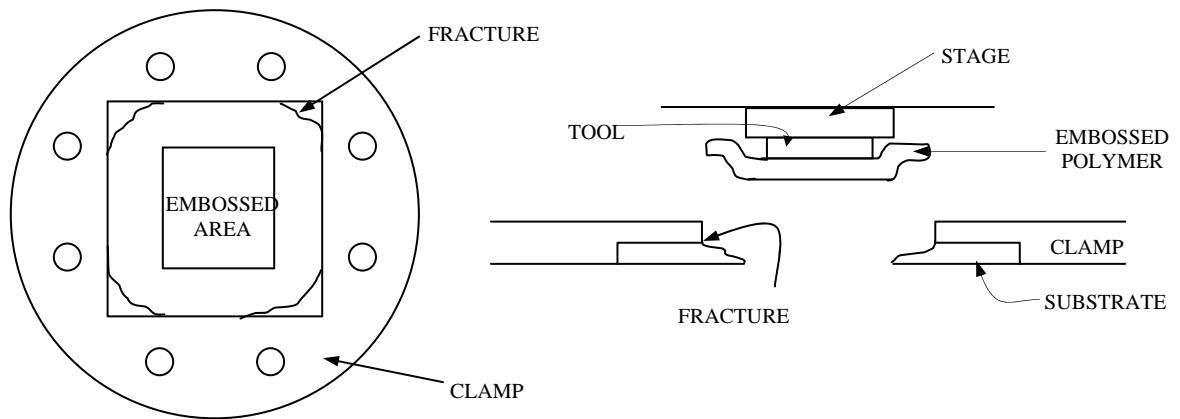


Figure 8.15 Schematic plan and cross section diagrams showing fractures that occur around the edge of the clamp in isothermally embossed samples

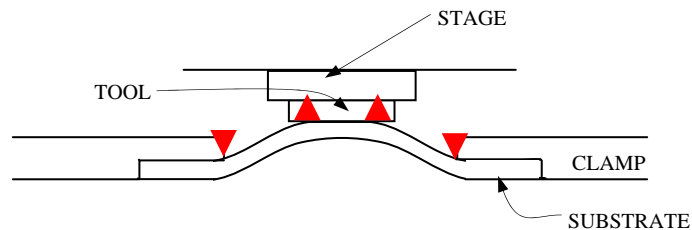


Figure 8.16 The de-embossing process approximated to a four point bend situation, which highlights the areas of greatest stress during de-embossing. These areas are the same as where cracks occur during de-embossing

The cracks will appear at points with the highest local tensile stress such that they will be present where the highest residual stress occurs, or where the tensile stress is at a maximum. Figure 8.15 shows a plan and cross-sectional schematic view of an isothermally embossed sample after fracture. It can be seen in this diagram that the fracture has occurred outside of the embossed area, at the edge of the clamp. Figure 8.16 shows the same sample just before fracture, and indicates how the de-embossing process can be approximated to a four point bend test. Thus, the areas of highest tensile stress, and therefore the most likely areas to fracture, are at the edge of the clamp and inside the embossed area. These two areas are where the fracture occurs. In the isothermal samples this is in the bulk polymer, near the edge of the clamp, and in the non-isothermal samples this is in the embossed area where polymer

flow predominantly occurs.

Another type of defect that can be seen in the embossings is damaged cavities. However, this defect is only present in the non-isothermally embossed samples, and is shown in Figure 8.14. One suggested reason for this is because deformation is focused in the embossed area much more in the non-isothermal samples compared to the isothermal sample.

The severity of the cavity damage and the severity of the cracking were considered for each of the embossings to identify any general trends that can help identify the appropriate parameters. By no means should it be thought as a way for predicting damage seen in the embossing but general patterns, however, can be observed. The embossings have been arranged on a chart with a y-axis of 'severity of cracking' and an x axis of 'severity of cavity damage'. By ranking the defects seen when the non-isothermal samples were studied, positions of the embossings can be plotted and are shown in Figure 8.17

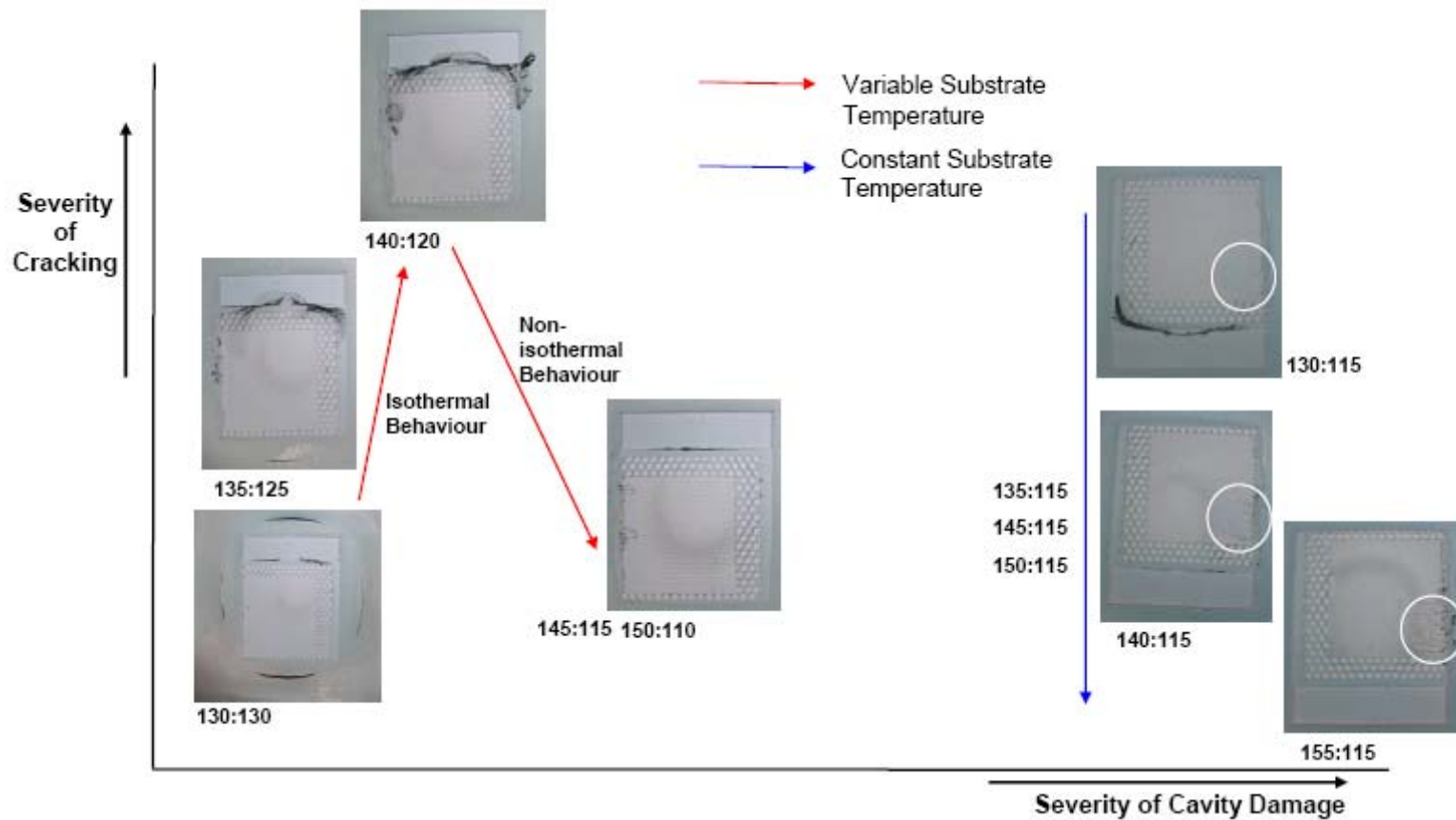


Figure 8.17 A chart plotting the position of each sample according to the severity of cavity damage (x-axis) and the severity of cracking (y-axis). Each sample was produced by changing the embossing temperature in non-isothermal hot embossing, and transition in behaviour is seen when the master tool temperature was varied as well as the master tool temperature

The chart only shows the two non-isothermal experiments since the isothermal experiments did not de-emboss successfully. In the non-isothermal samples, where the substrate temperature was not varied, the cavity damage remains similar throughout the increase in master tool temperature. The extent of the cracking does show some sort of trend, such that there is a similar crack in the samples (the crack in the 150°C sample is harder to see), with the exception of the 130°C sample that has a large crack on the edge of the embossed area. One reason for this larger crack could be because of the restricted polymer flow causing higher residual stress.

When considering the samples where the substrate temperature was also changed with the master tool temperature, a change in the behaviour can be seen. In the 130:130 sample, which is effectively isothermal, deformation of the bulk polymer can be seen, where the polymer has folded in on itself. As the temperatures become more non-isothermal, the deformation in the bulk polymer reduces, and cracks appear that are similar to those in the non-isothermal samples where the substrate temperature was not varied. More severe cracking is seen as the samples become more non-isothermal, up to 140:120. After this the severity of cracking decreases and the embossings appear much more like the non-isothermal embossings that are seen where the substrate temperature was not varied.

The chart indicates that at a higher master tool temperature less cracking occurs, and appears not to affect the cavity damage within each group of samples. Furthermore, the percentage mould fill can be increased by raising the temperature; such that this is a good method to increase the mould fill, without increasing the likelihood of the defects. The percentage mould fill increased more rapidly with non-isothermal embossing, and de-embossed more

successfully, such that it is recommended that only non-isothermal embossing is used for further investigation.

8.2.3 Embossing Load

An investigation into the effect of the embossing load on mould fill, de-embossing force and on the severity of the defects was carried out. Values close to the midpoints of the investigated ranges were used such that a master tool temperature of 145°C, a substrate temperature of 115°C, and a dwell time of 6 minutes used. The embossing load was varied from 1 kN to 1.9 kN in 0.1 kN increments.

8.2.3.1 Mould Fill

Figure 8.18 shows the effect of increasing applied load on percentage mould fill. The embossings did not emboss uniformly, so it was appropriate to characterise the amount of mould fill using maximum, minimum and average values. Whilst the error bars for the average mould fill have been removed for clarity, the lines of best-fit show good correlation with the data points.

The figure indicates that the percentage mould fill increases linearly with the applied load, and by using the 'average' line as an example it can be seen that the mould fill increases from 37% at 1 kN, to 58% at 1.9 kN. Thus, by almost doubling the load, the percentage mould fill has increased by a multiple of 1.5.

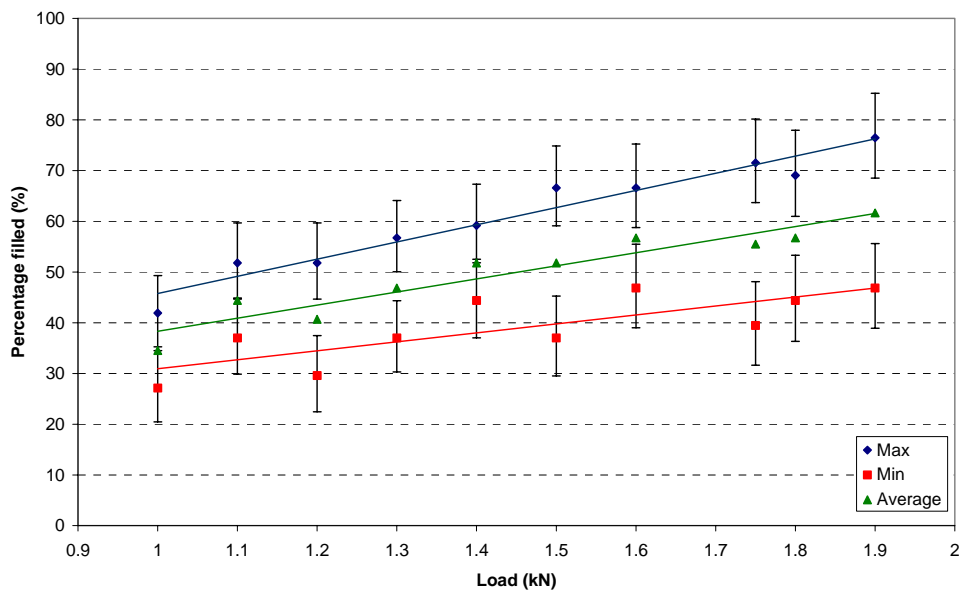


Figure 8.18 The effect of embossing load (at 145:115) on the percentage mould fill for the deepest and shallowest filled regions, and the mean.

8.2.3.2 De-embossing Force

The effect of the embossing load on the de-embossing load is shown in Figure 8.19. The figure indicates that the de-embossing force decreases linearly with the embossing load. However, given the scatter, and the decrease from 510 kN to 480 kN, it is considered that the de-embossing load has not changed. In particular this behaviour is significantly different compared to when the embossing temperature was varied.

The scatter is likely to be caused by the number of defects that have been seen in the samples, and are shown in section 8.2.3.3. It should also be remembered that the de-embossing load is limited by the ability of the embossing to withstand the de-embossing force. This means that the de-embossing force reflects the force required to remove the master tool, but also the stresses that the embossing can withstand before cracking. Therefore, a low de-embossing

force may occur because the master tool could be easily removed, or because a crack could easily be formed.

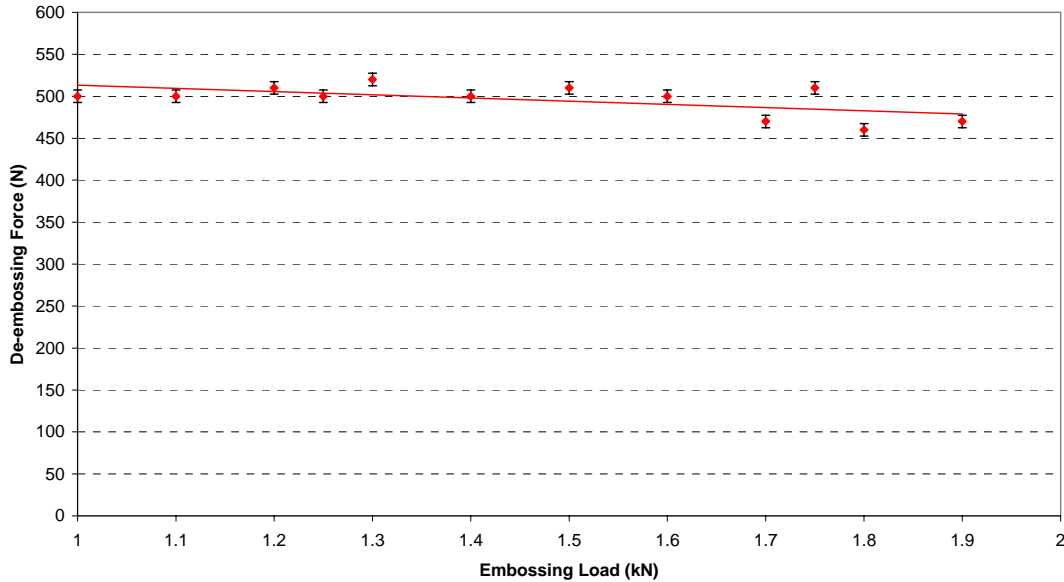


Figure 8.19 The affect of the embossing load (at 145:115) on de-embossing force, which shows only a change from 510 to 480 kN.

The de-embossing load can also be compared to the percentage mould fill. In section 8.2.2.2 there was some debate about whether the increase in de-embossing load was due to shrinkage, or the percentage mould fill. Therefore a similar graph to Figure 8.12 has been drawn by plotting the percentage mould fill against de-embossing load, and is shown in Figure 8.20. In this figure the percentage mould fill has little effect on the de-embossing force, which indicates that the change in de-embossing force is influenced by the shrinkage rather than the percentage mould fill..

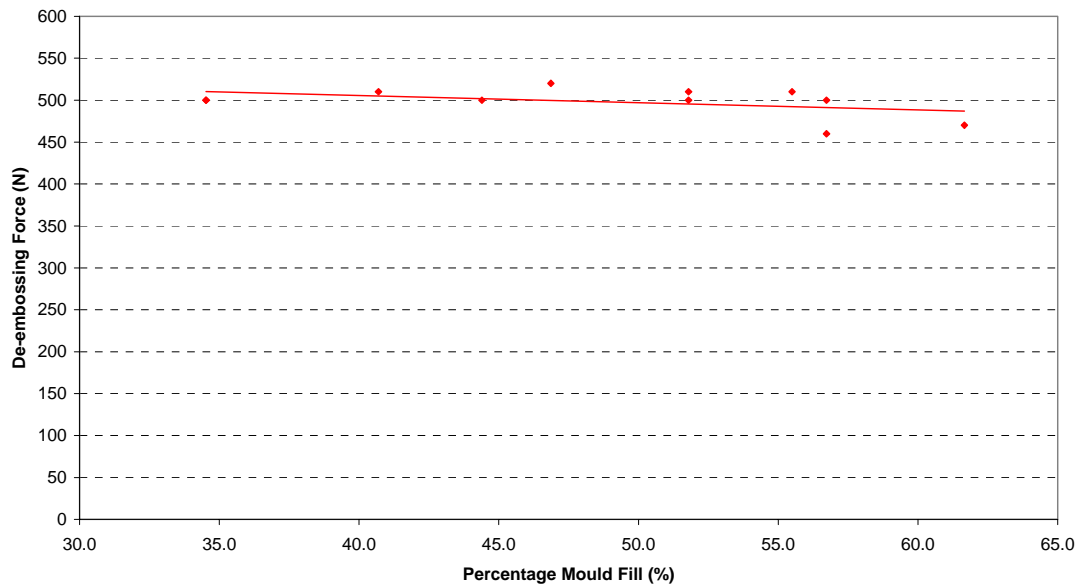


Figure 8.20 The decrease in de-embossing load with an increase in percentage mould fill which does not show the same behaviour as Figure 8.12, and indicates that the percentage mould fill is not the cause of the linear increase in de-embossing load seen in Figure 8.12

8.2.3.3 Common Defects

As described in section 8.2.2.3 the embossings can be arranged on a chart in order of the severity of the defects observed in them. A similar chart can be plotted for when the embossing load is varied and is shown in Figure 8.21. A general trend is shown in the figure, where the severity of the defects increases with the applied load. It can be seen that the type of defect does vary, such that a large crack or a large area of cavity damage occurs. This indicates that although increasing the embossing load increases the percentage mould fill, it also increases the risk of defects in the embossing; and is therefore a less preferable parameter to increase.

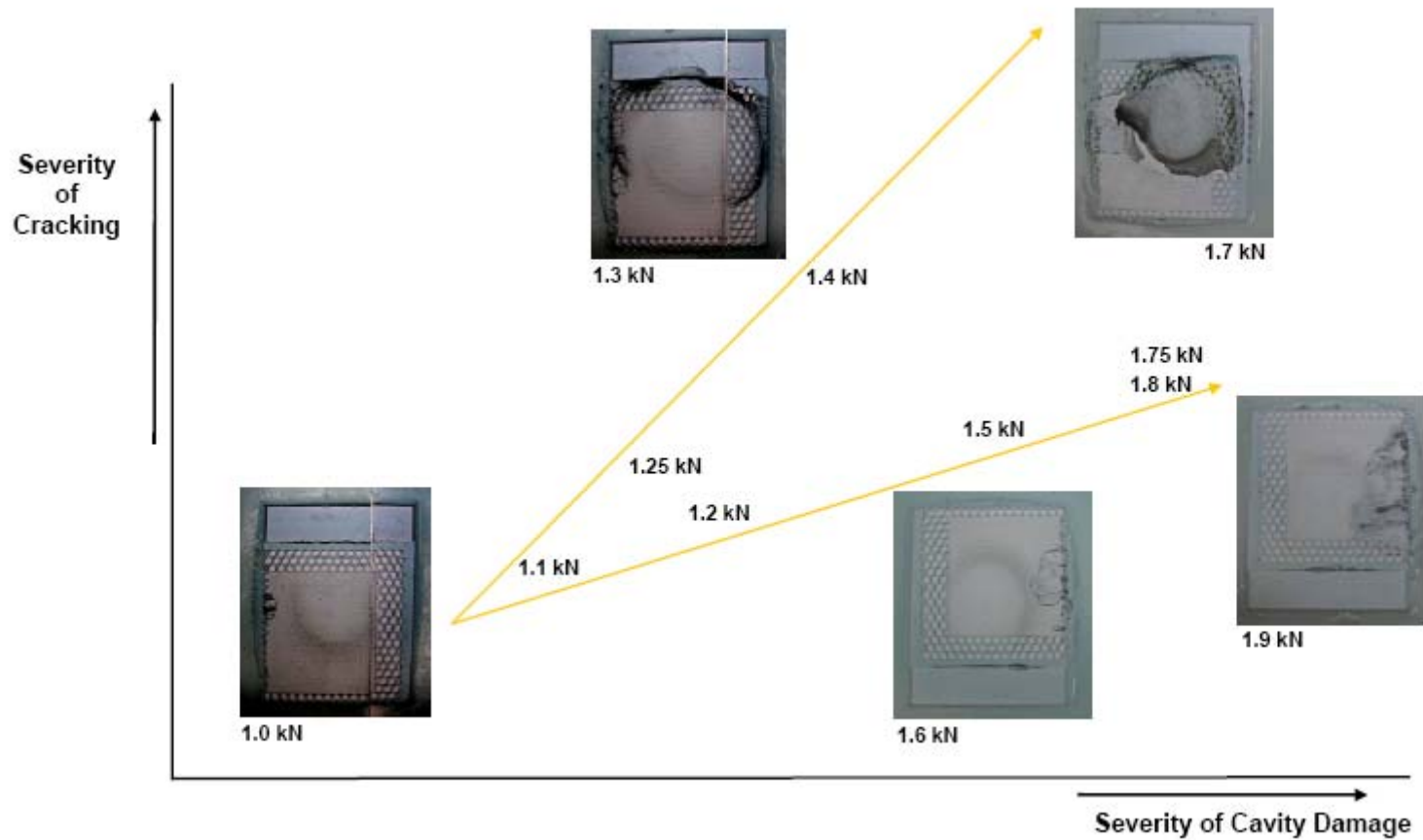


Figure 8.21 A chart showing the effect of increasing the applied load on both the severity of cracking and the severity of pillar damage. Higher embossing loads caused more severe defects, whether they were cracks or damaged cavities.

8.2.4 Dwell Time

The effect of dwell time on the mould fill, de-embossing force and defects was studied. The load used was 1.25 kN, and the master tool and the substrate temperature were 145°C and 115°C respectively. The dwell time was varied in increments of 1.5 minutes, ranging from 10s (~ 0 minutes) to 12 minutes.

8.2.4.1 Mould fill

The effect of increasing the amount of time that the substrate is held under constant load and temperature is shown in Figure 8.22. As in the previous sections, the substrate did not emboss uniformly, such that a maximum, minimum and average line were necessary to study the effect. The best-fit line dissects most of the error bars, with the exception of one result at 9 minutes.

The trendlines in Figure 8.22 show that the mould fill is linear and increases with the embossing time. The figure indicates that after 1.5 min the average percentage mould fill was 33 %, and then after 12 minutes the mould fill was 62 %. This means that when the embossing time is increased by a multiple of 7 the mould fill has almost doubled, and thus is not as effective at increasing the mould fill compared to the embossing temperature and the embossing load.

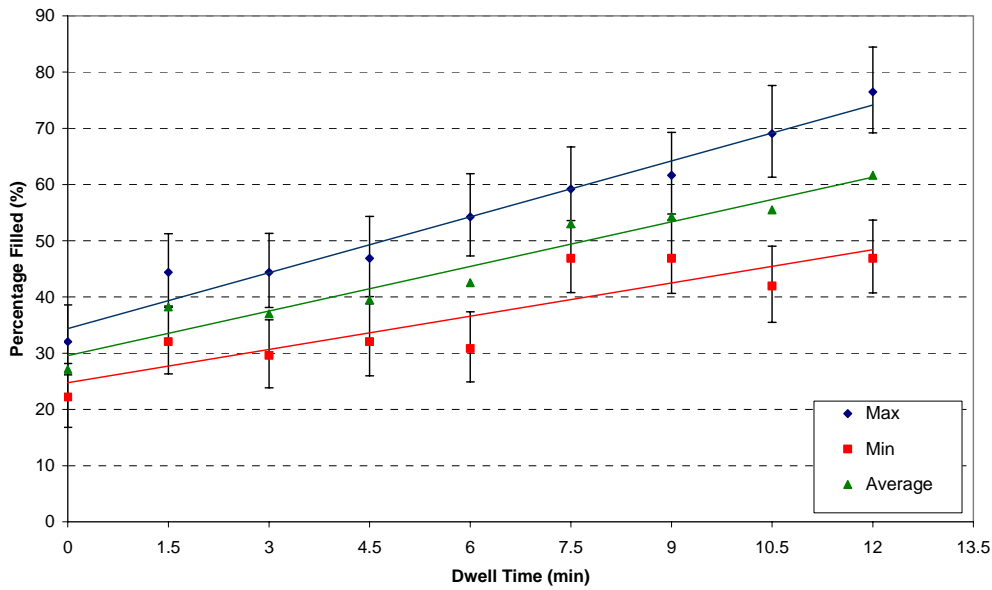


Figure 8.22 The linear increase in percentage mould fill with respect to an increase in de-embossing time, expressed in terms of maximum, minimum and mean

Creep occurs during hot embossing and is seen in Figure 8.23. This figure shows the distance that the platens have moved during the dwell phase of the hot embossing process. The steep gradient before 90 s represents the embossing load being applied, and the shallower gradient shows the polymer deformation during the dwell phase. In a typical creep test a constant load is applied that causes an instantaneous elastic response; then as the time increases, the rate of deformation slows before reaching a constant rate. The creep curve is described by Equation 8.4 [23], and describes the relationship between the strain, ε_t , at time, t , and the applied stress, σ_0 . Where, τ is ratio of the viscosity, η , to the Young's Modulus, E .

$$\varepsilon_t = (\sigma_0 / E) \{1 - \exp(-t / \tau)\} \quad \text{Equation 8.4}$$

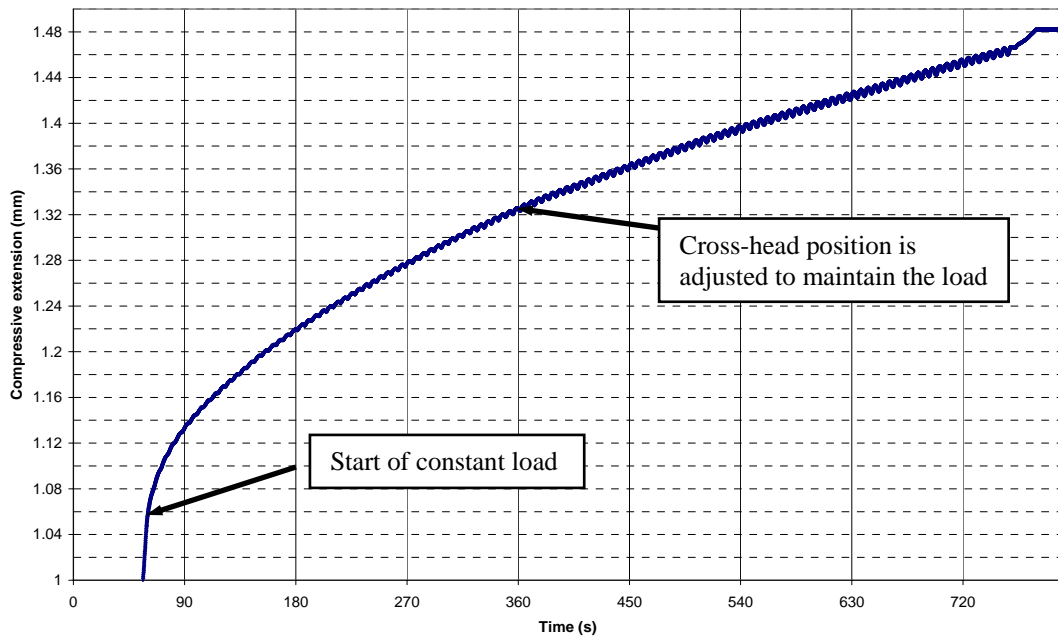


Figure 8.23 The distance moved by the platens of the hot embossing rig during the embossing phase of the process. The graph shows a vertical portion from the final stages of the load being applied followed by a non-linear creep curve.

Figure 8.23 is a measure of the displacement of the embossing rig cross-head position against time. The vertical portion of the graph reflects the cross-head speed as the embossing load is applied. After this, the gradient changes because the cross-head only moves to maintain a constant load on the polymer substrate i.e. as the polymer flows the force is reduced and the rig must then move the cross-head further to maintain the same load. The shape of Figure 8.23 is similar to that of a typical creep curve, showing extension against time, for a constant load. However it is not possible to relate this graph to Equation 8.4 since it is not simply a measure of the polymer flow between the pillars, but it is also affected by the polymer flow that occurs around the master tool. In addition, the polymer flow between the pillars is not only influenced by creep but is also restrained by the adhesion of the polymer to the pillar walls during flow. This is illustrated by Figure 8.24 where it can be seen that there is a curved surface on the top of the cavity walls. This indicates that the polymer flow rate is

faster the further the polymer is from the sides of the pillar walls and therefore the flow rate is restrained by them.

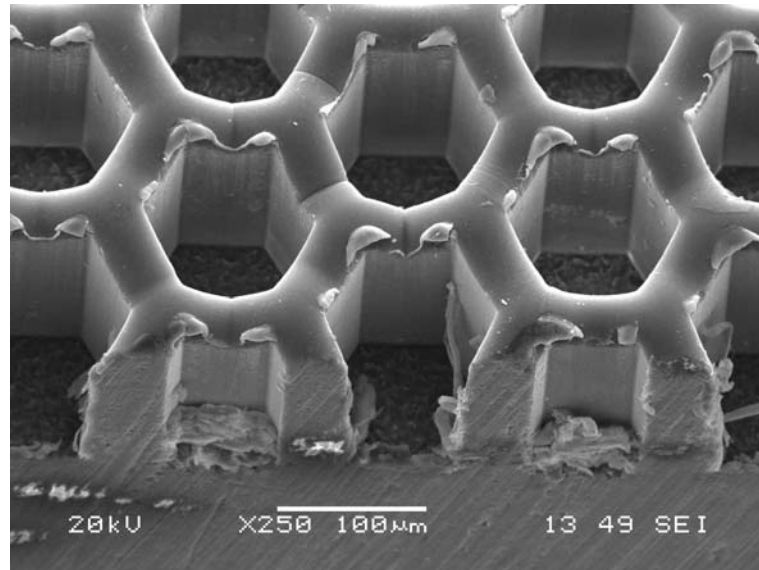


Figure 8.24 The curved surface on the top of the cavity walls indicates that the flow rate is faster the further the polymer is from the cavity walls, and is an example that creep is not the only process that occurs during hot embossing.

8.2.4.2 De-embossing Force

The effect of the dwell on the de-embossing force is shown in Figure 8.25, and shows a linear increase from 420 N to 470 N in 12 minutes. This range is slightly larger than the decrease due to the embossing load, and the data points are more consistent with the trend line, and show less scatter than when the embossing load was investigated.

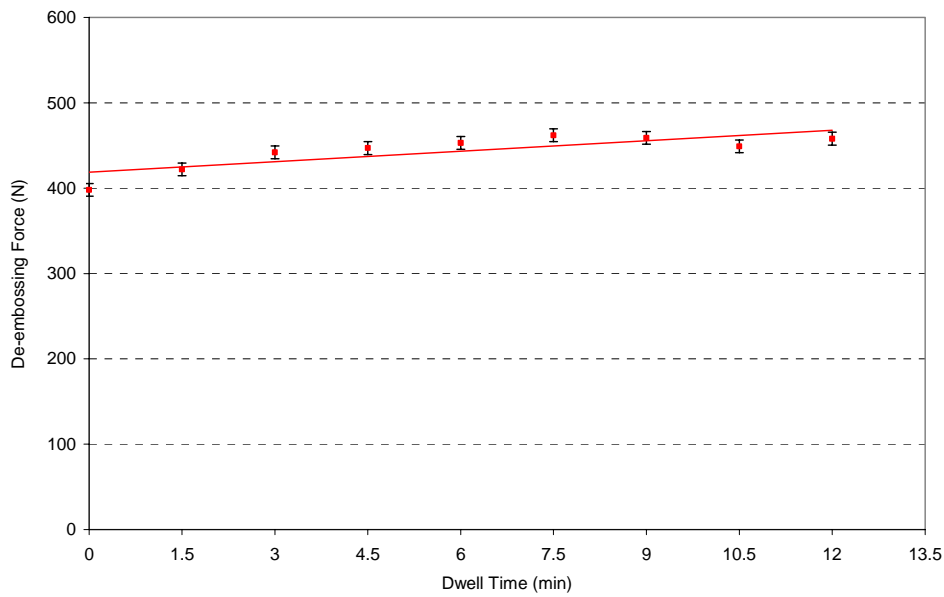


Figure 8.25 The increase in de-embossing force with respect to the dwell time

The relationship between the percentage mould fill and the dwell time is shown in Figure 8.26, and shows a similarity to Figure 8.25. This increase could be caused by an increase in percentage mould fill and is in contrast to the results described in sections 8.2.2.2 and 8.2.3.2. In the embossing temperature section, it is possible that the shrinkage was the dominant cause of the increase in de-embossing force, and masked the increase due to the mould fill. Whilst, in the embossing load experiment the large number of defects may have caused the de-embossing force to represent the load that could be withstood by the polymer, rather than the force required to remove the master tool. The change in the severity of the defects is shown in section 8.2.4.3 and shows little change with an increase in dwell. Therefore, it is unlikely that these defects have affected the de-embossing force.

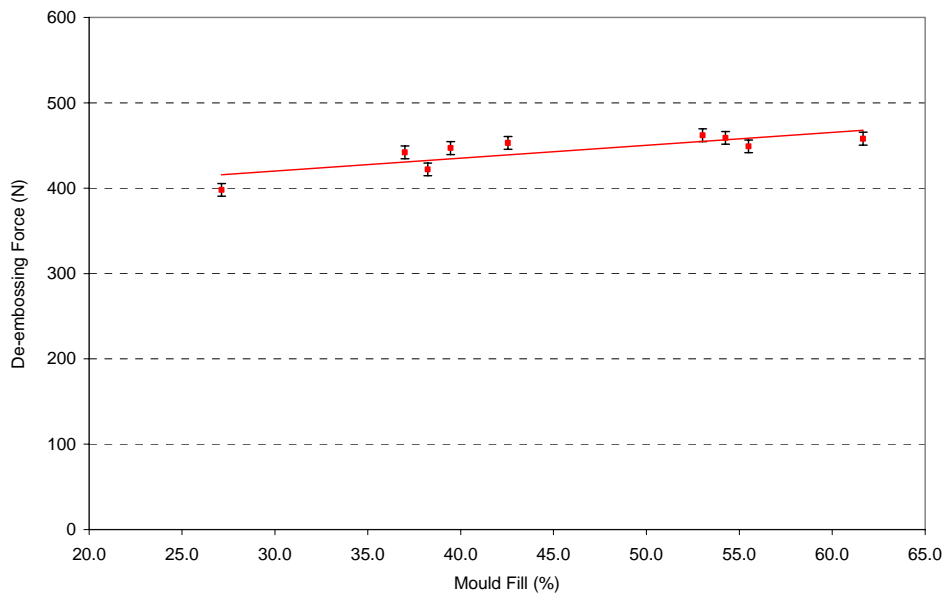


Figure 8.26 The increase in de-embossing load with respect to the increase in dwell time. This effect could be caused by an increase in mould fill that was previously masked in Figure 8.19 by the severe defects

8.2.4.3 Common Defects

As with Figure 8.17 and Figure 8.21 the defects seen in the samples have been arranged to identify any general trends. The chart with the embossings arranged according to the severity of the cracking, and severity of the cavity damage, is shown in Figure 8.27. It can be seen here that several of the embossings produced similar defects, and show no increase in the severity of the cracking, even though the de-embossing force has increased. Although there was no increase in the severity of the cracking, there was an increase in the severity of the cavity damage. It should, however, be acknowledged that this damage is minimal compared to that seen in the change in embossing load in section 8.2.3.3.

The slow increase in percentage mould fill and the small increase in cavity damage indicate that the dwell time should not be preferred to changes in the embossing temperature, as a way of increasing the mould fill. Increasing the dwell time does offer an alternative to increasing

the embossing load, as it does not result in such large increases in the severity of the defects. However, the overall cycle time must be considered before relying on this parameter.

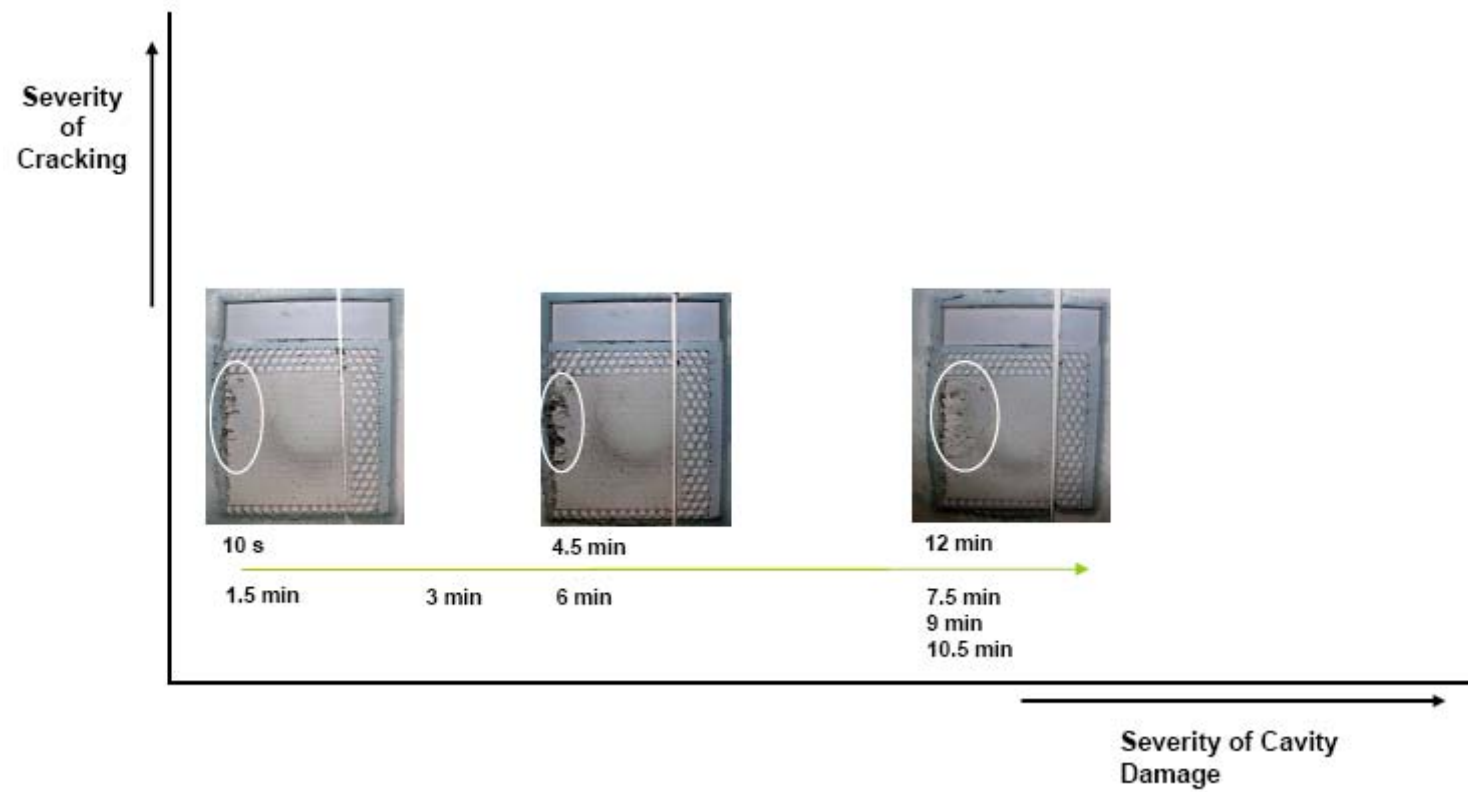


Figure 8.27 A chart showing no change in the severity of cracking with respect to the dwell time, but an increase in the severity of the cavity damage.

8.2.5 De-embossing Temperature

The de-embossing temperature was also investigated; and whilst it will not result in an increase in the percentage mould fill, it may result in a decrease in the severity of the defects by decreasing the de-embossing load, allow a higher embossing temperatures to be used without affecting the, ΔT , or simply reduce the cycle time.

The upper limit of de-embossing temperature is just below the T_g , since above this the polymer will deform and damage the embossed structure. Section 8.1.1.2 discussed the de-embossing temperature and concludes that this should be carried out at a range between 60°C and 95°C. However, the PMMA deformed at high temperatures such that a range from 60°C to 90°C was investigated. More detail about the method has been described in section 5.1.2 and 5.1.3.4.

8.2.5.1 De-embossing Force

The effect of de-embossing temperature on the de-embossing load is shown in Figure 8.28. The de-embossing load decreases linearly with an increase in de-embossing temperature, and ranges from ~ 260 N at 90°C to ~ 470 N at 60°C. As expected this behaviour is similar to the behaviour seen with the de-embossing load and embossing temperature.

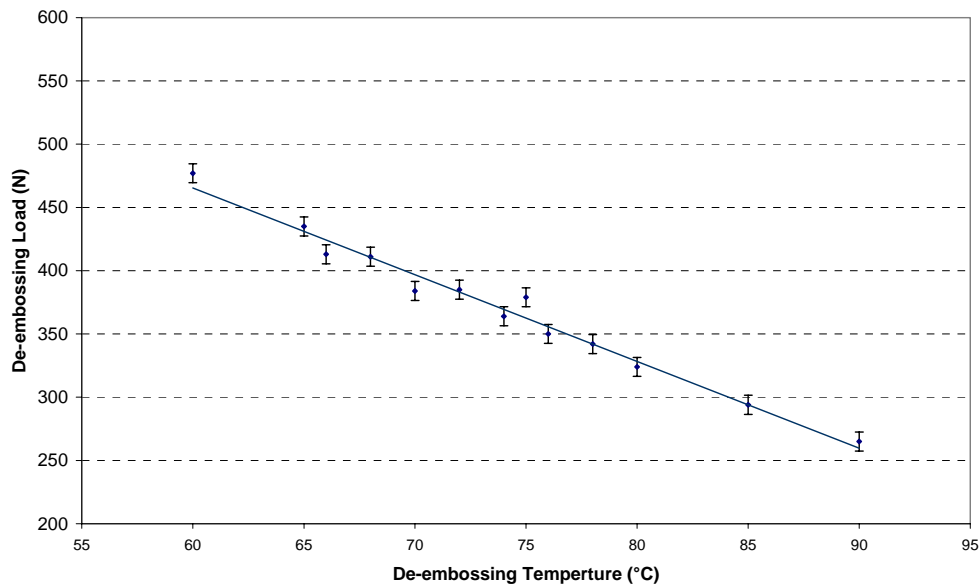


Figure 8.28 The linear decrease in the de-embossing load with respect to the de-embossing temperature. This behaviour is similar to the change seen when the embossing temperature was varied

The temperature change, ΔT , has been plotted against the de-embossing load in Figure 8.29 for both the temperature change caused by varying the embossing temperature and the de-embossing temperature. It can be seen from this figure that the gradients are very similar, and would show even more agreement if it were not for the result at 82°C. The gradient of the two curves can be calculated to be 6.9 and 7.7 N °C for when the de-embossing temperature and the embossing temperature were varied respectively. The similar behaviour of both experiments indicates that the shrinkage is responsible for the change in de-embossing load.

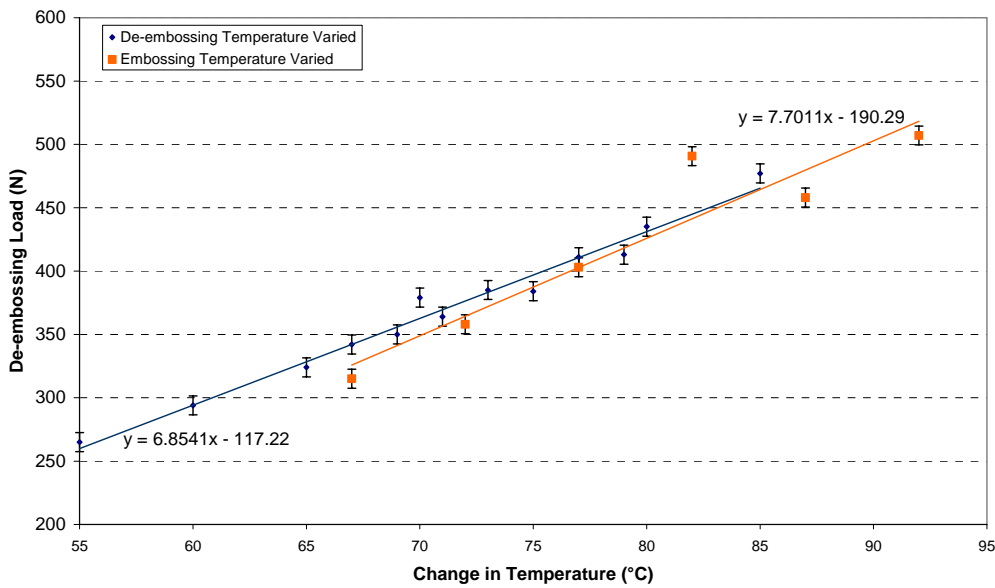


Figure 8.29 The increase in de-embossing load when the temperature difference is increased. A similarity in the gradient is seen for both the line generated by varying the de-embossing temperature, and the line generated by varying the embossing load.

8.2.5.2 Deformation to the Substrate during De-embossing

At de-embossing temperatures in excess of 80°C the embossings deform into a dome structure that is illustrated in Figure 8.16 and shown in Figure 5.3. This deformation was quantified by measuring the displacement of the underside of the embossing from its original position, and is described in more detail in section 5.1.3.4. The displacement of the embossing is plotted against the de-embossing temperature in Figure 8.30.

At 80°C the distance the polymer has been deformed by is ~ 325 μm, nearly the height of the pillars themselves. At values below 68°C the amount of displacement has reduced to 50 μm, and at these values the error bars begin to intersect the y-axis such that within the experimental error, the displacement close to zero.

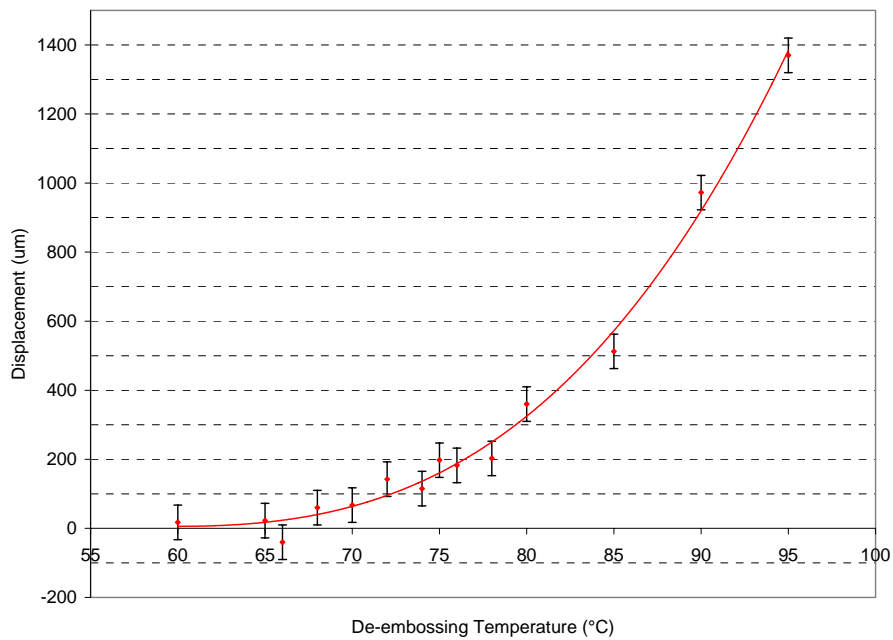


Figure 8.30 The affect of the de-embossing temperature on the amount of displacement from the platen surface, which is a measure of curvature.

The aim of increasing the de-embossing temperature was to reduce the de-embossing force and therefore the severity of the defects seen in the moulds. Figure 8.31 shows the range of defects seen when adjusting the de-embossing temperature. However, it can be seen from the figure that no significant improvement in the severity of the defects has occurred with respect to the change in de-embossing temperature. Therefore, whilst increasing the de-embossing temperature decreases the de-embossing load, it does not benefit the replicated structures, and causes the flat structure to become curved.

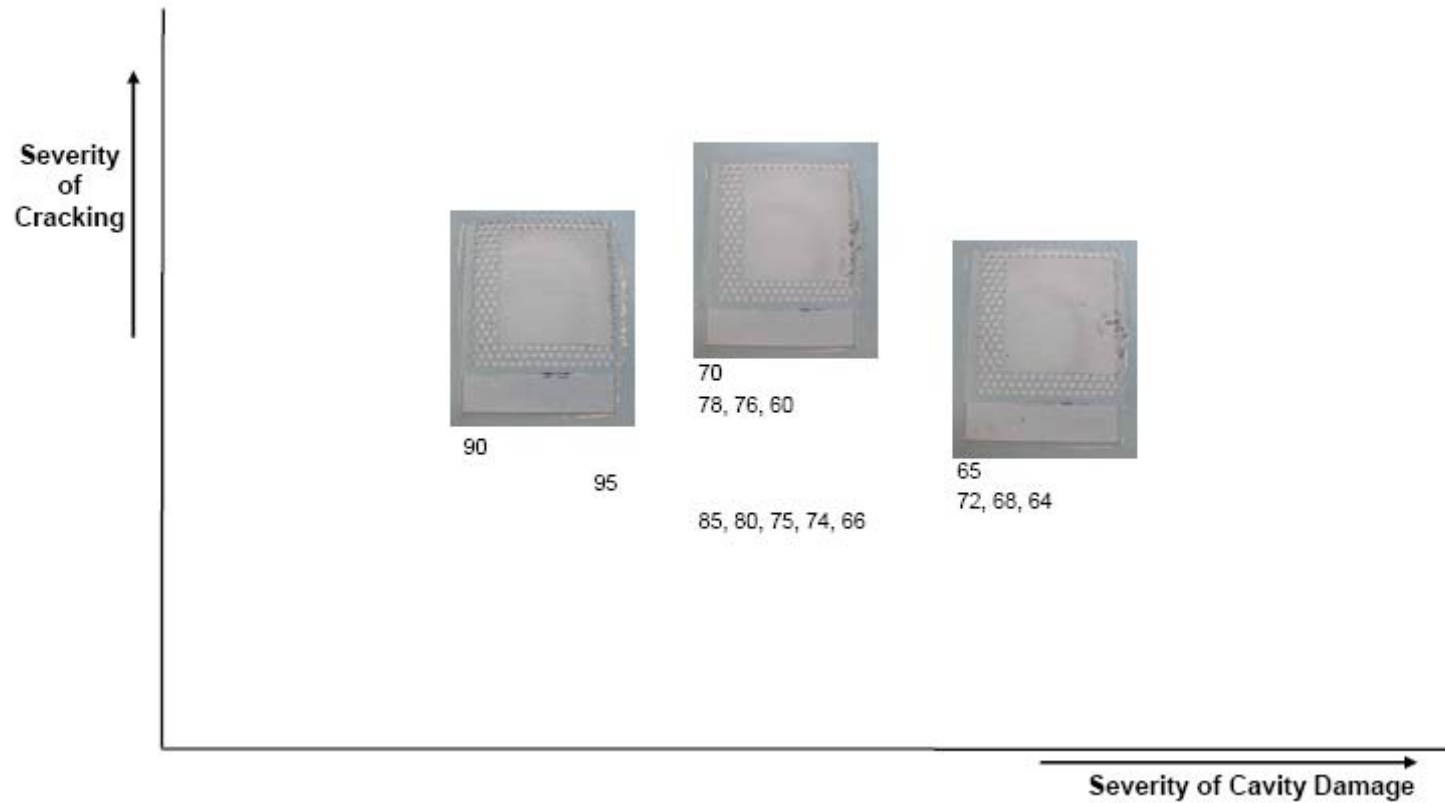


Figure 8.31 The different defects caused by varying the de-embossing temperature. The numbers represent the de-embossing temperature and where the corresponding image would be placed on the diagram, indicating that there is no obvious link between the defects and the de-embossing temperature.

8.2.6 Summary of the Effect of Parameter Changes

Increasing the master tool temperature leads to a rapid increase in mould fill. In the non-isothermal case, at constant substrate temperature, an increase from 30% to 90% mould fill was seen when the temperature was raised from 140°C to 155°C. The de-embossing force shows a strong relationship to embossing temperature, which increases linearly with an increase in temperature. The same temperature dependent behaviour is seen when plotting the de-embossing temperature against the de-embossing load, and indicates that the shrinkage plays a significant role in the de-embossing force. The percentage mould fill has been considered as a potential source of the increase in de-embossing load, but the relationship was less clear than the shrinkage. Furthermore, several authors have also commented on the effect of shrinkage on the de-embossing load [3, 20, 21].

Different defects were seen in the isothermal and the non-isothermal samples, but both showed cracking in regions of high stress. In the isothermal case these were seen in the bulk polymer, whilst in the non-isothermal samples cracks were seen in the embossed area. The cracking had a large effect on the isothermal samples, such that the severity of the crack would increase with temperature up to 150°C, where it would fully encircle the embossing, and prevent full extraction. In comparison, increasing the master tool temperature in the non-isothermal samples tended to reduce the severity of the defects whilst still improving the percentage mould fill.

An increase in the embossing load led to a linear increase in the mould fill, but a dramatic increase in the severity of the defects. As the embossing load was increased, the de-embossing load remained fairly constant. It is believed that this is related to the increase in

the severity of the defects, since the de-embossing load is not only related to the adhesion and friction between the master tool and the embossing, but by the ability of the embossing to withstand the de-embossing forces.

When the de-embossing force is plotted against the percentage mould fill in the dwell time experiments, an increase in de-embossing load was seen, which corresponded to the much smaller increase in the severity of the defects. Thus, it is believed that the mould fill does affect the de-embossing load, but in the case of the embossing load the severe cracking masked this increase. Similarly, in the case of the embossing temperature, the increase in shrinkage and therefore the friction also masked the effect.

To increase the mould fill and to minimise the severity of the defects, an increase in the master tool temperature is recommended during non-isothermal embossing. This is because an increase in the master tool temperature leads to a reduction in the severity of the defects, and a rapid increase in mould fill. An increase in dwell time is an alternative way to increase the mould fill. However, this leads to some increase in the severity of the defects, and is less effective at reducing the mould fill whilst it also increases the cycle time. Increasing the embossing load should be attempted last as this does increase the mould fill, but also the severity of the defects. It was found that increasing the de-embossing temperature does not alter the degree of mould fill, but does reduce the de-embossing load. This however does not result in a reduction in the severity of the defects.

The knowledge obtained in this chapter was used to develop the embossing parameters for replicating a mould for piezocomposites. The developed procedure is discussed in section 5.2.1, and resultant in the piezocomposites that are discussed in chapter 9.

8.3 Typical Cycle Times, Set-up Times and Equipment Costs

The original driving force for this work was to develop a route that could allow VP embossing to be made cost effective by the development of a mould production route that would have a sufficiently low cost for mould dissolution. Hot embossing was identified as viable route, not only because it is capable of producing small feature size, very high aspect ratio structures, but also because it is a flexible process, with short set-up times and low equipment costs. It does, however, have a longer cycle time than μ IM.

The low equipment costs of hot embossing have been demonstrated by modifying the Instron 2525 for < £3500¹. In this work it was found that the typical set-up time to change the master tool was ~ 20 minutes. However, this was due to the time taken to heat and cool the thermal tape holding the master tool to the stage. If a separate stage for each tool was used the set-up time would be improved to a few minutes. The cycle time depends on the process parameters such as the length of dwell, and the heating and cooling rates. However, if the values in section 5.2.1 are used, a typical cycle time would be 31 minutes. Such a cycle time is acceptable since the other steps in the VP embossing process, such as drying, sintering and mould dissolution, also require long periods of time.

The low equipment costs and flexibility that have been demonstrated here indicate that it is possible to scale up the process out of the laboratory. A major contributor to the cost is the master tool, which is a cost that occurs in any micro replication process. However, this cost can be reduced by using the Bosch process, rather than the more expensive LIGA process, because synchrotron radiation is not necessary. Furthermore, incorporating many designs on

¹ platens £1275, chiller £1100, control box £814 plus machining costs

a larger tool during scale up will reduce the master tool costs and increase the number of moulds that can be made per cycle.

8.4 Chapter References

- [1] Y. Zhao and T. Cui “Fabrication of high-aspect-ratio polymer-based electrostatic comb drives using the hot embossing technique” *Journal of Micromechanics and Microengineering* 13 (2003) 430-435
- [2] T. Koerner et al “Epoxy resins as stamps for hot embossing of microstructures and Microfluidic channels” *Sensors and Actuators B* 107 (2005) 632-639
- [3] H. Becker and U. Helm “Hot embossing as a method for the fabrication of polymer high aspect ratio structures” *Sensors and Actuators* 83 (2000) 130-135
- [4] Y-J. Juang, J. Lee and K. W. Koelling “Hot Embossing in Microfabrication. Part 1: Experimental” *Polymer Engineering and Science* 42 3 (2002) 539-549
- [5] D. Zhang “Fabrication of Ceramic Microcomponents” *PhD Thesis, The University of Birmingham* (2006)
- [6] Jenoptik Mikrotechnik GmbH “Application Aspect ratio 20, depth 155 μm ” *HEX01 Data Sheet* (2005) received 10/03/06 from G. Ungelenk at Jenoptik
- [7] Jenoptik Mikrotechnik GmbH “Application Aspect ratio 5, depth 150 μm ” *HEX01 Data Sheet* (2005) received 10/03/06 from G. Ungelenk at Jenoptik
- [8] Jenoptik Mikrotechnik GmbH *Example Images Sent via Email* (2005) received 10/03/06 from G. Ungelenk at Jenoptik
- [9] R.W. Jaszewski et al “Properties of thin-adhesive films used for the replication of microstructures in polymers” *Microelectronic Engineering* 35 (1997) 381-384
- [10] H.D. Rowland and W. P. King “Polymer deformation and filling modes during microembossing” *Journal of Micromechanics and Microengineering* 14 (2004) 1625-1632
- [11] H. Mekarū et al “Microfabrication by hot embossing and injection molding at LASTI” *Microsystems Technologies* 10 (2004) 682-688
- [12] D. Hardt et al “Process variability in Micro-Embossing” *Innovation in Manufacturing Systems and Technology* (2005) Massachusetts Institute of Technology, USA
<http://hdl.handle.net/1721.1/7463>
- [13] B. Ganesan “Process Control for Micro-Embossing: Initial Variability Study” *Master of Science Thesis, Massachusetts Institute of Technology, USA* (2004)
- [14] L-W Pan, X. Shen, L. Lin “Microplastic Lens Array Fabricated by a Hot Intrusion Process” *Journal of Microelectromechanical Systems* 13 (6) (2004) 1063-1071

- [15] J. Narasimhan and I. Papautsky “Polymer embossing tools for rapid prototyping of plastic microfluidic devices” *Journal of Micromechanics and Micromachining* 14 (2004) 96-103
- [16] JENOPTIK Mikrotechnik <http://www.jo-mt.de/cps/rde/xchg/SID-26EE34DB-E7B1AB0D/mikrotechnik/hs.xsl/2479.htm> as viewed 01/11/06
- [17] Specac Ltd “Atlas Series Heated Platens User Manual” 2I-15514 Issue 10 (2005)
- [18] C. Moss (clive.moss@specac.co.uk) “Atlas Series Heated Platens” email to T J Clipsham (tjc152@bham.ac.uk) (05/10/06)
- [19] H. Becker, U. Heim “Silicon as a Tool Material for Polymer Hot Embossing” *MEMS '99. The Twelfth IEEE International Conference on Micro Electro Mechanical Systems* (1999) 228-231
- [20] M. Worgull, M. Hecke, W. K. Schomburg “Large-scale Hot Embossing” *Microsystems Technology* 12 (2005) 110-115
- [21] Y He, J-Z Fu, Z-C Chen “Research on optimization of the hot embossing process” *Journal of Micromechanics and Microengineering* 17 (2007) 2420-2425
- [22] D. Yao, V. L. Virupaksha and B. Kim “study on squeezing flow during nonisothermal embossing of polymer microstructures” *Polymer Engineering and Science* 45 (5) (2005) 652-660
- [23] J.M.G. Cowie and V. Arrighi “Polymers: chemistry and physics of modern materials. 3rd Edition” *CRC press Florida* (2008) ISBN-13: 978-0-8493-9813-1

Chapter 9

Fabrication and Characterisation of Moulded Piezocomposites

9 Fabrication and Characterisation of Moulded Piezocomposites

One aim of the project was to develop an approach to fabricating cost effective moulds for the subsequent ceramic replication. A hot embossing rig has been fabricated and characterised, allowing the identification of suitable parameters that can fully replicate the master tool. In the following section, the ability of the rig to accurately replicate the tool is assessed, along with the characterisation of the shrinkage that occurs during the subsequent ceramic replication. A different master tool was used in this work compared to section 8.1.3, and allowed smaller feature sizes and higher aspect ratio structures to be achieved, the details of which are discussed in section 9.1

9.1 Master Tool

The master tool used for these experiments was an array of pillars produced by the LIGA process at the Institut für Mikrotechnik Mainz GmbH, Mainz, Germany. The tool is different to the one used in section 8.1.3 and was chosen to demonstrate the ability of the process, and the in-house rig, to replicate high aspect ratio, small feature size polymer moulds. Ideally, the master tool developed in chapter 7 would have been used here, however the time taken to develop the deep array structures meant that this LIGA tool had to be used to characterise the process. Images of the tool are shown in Figure 9.1 to Figure 9.3, showing an even distribution of high aspect ratio, well defined, nickel pillars with a hexagonal cross section and packed in a hexagonal array. The pillar width, kerf and the height of the pillars were measured using the method outlined in section 5.3.1.

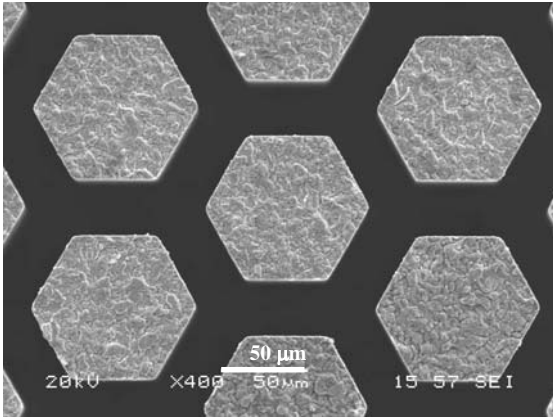


Figure 9.1 Plan view of five master tool pillars at x400 magnification

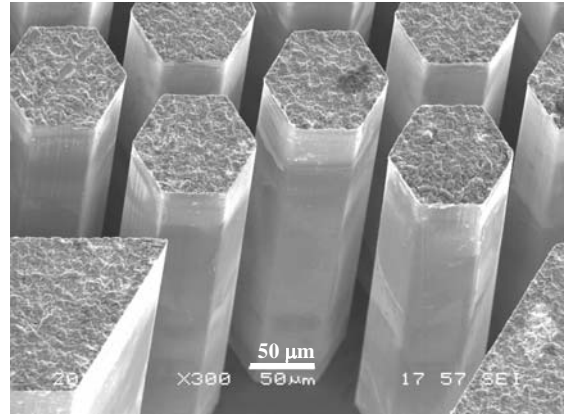


Figure 9.2 Perspective view of the master tool pillars at 25° tilt

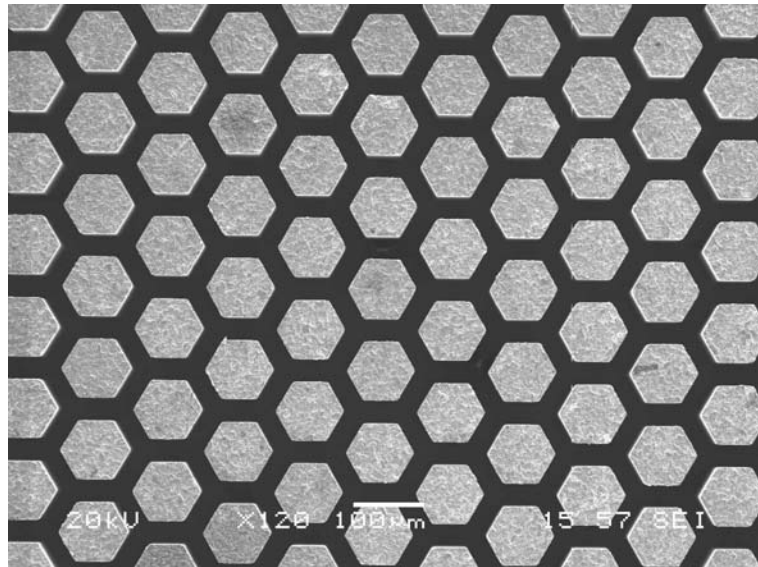


Figure 9.3 Plan view of the master tool showing a uniform array of pillars at x120 magnification

The data for the width of the pillars in the master tool are shown in a cumulative distribution curve in Figure 9.4. The interquartile range (IQR) is indicated by the width of the shaded region, with the first quartile (Q1), third quartile (Q3) and the median annotated on the chart. 25% of the data is less than 81.8 μm , 50% of the data is less than 81.9 μm , and 75% of the data is less than 82.1 μm , such that the central 50% of the data is within $\pm 0.2 \mu\text{m}$ of the median, 81.9 μm . Furthermore, the values between the 10% and 90% region show values

within $81.9 \pm 0.25 \mu\text{m}$, and indicate that, within experimental error, the majority of pillars are the same size.

The cumulative distribution curve for the kerf of the master tool is shown in Figure 9.5. The median kerf measures $31.5 \mu\text{m}$, with an IQR of $0.5 \mu\text{m}$ which is equivalent to the range of the experimental error, $\pm 0.25 \mu\text{m}$, whilst the values between at 10 % and 90 % are $31.1 \mu\text{m}$ and $32.1 \mu\text{m}$ respectively. The wider distribution of the kerf compared to the pillar width is believed to be caused by some of the pillars becoming bent during normal use. When this occurs this will effect the size of the kerf measured, and since this will make one kerf larger and another smaller, it will affect the distribution rather than the median. The distribution of the kerf can be described as $31.5^{+0.6}_{-0.4} \mu\text{m}$.

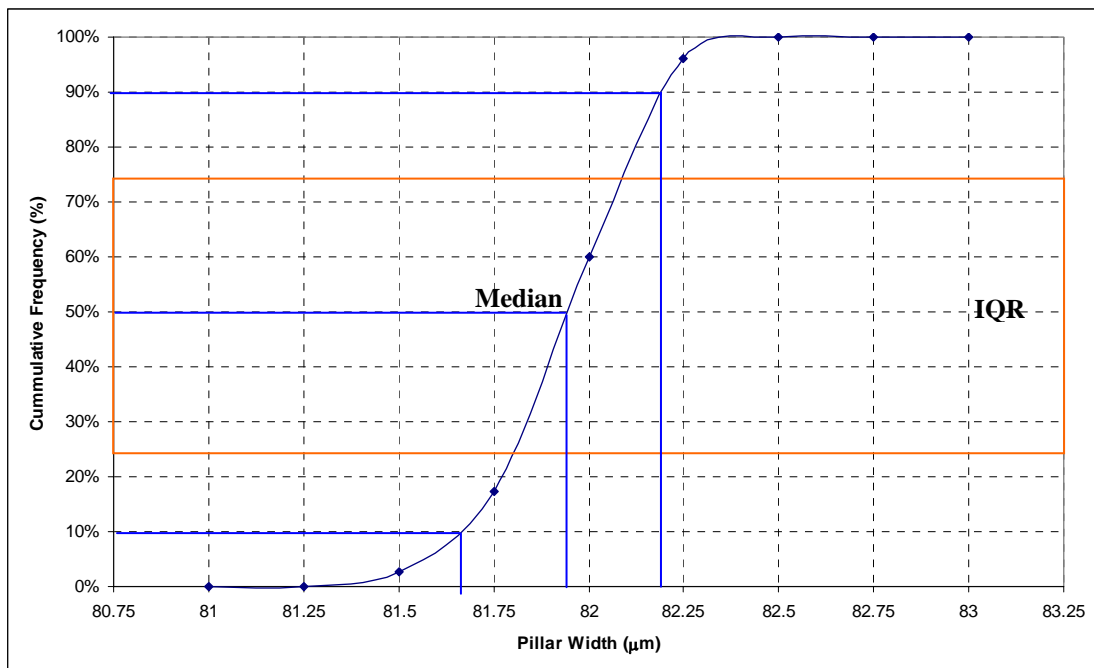


Figure 9.4 Cumulative frequency distribution of the measurements for pillars width, annotated with the position of the median, IQR (shaded region), and values at 10 % and 90 % cumulative frequency distribution. The chart shows the very good accuracy by the LIGA process.

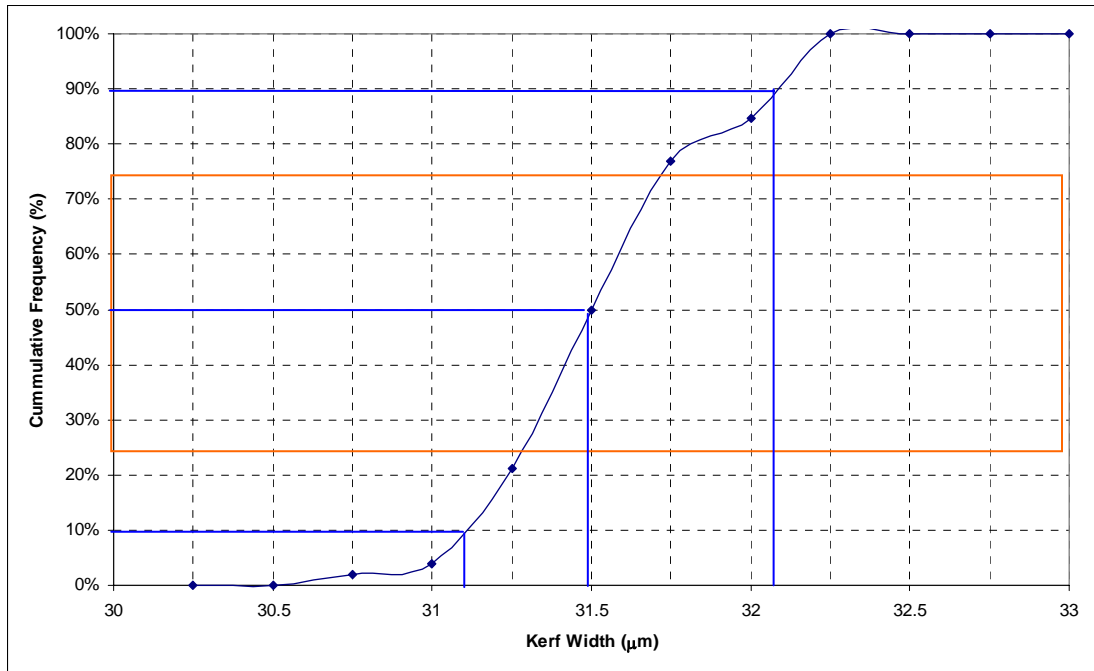


Figure 9.5 A cumulative frequency distribution curve of measurements for the kerf of the master tool, annotated with the position of the median, IQR (shaded region), and values at 10 % and 90 % cumulative frequency distribution. The distribution is broader than the pillar width because some of the pillars have become bent during normal use.

The height of the pillars was measured using the method outlined in section 5.3.3. The SEM stage is tilted so that the height of the pillars can be viewed, and then trigonometry is used to calculate the height. This method has the advantage of being non-destructive but it does result in a greater error compared to measuring the pillar width or kerf. The results are shown in Figure 9.6 which shows the median height of the pillars to be 446 μm with a Q1 and a Q3 value of 442 and 449 μm respectively. The range between the 10% and 90% values was found to be 27 μm which is a slightly larger variation than the kerf. It is not believed that the pillars vary by such a large degree, rather it is more appropriate that this distribution is caused by the degree of subjectivity involved in measuring the pillar height; which is then multiplied by the measurement angle, which increases the error further. This is discussed in section 5.3.3 and is believed to be within the estimated error of the measurements.

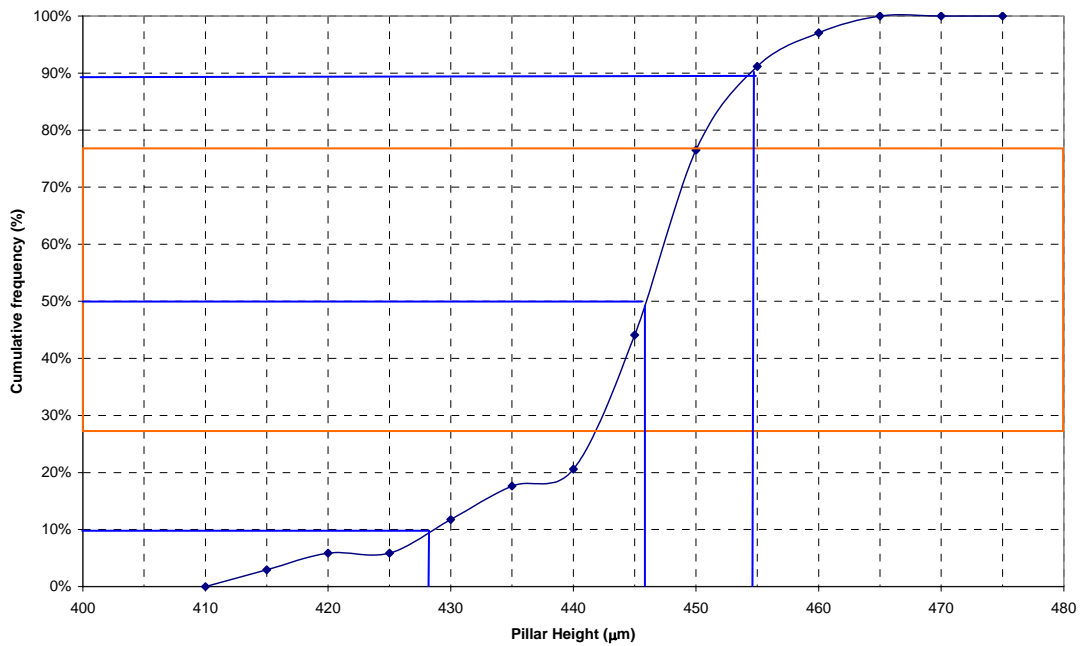


Figure 9.6 The cumulative frequency curve for the master tool pillar height, annotated with the position of the median, IQR (shaded region), and values at 10 % and 90 % cumulative frequency distribution. This variation is attributed to the measurement technique described in section 5.3.3

The pillar width, kerf and the height were found to be 81.9 μm, 31.5 μm and 448 μm respectively, and gives a maximum aspect ratio of 14.2. Since the minimum feature size is 31.5 μm, the master tool represents a small feature sized, very high aspect ratio structure.

9.2 Hot Embossed Moulds

Fifteen PMMA moulds were replicated from the master tool using the process parameters that were discussed in section 5.2.1. Examples of the embossed structures at various magnifications are shown in Figure 9.7 and Figure 9.8. Figure 9.8 (B) and (D) show a good similarity with the images of the master tool seen in Figure 9.1 and Figure 9.3. However some defects are present on the top surface of the moulds, figures (A) and (B), and whilst this is not ideal, the defects will not affect the functionality of the moulds. These defects will be transferred to the stock during VP embossing and will then be removed during lapping. These defects are likely to have occurred during demoulding where the polymer has fractured, rather than the bond between the bottom of the tool and the top of the mould breaking. Thus, it should be possible to reduce these defects by optimising the cooling rate or by adding a low friction coating to the master tool.

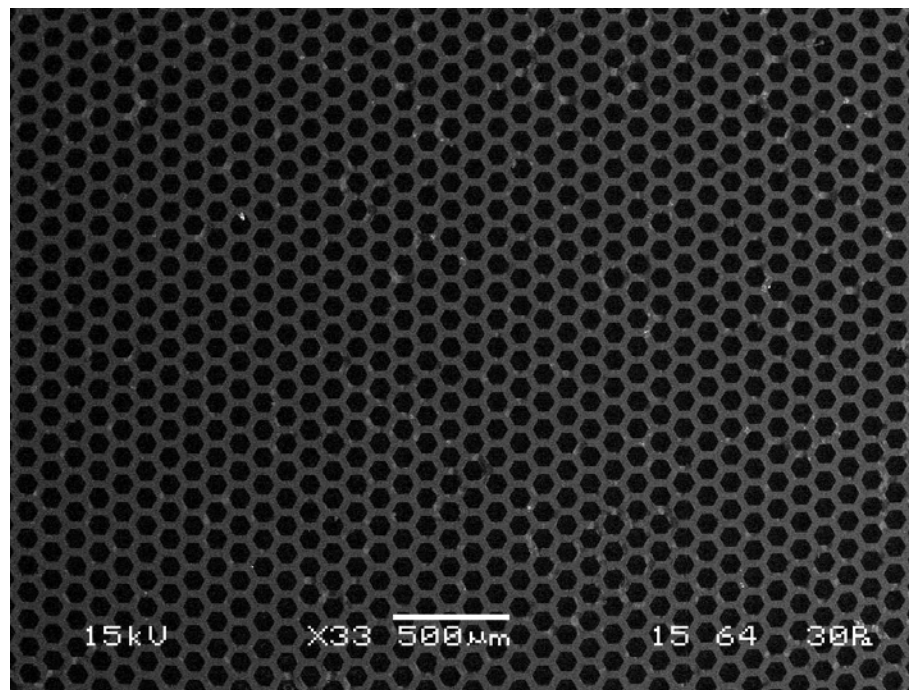


Figure 9.7 The PMMA mould at x30 magnification showing the uniformity of the mesh structure

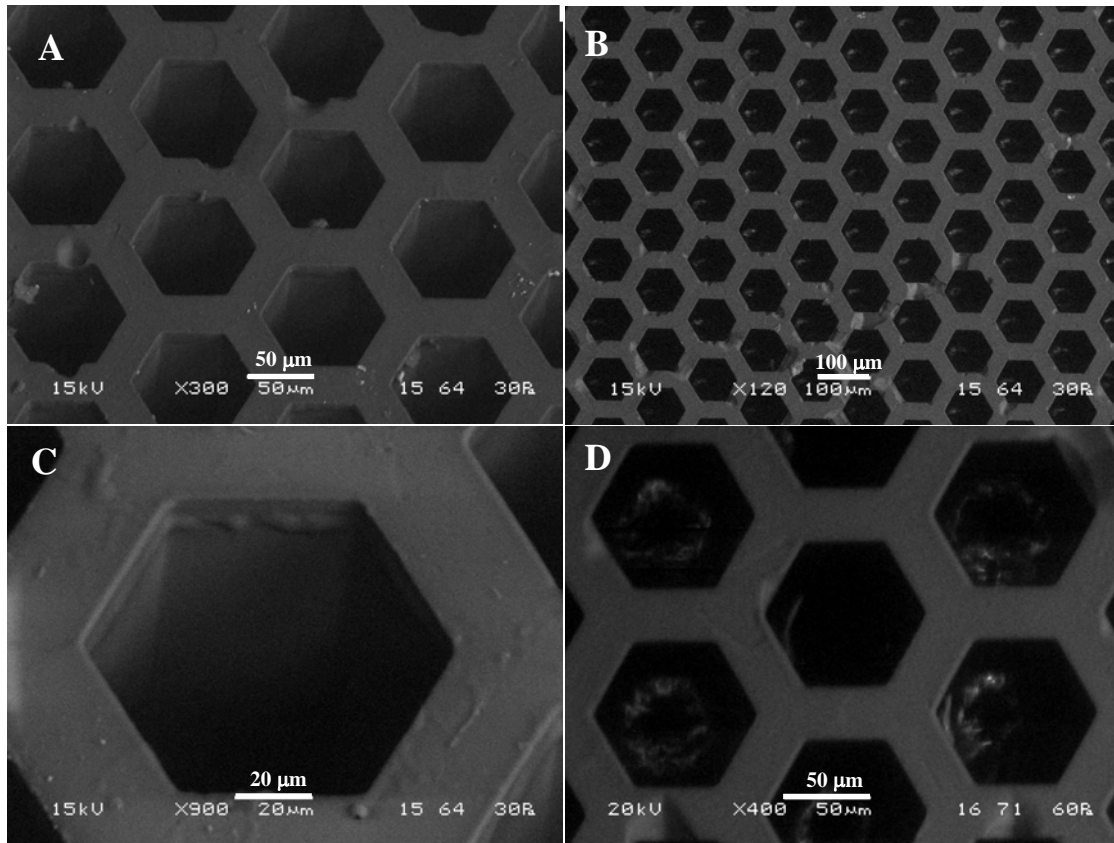


Figure 9.8 SEM images of the micro replicated PMMA mould at (A) x300 25° tilt, (B) x120, (C) x900 at 25° tilt and (D) x400. The uniformity of the array and the surface defects are clearly visible

The cavity width and cavity wall width were both measured using the method described in section 5.3.1. The median, Q1 and Q3 values can be obtained from the cumulative frequency curve shown in Figure 9.9. The median values of the mould and the master are both 81.9 µm. The quartile values for the mould are 81.4 to 82.3 µm, and for the master these are 81.8 to 82.1 µm. Thus, whilst the median size has not changed, the interquartile range has widened and has been extended to lower widths by the hot embossing process. Such behaviour is to be expected, as the polymer will shrink during cooling, and because the replication process will only add further variation to the variation that already existed in the tool. This increase in variation is further illustrated by considering the data between the 10 % and 90 % regions of

the cumulative distribution curve, which shows values of 80.8 μm and 82.6 μm respectively, such that 80% of the cavities measure $81.9^{+0.7}_{-1.1}$.

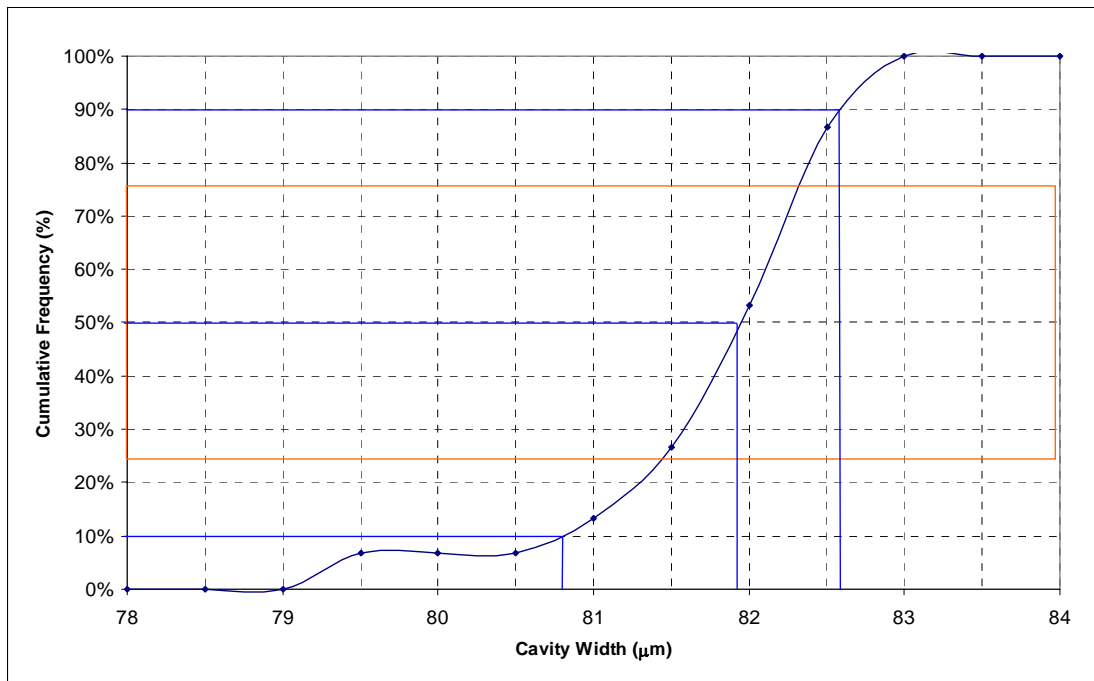


Figure 9.9 Cumulative distribution of median cavity width, annotated with the position of the median, IQR (shaded region), and values at 10 % and 90 % cumulative frequency distribution. This compares well with the pillar width measurements shown in Figure 9.4.

The width of the pillars of the master tool and the cavities of the mould can be further compared by studying Figure 9.10. This shows the variation between each sample relative to the median pillar width. The nature of the measurement technique means that the median is not necessarily in the centre of the Q1 and Q3 values, such that only the IQR or the error bar height should be compared to the median width of the master tool. When comparing the IQR and the error bar it can be seen that they are similar, indicating that most of the variation can be attributed to the measurement technique.

Most of the cavities are within 1 μm of the master tool pillar width, and many are within 0.4 μm which corresponds to the sum of the errors in measuring the pillars to within 0.2 μm , and the cavities to within 0.2 μm .

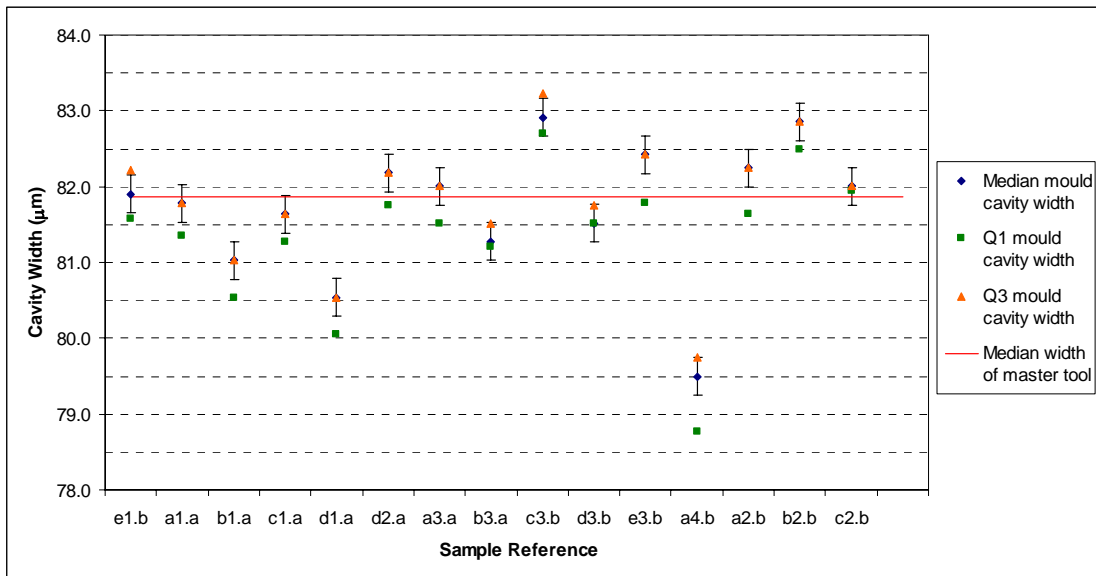


Figure 9.10 The cavity width of 15 hot embossed moulds, compared to the pillar size of the master tool. Most of the cavities are within 1 μm of the median pillar width and many have IQRs that intersect the median pillar width of the master tool

The width of the cavity walls was measured using the same technique as for the cavity widths. The measured values are displayed in Figure 9.11 showing the median, Q1 and Q3 values for each sample, and the median size of the kerf from the master tool. As with the pillar width, the Q1 and the Q3 values show a good correlation with the error bars, indicating a good reliability of the results. However, a greater scatter is seen between the samples than in Figure 9.10. The interquartile range for the cavity walls is twice as large as for the cavities and is 1.7 μm compared to 0.8 μm . Furthermore, the median cavity wall width has reduced by 1.6 μm to 29.9 μm , showing a significant difference in shrinkage compared to shrinkage of 0.0 μm for the cavity width. In terms of percentage shrinkage, this is a very large difference and ranges from 5 % for the cavity wall width to ~ 0 % for the width of the cavity.

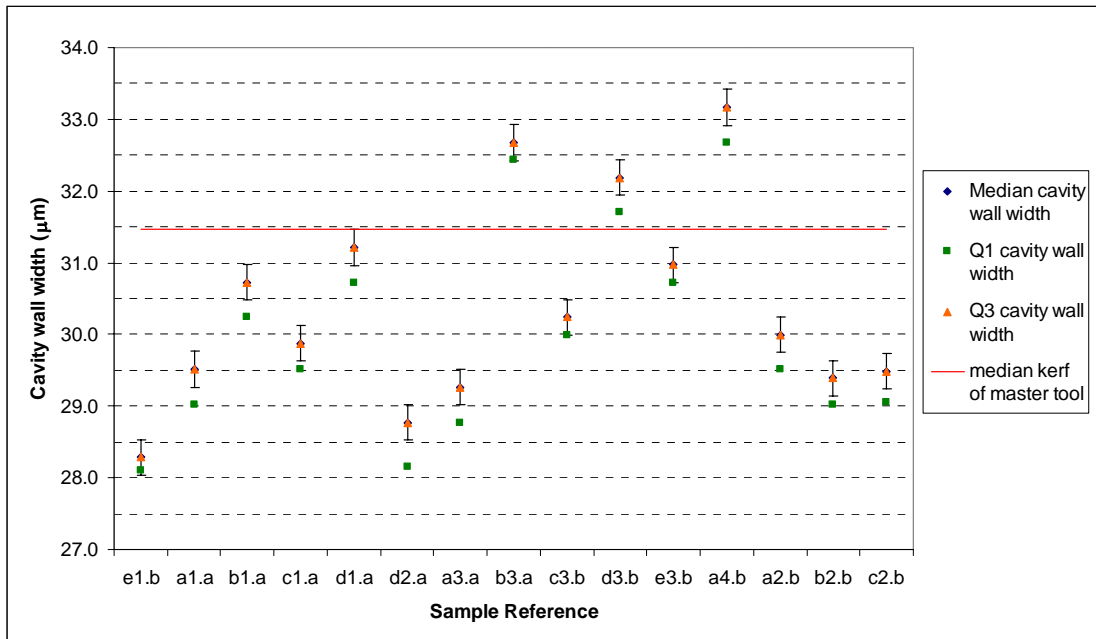


Figure 9.11 The width of the cavity walls for 15 hot embossed moulds compared to the kerf of the master tool showing a much broader scatter compared to the pillar width, but with most of the cell walls being smaller than the kerf of the master tool

The difference in shrinkage and scatter of the results can be explained by considering the mould as a mesh. Any changes in dimensions of the mesh occur by the shrinkage of the walls and not by the shrinkage of the cavities. Shrinkage in the width of the walls should result in the expansion of the cavities. However, the length of the walls also reduces, leading to a reduction in the length of the sides of each cavity. Thus, the change in cavity width is controlled not only by the reduction in the thickness of the cavity walls, but also by a reduction in the length of the cavity walls.

To identify the net change in the cavity width, compared to the wall width, we must consider the shrinkage seen in the moulds. The median shrinkage associated with the mould walls is 4.7 %, which for a width of 31.5 µm results in an absolute shrinkage of 1.5 µm. Thus, if this was the only direction of shrinkage the cavity would increase by 1.5 µm. However, assuming

uniform shrinkage, the length of the cavity walls must also shrink by 4.7 %. From geometry it can be shown that the length of one side of a hexagon, l , can be calculated from the parallel side width, p , by:

$$p = \sqrt{3}l \quad \text{Equation 9.1}$$

Thus, for a parallel side width of 82 μm the length of one side of a hexagon is 47 μm and the absolute shrinkage of this side is 2.2 μm . Through geometry it can be shown that the contraction of one side of a hexagon by 2.2 μm leads to the contraction across the cavity by 2.2 μm . Therefore, the net shrinkage of the cavity is calculated by the sum of the expansion and contraction, such that the cavity should reduce by 0.8 μm ($2.2 + - 1.5$). Such a value is realistic because it falls just outside the range set by the first and third quartiles, -0.1 and 0.6 μm , and the error associated with measuring the shrinkage is $\pm 0.5 \mu\text{m}$ as discussed in section 5.3.5.

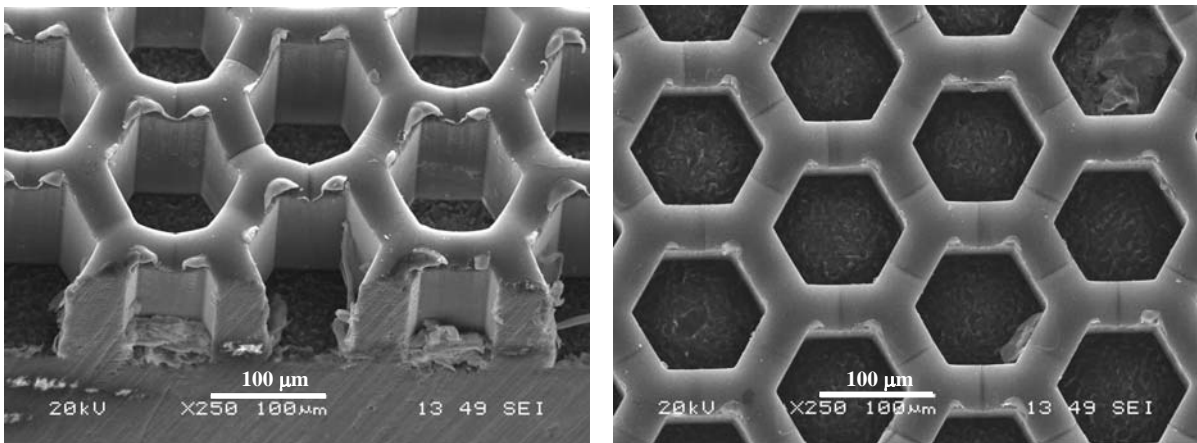


Figure 9.12 The surface of a hot embossed structure which has not been fully filled. The images show the characteristic raised areas at the cavity corners and the curved surface caused by the faster flow rate at the centre of the polymer structure

When the master tool has not been fully embossed, a curved surface with taller regions at the corners can be seen on the top of the replicated structure as shown in Figure 9.12. By

comparing this surface to the flat surface seen in Figure 9.8 it is possible to conclude that the moulds have been fully embossed. The moulds were measured according to the method described in 5.3.4, and have a median depth of 416 μm , with Q1 and Q3 values of 415 μm and 422 μm respectively. This represents a shrinkage of $\sim 7\%$, and is reasonable considering the kerf shrank by 5%. Using this height the maximum aspect ratio can be calculated to be 13.9, with a minimum feature size of 29.9 μm . An example of one of the images used to measure the height is shown in Figure 9.13

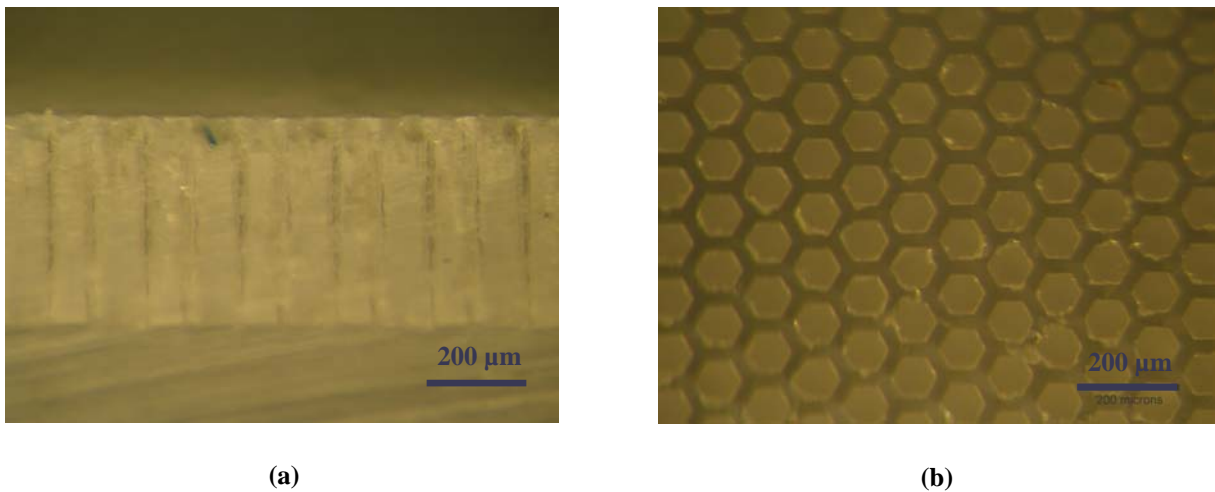


Figure 9.13 Optical micrographs showing the depth of the mould cavities (a) and the mesh structure from above (b). A scale was obtained from (b) to measure the depth of the cavities in (a).

The aspect ratio and feature sizes presented in this section compare well with the hot embossed structures found in the literature and described in section 3.1.4.3 and section 3.1.5. The highest aspect ratio found in these sections is 19 with a feature size of 8 μm , but this feature is attached to a much larger supporting structure. For a more accurate comparison it is more relevant to compare similar structures, such as pillar arrays or mesh structures. In the case of the pillar structures the highest aspect ratio is 11, but it is not formed by the polymer, but instead by the gap between the pillars and measures 70 μm [1]. When comparing the mesh structures, the largest aspect ratio achieved was 7.2 with a feature size of 55 μm . A

smaller feature size of 30 μm has also been achieved but only to an aspect ratio of 2.5 [2]. Therefore, it can be said that the hot embossed structures produced in this work, with aspect ratios of 14 and feature sizes of 30 μm show the best aspect ratio and feature sizes of any mesh structure seen in the literature.

9.3 Dried Pillars after Mould Dissolution

The PMMA moulds were embossed with the VPP dough and dried before dissolving the mould, as described by section 5.2.3 to section 5.2.5. Typical images of the dried PZT pillars are shown in Figure 9.14 to Figure 9.17, and show the pillars at x30, x120, x400 and at x300 (25° tilt), respectively. From the images it can be seen that the pillars have flat tops with well defined edges and show a uniform distribution. These flat tops replicate the flat surface at the bottom of the moulds seen in Figure 9.12, and demonstrate that the mould has been fully filled.

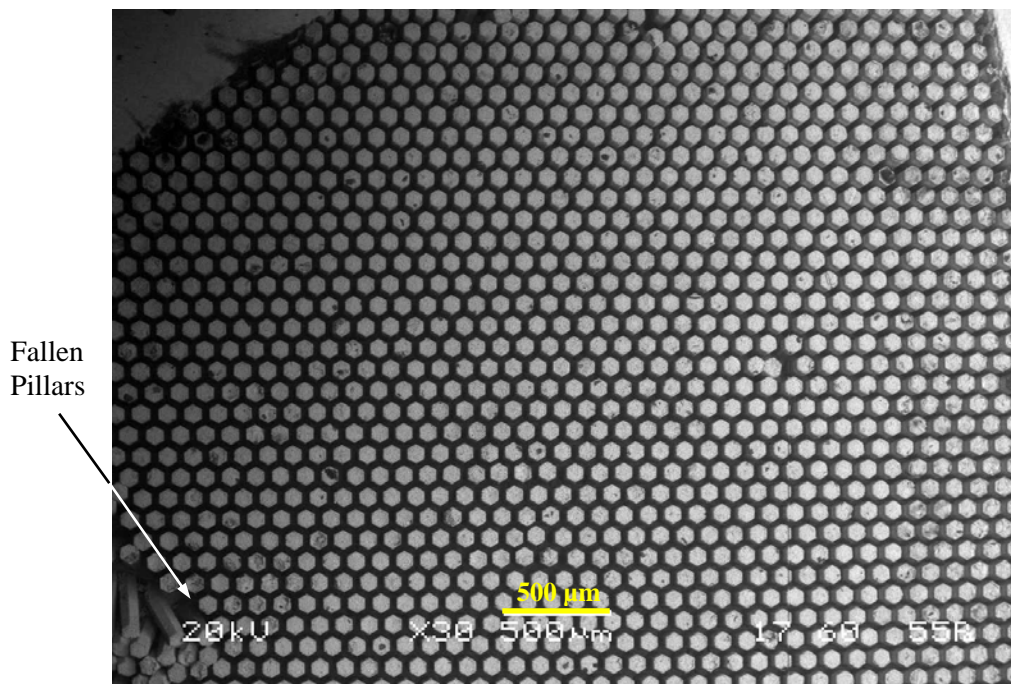


Figure 9.14 x30 SEM image of a demoulded PZT pillar array

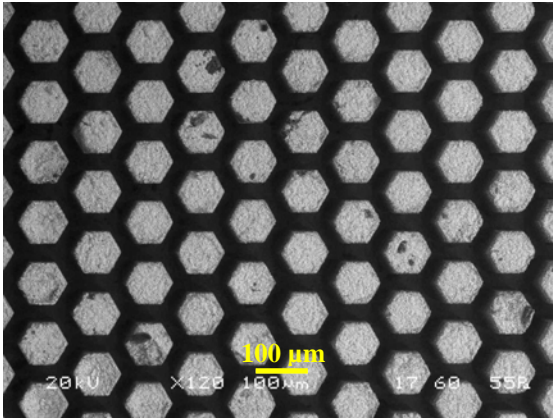


Figure 9.15 x120 SEM image of the green PZT pillar array

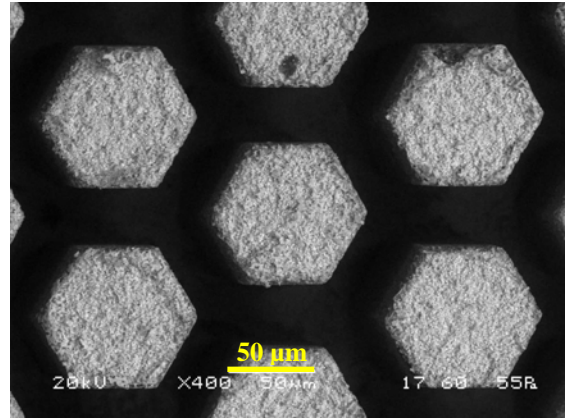


Figure 9.16 x400 SEM image of the demoulded green PZT pillars used for dimensional analysis

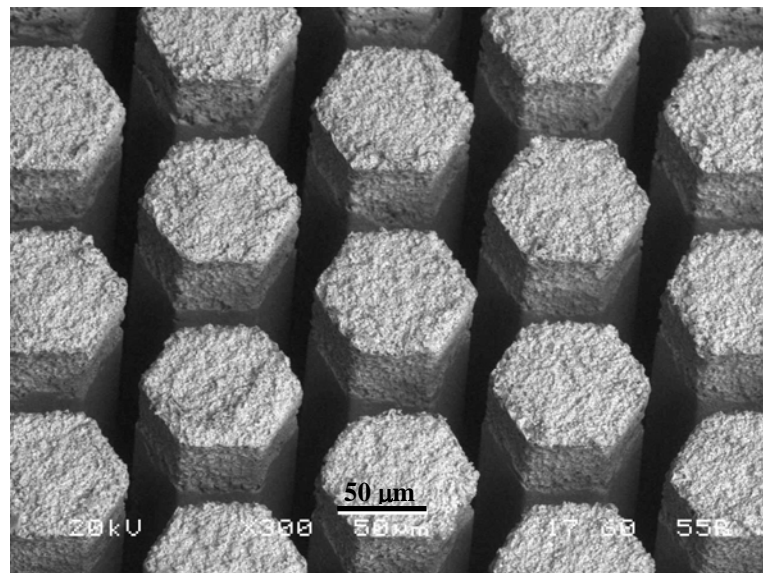


Figure 9.17 A 25° tilted SEM image at x300 magnification showing a uniform PZT pillar array with rough tops

Figure 9.17 shows the pillars with a tilted view. Here it can be seen that the top region is rougher than the bulk of the pillars and is likely to be caused by the dough not being fully pressed into the mould. A similar effect is known to occur in die pressing; whereby the friction on the side of the barrel results in a reduction in load or pressure on the powder with increasing mould depths. Furthermore, rheological investigations into PZT based VPP material has shown a different relationship between the extrusion pressure and velocity at

high and low shear rates. Researchers extruded VPP material through a range of dies with a different die land length to die diameter ratios (L / D) and at different velocities. They found that at small L / D ratios and slow velocities, i.e. low shear rates, the extrusion pressure and velocity showed a linear relationship. At higher shear rates (high L / D ratio, and rapid velocities) the VPP material showed a non-linear shear thinning behaviour [3]. Thus, it is felt that this less compacted region can be avoided by adjusting the VP embossing load, or velocity.

In Figure 9.14 it can be seen that some of the pillars are leaning to one side or have fallen over. However, this was a very small minority and it is not believed to affect the piezocomposite performance. The leaning is caused by the mould dissolution process, where, in the latter stages of mould dissolution, residual webbing between the pillars can be seen and the force exerted on the pillars can cause them to bend. If the pillars are not sufficiently strong, perhaps due to incomplete drying or air entrainment, they can break. Figure 9.18 shows the webbing that causes the leaning of the pillars, which was obtained from a preliminary sample.

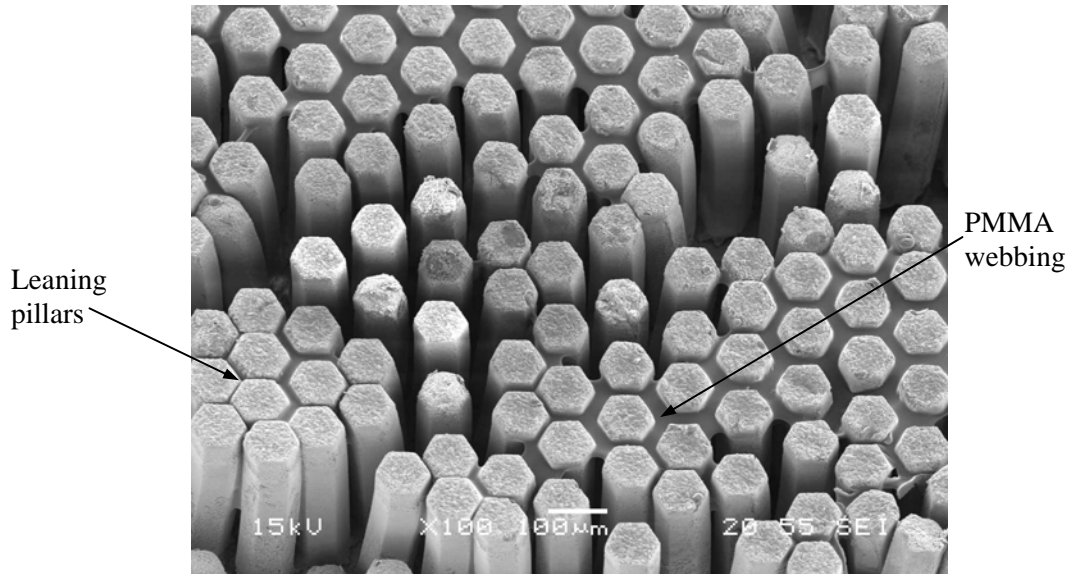


Figure 9.18 The PMMA webbing seen during the latter stages of mould dissolution that causes damage to the pillars and widens the distribution of the kerf

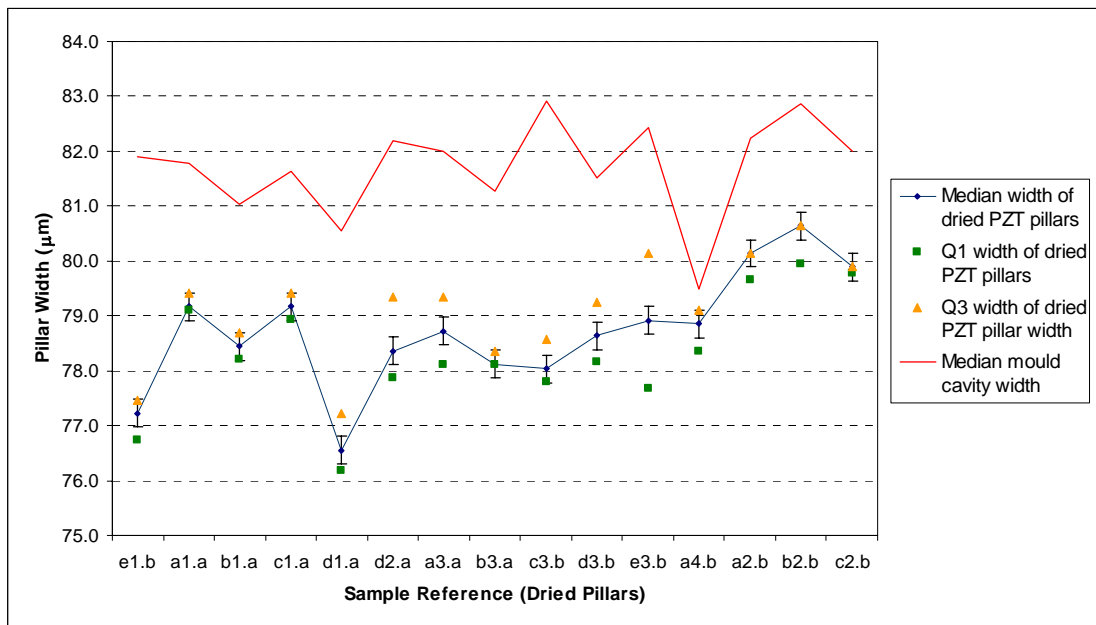


Figure 9.19 The median, Q1 and Q3 values for the pillar width of each sample relative to the cavity width of the mould. The median pillar width of the dried PZT pillars shows some similarity, but not complete similarity, with the median mould cavity width and is likely to be partly caused by the variation in shrinkage.

Figure 9.19 shows the median, Q1 and Q3 values of the pillar width for each dried sample. The figure also shows a line representing the median cavity width of the corresponding mould. It would be expected that the lower line, created by connecting the values of the

median PZT pillar width, would trace out exactly the same as the upper line representing the median cavity widths. There are similarities between the two lines, but the lines are not parallel to one another. This difference is caused by variations in the shrinkage from sample to sample, and is seen in Figure 9.20 and Figure 9.21. This variation between the samples is believed to be caused by insufficiently homogenised VPP dough from an unoptimised VPP composition and mixing procedure

The median pillar width has reduced to 78.7 μm , with the first and third quartile values at 78.2 μm and 79.2 μm , which are 0.5 μm either side of the median. Furthermore, the data shows that despite having undergone drying and replication, the ceramic pillars are now only $3.2 \pm 0.6 \mu\text{m}$ smaller than the master tool pillars. The main reason for the reduction in pillar size after two stages of replication is because the pillars are now dry, and have lost all of the solvent present from the dough.

It was not possible to use the same dough to VP emboss all of the moulds so instead two batches of dough of the same starting composition were used. The shrinkage of dough A is shown in Figure 9.20 and the shrinkage of dough B is shown in Figure 9.21. Dough A shows a smaller range compared to dough B suggesting that dough A is more homogenous. Nevertheless, the doughs show similar mean values of shrinkage, being 3.8 % and 3.5 % respectively. The absolute error associated with determining the shrinkage is $\pm 0.6\%$ as described in section 5.3.5 and therefore it is reasonable to say that these values show good agreement. If the two doughs were considered as one, there are a sufficient number of values to describe the distribution in terms of the median, Q1 and Q3 values. In this case the distribution is described by the values 3.5 %, 2.9 % and 4.5 % respectively. The Q1 value is

within the experimental error of the median, whilst the Q3 value is just outside of the absolute experimental error of 0.6 %, which indicates a good reliability of the results. Furthermore, these values agree well with the literature, which comments on the linear shrinkage of VP processed tape to be between 3 to 4 % depending on the direction of shrinkage [3].

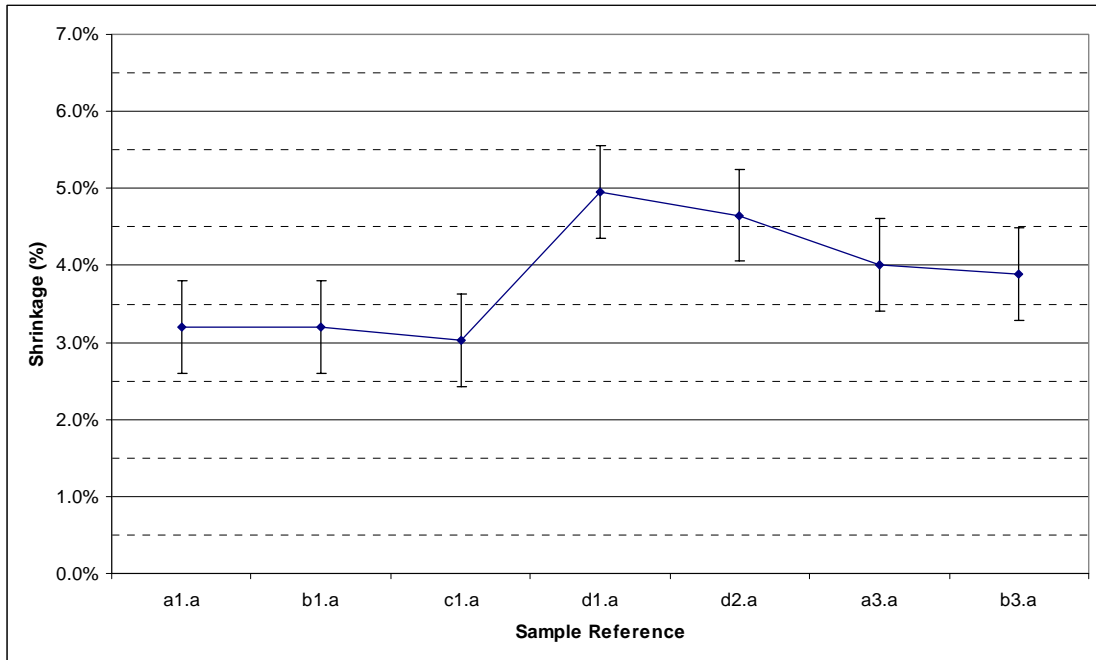


Figure 9.20 The drying shrinkage seen in samples replicated using dough A showing a large variation of 2%

The kerf of the pillar arrays was measured using the same procedure as in the previous sections. However, the kerf is influenced strongly by the leaning of pillars so it was necessary to measure the kerf in all three 3 directions, leading to a total of ~ 50 measurements per sample. The resultant median, Q1 and Q3 values for each sample are shown in Figure 9.22, along with the cavity wall width for the polymer mould.

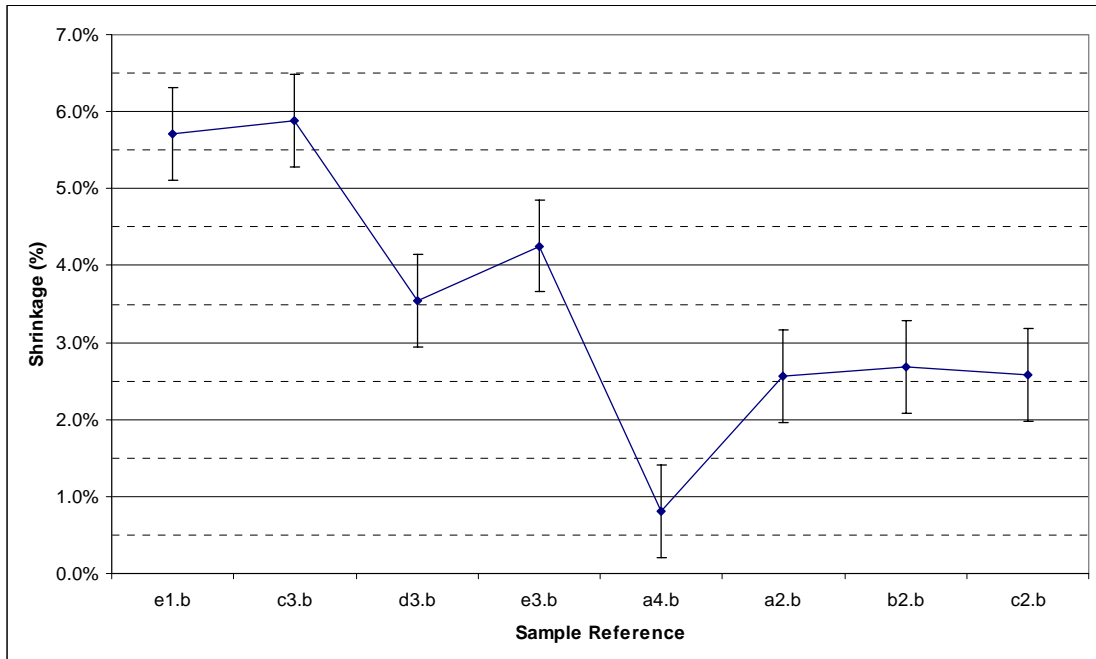


Figure 9.21 The drying shrinkage seen in samples replicated using dough B, which shows a very large variation in shrinkage of over 5%

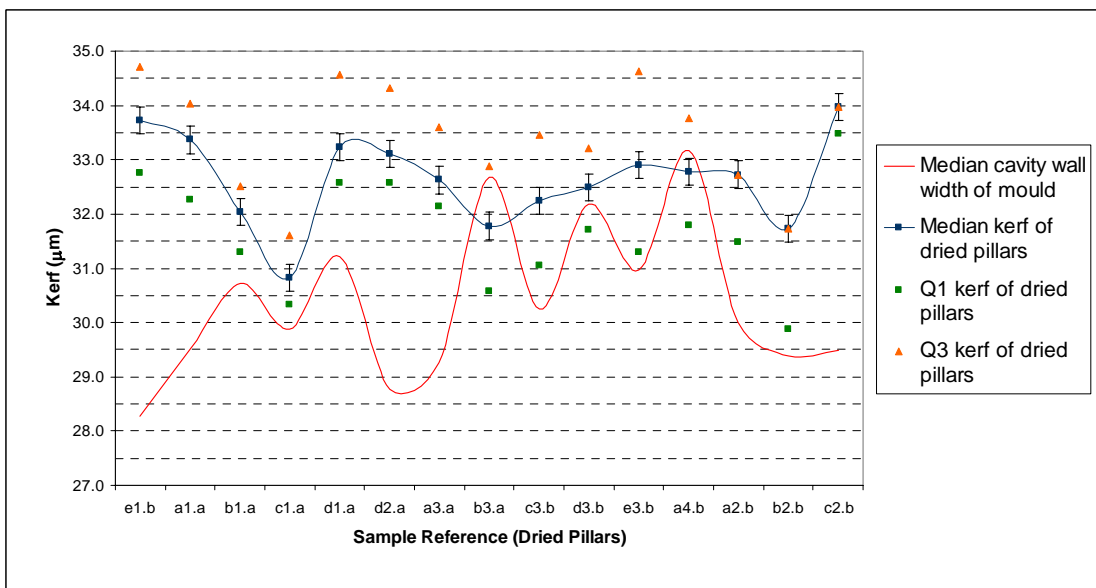


Figure 9.22 The median, Q1 and Q3 values of the kerf relative to the width of the cavity walls. A poor similarity between the two lines occurs because of the distortion of the array by the webbing during dissolution.

From the figure it is evident that the median size of the kerf has increased. The median kerf of the dried pillars is now 32.7 µm and the Q1 and Q3 values have increased to 32.1 µm and

33.2 μm respectively. It can also be seen that the line drawn by connecting the median values of the kerf shows a limited similarity to the cavity wall width. This limited similarity is caused not only by the distortion caused by the webbing but also by the variation in shrinkage. The unexpected increase in the kerf can be explained by the PZT pillars drying in the mould.

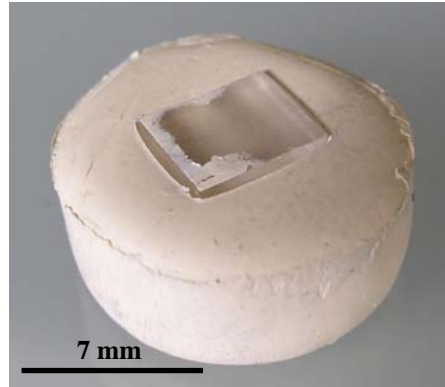


Figure 9.23 An example image of the mould embedded in the PZT dough, such that the contraction of the stock is limited by the mould

If the pillars were demoulded before drying then the stock would be free to contract and would be able to draw the pillars together and maintain the volume fraction. However, in this case, the mould is embedded in the dough, as shown in Figure 9.23, such that when the dough shrinks it contracts around the mould. Therefore, the pillars are able to shrink but the stock, and hence the kerf, is restrained by the mould. The lower limit of the kerf is defined by the cavity wall thickness whilst the largest value is limited to the width of the wall plus the shrinkage of the pillar.

The height of the dried pillars was measured from some of the samples to gain an approximation of the height and aspect ratio of the pillars. The height of all of the samples was not measured because this would have required a destructive investigation. Where it was possible to see the full length of a pillar a measurement was taken, and an example image is

shown in Figure 9.24. The height was found to be approximately 400 μm giving a pillar aspect ratio of 5 and a linear shrinkage of under 5 %. As highlighted in section 5.3.3, this shrinkage appears to be a good approximation, since it is close to the shrinkage seen for the pillar width but is slightly higher. This discrepancy is to be expected since the pillars did not fracture at the absolute bottom of the pillar. Nevertheless the similarity indicates that this is a reasonable approximation.

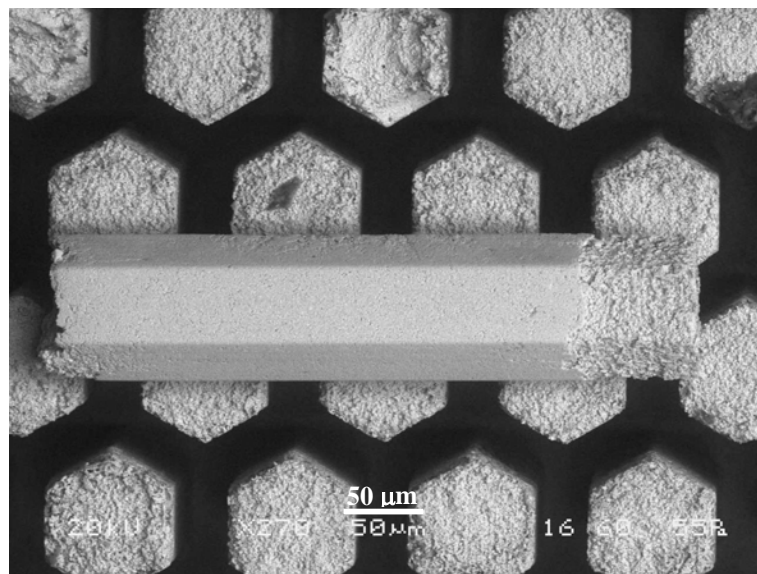


Figure 9.24 A x270 SEM image of broken pillar used to determine the height of the dried PZT pillars. Since the pillar was broken this represents an underestimate of the height of the pillars. The figure also shows the rough surface that is present at the top of the pillars that was discussed at the start of this section

9.4 Sintered Pillars

The demoulded pillars were burnt out and sintered according to the schedule outlined in section 5.2.6. Due to the shrinkage associated with the sintering, the dimensional analysis was carried out on images taken at x450 magnification rather than x400 and improved the absolute error to $\pm 0.22 \mu\text{m}$. Images of the sintered pillar array are shown in Figure 9.25 and Figure 9.28 at magnifications x30, x120, x450 and x900 with a 25° tilt. They show an increased amount of distortion to the array compared to the moulds and the dried pillars. This is caused by creep during sintering, which is a common problem in the production of all PZT components and is not specific to VPP material [3]. Creep can be driven by residual stresses, or even by the pillar's own self weight, if the pillar has moved from its vertical axis. Therefore, the pillars presented here were sintered upside down to maintain their vertical alignment.

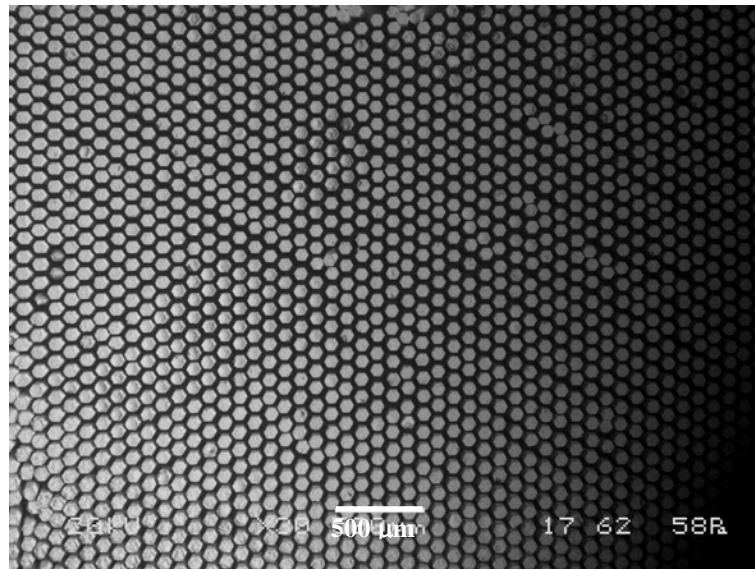


Figure 9.25 A sintered PZT pillar array at x30 magnification showing reasonable uniformity

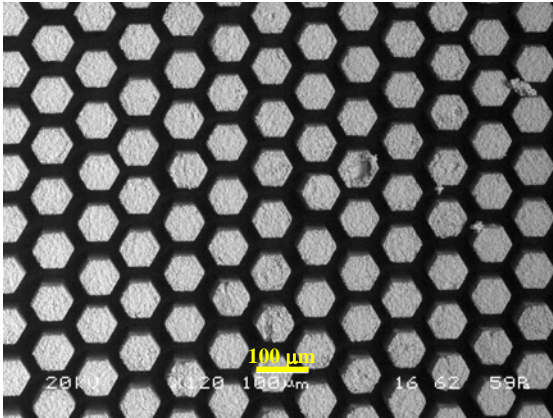


Figure 9.26 A sintered PZT pillar array at x120 magnification

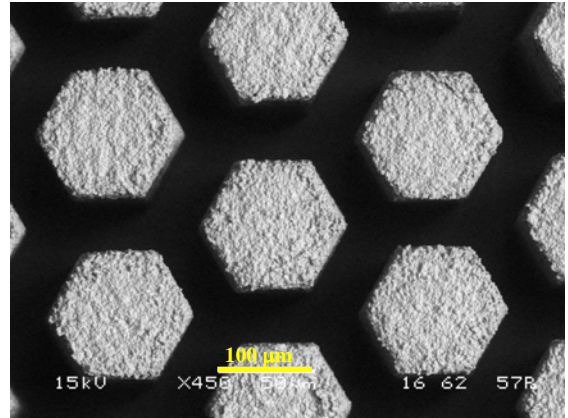


Figure 9.27 Sintered PZT pillars and kerf at x450 used for dimensional analysis

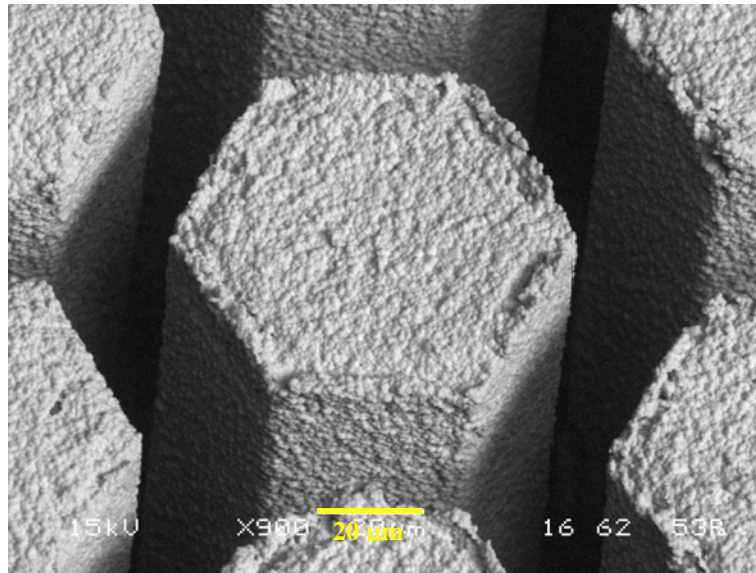


Figure 9.28 A sintered PZT pillar at x900 magnification and 25° tilt with well defined edges and sintered surface

The width of the sintered PZT pillars was measured and the median, Q1 and Q3 values are shown in Figure 9.29, along with a line representing the median size of the dried PZT pillars. As is evident from the figure, the interquartile range of each sample is within experimental error, and indicates a good reliability in the results. The median sintered pillar width is 68.7 μm , and the first and third quartile values are 68.2 and 69.5 μm respectively. The interquartile range has now increased to values six times greater than the experimental error, but has actually only increased by a further 0.3 μm from the dried and demoulded pillars.

This suggests that an interquartile range of such a value is caused by the succession of process stages rather than the sintering stage itself.

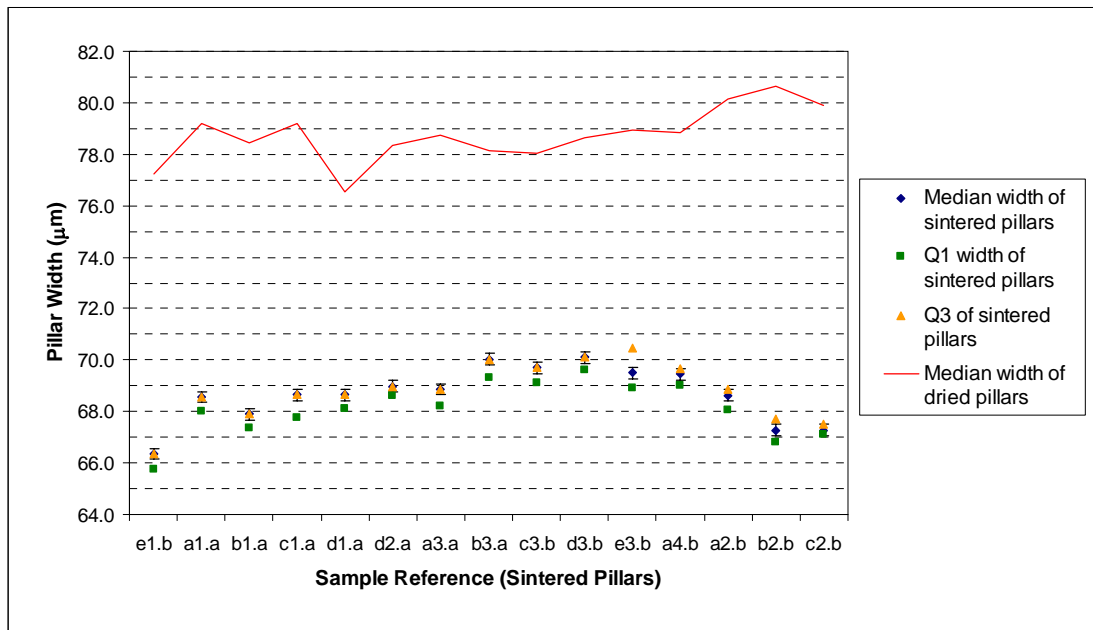


Figure 9.29 A plot of the sintered pillar width and the dried pillar width of each sample. The chart shows little similarity between the to the original width of the dried pillars and the pillar width of the sintered pillars which is believed to be caused by variation of the sintering shrinkage

The shrinkage from the dried pillar stage to the sintered stage, for both dough A and B, are shown in Figure 9.30. In this figure 80 % of the data falls within a rather broad band between 10 and 14 % shrinkage. The median shrinkage of the two doughs is 12.5 %, which matches well with the mean of 12.8 %. The first and third quartiles are at 11.4 % and 13.8 %, and are 0.9 and 1.3 % away from the median respectively. The variation in shrinkage is larger than the experimental error of ± 0.6 % and is most likely to be caused by the difficulties encountered in measuring the leaning pillars. The literature reports that the shrinkage of VP tape is around 14 % [3], which is at the upper end of the shrinkage range of the sintered pillars presented here. The slightly smaller shrinkage compared to the literature can be attributed to the different forming processes used after mixing. The researchers

measured the shrinkage using calendared VPP tape that was then dried and sintered. Not only are the dimensions of the tapes much larger, making the shrinkage easier to quantify, but the different processing conditions can affect the shrinkage too.

PZT creeps during sintering [3] and is driven by the residual stresses and the component's self weight. Thus, components that undergo different processing conditions will distort and shrink in different ways. The residual stresses that remain in the dough after calendaring are different to the stresses that occur in the pillars after VP embossing. For example, tapes are typically dried under a weight, which also gives different drying conditions to the pillars that are dried in a PMMA mould. Tapes are typically sintered under weights, or are buried in zircon sand, whilst the PZT pillars are sintered upside down in the sand but do not contact the sand, such that they are free to move under their own self weight. In addition, the composition of the VPP dough in the literature was different to the PZT used in this work. In the tapes PZT-5A, from Morgan Advanced Ceramics, was used but in this work TRS610C, from TRS Ceramics, was used. The other constituents are not given in the literature but, for example, an increase in binder or solvent quantity, or indeed the use of a different binder-solvent system, is likely to lead to a greater shrinkage during drying and sintering. Therefore, a difference between the mean shrinkage of ~12.5 % shows a reasonable comparison to the reported 14 % for PZT tapes. The variation of the shrinkage is a concern and the VPP mixing procedure and composition should be optimised to study the shrinkage further. Once this has been carried out the effect of shrinkage can be eliminated as a cause of the variation of the pillar width and the kerf.

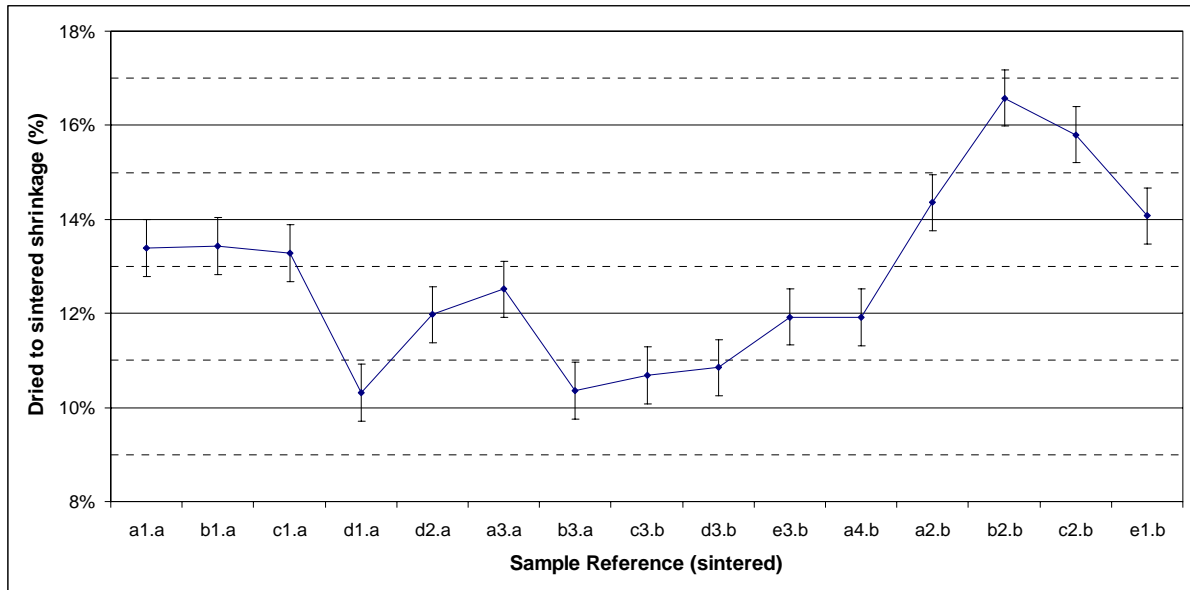


Figure 9.30 A plot of the shrinkage that has occurred from during sintering (only) for every sample. The second letter in the sample reference records the batch of dough that was used for the sample

The median sintered kerf, Q1, Q3 and the median dried kerf for each sample are plotted in Figure 9.31. The upper and lower lines from the median kerf of the dried and sintered samples show a limited similarity. The IQR within each sample is very large and is typically 4.5 μm , and is 3 times larger than is seen in the dried kerf. This large interquartile range reflects the distortion caused by creep of the sintered pillars, and is no longer representative of the experimental error. The median kerf of the sintered pillars is 29.8 μm and the Q1 and Q3 values are 29.3 and 31.0 μm . This gives an interquartile range between all of the samples of 1.7 μm , which compares well to an IQR of 1.7 μm for the mould cavity walls, but is greater than the IQR of the dried pillars which was 1.1 μm .

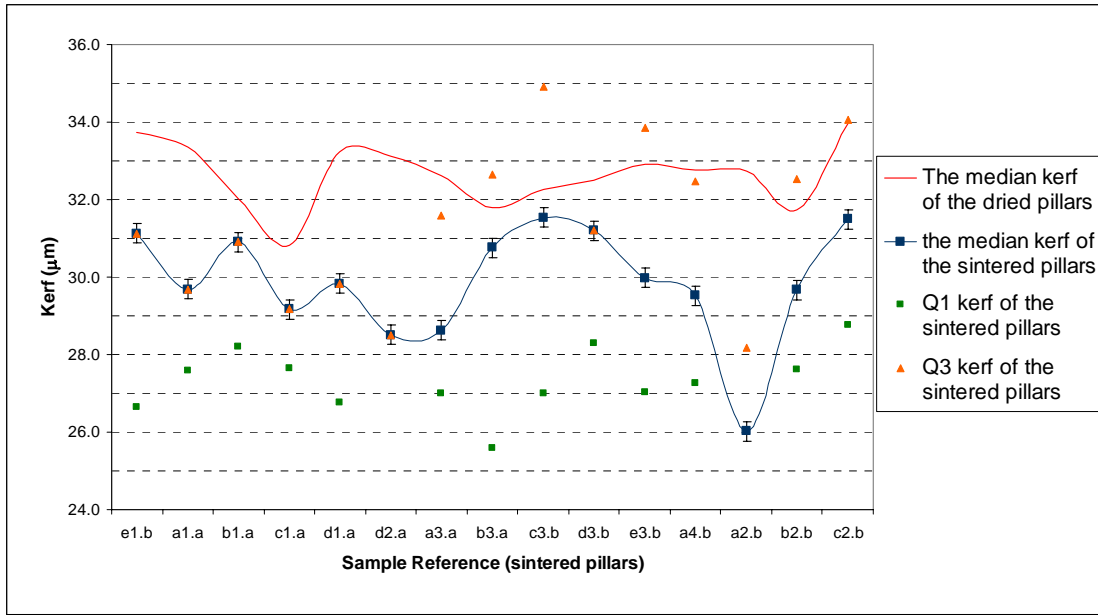


Figure 9.31 A plot of the size of the kerf for each sample at both the drying and sintering stage. The chart shows a wide IQR relative to the previous stages and poor similarity between the dried and sintered pillar arrays due to variable shrinkage and distortion caused by creep.

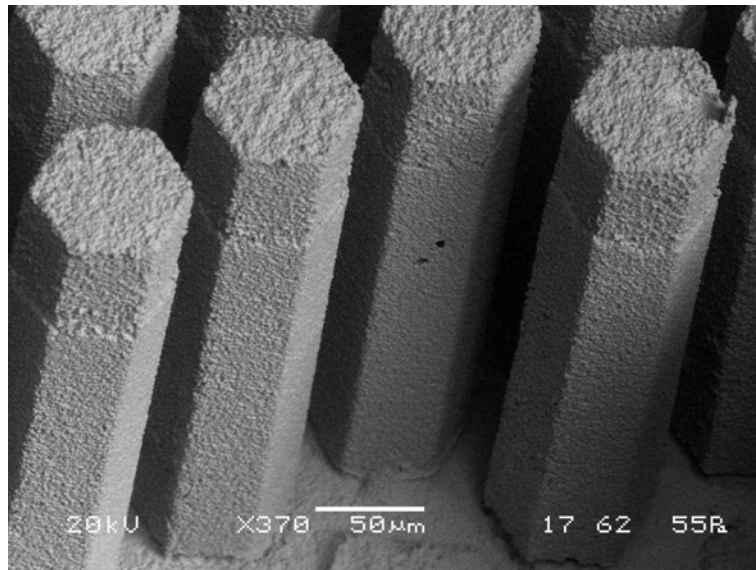


Figure 9.32 A typical SEM image at x370 magnification that was used to measure the height of the PZT sintered pillars, which also shows the rough tops of the pillars that were discussed in section 9.3

The height of some of the pillars was measured using the same method detailed in section 9.3. An example of the image used to calculate the height is shown in Figure 9.32. It was found that the height was approximately 350 μm , giving a linear shrinkage of 13 %. This

level of shrinkage shows a good agreement with the shrinkage calculated from the pillar width data and the literature.

The pillar width of 68.7 μm is well below what is typically achieved using dice and fill [4, 5]. The height of the bristle block means that the aspect ratio of the pillar is 5 and the aspect ratio of the kerf is 11.7. The previous best for VP embossing into hot embossed moulds was achieved in [2] and produced $\sim 63 \mu\text{m}$ wide pillars, with a kerf of 58 μm , resulting in a maximum aspect ratio of 4.3. Therefore, despite the pillar width in this work being slightly larger, the kerf of 29.8 μm is significantly smaller than has previously been achieved by this method, and the aspect ratio is greater than the 7.2 seen for dried pillars in Table 3.6 [2].

9.5 Piezocomposite Performance

Two samples that showed the most uniform pillar arrays from the sintered samples were fabricated into piezocomposites by the process steps outlined in section 5.2.7 to 5.2.10. The piezocomposites were lapped down to thicknesses of $\sim 160 \mu\text{m}$, giving a pillar aspect ratio of 2.3, which is larger than the aspect ratio required for the correct pulse response of piezocomposites [6]. The sintered samples were tall enough to produce higher aspect ratio piezocomposites, and therefore an improved k_t , but this would have resulted in a lower operating frequency.

The uniformity of the pillar array has been improved by the lapping stage, whereby distortion from the upper and lower sections is removed from the sintered arrays. This improved uniformity is demonstrated by comparing Figure 9.33 to Figure 9.25 and Figure 9.26. The improved uniformity will lead to more pronounced resonance peaks.

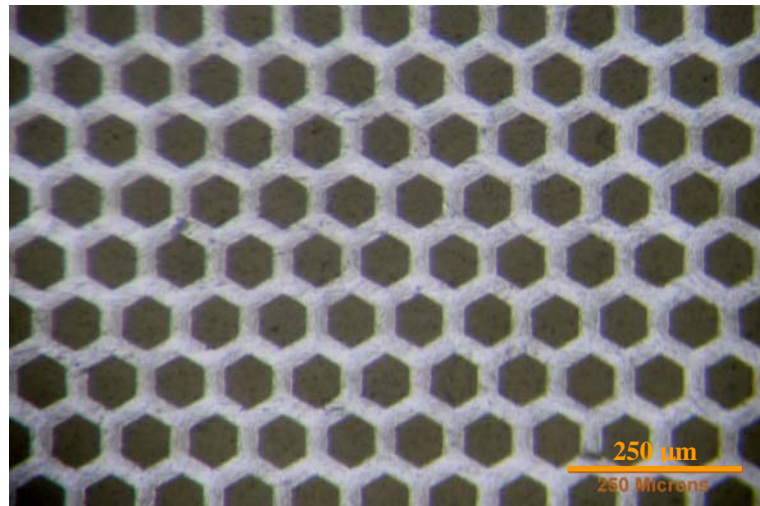


Figure 9.33 An optical micrograph of the backfilled and lapped piezocomposite. The defects and distortions seen in the previous sections have been removed by the lapping process leaving a highly uniform array

By rearranging Equation 2.6 the velocity of sound can be calculated. The thickness of each sample was measured using a micrometer, to $\pm 1.6 \mu\text{m}$, and gave thicknesses of 160 and 165 μm . The velocity of sound in a piezocomposite can be calculated by using the velocity of sound in the epoxy and the ceramic, which could then be substituted into the Equation 2.6. The velocity of sound in the epoxy has already been determined in a detailed investigation by another author and was found to be $2640 \text{ ms}^{-1} \pm 1\%$ [7]. The velocity of the sound in the ceramic was found by using the method outlined in section 5.3.6 and was found to be $4700 \pm 200 \text{ ms}^{-1}$.

Table 9.1 The predicted operating frequencies based on the measured volume fractions, speed of sound and thickness for samples a1.a and d2.a. The calculated volume fraction from the spreadsheet have also been used, with the measured values, to predict an operating frequency

	a1.a				d2.a			
	Max	Measured	Min	Spreadsheet	Max	Measured	Min	Spreadsheet
V_p (%)	51	49	48	44	49	49	48	46
c_p (ms^{-1})	3800	3650	3500	-	3800	3650	3500	-
t (μm)	162	160	158	-	167	165	163	-
f (MHz)	12	11.4	10.9	11.1	11.5	11.1	10.6	10.9

The volume fraction of both the ceramic and the piezocomposite can be determined from the cross-section of the piezocomposite and by using image analysis software. The approach requires a greyscale image that shows a contrast between the two phases. The pixels that represent the ceramic pillars in the image are darker than the epoxy and therefore have a higher 'grey value'. The user can then select a range of values to identify one of the phases, and the software can calculate the ratio of the two phases. Since the user is involved in this process then there is a degree of subjectivity, and the main error is determined by the range of grey values selected by the user. Therefore, when this process was carried out, three measurements were taken: the measured value; an underestimate; and an overestimate. This gave a typical absolute error of 1%. In addition, the volume fraction can also be calculated

using the dimensions of the sintered pillars and the spreadsheet derived in section 6. The calculations used the median values for each sample, such that for a1.a the kerf and pillar width were 29.7 μm and 68.6 μm , and for d2.a they were 28.5 μm and 69.0 μm respectively. Table 9.1 shows the measured, maximum and minimum values of all of the parameters required to predict the operating frequency of the piezocomposite. In addition the table also shows the estimated operating frequency based on a calculated volume fraction from the spreadsheet. By substituting these parameters into Equation 2.6 the operating frequency can be predicted. Thus, it is expected that the operating frequency of the piezocomposites should be between 10.9 and 12 MHz for a1.a and between 10.6 and 11.5 MHz for d2.a. Figure 9.34 and Figure 9.35 show the impedance and phase spectrum of samples a1.a and d2.a respectively. The figures show well defined peaks at 12.3 MHz, and a smaller peak at 19 MHz for both samples. A pulse echo method indicated that the operating frequency of the two piezocomposites was 12.3 and 12.7 MHz respectively. The pulse echo method is a less accurate method for determining the operating frequency; however, it only uses the thickness mode such that the reading confirmed that the operating frequency of the piezocomposites occurred at 12.3 MHz.

The measured operating frequency showed some discrepancy with the predicted values, and whilst the values were roughly similar, the measured operating frequency is still outside of the error proposed by the prediction. However, the master tool used in this work had not been designed for piezocomposites, such that the lateral resonance mode occurred at 19 MHz, and was less than double the operating frequency. This is believed to have occurred because the lateral resonance mode was too close to the operating frequency. In

this situation it is known that the lateral mode is able to draw the operating frequency towards it [8].

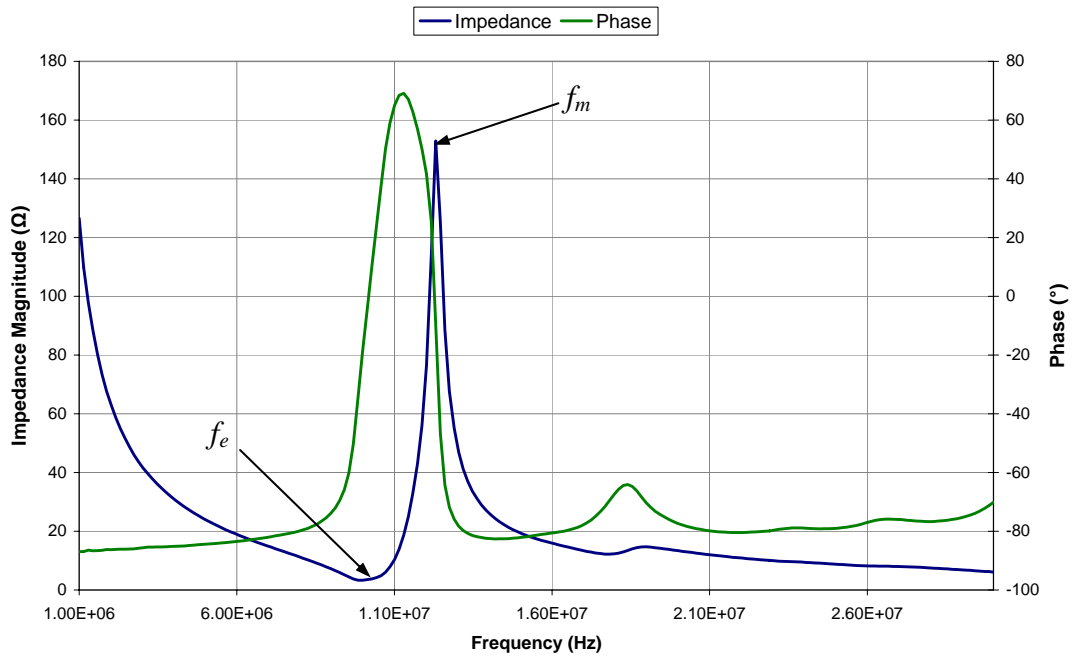


Figure 9.34 The impedance and phase spectrum for sample a1.a showing the position of the electrical resonance frequency, f_e , and mechanical resonance frequency, f_m .

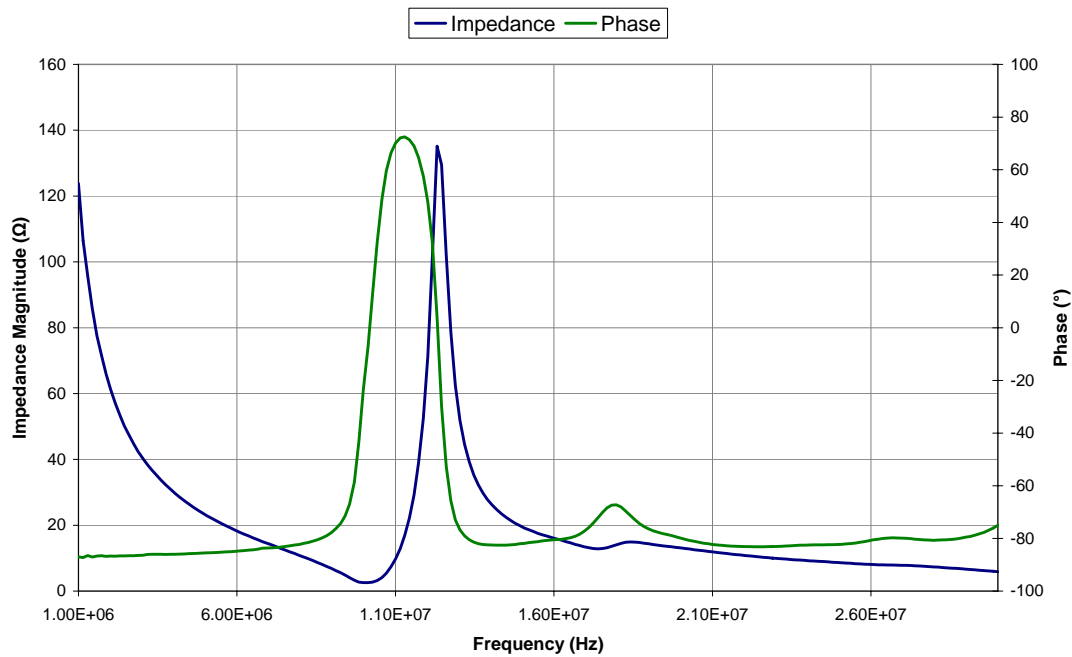


Figure 9.35 The impedance and phase spectrum for sample d2.a

The acoustic impedance has been discussed in section 2.2.1 and is the product of the density of the composite and velocity of sound through it. The densities of a1.a and d2.a were calculated by the ratio of the mass to the volume and were found to be 4900 and 4500 kg m⁻³ respectively. By rearranging Equation 2.6 it was also possible to calculate the velocity from the operating frequency, to enable the acoustic impedance to be calculated to be 19 and 18 MRayl respectively. These values are just outside the typical values for a piezocomposite which are 4-15 MRayl [9], but are comfortably below the typical acoustic impedance of a monolithic PZT transducer which is 35 MRayl. The density values appear to be slightly higher than expected and would therefore increase the calculated acoustic impedance. Nevertheless, these values are reasonable given the relatively high volume fraction.

The typical range of k_t values for piezocomposites is 60-75% [9, 10] and is discussed in section 2.2.3. This can be calculated using the electrical resonance frequency, f_e , and mechanical resonance frequency, f_m , which are shown in the impedance spectrum of Figure 9.34, and can be substituted into Equation 9.2 [11]:

$$k_t = \sqrt{\frac{\pi f_e}{2 f_m} \tan \frac{\pi f_e}{2 f_m}} \quad \text{Equation 9.2}$$

The f_e and the f_m for sample a1.a were 9.99 MHz and 12.3 MHz respectively, giving a k_t of 0.62. For d2.a, f_e and f_m were 10.1 MHz and 12.3 MHz respectively giving a k_t of 0.61. Thus, the k_t of the piezocomposites produced was at the lower end of the typical range for 1-3 piezocomposite. This is hardly surprising, since the pillar aspect ratio was 2.3 and was much

lower than the required aspect ratio of 5 to maximise it [5]. Nevertheless, the k_t was significantly better than either, monolithic PVDF or PZT [9, 10].

The results presented in this section appear just outside of the range of anticipated values, both in terms of operating frequency, acoustic impedance and the k_t . This is because the piezocomposites were fabricated using a master tool that was not originally designed for 1-3 piezocomposite fabrication, nor were the piezocomposites produced using an optimised VP embossing processes. However, they do demonstrate that hot embossing and VP embossing can be used to produce 1-3 piezocomposites with a kerf of $\sim 29 \mu\text{m}$ and a pillar width of $69 \mu\text{m}$.

9.6 Process Overview

The previous sections have focused on the individual process stages for the replication of a nickel master tool into several ceramic and polymer piezocomposites. The ability to successfully replicate the micron scale structures is dependent upon the variability that occurs from pillar to pillar, and the variability seen between the average values of each sample. Furthermore, uniform shrinkage of the structure is beneficial, because it leads to smaller feature sizes, and a higher operating frequency. However, uneven shrinkage complicates the replication process because it changes the ratio between the dimensions and results in a different structure to the one being replicated. This affects the volume fraction, which alters the properties of the piezocomposite. Therefore, it is important to get an idea of where any changes of structure occur in the process, in terms of shrinkage and variability between each sample and within the samples themselves.

Knowledge of the variability within each sample is important because it represents how well the structure has been replicated and is particularly important in an array structure, where the repeating nature of the structure is fundamental. As discussed throughout section 9 a degree of the variability has occurred because of the accuracy of the measurement technique. Thus, an error of $\pm 0.25 \mu\text{m}$ on a perfect array, with no variation in pillar width, could still produce a maximum IQR of $0.5 \mu\text{m}$. It is therefore most appropriate to represent the variability as a function of the error; such that the 'relative variability' is calculated by the interquartile range divided by the maximum range of the error. Values less than one indicate that the repeatability within the sample is better than the repeatability of the measurement technique. Values between 2 and 4 indicate that there is variability within the sample that can be

comfortably detected by the measurement technique, and values greater than 4 show a very large variability, particularly for an array structure.

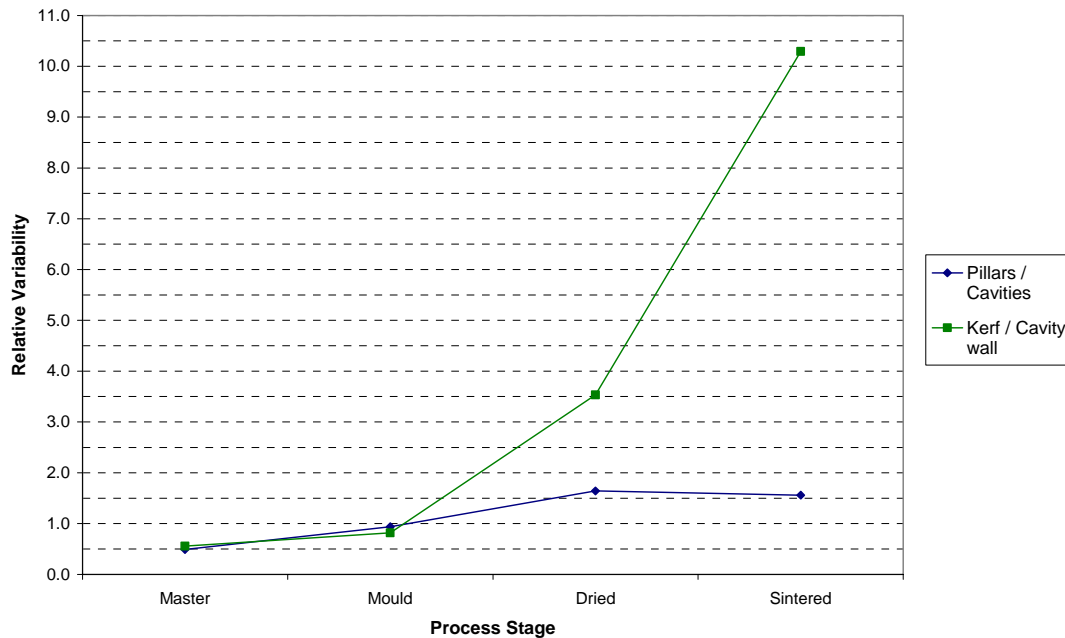


Figure 9.36 The mean relative variability within a sample at each process stage. The figure indicates that the pillar width has remained relatively consistent within each sample at each process stage; but not in the case of the kerf, where the distortion of the array has increased dramatically after drying and sintering.

Figure 9.36 shows the mean relative variability of the pillars and the kerf across all of the samples at each process stage. For both master and mould the relative variability within each sample is below 1 such that to characterise this fully, the measurement technique needs to be made more precise.

After VP embossing the repeatability of the samples decreases, such that the kerf at the drying stage is at 3.5 and the pillar width is 1.5. This change in the variability of the dried pillars is only an increase in the IQR of $0.25\ \mu\text{m}$, or 1 pixel, and can be attributed to the rough edge of the pillar that makes it difficult for the user to identify the boundary accurately. This can be rectified by increasing the VP embossing load to ensure that the pillar attains a smoother surface, or by using a more precise measurement technique. The variation of the dried kerf is

likely to have occurred because of the dissolution process. It is known that the pillars are drawn towards one another by webbing that forms from the remaining polymer in the final stages of dissolution. Improving the green strength of the pillars is very important in this stage, which can be achieved by ensure complete filling and consolidation of the pillars in the mould, drying the arrays for longer to ensure complete removal of the solvent, or by using additives such as a dispersant that may improve the homogeneity of the dough and increase the green strength by cross linking with the binder [2].

During sintering the relative variability of the pillars does not change, which indicates a reliable shrinkage within the sample. By contrast, a dramatic increase in the relative variability is seen during sintering of the kerf. This was discussed in section 9.4, and is likely to be caused by creep. To reduce the variability of the kerf, at both drying and the sintering stages, further work should be carried out to understand the changes that occur during dissolution, and to reduce the effects of creep by optimising the arrangement of the samples in the furnace.

Figure 9.37 shows the relative variability that occurs between each of the sample medians. In this case the relative variability of the master is zero because there is only one master to study. The moulds replicated from it show a relative variability of 1.6 for the cavities, and 3.3 for the cavity walls. This variability is likely to have occurred because of the differences in the shrinkage between the samples, as previously discussed in section 9.2. In addition the shrinkage of the cavities is driven by the shrinkage of the mould walls, such that the walls are likely to vary more than the cavities.

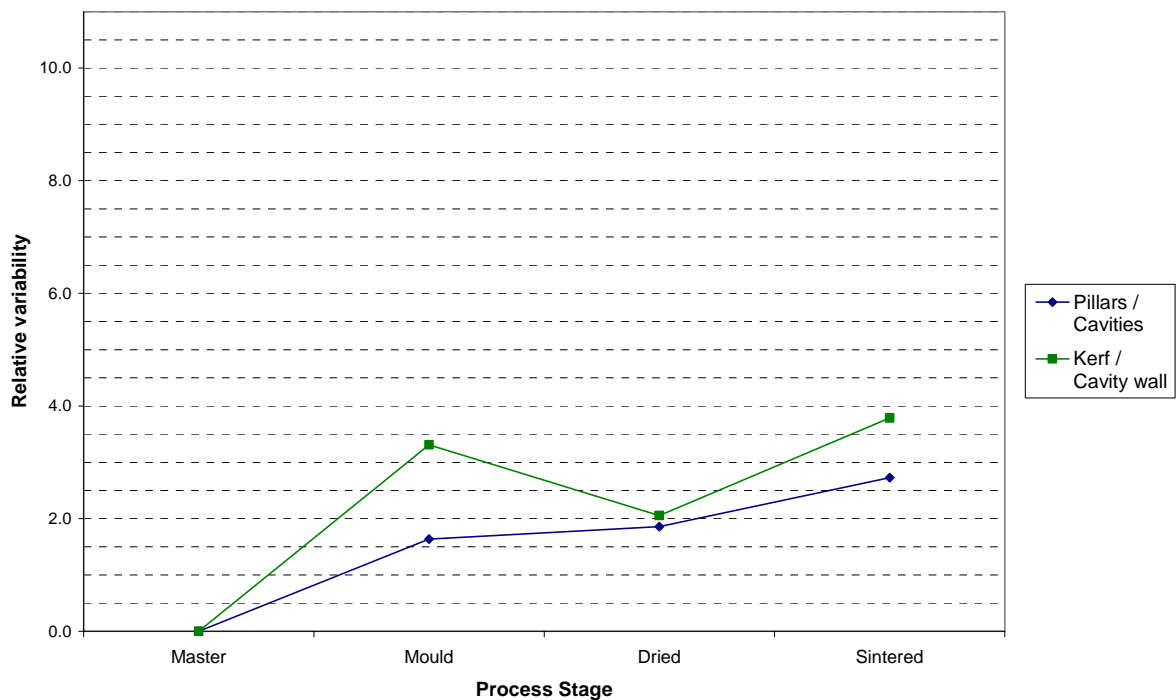


Figure 9.37 The relative variability between samples at each process stage. Between samples the variability is much less than within each sample, such that each sample shows similar levels of distortion. As expected the kerf shows more variability than the pillar width

The VP embossing and drying stage seems to have affected the variability of the pillars by a negligible amount. Such a change corresponds to an increase in the interquartile range of $0.15\ \mu\text{m}$, or less than a pixel. By contrast, the variability of the kerf has reduced from the variability seen in the moulds. At this stage the moulds have been filled with VP dough, which has dried inside the mould, and has undergone mould dissolution. There are several factors that play a part in this process, such as the adhesion of the dough to the cavity wall, the internal stresses from moulding and non-uniform drying, and the effect of the webbing that occurs during dissolution. Obviously, the combination of factors has led to a reduction in the variability between the samples, but it is important that this stage is studied further to control the relationship between the master and the final piezocomposite.

The variability of the kerf and the pillars increases during the sintering stage. This increase is similar in magnitude for both the pillars and the kerf, and is likely to be caused by non-uniform shrinkage between the samples, such that within each sample the shrinkage is uniform, but between the samples it is not. Thus, greater attention should be paid to the VP dough to make it more homogeneous and to develop a predictable shrinkage.

The shrinkage of the kerf and the pillars is not always the same. In some cases the kerf is seen to increase whilst the pillars shrink, which leads a change in the volume fraction. This change in volume fraction is particularly important because it leads to changes in the performance of the piezocomposite. Being able to predict these changes enables a master tool to be designed that will produce the required performance from the piezocomposite.

Table 9.2 The change in median kerf, pillar width and volume fraction with each process stage. The pillar width decreases with shrinkage, whilst the kerf varies because of the distortion and constrained shrinkage leading to a change in volume fraction

Process stage	Pillar / cavity width (μm)	Kerf / cavity wall width (μm)	Volume fraction of pillars / cavities
Master	81.9	31.5	48%
Mould	81.9	30	50%
Dried	78.7	32.7	46%
Sintered	68.7	29.8	45%

The median dimensions of the arrays have been used to calculate the volume fraction of the pillars / cavities, and are shown in Table 9.2. Overall the volume fraction has changed from 48% in the master tool to 45% in the bristle block. Each stage has caused a change in the volume fraction, despite the fact that in an ideal replication process no change should occur. Many of these changes are inherent in the process, such as hot embossing where the cavity cannot reduce to less than the master tool because they are cooled together. However, by

understanding these changes and optimising the process it will be possible to design a master tool so that a piezocomposite with the desired features can be produced.

9.7 Chapter References

- [1] X.-J. Shen et al “Microplastic embossing process: experimental and theoretical characterisations” *Sensors and Actuators: A* 97-98 (2002) 428-433
- [2] D. Zhang “Fabrication of Ceramic Microcomponents” *PhD Thesis, The University of Birmingham* (2006)
- [3] N. J. Porch et al “Net shape processing of piezoelectric ceramics and novel devices” *Processing of Electroceramics Conference, Aug-Sept 3, 2003, Bled, Slovenia* (2003) 293-312
- [4] A. Safari, V. Janas and A. Bandyopadhyay “Development of Fine-Scale Piezoelectric Composites for Transducers” *Ceramics Processing* 43 (11A) (1997) 2849-2856
- [5] K. Lubitz, A. Wolff, G. Preu “Microstructuring Technology” *Ultrasonics Symposium* (1993) 515-524
- [6] A. Abrar et al “1-3 Connectivity Piezoelectric Ceramic-Polymer Composite Transducers made with Viscous Polymer Processing for High Frequency Ultrasound” *Ultrasonics* 42 (2004) 479-484
- [7] A.L. Bernassau “Micro-engineering for High Frequency Ultrasound Arrays” *PhD Thesis, University of Dundee* (2009)
- [8] C. Demore (c.demore@dundee.ac.uk) “ODM” email to L. Garcia-Gancedo (L.GarciaGancedo@bham.ac.uk) (31/10/09 14:15).
- [9] W. A. Smith “The Application of 1-3 Piezocomposites in Acoustic Transducers” *IEEE 7th International Symposium on Application of Ferroelectrics* (1990) 145-152
- [10] W A Smith “Modelling 1-3 Composite Piezoelectrics: Thickness Mode Oscillations” *IEEE Transactions on Ultrasonics, Ferroelectrics and frequency Control* 38 (1) (1991) 40-47
- [11] Y. Hirata “Effects of Aspect Ratio of Lead Zirconate Titanate on 1-3 Piezoelectric Composite Properties” *Japanese Journal of Applied Physics* 36 (1997) 6062-6064
- [12] J. W. Hunt et al “Ultrasound Transducers for Pulse-Echo Medical Imaging” *IEEE Transactions on Biomedical Engineering BME-30* (8) (1983) 453-480

Chapter 10

Summary, Conclusions and Further Work

10 Summary, Conclusions and Further Work

10.1 Summary

Array designs based on circular, square, hexagonal and triangular pillars have been considered in both square and hexagonal packing. Throughout the investigation hexagonally packed, square pillars have demonstrated that they are the most appropriate for hot embossing since they allow the largest feature size, and smallest aspect ratio, to be used for a specific volume fraction. Furthermore if a taper is used, hexagonally packed square pillars show the least variation in volume fraction with respect to depth, and thus will allow a greater range of tapers to be used without affecting the performance of the device.

The calculations also highlighted a significant problem in all 1-3 piezocomposite fabrication routes. Whilst most piezocomposite dimensions scale with each other, the lapping stage has a significant effect because the amount of material that is removed is largely dependent on the skill of the operator, and does not scale with size. Therefore, as the size of the piezocomposite is reduced, the aspect ratio of the device increases, and the proportion of the structure that is lost in the lapping process increases.

The chosen design aimed to produce a piezocomposite with a volume fraction of 50 %, a pillar aspect ratio of 2.5 and pillars with a taper of 0° to 4° . The resultant master tool would therefore have an average pillar width of 112 μm , an average kerf of 46 μm , a maximum aspect ratio of 8.7 and a pillar aspect ratio of 3.6. The design was chosen to minimise the effect of the lapping, since at smaller pillar widths the aspect ratio increased dramatically. A larger scale device, with a smaller aspect ratio, was not chosen because the Bosch process struggled to produce structures that were taller than 400 μm .

The literature review of micro fabrication techniques identified UV lithography, laser ablation and the Bosch process. All of these processes enable a master tool to be produced indirectly, by fabricating a pre-form that can be electroformed into the actual master tool. Feasibility studies into producing the master tool designs were carried out for both excimer laser ablation and the Bosch process. The Bosch process produced tapers ranging from -0.2° to 2.6° , with a surface finish of > 45 nm, and was selected as the micro fabrication technique in this project.

In the Bosch process the upper dimensions of the pillars are controlled by the mask, whilst the pillar taper, and therefore the dimensions at the base, are controlled by the process parameters. Thus, to obtain the required design many iterations are needed to achieve the desired result. Unfortunately, due to time constraints only one taper angle was produced, which was approximately 0.3° . Several pillar arrays were produced, and the best array had a pillar width $121\ \mu\text{m}$, a kerf of $42\ \mu\text{m}$, an aspect ratio of 8.2 and a depth of $346\ \mu\text{m}$. When considering the structures seen in the literature these structures are significant. If just depth, aspect ratio, or an array geometry is considered there are structures with 'better' feature sizes or aspect ratios, however, few combine all three. For example, the high aspect ratio array structures seen in the literature all have very small feature sizes, but none are deeper than $30\ \mu\text{m}$ and therefore are not applicable for piezocomposites. The dimensions achieved here, through the collaboration with the SMC, are the deepest array structure, the second deepest structure, and the third highest aspect ratio array structure made by the Bosch process. Furthermore, it should also be recognised that these structures were significantly taller before lapping, and based on their silicon wafer thickness of $400\ \mu\text{m}$, would have had an aspect ratio of 9.5.

At the University of Birmingham the facilities for hot embossing were not available, and the modification of a materials testing machine was required. The design of the hot embossing rig allowed the heating rate, cooling rate, and the set temperature of the platens to be controlled independently. The range of rates that were made possible by this modified machine was greater than had previously been achieved in the literature; and in particular, better than the cooling rate of the commercial machine, the HEX01. This allowed the possibility of a greater range of parameters to be investigated, and therefore an improved ability to replicate higher aspect ratio, and smaller feature sized moulds.

The low equipment costs and the flexibility of hot embossing have been demonstrated by the modifications costing < £3500, and the set-up times estimated to be a few minutes. The cycle time for producing the hot embossed moulds was 31 minutes. It is considered that this is acceptable, particularly since during scale up more moulds could be produced in one cycle.

Familiarisation work with the hot embossing rig was carried out with the aim of understanding the process sufficiently that a group of parameters could be selected, which would be able to achieve small feature size and very high aspect ratio moulds. The work identified that non-isothermal embossing provided an increased mould fill, and a reduction in the severity of the defects. A linear increase in the de-embossing force was observed with an increase in master tool temperature; and was believed to be caused by shrinkage, particularly when the same effect was observed when the de-embossing temperature was adjusted.

The work also demonstrated that the severity of the defects increased with the embossing force. Thus, once a suitable load had been identified, which did not produce severe defects,

the embossing temperature should be increased first to improve the mould fill. If this was not sufficient, the dwell time can then be increased, with the obvious balance between mould fill, defects, and the cycle time.

The de-embossing temperature was also investigated to identify if a reduction in the de-embossing load resulted in an improvement in the severity of the defects. This investigation demonstrated that the severity of the defects did not change, but resulted in increased deformation of the embossing.

The familiarisation process allowed a selection of process parameters to be identified that enabled small feature size, high aspect ratio structures to be produced. However, time constraints in the project meant that a different master tool to the one produced by the Bosch process was used. This master tool consisted of hexagonally packed, hexagonal pillars and was made by the LIGA process, and therefore did not have a taper.

The pillar width of the master tool was replicated almost perfectly, with both median values measuring 81.9 μm , and a small increase in the IQR from 0.3 μm to 0.8 μm . The kerf, however, was not replicated as well and showed 5 % shrinkage. This resulted in the kerf of the mould measuring 29.8 μm , with an increase in IQR from 0.9 μm to 1.7 μm . The moulds were embossed fully and were measured to be 416 μm high, giving an aspect ratio of 14. When comparing these dimensions to those achieved in the literature it can be seen that only two structures achieved higher aspect ratios, at 19. Several structures have been replicated with feature sizes smaller than 30 μm ; however, all of these structures are not in an array geometry or are connected to a supporting structure. When an array geometry is considered,

the significance of this work can be seen clearly because the moulds produced here have an aspect ratio that is almost twice the size of the previous 'best' aspect ratio. The feature size of the moulds is equal to the previous 'best'. However, the mesh structure with a feature size of 30 μm had only achieved an aspect ratio 2.5 and a depth of 75 μm .

The moulds produced by hot embossing were then VP embossed to produce PZT replicas of the original master tool. After sintering, the pillar width had reduced to $68.7_{-0.5}^{+0.8}$ μm , with a kerf of $29.8_{-0.5}^{+1.2}$ μm . The depth of the pillars was measured to be 350 μm giving a pillar aspect ratio of 5 and a maximum aspect ratio of 11.7. Previously the best bristle blocks produced by VP embossing had a pillar width of 63 μm and kerf of 58 μm giving a pillar aspect ratio of 4.3 and a maximum aspect ratio of 7.2. The work produced here has significantly improved on the previous bristle block made by VP embossing into hot embossed moulds by producing taller pillars with a higher aspect ratio and a smaller kerf. This smaller kerf means that a higher volume fraction has been achieved, and the detrimental resonances that are caused by a similar sized kerf and pillar width do not occur at the operating frequency.

Some of the bristle blocks were taken forward and fabricated into 1-3 piezocomposites. These piezocomposites had operating frequencies of 12.3 MHz, an acoustic impedance of between 18 and 19 MRayl, and a k_t of 61 %. These properties are all on the periphery of typical values for 1-3 piezocomposites, and are attributed to the master tool not being specifically designed for this application.

The work described here is the first time the design of the master tool has been related to the final working piezocomposite. VP embossing into hot embossed moulds has been previously

achieved however this is the first time the whole process from master to piezocomposite has been considered and demonstrated. It is believed that the low capital cost and flexibility of the hot embossing process, will allow this piezocomposite fabrication technique to move out of the laboratory.

10.2 Conclusion

1-3 Piezocomposites offer improved performance over monolithic materials, such as better acoustic and electrical impedance matching and an improved electromechanical coupling factor. Increasing the operating frequency offers the opportunity for their use in many more medical applications. However, the fabrication of piezocomposites for high frequencies is difficult because they require small feature sizes and very high aspect ratio features. VP embossing has been identified as a method for fabricating these devices, but uses the lost mould technique to realise the ceramic structure. Thus, a replication technique is required to overcome the cost of producing and destroying moulds with such a demanding structure.

Hot embossing has been used to replicate PMMA moulds from a designed master tool. Typically, hot embossing uses master tools made by the LIGA process, which is limited by cost and access. An alternative master tool fabrication process has been developed using the Bosch process and electroforming. This process has produced deep array structures with a minimum feature size of 42 μm and an aspect ratio of 8.2, which represents the deepest array structure previously produced by the Bosch process.

Previously, hot embossing has produced array structures with a minimum feature size of 55 μm and an aspect ratio of 7.2 μm . To achieve these structures it was believed that a taper would be required to help de-embossing. However, this proved unnecessary as a master tool without a taper was used to produce PMMA moulds with an aspect ratio of 14, and a feature size of 30 μm , on an in-house hot embossing rig. Two structures have previously been fabricated with an aspect ratio greater than 14, however neither of these were in a geometry applicable to piezocomposite moulds. When mesh structures are considered the aspect ratio

demonstrated here is almost double. The feature size in this work is the same as the previous best, however, the aspect ratio associated with that structure was only 2.5.

The hot embossed structures were subsequently used as moulds in the VP embossing process and produced sintered ceramic structures with 69 μm wide pillars, a kerf of 30 μm and a maximum aspect ratio of 11.7. The previous structures produced by this method only had a kerf of 58 μm and an aspect ratio of 7.2 such that the aspect ratio and the kerf produced here is significantly 'better'. Furthermore they represent an opportunity to produce a piezocomposite that had a kerf that was sufficiently smaller than the pillar width such that detrimental resonances did not occur at the operating frequency.

Several sintered bristle blocks were fabricated into piezocomposites and produced an operating frequency of 12.3 MHz, an acoustic impedance of 18 MRayl, and a k_t of 61 %. These properties were on the edge of the typical ranges for 1-3 piezocomposites, and were caused by the master tool not being specifically designed for piezocomposite applications.

The work presented here is the first time the whole piezocomposite production route has been considered, from design to final piezocomposite. The master tool production technique, mould replication technique and VP embossing technique have all been demonstrated. It is believed that the process presented here will be sufficiently cost effective, after scale up, such that it will enable the piezocomposite fabrication route to move out of the laboratory.

10.3 Further Work

All of the aims and objectives defined in section 4 have been achieved with the exception of identifying the most appropriate taper for de-embossing and piezocomposite performance. This is because aiming for a certain taper is demanding when the master tool is already required to be very high aspect ratio, have a small feature size and a smooth surface finish. It was acknowledged that this would be difficult, and the procedure was developed so that there was a design of each of the target tapers on the mask. Thus, if the combination of Bosch parameters produced a taper of a certain amount, despite this not being the angle that was aimed for, the mask design would be available to produce the correct dimension cavities. Using larger features sizes and smaller aspect ratios, was thought to aid the master tool fabrication, but as the size of the master tool increases so does the depth, which restricts the Bosch process further. Nevertheless, the deepest array structure seen in the literature has been produced. It should therefore be recognised, that the limiting stage in the whole process, is not the de-embossing phase of the hot embossing process, but the fabrication of the pre-form for the master tool.

The initial concept of adding a taper was to improve the aspect ratio and feature size of array structures made by hot embossing. This improvement has been achieved in this work without a taper. Therefore, further work should not focus on producing the remaining four designs, but instead focus on hot embossing with the master tool made by the Bosch process and electroforming. This will indicate if the surface finish of $\sim 1 \mu\text{m}$ is sufficient for hot embossing, and will indicate if the surface finish should be improved. Alternatively, work should also concentrate on producing smaller arrays that will reduce the required depth and increase the operating frequency of the end piezocomposite.

Reducing the feature size of the pillar array structures exposes the design to the issue of lapping depth, such that the required aspect ratio, both for the master tool and the hot embossing process, is increased. A reduction in the amount of material that is removed during lapping is very important; not only for the final stages of piezocomposite fabrication, but also for the master tool fabrication process. Thus, a refinement in the techniques used here will benefit the process twice. The major limitations of lapping were judging the remaining material that needed removing and removing only a few tens of microns at a time.

The lapping depth increases the required aspect ratio for the master tool and thus presents a problem for the master tool fabrication route, but not necessarily for hot embossing. The work presented here has demonstrated that very high aspect ratio, small feature sized array structures can be replicated, but has not identified where the true limit lies. The dimensional stability is the most important feature of hot embossed structures for 1-3 piezocomposites, rather than the surface characteristics for microfluidics, or the residual stress for optical components. In particular, surface defects can be tolerated by the VP embossing process because the replicated defect is removed during the lapping process of the piezocomposite. Therefore, replicating polymer moulds for VP embossing has the potential to produce even smaller feature sizes, and higher aspect ratios without a taper, and should be investigated to determine the true limit.

It may also be possible to reduce the severity of the defects by adding a vacuum clamping system to the lower platen. This will clamp the substrate on its back face rather than just at the edge. This will eliminate the four point bend scenario described in section 8.2.2.3, which

concentrates the stresses and causes the doming effect at higher de-embossing temperatures. Such a clamping system may also be necessary for scale up, as the larger master tool size will only increase the doming effect. Furthermore, the uneven embossing that occurred when the mould fill was investigated may be relieved by adding a ball and socket joint to the upper platen to ensure complete parallelism.

The characterisation of the whole process identified that the replication of the master tool into a polymer mould was relatively accurate compared to the VP embossing phase. However, during the VP embossing process, distortion of the array was seen, and the pillar width and kerf shrank by different amounts. Before a full understanding of the processes involved can be gained, optimisation of the dough composition, mixing procedure and sintering procedure must be achieved. These investigations will demonstrate uniform shrinkage in the dough and minimise creep. Further work should then be carried out in understanding the mould dissolution and drying process, such that the distortion and uneven shrinkage can be controlled.

Chapter 11

Appendix

11 Appendix

11.1 The Glass Transition Temperature of the PMMA

Figure 11.1 shows the glass transition temperature of the PMMA used for hot embossing. The T_g was measured using a differential scanning calorimeter at a heating rate of $10\text{ }^\circ\text{C}/\text{min}$ from $20\text{ }^\circ\text{C}$ to $160\text{ }^\circ\text{C}$. It can be seen from the figure that the T_g was found using the graphical method and was $113\text{ }^\circ\text{C}$.

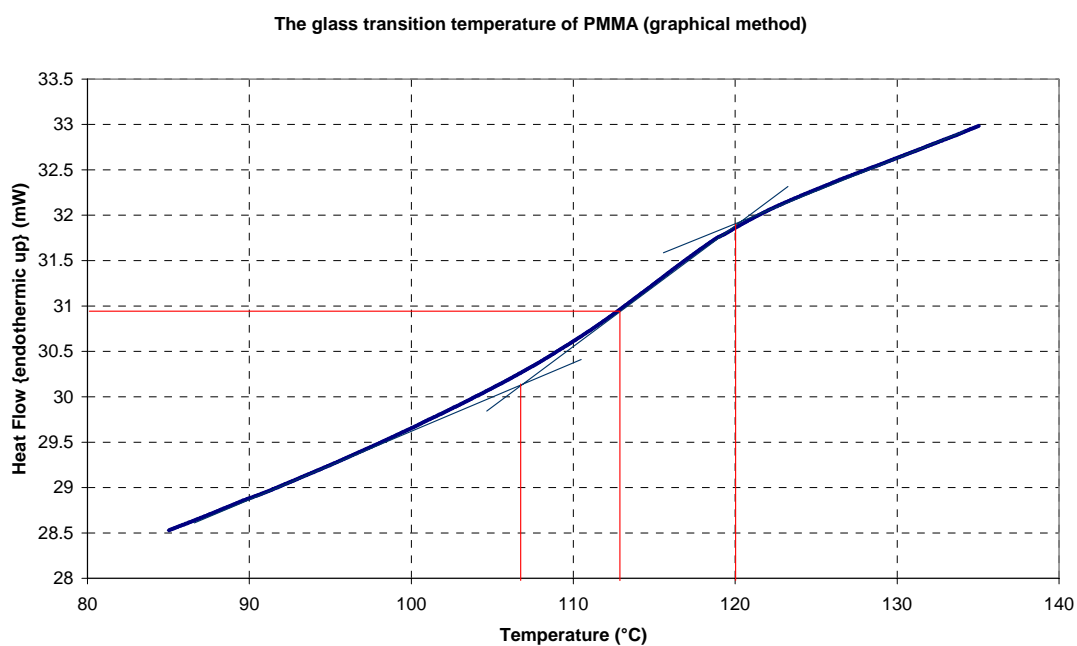


Figure 11.1 The graphical calculation of the glass transition temperature of PMMA measured at $10\text{ }^\circ\text{C}/\text{min}$ and indicates that the glass transition temperature was $113\text{ }^\circ\text{C}$

11.2 Particle Size Distribution

The PZT powder contained hard agglomerates that required breaking-down. This was achieved by vibra-milling in distilled water for 48 hrs, and then freeze drying. The particle size was analysed using laser diffraction in a Helos (H0972) from Sympatec, Bury. The particle size distribution is shown in Figure 11.2, and shows a median particle size of 1.24 μm with Q1 and Q3 values of 0.7 μm and 1.9 μm .

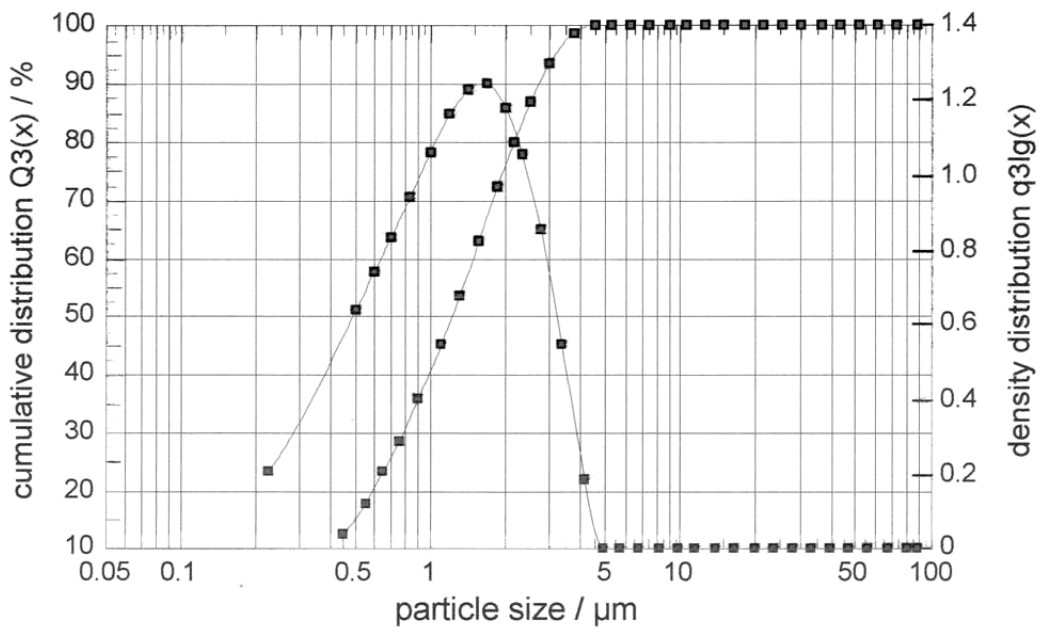


Figure 11.2 The particle size distribution of the PZT after vibra-milling and freeze drying. The median was found to be 1.24 μm and the Q1 and Q3 values were found to be 0.7 and 1.9 μm respectively

11.3 Expanded Technical Drawing of the Corona Poling Jig

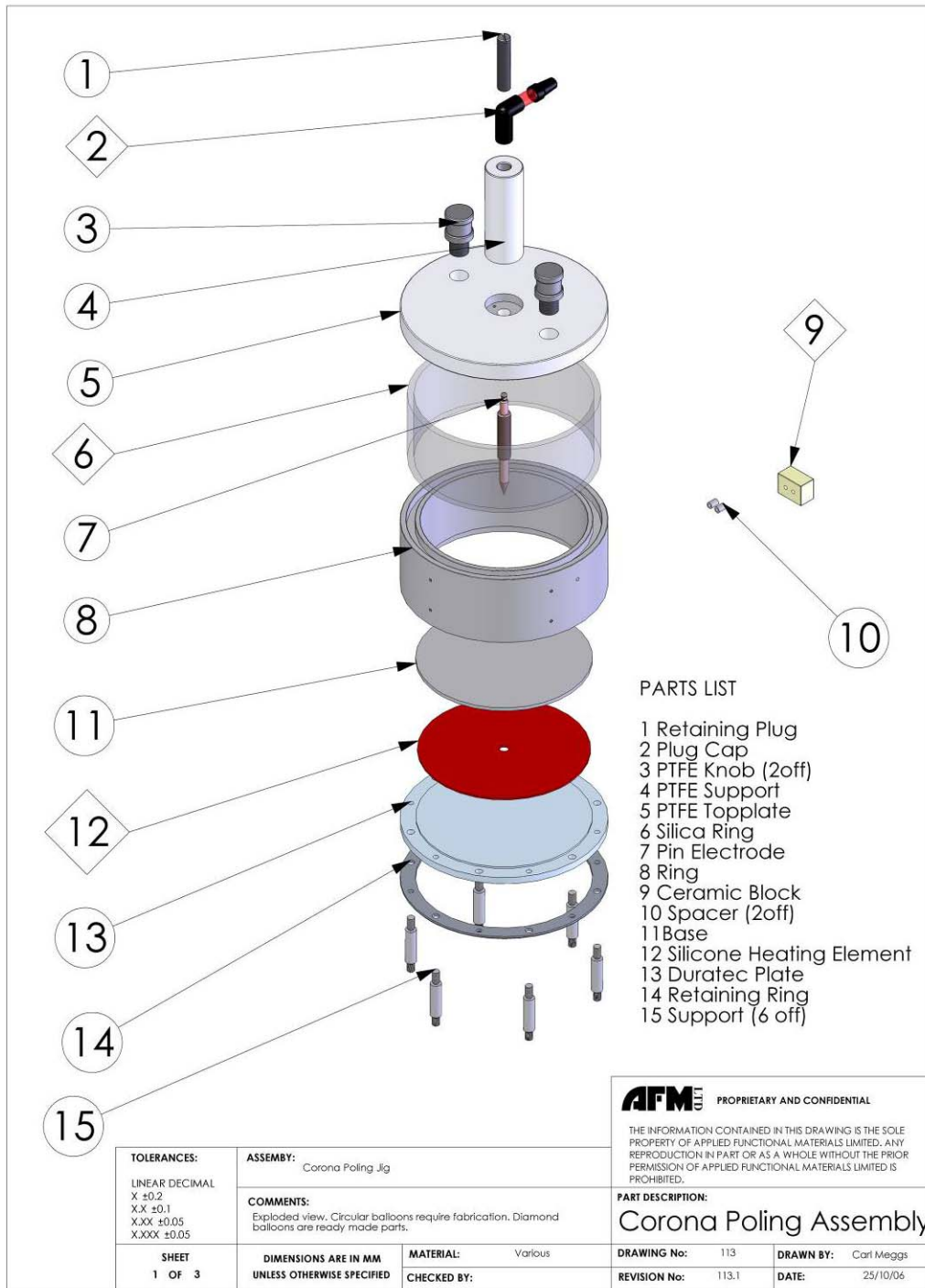


Figure 11.3 An expanded technical drawing of the corona poling jig showing the components used. The jig generates a corona discharge in a heated chamber which makes the piezocomposites piezoelectrically active

11.4 Spreadsheet Screen Shot

A screen shot of the spreadsheet used to calculate the dimensions of the piezocomposite and master tool is shown in Figure 11.4. The figure shows the areas where data is inputted, which includes the required pillar aspect ratio, the pillar width of the finished piezocomposite and volume fraction. The figure also shows where data is outputted to in terms of the pillar width and kerf at the top and the bottom of the array. The worksheet shown in the screen shot calculates the changes in dimensions with respect to a change in the pillar width only, such that a separate worksheet is required to calculate the change in pillar array dimensions with respect to the taper.

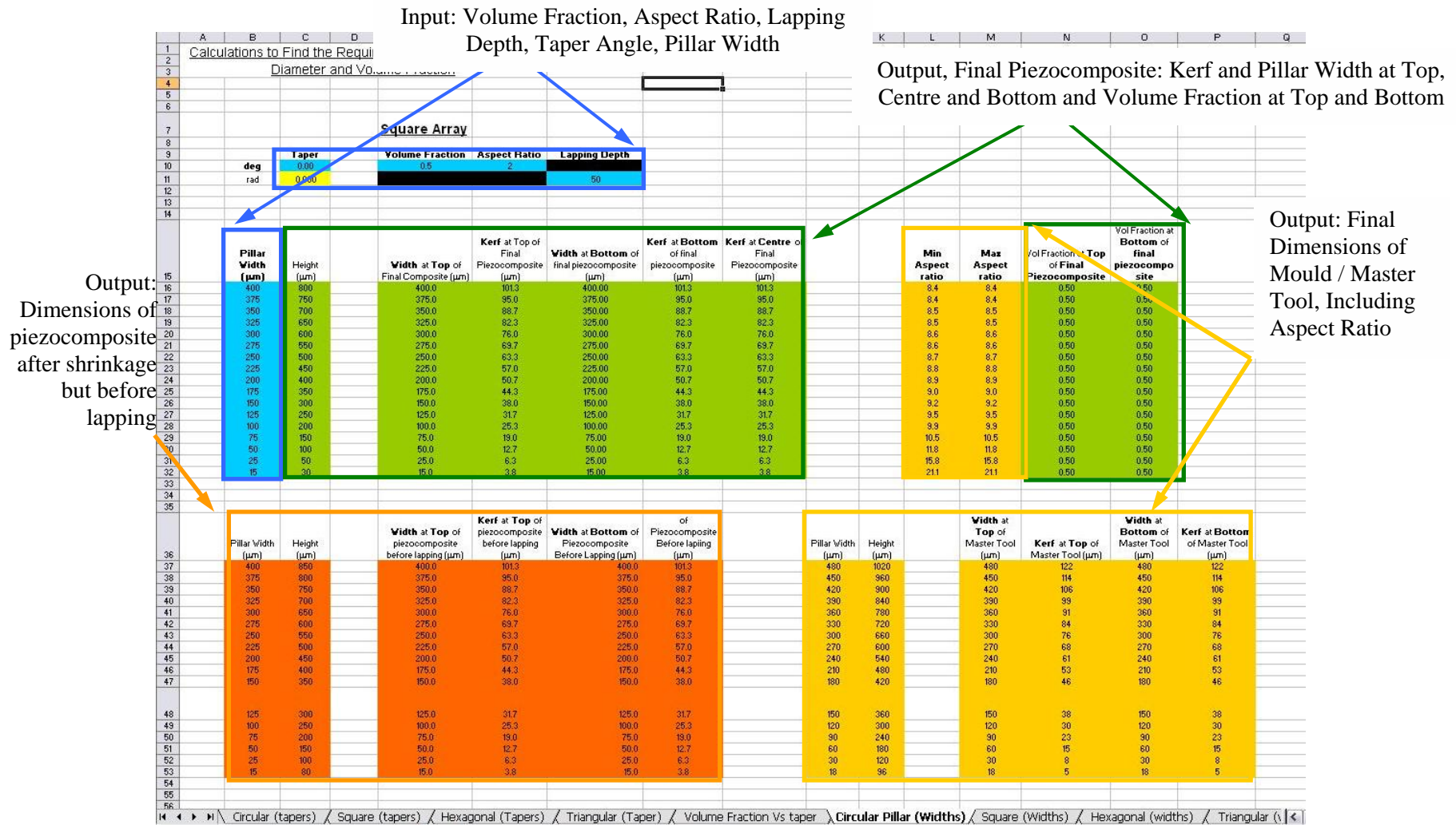


Figure 11.4 An annotated screen shot of the spreadsheet used to calculate the geometry of the piezocomposite and the master tool, showing where data is inputted and where it is outputted. The spreadsheet calculates the pillar width and the kerf at the top and at the bottom of each array for a specified pillar width in the finished piezocomposite

11.5 Additional Details of the Hot Embossing Rig

11.5.1 Mounting Bars

The lower and upper mounting bars are shown in Figure 11.5 and Figure 11.6. The upper mounting bar attaches to the 30 kN load cell and is mounted using a clevis pin, whilst the lower mounting bar screws directly into the load frame. Both bars have an internal thread so that the platens can be screwed into place.

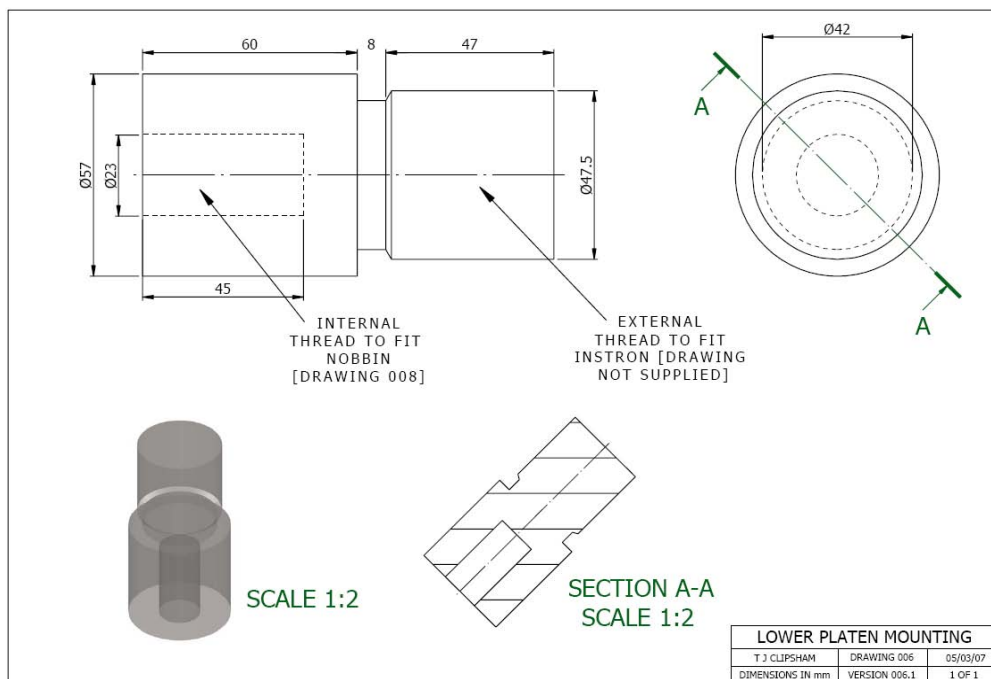


Figure 11.5 Technical drawing of the lower mounting bar, which has an outer thread to screw into the Instron and an internal thread to attach to the platen

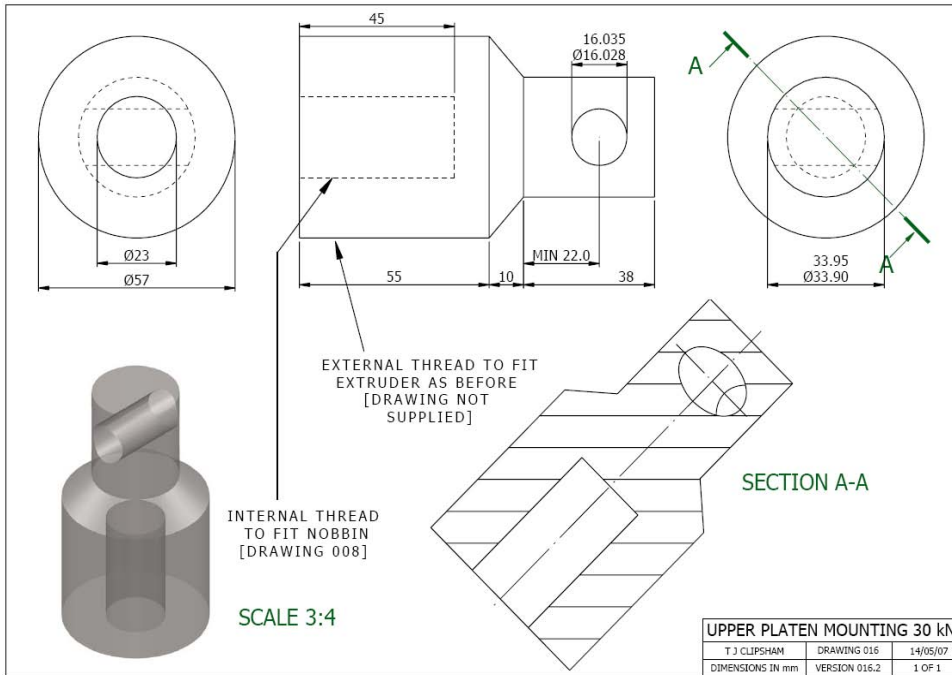


Figure 11.6 Technical drawing of the upper mounting bar that has an internal thread to screw into the upper platen and then a hole for a clevis pin to attach to the load cell.

11.5.2 Control Box Parts list

The components were supplied by RS Components, Corby, and are shown in Table 11.1.

Table 11.1 The equipment list for the electronic components of the control box

Component	Code	From	QTY
SP Snap-in Fused Horizontal Plug w/neon 10A	211-0985	RS	1
Black rewirable straight Socket, 10A 240Vac	488-208	RS	1
K glass miniature fitted plug thermocouple, 2m	363-0294	RS	4
Type K miniature thermocouple inline socket	455-9792	RS	4
12mm blue LED bright satin chr, 12Vac/dc	384-4869	RS	1
12mm IP67 red LED bright satin chrome, 230Vac	384-5339	RS	2
Fuse Holder Screw Cap (5 x 20mm)	359-5999	RS	5
1/16DIN temp controller, 95001PA009	348-8863	RS	2
Temperature indicator/K/N type 10-30Vdc	442-0701	RS	2
Solid state relay assembly, 13A 24-280Vac	492-5767	RS	2
8 pin DPCO plug-in relay, 10A 24Vdc coil	345-886	RS	2
8 pin socket for 10A DPCO plug-in relay	403-213	RS	2
SF series thermal fuse, 240degC 10A	176-9356	RS	5
Standard DIN rail terminal, 2in/1out	426-193	RS	40
Grey 2 tone housing case, 432x280x177mm	222-092	RS	1
WPE 35 earth terminal	193-124	RS	10
3 way ITT JC cable socket, 10A	297-6684	RS	2
3 way ITT JC cable plug, 10A	297-6549	RS	2
IP68 2 way cable plug, 8A	426-0896	RS	1
IP68 2 way chassis socket, 8A	426-1057	RS	1
Power supply, DIN rail, 24Vdc, 2.1A, 50W	528-7915	RS	1
Black re-wireable straight plug, 10A 250Vac	449-922	RS	1
SPST green illuminated rocker switch, 16A	664-935	RS	2

11.5.3 Control Box Layout

The computer aided design software, PowerSHAPE by Delcam, Birmingham, was used to produce models of each component to identify the most suitable layout for the components both internally and externally. These components must be arranged logically so that the

displays can be easily interpreted and the external connections can be connected easily. The external connections, such as the power supply, thermocouples and the flow switch were achieved using plugs and sockets so that the box could be removed from the platens and the Instron.

Figure 11.7 to Figure 11.10 show the different views of the control box and the design images. The displays on the front of the box are split in half, with the displays on the left hand side of the box corresponding to the upper platen whilst the displays on the right correspond to the lower platen. Similarly the same method is used for the sockets, such that if you turn the box around the upper platen sockets are now on the right hand side of the box.



Figure 11.7 The front view photograph of the control box

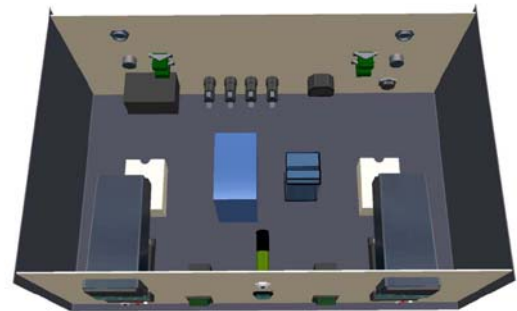


Figure 11.9 CAD drawing of the layout of the rear components inside the control box



Figure 11.8 The rear view photograph of the control box



Figure 11.10 The rear view CAD drawing of the control box